THE STRUCTURE OF AMORPHOUS HYDROGENATED CARBON

A THESIS SUBMITTED TO

THE UNIVERSITY OF KENT AT CANTERBURY

IN THE SUBJECT OF PHYSICS

FOR THE DEGREE

OF DOCTOR OF PHILOSOPHY.

By

Jennifer Walters

July 1995

The endless cycle of idea and action,
Endless invention, endless experiment,
Brings knowledge of motion, but not of stillness;
Knowledge of speech, but not of silence;
Knowledge of words, but ignorance of the Word.
All our knowledge brings us nearer to our ignorance,
All our ignorance brings us nearer to death,
But nearness to death no nearer to God.
Where is the Life we have lost in living?
Where is the wisdom we have lost in knowledge?
Where is the knowledge we have lost in information?

T.S.Eliot

Acknowledgements

Thanks to everyone who has provided help and encouragement over the last three years, especially my supervisor, Bob Newport. I am grateful to the Chemistry Department (UKC) for their assistance with combustion analysis and infrared measurements, and to Spencer Howells and Stewart Parker (RAL) for their help with performing experiments and data analysis. Also, I would like to thank Robert McGreevy, Vicky, and Jim for their help with the RMC work.

Abstract

The structure of several amorphous hydrogenated carbon (a-C:H) samples has been studied in detail using time-of-flight neutron diffraction, inelastic neutron scattering, infrared spectroscopy and reverse Monte Carlo (RMC) computer modelling. Supplementary work has also included combustion analysis. The results are presented as evidence for a new structural model for a-C:H.

The high-resolution real-space neutron diffraction data allows direct determination of the single:double bond ratio, and also shows the presence of sp^1 hybridised carbon bonding environments in some samples. There is limited evidence for the presence of molecular hydrogen "trapped" within the amorphous network. The spectroscopic data is then used to provide information on the C-H bonding environments, so that using a combination of experimental techniques a detailed picture of the atomic scale structure has been produced.

For the hard carbon samples, prepared using acetylene and propane, the carbon-atom sites are found to be predominantly sp^2 bonded, with a single:double bond ratio for carbon-carbon bonds, of about 2.5:1. The effect of beam energy on the structure of the material is also investigated, and comparison made between samples prepared using a fast-atom (neutral particle) source and those prepared by plasma enhanced chemical vapour deposition, from acetylene. The results show that in both deposition methods, increasing the beam energy produces a lower total sp^2 hybridised carbon content in the material with evidence for a shift from pure olefinic to some aromatic/graphitic bonding in one sample. This trend to a more aromatic bonding environment is also observed in samples prepared from a cyclohexane precursor.

The spectroscopy results show that for all samples the hydrogen bonding environments are similar, although there is some evidence for changes in the distribution of hydrogen within the network with deposition energy. The spectra for all the samples show similarities to those for the polymeric materials, polyethylene and rubber.

In addition, the results of a study of the structure of a-C:H up to a maximum of 1000°C are presented. The data show clearly the effect on atomic correlations of elevated temperatures, with the initial room-temperature amorphous network (a mixture of single bonds and olefinic double bonds) becoming progressively aromatic, then graphitic as hydrogen is evolved. Infrared spectroscopy results would seem

to indicate that sp^3 CH is the primary source of hydrogen for effusion, such that, on annealing, molecular hydrogen is formed wherever there are two neighbouring hydrogen atoms. Structural transformations are seen to occur throughout the heating process.

Finally, the RMC method has been used to produce a model for the structure of a-C:H, by fitting to experimental data from neutron and X-ray diffraction experiments. The RMC method was implemented with the introduction of additional constraints on the minimum number of atoms in a ring, and on the maximum coordination number. Once the data has been fitted, it is possible to generate model partial pair distribution functions, bond angle distributions, coordination number distributions, etc.. By fitting all the experimental data sets simultaneously, there is sufficient information to generate a viable "physical" model for the structure of these materials. The effects of increasing number density within the model have also been investigated, and this confirmed that the density is a crucial parameter in the modelling process.

Contents

List of Tables

List of Figures

Chapter 1

Introduction

For a period of over two decades there has been continual growth in our knowledge of amorphous materials and our understanding of their properties, accompanied by their technological exploitation. However, important questions concerning their properties remain unanswered - a situation exacerbated by the increasing complexity of novel materials - and therefore amorphous materials maintain their position of fundamental and technological interest. A prime example of this is the now extensive work on amorphous hydrogenated silicon, a-Si:H [4]. In fact, as novel materials continue to be generated, the range of questions only increases.

The material at the focus of this work, amorphous hydrogenated carbon, a-C:H, is of particular interest as it may be prepared harder, denser and more resistant to chemical attack than any other solid hydrocarbon [1, 5], which, together with the high degree of transparency to the infrared and histocompatibility, have led to many applications [6, 7]. The macroscopic properties are, however, critically dependent on the conditions under which it was prepared [8]. a-C:H can be prepared in forms varying from the soft polymeric (high hydrogen content with many -CH_2- chains) at

one extreme and graphitic (high sp^2 content, low hydrogen content) at the other. Polymeric a-C:H are deposited under conditions having intrinsically low incident particle energies, whereas the graphitic analogue arises from deposition conditions in which there are high incident energies which causes preferential sputtering of hydrogen. Hard, or "diamond-like" a-C:H form under conditions of intermediate deposition energies, which result in a large degree of cross-linking and structural rigidity and an intermediate hydrogen content [1].

In spite of the great potential of the material and the studies so far undertaken (see for example [8, 9, 10]) the structure of these materials at the atomic level is not fully understood; this is of course largely due to the range of potential bonding environments, which allows a complex mixing of atomic-scale correlations.

Current models for the structure involve aromatic/graphitic clusters of sp^2 carbon interconnected with a hydrogenated (or polymeric) sp^3 phase, where it is these interconnections which are said to govern the overall mechanical properties of the material; a more detailed account of these models can be found in the reviews by Angus et al. [1] and Robertson [5, 8, 11, 12]. Data presented in this work suggest this may be an unsuitable model for a-C:H, especially at higher hydrogen concentrations, where sp^2 carbon concentrations are lowest.

This suggestion is supported by the recent results of Frauenheim et al. [13, 14] on molecular dynamics simulation studies of viable structures. Their findings show a system of short chainlike segments showing a markedly low tendency towards aromaticity. The sp^2 atoms are interconnected by homogeneously distributed sp^3 chainlike segments. One must bear in mind the limitations of finite box-size (in this case 64-192 atoms) simulations using approximated potentials, but the molecular dynamics results are clearly at variance with the current models.

The precise nature of the bonding in a-C:H obviously has a crucial role to play in determining the bulk properties, particularly the sp^2 : sp^3 ratio, as these two carbon bonding environments lead to vastly different physical characteristics (for example, diamond and graphite). Of the studies carried out hitherto the results have given sp^2 : sp^3 ratios varying between 1:2 and 2:1, depending on exact deposition conditions, with optical band-gap measurements consistent with the current model of a high degree of clustering of sp^2 carbon sites which would indicate that intermediate, as well as short-range order is important. NMR [15, 10, 16, 169], however, provides reliable information on this ratio and suggests that sp^2 atom concentrations will be slightly greater than that for sp^3 atoms for most a-C:H samples. New NMR results [17] provide a very much more detailed picture on these structural questions.

Attention should also be drawn to the important role played by hydrogen in determining the properties of a-C:H; a role which is crucial to a full understanding of the material. Within the Robertson model, for instance, the hydrogen is seen to stabilise the sp^3 regions, reducing the number of network-terminating bonds, and therefore leading to a maximum hardness at intermediate hydrogen concentrations. Inelastic neutron scattering and infrared spectroscopy can be used to focus on the hydrogen vibration modes in a-C:H and can therefore act as detailed probes for looking at the hydrogen bonding environment. Another question which will be considered concerning the role of the hydrogen in a-C:H, is the possible existence of molecular hydrogen "trapped" within the network.

Diffraction experiments on the other hand provide an opportunity to obtain direct information on interatomic distances and on the average numbers of atoms in each coordination shell. These have been mainly limited to X-ray [18] and electron diffraction [19] thus far; both these probes interact with the electrons surrounding

the nucleus rather than the nucleus itself, and as a consequence of this light elements, especially hydrogen, are virtually invisible and therefore not well detected by these methods. Also the range of data available in k-space is intrinsically too restricted to allow the extraction of high-resolution real-space information. In particular, it is not possible to distinguish different carbon bonding environments on interatomic separations alone; only the mean separation and coordination may be used, with the additional concern that coordination numbers are hard to determine accurately on the basis of X-ray or electron diffraction data.

Neutron diffraction, especially from a pulsed source, overcomes this problem by allowing a significantly wider dynamic range, and with its reliance on scattering from nuclear centres rather than electron distributions, enables the hydrogen bonding environment of a-C:H to be studied. Moreover, the interference function (or structure factor) derived from a neutron diffraction experiment may be placed on an absolute scale: the data are fully quantitative.

The neutron diffraction data presented here is of superior real-space resolution to that available hitherto and the information derived from it has been used to discuss the validity of current models for the structure of a-C:H. Complementary studies using inelastic neutron scattering and infra-red spectroscopy have enabled a detailed investigation into the hydrogen bonding environment, as well as being suggestive of the nature of the network structure. For two samples in particular magic angle spinning (MAS) NMR measurements [17] and molecular dynamics (MD) simulation results [14] have provided significant additional information and a combination of all these results has led to the suggestion of a modified structural model for a-C:H.

The effect of temperature of the structure of a-C:H has also been investigated by neutron scattering and infrared techniques, up to a maximum temperature of 1000°C.

This is important since many of the applications of a-C:H are as hard coatings which may be required to withstand conditions of extreme temperature (and pressure).

In addition, the Reverse Monte Carlo (RMC) method has be used to "model" the data obtained from neutron diffraction experiments. RMC is a method for producing three-dimensional models of the structure of disordered materials that agree quantitatively with the available data, usually diffraction data. Although the model produced must be consistent with the experimental data it cannot be regarded as unique given the intrinsic limitation imposed by using a one-dimensional basis data-set. Unlike MD and other Monte Carlo-based simulation methods, RMC requires no interatomic potential, and it also allows complete data-sets from different sources e.g. diffraction of neutrons and X-rays, to be fitted simultaneously. These factors make it appealing in the study of a system such as a-C:H where an interatomic potential is difficult to define, but a range of high quality experimental data is available.

Chapter 2

Amorphous hydrogenated carbon, a-C:H

Introduction

In order to understand why a-C:H is such a complex material, it is necessary to take a fairly detailed look at the types of bonding that may be present, particularly the different carbon bonding environments. In this Chapter the bonding and structure of a-C:H are examined, and structural models are discussed. These are then related to the properties of these materials, and their applications. Since the structure of a-C:H depends on the conditions under which it is prepared, a discussion of growth processes and mechanisms concludes this Chapter.

2.1 Carbon

Carbon is the most common and probably the most widely studied of the known elements. The electronic structure of the carbon atom ($1s^2 2s^2 2p^2$) makes this element unique in its ability to form three different types of chemical bond, i.e. three different

hybrid electronic orbitals: sp^1, sp^2 and sp^3. Consider, briefly, the characteristics of each of these hybridisations:

sp^3 (found in diamond)

Each of the four valence electrons ($2s^2 2p^2$) forms an sp^3 hybrid orbital which is tetrahedrally directed and can form a strong σ-bond with an adjacent atom. In this case, each carbon atom is 4-fold co-ordinated. This type of bonding is commonly called a "single bond", denoted C-C.

sp^2 (found in graphite)

Three of the four valence electrons form trigonally directed sp^2 bonds (the strong intralayer σ-bonds in graphite), while the remaining valence electron forms a $p\pi$ orbital perpendicular to the (trigonal) bonding plane, which can produce weak π-bonds by overlapping with neighbouring π-orbitals (the weak interlayer π-bonds in graphite). This π-bonding is sometimes referred to as unsaturated bonding, or a "double bond", denoted C=C. With sp^2 bonding the carbon atoms are 3-fold co-ordinated. It should also be noted that there are three different kinds of sp^2 bond which have different bond lengths: graphitic (1.42Å), aromatic (e.g. cyclohexane, 1.395Å) and olefinic (e.g. ethene, 1.34Å).

sp^1 (found, for example, in acetylene, C_2H_2)

Two of the valence electrons form linear sp^1 hybrid orbitals which result in the formation of strong σ-bonds, and the remaing valence electrons form $p_y\pi$ and $p_z\pi$ hybrid orbitals (see diagram below). Carbon in this bonding environment is only 2-fold co-ordinated and this type of bond is commonly known as a "triple bond", denoted

C≡C. Note that structures containing sp^1 bonding usually require elements other than carbon to be stable.

Schematic diagrams to represent each of the hybrid orbitals are shown in Figure 1:

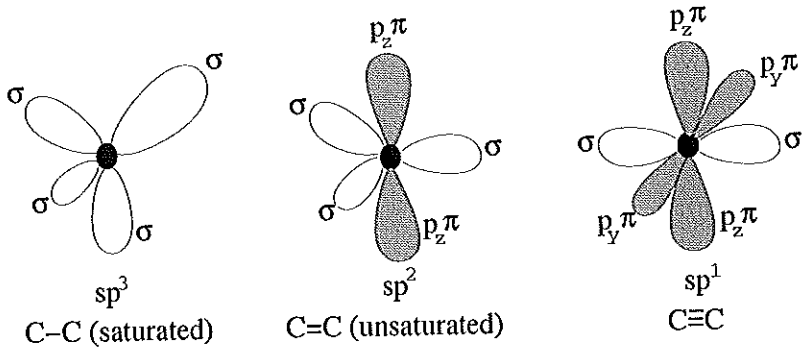

Figure 1: The three hybridisations of carbon.

The ability of carbon to form these different hybrid orbitals is due to the small difference in energy between the $2s$ and $2p$ electronic levels, and more details about hybridisation in carbon can be found in [20].

Perhaps the most familiar forms of carbon are diamond and graphite, but other forms do exist. Graphite is the most stable structure and the atoms are in a hexagonal layer arrangement. Each carbon atom is sp^2 bonded and has three nearest neighbour atoms in a two-dimensional arrangement (σ-bonded). The remaining π-type orbital lies perpendicular to this plane as a "dangling bond" (or π electron band). Cubic diamond on the other hand (the most common and tetrahedral form) is a metastable structure. Like all other metastable forms of carbon, cubic diamond is stable under high pressure and temperature conditions. It has a tetrahedral structure with only sp^3 bonding, without any "dangling bonds". The four other metastable carbon structures are: hexagonal diamond (Londsalite) [21, 22], another hexagonal phase (Chaolite) [23, 24] and two other cubic phases [25, 26]. The properties of each of these different

phases obviously depend on the nature of the carbon bonding i.e. the hybridization state of the carbon. At present, however, the characterisations of amorphous forms of carbon (and hydrogenated carbon) tend to refer to the known properties of diamond and graphite, and this comparison has been continued in this work.

2.2 The structure of a-C:H

Most authors seem to agree that a-C:H contains a mixture of sp^3, sp^2 and (sometimes) sp^1 carbon bonding. By whatever method the sample was deposited, the structure is consistently intermediate between diamond, graphite and hydrocarbon, and can contain variable amounts of hydrogen, sp^1, sp^2, and sp^3 bonding. For example, forms of amorphous carbon with an almost entirely diamond-like structure are known to exist [27]. For a-C:H, however, the main questions concern the distribution of sp^2 and sp^3 carbon in the structure, i.e. is there a random network of sp^2 and sp^3 carbon, or does the sp^2 carbon exist as graphite-like clusters as the theoretical arguments of quantum chemistry [8] seem to suggest?

It is also necessary to consider the role of hydrogen. There is evidence [16] that hydrogen tends to satisfy any "dangling bonds", so, primarily, hydrogen incorporation will saturate π-bonds thereby converting sp^2 carbon to sp^3 carbon sites. Most studies agree that hydrogen bonds to both sp^2 and sp^3 carbon, but preferentially to sp^3 carbon. For example, infra-red data [28, 29, 30] find mainly sp^3 C-H bonds in hard a-C:H, and find sp^3 CH_3, sp^3 CH_2 and sp^2 CH_2 bonds in soft a-C:H. The incorporation of hydrogen is also found to lower the density of the material [16]. This is not primarily an effect of the low mass of the hydrogen atom, but reflects a reduced amount of cross-linking of the carbon network due to the presence of hydrogen. Hydrogen incorporation and/or graphitic bonding both tend to result in a reduction of

the average co-ordination number [1].

So far we have only considered bonded hydrogen, however, there is evidence to suggest that a third to a half of the hydrogen in a-C:H is not chemically bonded to carbon [31, 32, 33]. The role of hydrogen still seems unclear, but experiments suggest the following possibilities:

1. bound and in clusters [32]
2. intercalated between turbostatic graphite layers [34]
3. chemisorbed on internal surfaces [35].

The presence of hydrogen not bonded to carbon may also indicate the presence of microscopic and macroscopic voids throughout the volume of the material, indeed, in an amorphous carbon sample a void network has been found [36].

2.2.1 Structural models

The simplest model consistent with H:C and sp^2:sp^3 ratios is a "Polk-type" [37] model, which consists of a covalent random network of tetrahedrally and trigonally co-ordinated carbon atoms with some bonds terminated by hydrogen [38, 29]. This model gives a simple, homogeneous structure, however, experimental data suggests that the structure should be more heterogeneous. In the interpretation of optical constants, Smith et. al. [39] envisaged a multiphase structure of amorphous, graphitic, diamond-like and polymeric regions with a heterogeneous distribution of hydrogen over the different carbon fractions. Electron spin resonance (ESR) [40] and electron energy loss spectroscopy (EELS) [41] experimental data suggested a structure where regions of polycyclic aromatic hydrocarbon are interconnected with sp^3 carbon. However, the model most commonly used in the interpretation of experimental results at present,

is the non-crystalline "2-phase" model [41], which originated from electron diffraction data [19]. The first phase consists of π-bonded (sp^2) clusters which are embedded in the second phase, a major sp^3 bonded phase which in hard a-C:H is highly cross-linked and in soft a-C:H is a polymeric hydrogenated phase. This model was adopted by Robertson in his quantum chemical calculations, and is discussed in more detail in Section 2.2.3. A summary of this model is given in Table 1 .

	sp^2 phase	sp^3 phase
evaporated a-C	sheets	sheet rims
a-C:H	small clusters	sp^3 or polymeric matrix
determines	electronic properties	mechanical properties

Table 1: Summary of the 2-phase model.

2.2.2 Electronic structure

Before we can appreciate the theoretical work of Robertson on the 2-phase model, it is first necessary to consider briefly the electronic structure of a-C:H. For a complex system such as this, the electronic structure is by no means straightforward, and more detailed accounts can be found in [42].

For any system, the atomic and electronic structure are obviously intimately related. In section 2.1 we saw that carbon can form π- and σ-type bonding, therefore electrons can reside, depending on the carbon bonding environment, in π-, σ-bonding, of π^*-, σ^*-antibonding states. The filled π and σ states form the valence band and the empty π^* and σ^* states the conduction band. The electronic structure of the carbon atom ($1s^2 2s^2 2p^2$) has no core p electrons, so that the $2p$ electrons feel the full core potential. The $2s$ electrons, however, feel a pseudopotential with the short range part screened out by the inner $1s$ electrons. This means that, relatively, the $2p$ orbitals are

more tightly bound that the 2s orbitals, which leads to a stabilization of sp^2 bonds compared to sp^3 bonds (the difference in stability between graphite and diamond is 0.03eV at normal temperature and pressure). Therefore the π-states (which are associated with sp^2 sites) lie closest to the Fermi level and control the size of the band gap. A schematic representation of the electron density of states for diamond, graphite and a-C:H is shown in Figure 2 [12].

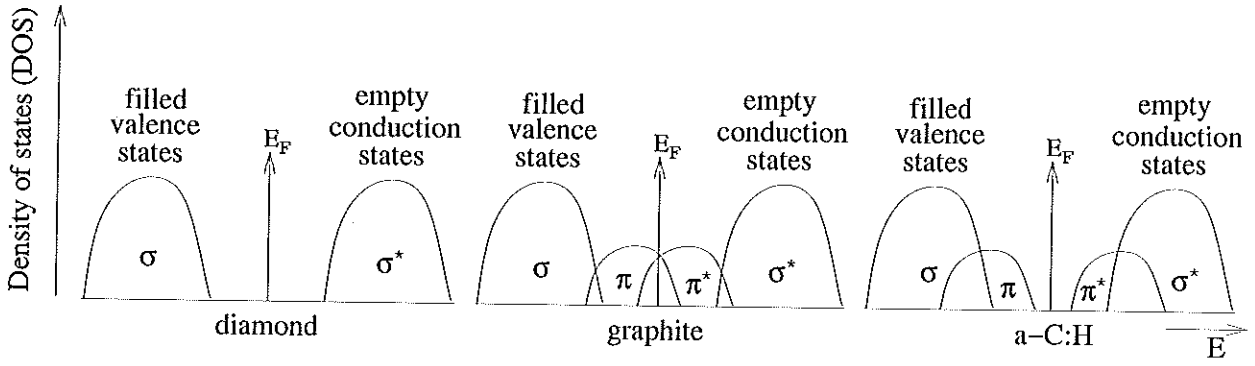

Figure 2: A representation of the electronic density of states for diamond, graphite and a-C:H.

From the diagram above a very obvious difference in the electronic structure is made plain: the size of the band gap. In diamond the band gap between the valence and conduction states is relatively large, making diamond a poor conductor. On the other hand, for graphite there is no band gap, although a minimum in the DOS does occur at the Fermi energy, E_F, giving graphite its properties as a good conductor. The third diagram is for a typical a-C:H sample and shows that although there is a band gap, it is not as wide as that of diamond, which means that a-C:H can be treated as a wide gap semi-conductor. Of course, the size of the band gap in a-C:H is sample dependent and is related to the sp^2:sp^3 and C:H ratios. But the nature of a-C:H, intermediate between diamond and graphite, is clearly shown.

π and σ electron states behave very differently. For the σ-states the bonding is

very localised and so σ electrons control the short range order of the network, i.e. bond lengths and angles, leaving the long range order undefined. The π-states are much more complex: they can form localized bonds, as in ethylene, and resonant, non-local bonds, as in graphite and benzene. So, in this way, π electrons may introduce medium range order into the structure.

To a good approximation σ and π states may be treated separately since in the planar sp^2 sites the electronic orbitals lie perpendicular to each other, and also because the states tend to lie in different energy ranges so the extent of coupling between them is reduced.

2.2.3 The 2-phase model: the Robertson model

Robertson took the 2-phase model and used theoretical calculations to obtain detailed information on the nature of the two phases, particularly the extent and structure of the sp^2 phase. One reason for first proposing a model with aromatic clusters embedded in an sp^3 matrix was the relatively small band gap measured for a-C and for many a-C:H samples. This cluster model was developed using Huckel calculations to model the electronic density of states measured experimentally. A key feature of this method is that creating a band gap at E_F will lower the energy of the occupied states and stabilise the structure.

The Huckel model [43] uses a simplified tight-binding Hamiltonian considering only the π orbitals and nearest neighbour interactions. In this way sp^3 sites are seen as blocking the π interaction from passing through that site (as there are no π states present at that site). So the Huckel model maps the C-H network onto a series of π-bonded clusters and finds a stable structure by maximising the total binding energy per site (E_{tot}) of each cluster.

Investigations using many possible structures have led to the following observations:-

1. Clusters tend to be planar.
2. There should be an even number of sites in each cluster.
3. Olefinic chains are not particularly favoured.
4. E_{tot} is dramatically reduced when aromatic rings form in the structure.
5. E_{tot} is increased if the aromatic rings are fused into layers $\Rightarrow$ graphitic (layer) clusters are favoured over acenic (row) clusters.
6. Compact clusters are favoured over acenic clusters.
7. Quinoid groups are unfavoured.
8. 4-, 5-, 7- and 8-fold rings are unfavoured.

Using this information therefore, we can see that the band gap depends mainly on the MRO, i.e. the degree of clustering. For example, the Huckel model gives the following results, where M is the number of rings:

- for hard a-C:H, typical band gap = 1.2eV: M=25 (largest clusters), M=6 (average cluster)
- for soft a-C:H, typical band gap = 2.5eV: M=5 (largest clusters), M=2 (average cluster).

The important conclusions from this model are that π-bonding strongly favours aromatic rings over olefinic chains and favours the clustering of separate rings into graphitic sheets, making aromatic ring clusters the dominant sp^2 site species. Bredas

and Street [44] independently reached the same conclusions using a more sophisticated model. Also, experimental data from optical absorption, Raman spectroscopy and luminescence spectroscopy are consistent with this model [8].

Note that a necessary part of the Huckel model is that σ and π states can be treated separately. This is justified because the sp^2 clusters tend to be planar so that parallel π states on adjacent sites tend to lie perpendicular to the σ-bonding plane. However, any warping or cross-connection of sp^2 layers may produce σ-π mixing.

2.3 General properties of a-C:H

The properties of a-C:H depend primarily on the nature of the bonding in the material i.e. sp^2:sp^3 and H:C ratios, etc., and these quantities obviously depend on the conditions under which the sample was prepared (a relationship which will be examined in sections 2.6, 2.7. It will be seen that the most important parameter is the ion impact energy. Figure 3 shows the types of films produced at different impact energies for a-C:H deposited from a hydrocarbon source.

As can be seen from this diagram, the properties of a-C:H can vary widely, with a range of many orders of magnitude between diamond and graphite [1, 45, 46].

Koidl et. al. [47, 48] suggested that for some a-C:H samples deposited by plasma deposition the properties are independent of the source gas. This is based on the fact that at high bias voltages the source gas essentially decomposes and maintains none of its original characteristics. However, it was found that although optical and electronic properties follow this rule quite well, other properties such as density, refractive index and hardness do not. According to Tsai [49], density, hardness, stress and optical and electrical properties are primarily determined by the hydrogen content of the material. If we consider the density of an a-C:H sample, for instance, this will depend

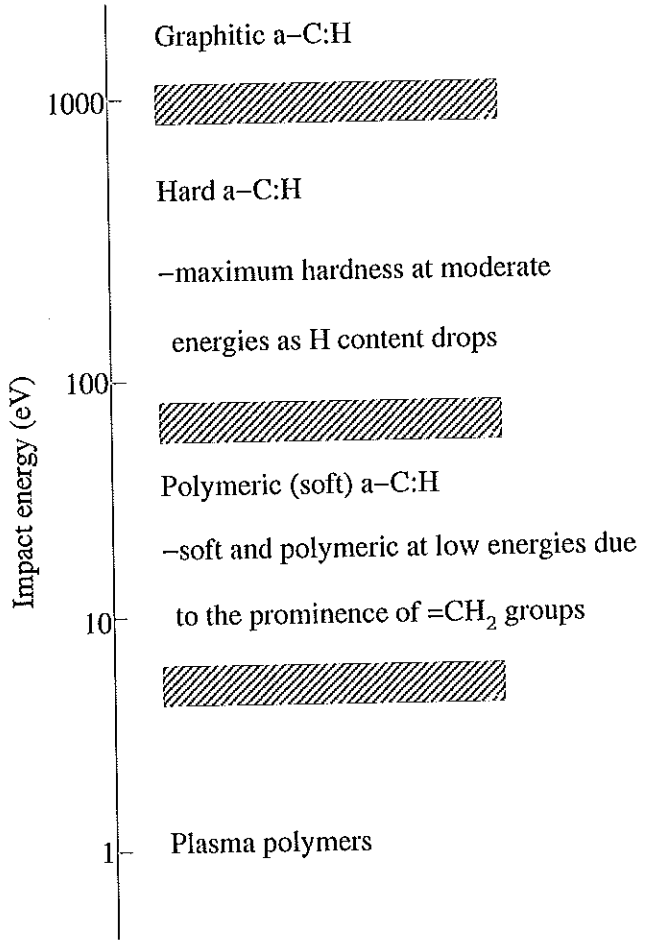

Figure 3: The nature of a-C:H as a function of impact energy [1].

on whether the hydrogen is bonded or just "buried/trapped" within the structure, and so the range of densities reported for these materials is quite broad (see Table 2). And we must also take into account the fact that the microscopic density of the sample may be considerably less than the bulk material due to the presence of voids. So, the properties of a-C:H are fairly complex and can be extremely varied. Table 2 gives a comparison of some of the properties of two a-C:H samples with those of diamond, graphite and polyethylene.

Sample	Density (gcm^{-3})	Hardness (GPa)	% sp^3	at.% H	Gap (eV)	Reference
Diamond	3.515	100	100		5.5	[50]
Graphite	2.267		0		-0.04	[51]
a-C:H (hard)	1.6-2.2	10-20	30-60	10-40	0.8-1.7	[52]
a-C:H (soft)	0.9-1.6	<5	50-80	40-65	1.6-4	[52, 53]
Polyethylene	0.92	0.01	100	67	6	[54]

Table 2: A comparison of some of the properties of a-C:H with diamond, graphite and polyethylene.

Also, a-C:H is generally chemically unreactive to the extent of being inert to organic solvents and inorganic acids including HF.

For some a-C:H materials contamination during deposition, depending on the process, often occurs. The most common contaminants are O, N and inert carrier gas atoms such as Ar, Kr. Inclusions of relatively large graphite fragments can also be a problem for some deposition methods.

Having discussed the general properties of a-C:H, let us consider in more detail three specific properties which lie at the root of many of the applications of a-C:H.

2.3.1 Electrical properties

The electrical properties of a-C:H are determined by the proportions of sp^2 and sp^3 bonding and their distributions within the structure, and therefore have a strong dependence on deposition parameters. Generally, the experimental measurements are consistent with a structure containing both sp^2 and sp^3 carbon, and as the sp^2 fraction is increased there is a greater probability of orbital overlap and therefore there is enhanced conductivity through extended states [55, 56]. So, a high electrical resistivity tends to result when polymeric and sp^3 components are dominant. The resistivity of a-C:H can be up to 12 orders of magnitude higher than that of a-C [57] due to the stabilisation of sp^3 bonds and the passivation of "dangling" bonds by hydrogen: C-H bond formation reduces the density of states in the gap which results in increased resistivity. According to [55], percolation theory implies that at least 50% of the carbon atoms must be sp^2 bonded to give appreciable conductivity, which would indicate that there should be an interconnected network of π orbitals throughout the structure.

There are three observed conduction mechanisms in a-C:H :-

1. hopping between states near E_F
2. thermal activation to a higher density of localised states near a mobility edge
3. thermal activation and conduction in extended states above a mobility edge.

However, the dominant process is hopping between localised states [41].

So far, doping of a-C:H has only caused an increase in conductivity of a few orders of magnitude [58], although the effects of doping are greater in some circumstances, especially for a-C:H produced at higher temperatures [59]. In a-C:H doping is not

seen to be simply substitutional, but involves a combination of substitutional and self-compensation processes [60].

Summaries of the dielectric properties of a-C:H are given by [61, 62]: dielectric constants for a-C:H range from 8-12 and breakdown voltages are $\sim 10^6 \mathrm{Vcm}^{-1}$.

2.3.2 Mechanical properties

In general the mechanical properties of a-C:H depend on the strength of the component bonds and the extent of cross-linking in the sp^3 phase. They will always be inferior to those of diamond due to the finite sp^2 and hydrogen content. Some of the mechanical properties of a-C:H compared to those of diamond, graphite and polyethylene are given in Table 3.

Sample	Young's modulus (GPa)	Bulk modulus (GPa)	Shear modulus (GPa)	Poisson's ratio	Yield stress (GPa)	Hardness (GPa)	Reference
diamond	1050	442	478	0.104	59	103	[50],[63], [64],[65]
graphite	686						[64]
a-C:H (hard)	145	52	24	0.4	9.7	16	[66],[67]
a-C:H (soft)	55	53	31	0.2	31	6.3	[66],[67]
polythene	~0.1					0.01	[54]

Table 3: Some mechanical properties of a-C:H compared to diamond, graphite and polythene (c.f. Table 2).

Hardness is one of the most important and exploited properties of this material. A high hardness is generally associated with high cohesive energy, short average bond length and a high degree of covalent bonding. Measurements of hardness are difficult to obtain for a-C:H as all samples are produced in the form of thin films, however,

looking at the values given in Table 3 and the qualitative observations of [68, 69], we can see that hardness depends strongly on the growth/deposition conditions.

Diamond has a low friction co-efficient so it is expected that a-C:H will generally have a similar frictional behaviour, but with a higher absolute value for the friction co-efficient. Values in the range 0.01-0.28 have been measured [70, 69] for a-C:H.

Wear can occur by several mechanisms (e.g. adhesion, abrasion, tribochemical). The abrasive wear rate of a-C:H varies systematically with hydrogen content, since hydrogen reduces the amount of cross-linking in the network and as it can only form one bond, acts as a network terminator [71]. In one particular study [16], an increase in hydrogen content from 0 to 60% led to a decrease in hardness and an increase in the wear rate of a-C:H by a factor 10^6. Thus wear can be an important limitation in the applications of a-C:H films.

Adhesion is the capacity of a film to remain completely attached to the substrate when the couple is subjected to mechanical sheer or tensile stress [49]. It characterises the rupture strength of the coating/substrate interface and is a very important consideration in many applications of a-C:H, since a coating is only as good as its adhesion to the substrate. Very good adhesion is usually achieved by CVD and ion-plating techniques [72], and sputtering usually results in fairly good film-substrate adhesion. Adhesion is generally limited by the substantial internal stress that a-C:H films usually possess. These tend to limit the adhesion of thicker films especially, and their potential applications. Internal compressive stresses of up to $10^{10}\mathrm{Nm}^{-2}$ have been measured for some a-C:H films [70, 73]. Residual stress develops during deposition due to processes which impede atomic rearrangement, for example, differential thermal expansion, incorporation of impurities, structural re-ordering, etc., and the total stress tends to increase with the film thickness. So, adhesion depends on the substrate

and the deposition method: the best adhesion is to carbide forming substrates, e.g. Si, Fe, Ti. Both adhesion and internal stress thereby determine the stability of the coating/substrate composite, and therefore the durability of the component.

Note that measurements of tribological behaviours such as those mentioned above, are closely related to the testing environment, and that wear and friction are not intrinsic properties of the material, but depend also on the substrate onto which it is coated.

2.3.3 Optical properties

Like the electrical properties, the optical properties of a-C:H are dominated by the relative amounts of sp^3 and sp^2 bonding, such that optical transparency is a result of dominant sp^3 and polymeric components. a-C:H has a characteristically large refractive index, $1.8 \leq n \leq 2.3$ [74, 75] (c.f. for diamond n=2.4), where low index a-C:H tends to be more polymer-like a-C:H. The most important point about optical properties, in terms of potential applications of a-C:H, is that the materials can quite easily be tuned by the deposition parameters [75] to suit particular requirements. This is one reason why most of the applications of a-C:H are in optical coatings (see Section 2.4).

2.4 Applications

Many applications of a-C:H arise to a large extent because of the combinations of unique properties these materials possess. The main useful properties are: transparency (to IR), electrical insulation, high breakdown voltage, high thermal conductivity, chemical inertness to most acids, bases and organic solvents, barrier properties,

hardness, good adhesion to many substrates, low friction co-efficient, wear resistance and smoothness.

Most applications have been as coating materials, especially as a hard, inert, transparent optical coating material, and most make use of the "diamond-like" properties (hardness, chemical inertness, transparency in IR, high refractive index). The possibility of "tailoring" the properties of the deposited material for specific purposes is advantageous for many other applications apart from optical ones, including protective films for magnetic recording materials, heat sinks, solid state devices, moisture barriers, low friction coatings, hard coatings for mechanical tools, and protective coatings compatible with body tissues for medical application [76, 77, 78, 79, 80]. The low deposition temperature also means that a-C:H can be applied to a wide range of substrate materials, however, there can be problems caused by high internal stresses, poor adhesion and poor thermal stability.

Let us briefly list a few specific uses of a-C:H in optics and medicine:-

- Optical - protective coatings for plastic lenses [81]; coatings to improve the transmission of Ge IR optics [82, 47]; coatings for optical elements in high powered lasers [83]; coatings to increase optical loss [83]; coatings on glass fibres to reduce loss of strength with time due to corrosion by water vapour and stress [84, 85]; and for the future perhaps, selective absorbers for solar heating panels.

- Medical - blood compatible coatings for use in the artificial heart program [86, 87]; tissue compatible coatings for artificial organs or biological implants (for the future).

It is in the area of medical coatings that we will perhaps gain the most direct benefit from these materials. a-C:H is particularly useful in this context as it is

not automatically rejected by the body's immune system i.e. it is histocompatible, is biologically inert to blood contact, can prevent harmful substances from artificial organs (such as plasticisers) from leeching into the blood, and conversely, can prevent blood components leeching into the artificial implant and degrading its performance and lifetime.

2.5 Deposition methods

A variety of methods are currently used in the production of carbon films, however, these can all be characterised in terms of these basic approaches:

1. bombardment of a substrate or target with energetic species, and
2. chemical reactions involving hydrocarbons and hydrogen.

Before considering the detailed preparation of the a-C:H samples studied in this work, let us briefly look at the three principal deposition methods. Most of the commonly used methods are modifications or variations on one of these three techniques.

(i) Ion beam deposition (IBD)

Low energy ($\sim 10eV$ - $1000eV$) carbon containing species impinge on a target material or substrate. Variations on this method include:

mass-selected ion beam deposition (MSIB)

- carbon containing ions are selected according to their mass and the energy and momentum of the impinging species is thereby controlled.

sputter ion deposition

- Ar^+ ions (usually) bombard a graphite target and sputter carbon containing species from which the film is deposited.

dual ion or ion assisted deposition

- two sources of ions, one carbon containing and the other (usually) Ar^+, simultaneously impinge on the target.

(ii) Plasma deposition

Energetic species formed in a plasma derived from various hydrocarbon gases bombard substrates placed on a (negatively or positively) biased electrode. Films prepared by this method tend to have a relatively high hydrogen content.

(iii) Chemical vapour deposition

Chemically active hydrocarbon fragments react on the substrate to grow spontaneously the films, under rather unstable conditions. Typically, a high substrate temperature must be maintained.

Obviously, different deposition methods result in films with different structural characteristics. This has led to the development of many different techniques for the production of films with highly specific properties.

2.6 Deposition parameters

In the previous section the general types of films produced by different deposition methods were mentioned. Now a detailed discussion of the factors which will affect the final film and the nature of the changes induced by variation of these factors will

be presented, mainly with reference to ion beam deposition, although many of the arguments also apply to other deposition methods.

1. Impinging species

Most deposition processes involve an unidentified mixture of several species, including carbon ions (positive and negative) and atoms, hydrocarbon radicals and ions, carbon cluster ions (C_n^+), neutral species, and non-carbon species such as hydrogen and argon. Generally, deposition from hydrocarbon species results in a high concentration of hydrogen in the film (a-C:H); Ar is believed to sputter graphitic and amorphous constituents preferentially, enriching the diamond constituent of the film; hydrogen is believed to stabilise sp^3 carbon regions by the saturation of "dangling bonds" and by preferentially etching graphitic constituents.

2. Ion energy

This is the primary parameter that modifies the properties of carbon films. The term "thermal spike" is often used in describing the physical processes involved in this modification. A "thermal spike" refers to the effective local temperature (and pressure) changes produced on ion impact and is therfore related to the kinetic energy of the impinging species. Although this is an extremely localised effect significant modification of the film structure may result. Most carbon deposition systems use species of a broad and sometimes unknown energy distribution.

3. Incident flux

Incident flux has most influence on films prepared from thermal evaporation, although it does have some effect in all deposition methods. Apart from its influence on the

film growth mechanism, the incident flux can be associated with secondary effects such as: substrate temperature, ambient pressure, charging of insulating targets, and the ratio of primary atoms to residual impurity atoms.

4. Angle of incidence

Several phenomena that affect carbon growth are sensitive to the angle of incidence of the impinging species, e.g. the sputter-etch rate, the penetration depth and the reflection co-efficient of the bombarding species. Plasma deposition processes tend to have a wide range of incident angles, while glancing angles are used for Ar bombardment in ion assisted or dual beam deposition: although, generally, ion beam techniques use normal incident angles.

5. Nature of the substrate

The chemistry of the carbon-substrate system affects the adhesion and evolution of the films: carbide forming substrates are more likely to form adherent films and have a high reaction probability for carbon. Also, the carbon-substrate solubility and diffusion rates determine the purity of the resulting film. The nature of the substrate (amorphous, polycrystalline or single crystal, crystal orientation, phase) affects the possibility of crystalline orientated or epitaxial growth, and the site occupation of impinging species - collectively these are known as "mould" effects. In CVD processes, surface roughness is known to induce the nucleation of diamond crystallites and surface cleanliness is also important.

6. Substrate temperature

Substrate temperature influences the structure and the phase of the films by determination of the diffusion rate (of carbon, and of substrate substitutional and interstitial atoms and vacancies) and the thermodynamic equilibrium of the carbon-substrate system. CVD processes normally require elevated substrate temperatures, but in IBD and plasma deposition, high substrate temperatures are often associated with low sticking probability of impinging species and graphitization of the films.

7. Environment

Poor, uncontrollable vacuum conditions may be one of the reasons for poor reproducibility of films in many deposition systems. Also, since some of the residual gases are incorporated in the evolving films, a high ratio of deposition flux to residual gas flux is needed - the purity of the film may be significantly affected if the practical fluxes obtainable are not high enough to dominate the effects of a poor base vacuum.

2.7 Film deposition and growth

The relationship between the deposition parameters and the nature of the deposited film is obviously not straightforward. In any deposition technique, there are many chemical and physical processes occurring simultaneously, so that even if all these processes are well-characterised in isolation, devising a scheme to describe their interaction is very difficult indeed. This is not helped by the fact that many of the deposition parameters described above are often unknown, or poorly defined. Nevertheless, it is worthwhile considering the type of processes involved in deposition and growth of these films and then looking in detail at how some of the deposition

parameters affect the structure of the resultant film.

In a somewhat simplified description, there are three basic processes which contribute to net film growth:

(i) shallow ion implantation, or "suplantation", by hyperthermal species

(ii) continual surface deposition by thermal species, and

(iii) (sometimes) chemical reactions at the surface.

The last two on the list are fairly self-explanatory and are described by surface chemistry which will not be covered here. The interesting, and possibly the dominant, mechanism in IBD is subplantation. The subplantation model for the growth of films was developed by Lifshitz in 1989 [88, 89], succeeding the "thermal spike" model of Weissmantel [45] and the explanation in terms of "preferential sputtering" by Angus et. al. [1], although minor refinements of the original model have since been made.

2.7.1 The subplantation model

In the subplantation model, growth of the film occurs via the following steps:

1. Penetration by the bombarding species in the target matrix.

2. Stopping of the energetic species in the target matrix.

3. Occupation of a site in the host matrix.

4. Internal subsurface growth.

5. Change in the surface composition.

6. Determination of the film structure.

The penetration depth, trapping efficiency and distribution in the target material depend on the type and energy of the bombarding species and the nature of the target material (i.e. its mass, chemical composition, phase and crystallinity). Also, some of the bombarding species may be reflected and therefore do not contribute to the growth of the film directly, but may transfer energy to the target atoms. Once the impinging species have penetrated the target surface, energy loss occurs by three principal mechanisms: atomic displacements, phonon excitations and electron excitations. These mechanisms can play a significant role in determining the final structure of the film. Also, it is assumed that the trajectory and energy loss process for each impinging atom are independent, however, this is not always the case, e.g. for high fluxes of penetrating atoms, or for the impingement of molecules. In these cases, the energy loss processes of two or more species simultaneously entering the same region are interdependent.

The possible initial states occupied by the stopped atom are determined by the host matrix, i.e. the matrix serves as a "mould" for the structure of the film. This is especially important for films grown on crystalline substrates, where epitaxial and/or preferred orientation of the films may occur. With further impingement of energetic species, re-crystallization may occur, due to collisions or compositional changes, and atoms may be moved from their initial sites.

Continued penetration of the target matrix results in an increase in the concentration of bombarding species in the host matrix which form an inclusion of a new phase and also produce outward expansion of the subsurface layer. As the process proceeds, the surface (initially composed of substrate atoms) is sputtered and/or diluted by ion mixing mechanisms until it consists of only projectile species. Therefore, for the case of a non-carbon substrate, initially there is "heterodeposition" which will be followed

by "homodeposition".

The phase and structure of the evolving film are determined by:

(i) the "mould" of the host matrix - this determines the site occupancy of the penetrating species and constrains the initial evolution of the new phase,

(ii) the preferential displacement of low displacement energy (E_d) atoms, leaving atoms with high E_d in their more stable positions,

(iii) the diffusion rates of vacancies and interstitials created in the deposition process - if a high concentration of interstitials is formed, then an athermal spontaneous transformation to a new phase occurs.

It should be pointed out that, simultaneously with the mechanisms described above for the growth of films, processes are occurring which contribute to "erosion" of the evolving film, e.g. collisional and chemical sputtering. Therefore, for film growth to happen at all, it is necessary that film growth processes exceed sputtering.

2.7.2 The roles of various factors in the subplantation model

1. Incident flux

Films generally evolve through three phases: carbidic → graphitic → diamond-like. Firstly, penetration of carbon into the substrate matrix (M) forces the formation of C-M bonds, even when no stable carbide is known. At high fluxes, the increase in local carbon concentrations results in the formation of a two-dimensional carbon layer (graphitic). If the local carbon concentration is increased further still, then a three-dimensional carbon phase is formed - this may be graphitic or diamond-like depending on the deposition conditions.

2. Energy

The energy of the bombarding species is the critical parameter affecting the nature of the resultant film. A minimum energy of 10s of eV or more is required for true subsurface entrapment of the carbon and a small migration probability to the surface, so the energy of the impingent species determines its penetration depth. For example, for species with energy $\sim 1keV$, a very high flux is needed for the incorporation of a local concentration of carbon and a substrate layer of at least $\sim$ 30-50Å has to be sputtered before the pure carbon layer is exposed.

Energy is also an important consideration for the extent of sputtering and damage. Preferential sputtering of graphitic and amorphous carbon constituents, enriching the diamond-like content of the film has been suggested as a mechanism for diamond growth. However, no experimental or theoretical results support this; instead, currently accepted mechanisms invoke the idea of preferential displacement, i.e. atoms in certain sites are more easily displaced than others. The experimentally determined displacement energies (E_d) associated with graphite ($25eV$) and diamond ($80eV$) (although there exists some disagreement about these values) suggest preferential displacement of low E_d (graphitic and amorphous carbon) atoms, leaving high E_d (diamond) atoms in their more stable positions. The number of displacements per impinging ion is high for both graphite and diamond at high energies, causing significant damage and amorphization. So, at high energies ($> 500eV$) amorphous carbon films are expected: the optimum energy range of C^+ and C^- ions for the growth of diamond or diamond-like films is $\sim 100 - 200eV$.

At low energies (but high enough for subsurface entrapment), impinging species cause very little displacement and penetrating species tend to be trapped as interstitials. If the interstitial concentration becomes high then an athermal, spontaneous

transition to a new phase may occur. The "mould" effect of the substrate may favour diamond formation, as may the highly excited environment due to the electron and phonon excitations, i.e. "thermal spikes". A denser, diamond-like phase is also favoured as it reduces the volume expansion and stress involved in the transformation.

At intermediate energies, preferential displacement becomes effective, favouring the formation and stabilization of diamond sp^3 inclusions. At high energies the damage is high for all carbon forms and an amorphous material results.

3. Angle of incidence

Glancing angles of incidence are expected to result in shallower subplantation, and increased backscattering. The enhanced backscattering increases the sputtering yield of different carbon phases, therfore, for normal angles of incidence, the sputtering yield is expected to be low. The amount of damage and the relevance of the preferential displacement mechanism are also sensitive to the incident angle. This is due to the different displacement energies needed for recoiling atoms along different crystallographic directions. Impingement at grazing angles is associated with a large velocity component parallel to the surface which enhances surface mobility and may contribute to surface, rather than subsurface, deposition.

4. Nature of the substrate

Since the first step in film deposition involves the interaction between the projectile and the substrate, it is obvious that the substrate material plays a significant role in film deposition. For instance, the purity of the film depends, amongst other things, on the extent of the inter-mixing between projectile and target atoms (either collisional

or diffusional). When the diffusion rate of the carbon species is high compared to the incident flux, a low concentration carbon solution in the substrate results.

As we have already seen, the "mould" effect of the substrate material may have a significant influence on the structure of the film. While the initial stage of film growth on a non-carbon substrate involves heterodeposition, the second stage involves homodeposition of carbon on a carbon layer: this is a more favourable matrix for epitaxial growth. Also, the "sticking probability" or adhesion of the impinging carbon species is affected by the carbide-forming capability of the substrate.

5. Substrate temperature

Two different considerations are involved in discussions of the effect of substrate temperature:

(i) the thermal stability of the final film, and

(ii) the evolution of the film upon bombardment by carbon species on a hot substrate.

Carbon films (hydrogenated and unhydrogenated) tend to graphitize upon annealing to temperatures of $\sim 400°C$ and higher (graphitization of a-C:H is associated with hydrogen release). This tendancy is accelerated when interdiffusion between the carbon layer and the substrate exists.

During deposition, evolution of the carbon structure with substrate temperature is associated with the mobility of carbon interstitials, which increases with temperature. Impingement of carbon species at low substrate temperatures creates immobile carbon interstitials, whose concentration increases with incident flux, inducing strain within the matrix. This may then result in a spontaneous transformation as mentioned previously. Athermal transformations such as these tend to result in the formation

of a diamond phase. If the substrate temperature is increased then the interstitials become mobile and migrate to the surface, thereby releasing stress in the film, and leading to the formation of graphitic layers. This is in contradiction with the "thermal spike" model where the evolution of diamond films is predicted to be independent of substrate temperature.

6. Impinging species

(i) C_n species ($n > 1$)

Assuming that the impinging fragments have sufficient energy to penetrate into sub-surface layers, for single isolated atom impingement it is reasonable to assume (due to the short relaxation periods of excited atoms along a single trajectory) that each single trajectory is independent. This is not the case for correlated molecular fragments. In this case, it is assumed that each fragment moves in a matrix excited by the other fragments resulting in a virtual matrix with (effectively) reduced displacement and binding energies.

(ii) Charge

Ions approaching the surface are neutralised by excitation processes in the surfaces that depend on the ion-surface interaction. There are also practical problems associated with deposition from charged species such as charging of insulating targets. No significant effects are expected for deposition from ions of energy $\sim 50 - 100eV$ as the energy difference between the electronic configurations of, for example, C^+ and C^- is small ($\sim 10eV$) compared to the ion energy ($\sim 100eV$).

(iii) Argon and hydrogen

Ar hyperthermal species are often used (simultaneously with carbon species) for carbon deposition, where they are supposed preferentially to etch amorphous and graphitic carbon constituents of the film. Ar, however, contributes no carbon interstitials to the evolving film (essential for the evolution of diamond layers according to the subplantation model) and is trapped within the film matrix, contributing to stress and damage, and changes of properties induced by the presence of impurity atoms. Also, the sputtering yield of carbon by Ar ions is extremely low: an Ar flux at least 100 times more intense than the carbon flux is needed to sputter the amorphous carbon and graphitic constituents effectively. In fact, Ar entrapment and damage is expected under these conditions. Efficient preferential sputtering by Ar of carbon, at glancing angles, to form diamond is not practically obtainable.

Hydrogen plays an essential role in CVD processes where it preferentially etches non-diamond constituents, but very high hydrogen concentrations and substrate temperatures are needed. In IBD processes, however, hydrogen has a low displacement efficiency, low sputtering yield and high backscattering yield for bombardment of carbon. Hyperthermal hydrogen species are thus inefficient at preferential displacement and preferential sputtering processes, although the hydrogen is expected to be entrapped in the carbon layer, forming films with high hydrogen concentration. The range of penetration depths for hydrogen species is expected to be large, but they are not expected to produce very much damage. The main energy loss mechanism for hydrogen species is electronic excitation. Generally, amorphization may be associated with ionization processes in the graphitic film and with C-H bond formation. Chemical sputtering of carbon by low energy hydrogen may result in the enhancement of collisional sputtering and removal of Ar (if present).

(iv) Hydrocarbon species

Impingement by hydrocarbon species is a complex phenomenon even under controlled, well-defined conditions, making a rigorous treatment of film growth phenomena practically impossible. However, the subplantation model produces the following arguments:

1. Impingement of low energy hydrocarbons where the energy is insufficient for dissociation, results in the deposition of hydrocarbon polymer films.

2. Higher energy impingement by C_mH_n molecules results in complete dissociation of the C and H constituents. Then, the average energy of each atom is proportional to its mass:

$$E_C = \frac{12E}{12m+n} \; ; \; E_H = \frac{E}{12m+n}$$

where E is the energy of the undissociated hydrocarbon fragment and E_C and E_H are the energies of the dissociated carbon and hydrogen atoms, respectively. Notice that $E_C = 12E_H$.

3. The low energy hydrogen can: (i) be trapped, (ii) be reflected, or (iii) chemically etch the evolving carbon layer.

4. The trajectories of all the species in the target matrix are correlated and the same argument concerning the effective lowering of displacement energies, etc. apply as for the C_n clusters.

5. Due (mainly) to the difference in energy, the projected range of the penetrating hydrogen species is much lower than that of carbon species. This may lead, at high enough energies, to separation and the formation of a shallow a-C:H

layer and a deeper, dense carbon layer. If, in the shallow region, the amount of hydrogen reaches saturation, a significant portion of it will be released. Also, if the etching efficiency of low energy hydrogen is high enough, the a-C:H layer will be etched leaving a dense carbon film with a low hydrogen content.

6. The lower mass of hydrogen means that it has a lower E_d than carbon. So preferential displacement of hydrogen atoms leaves carbon atoms in their positions and also leads to preferential C-H bond breaking ($\Delta H = 3.5eV$ for C-H, $7.5eV$ for C-C). These mechanisms tend to assist in the formation of dense diamond-like carbon films.

   Generally, for deposition involving hydrocarbon species, the following trends in the nature of the deposited films are observed (see also Figure 3):

   (i) polymer hydrocarbon film formation at low energies,

   (ii) amorphous hydrogenated carbon films at intermediate energies,

   (iii) dense, diamond-like carbon film formation (with low hydrogen content) at high energies, and

   (iv) at very high energies graphitic films.

2.7.3 Deposition of a-C:H

We now wish to apply models for the growth of carbon films to the deposition of the samples used in this study. Unfortunately, as the deposition parameters are not well-known, we will not be able to obtain a detailed mechanism for the growth of these films, however, we can use the information we do have to attempt to predict trends in the structure with deposition energy and precursor gas.

A detailed description of the fast-atom deposition method will be given in the section covering sample preparation (in Chapter 4). For a discussion on growth mechanisms though, we have the following information available:

- the bombarding species are predominantly neutral

- the range of (maximum) effective beam energy covered is $\sim 500 - 900eV$

- the incident flux consists of dissociated atoms and an unknown range of hydrocarbon fragments

- a normal angle of incidence is used

- a copper substrate is used which is at room temperature

- the precursor gases used are: acetylene, propane, cyclohexane and deuterated cyclohexane. A schematic representation of some of the processes to be considered is shown in Figure 4.

Perhaps the most obvious point is that hydrogen is present in all the precursor gases, so we expect to deposit a-C:H, not pure carbon films. A Cu substrate is used so that the samples can be prepared as powders. Cu and carbon atoms do not form a stable carbide, and indeed appear to be largely immiscible, and no Cu-C bond formation is observed. So the film adheres to the substrate in only a very weak fashion and for only a short length of time before dropping off as a powder. The immiscibility of Cu and carbon also means that the "mould" effect of the Cu substrate on the evolving film is negligible. Finally, Cu is effective at rapidly distributing the energy of relaxation processes, thereby reducing the effect of thermal processes post impingement. The compressive stresses induced in the film during deposition assist the rapid precipitation of the powder, although one might consider that with such a short contact time, there is the possibility that a layer of substrate atoms may be entrapped between the subplantation and surface growth. The observed high purity

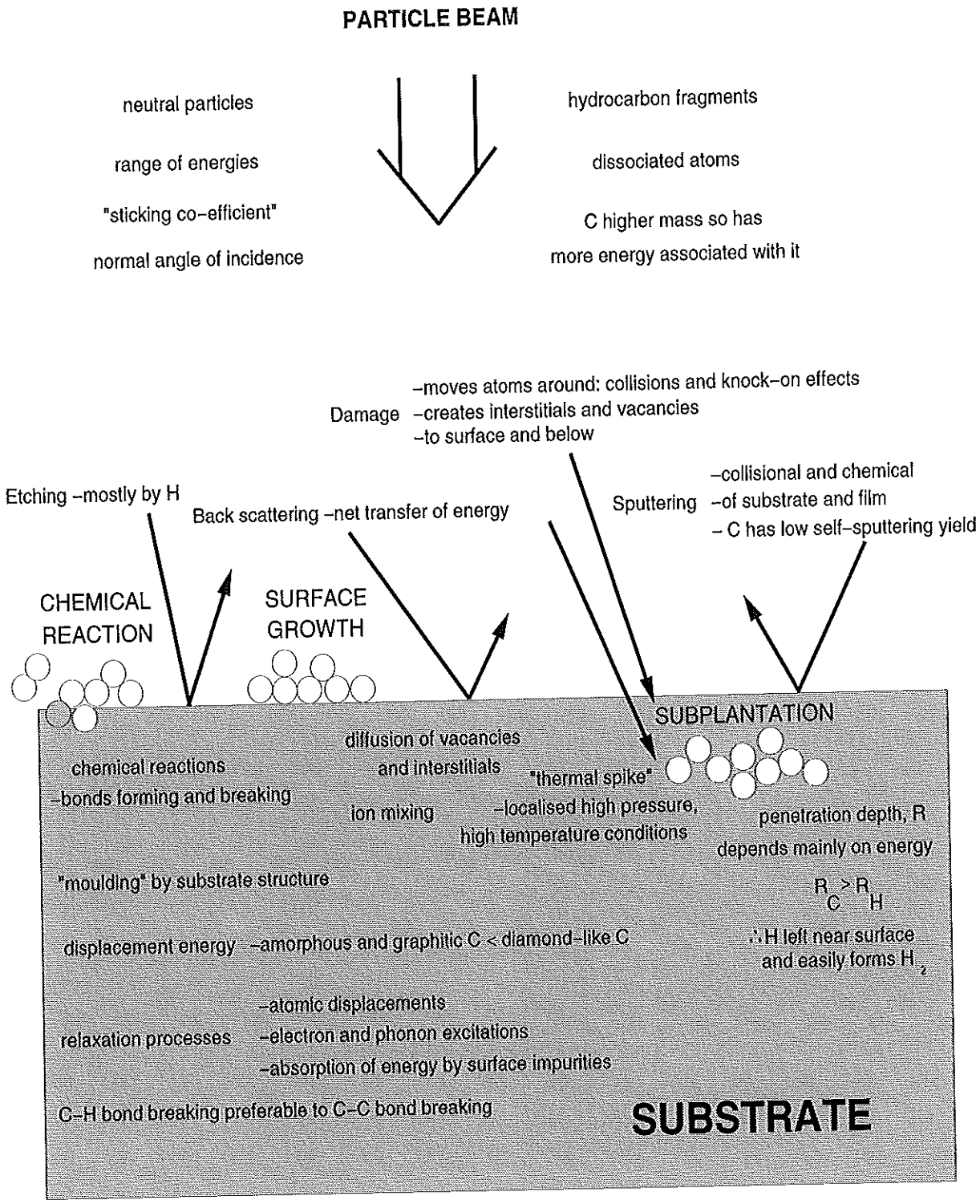

Figure 4: Schematic diagram illustrating the processes involved in the growth of a-C:H.

of the deposited films shows that this does not happen, which implies that the Cu atoms can rapidly diffuse back into the main substrate matrix. So, the use of a Cu substrate tends to produce uniform, high purity a-C:H films.

Since information concerning the nature of the impinging species (except for their maximum energy) is unavailable, it is postulated that a range of species, from dissociated atoms to large hydrocarbon fragments, is present. There is also the possibility that some precursor gas molecules do not break up until they collide with the substrate. For dissociated atoms, the processes in the deposition of the film will be similar to those described previously, with the subplantation of atoms, sputtering, damage, etc. . For the hydrocarbon fragments, it is reasonable to assume that all the fragments dissociate on impingement at the substrate. Some will then contribute to surface growth, but some will have enough energy to penetrate the substrate, as described by the subplantation model. However, a separation into two layers (a shallow a-C:H layer and a deeper carbon layer) is not likely to occur, mainly because of the lack of substrate-projectile atom mixing.

Consider now the effects of energy on the structure of these samples. a-C:H samples deposited at $\sim 500eV$ were prepared using acetylene and propane. These two gas molecules are similar, so the nature of the impinging species is also expected to be similar. For an effective beam energy of $\sim 500eV$, the average impact energy of the projectile species is in the range where the formation of sp^3 diamond-like regions is possible. The formation of these regions depends on the magnitude of the "thermal spike" and the mobility of interstitial carbon atoms. For acetylene and propane precursors it is expected that there will be sufficient numbers of both interstitial carbon atoms and hydrocarbon fragments with enough energy to result in an "sp^3-producing thermal spike", and therefore we expect to observe a significant amount of

sp^3 bonding in these samples. Some sp^2 bonding will also be present as a result of the impingement of lower energy hydrocarbon species. Hydrogen is expected to stabilise sp^3 regions by the saturation of "dangling bonds", and the energy is not high enough for etching and sputtering by hydrogen (collisional and chemical) to play a significant role.

For samples prepared at higher effective beam energies, $\sim 900eV$, (from cyclohexane, deuterated cyclohexane and acetylene) damage and etching/sputtering processes are now expected to dominate, since the average impact energy of the projectiles is increased. In this case, the subplantation model predicts samples with an amorphous, graphitic structure and with lower hydrogen concentrations.

The difference between samples prepared from hydrogenated or deuterated cyclohexane is expected to be slight, however, acetylene and cyclohexane molecules are very different. The major effect will be the average mass of the impacting species, which is expected to be higher for the cyclohexane molecule. This means that the energy associated with an impinging fragment will be distributed between more atoms, resulting in a lower "energy per atom". Also, the damage caused by the impact of a large fragment will be greater than for a smaller one. At the high deposition energies used for these samples though, these effects are not likely to result in significantly different structures. But, we also need to consider the amount of hydrogen present. There is six times as much hydrogen per molecule associated with cyclohexane than with acetylene. At these high energies a high hydrogen content in the incident flux is predicted to result in a lower hydrogen concentration in the sample, due to efficient etching and sputtering of hydrogen (mostly by hydrogen).

As we shall see in the results chapters, the experimental data are broadly in agreement with these posited structural characteristics.

2.8 Experimental techniques used to study a-C:H

In order to discover more about the atomic structure of a-C:H, many different experimental techniques have been employed. Broadly speaking, these tend to fit into one of two categories: those which probe the atomic structure directly, and those which probe the electronic structure. A summary of these will now be given accompanied by a short description of the information that each can provide.

Diffraction studies

Diffraction studies provide very detailed information on the local structure, i.e. bond lengths, bond angles and coordination numbers. X-ray and electron diffraction [19], however, can only give information on the carbon bonding, and with fairly low real-space resolution. Neutron diffraction looks at both hydrogen and carbon sites and the highest real-space resolution data allows the determination of the bond lengths associated with different types of carbon bonding, and the single:double:triple bond ratio [90, 91]. Diffraction techniques can also be used to examine the extent of medium range ordering (MRO) [92, 93].

Spectroscopic studies

It is possible to obtain qualitative information on the sp^2:sp^3 bonding ratio using ^{13}C NMR [16, 17], and this is generally a powerful method for studying bonding type and short range structure [94, 95]. ^{1}H NMR has also been used to look at the hydrogen bonding environments in a-C:H [17]. More qualitative spectroscopic information can be obtained from the popular methods of Raman and infrared (IR) spectroscopy. Both techniques investigate vibrational modes and, by comparison with vibrational frequencies for known structures, give information on the structure of a-C:H.

In principle Raman spectroscopy should provide considerable information on the local bonding in a-C:H, but the Raman cross-section for graphite is ~30-60 times that of diamond which means that sp^2 regions tend to dominate the spectra, so that they all have similarities to that of microcrystalline graphite. However, Raman spectroscopy has provided some insights into the structure of a-C:H [52, 96, 97] and has even been used to determine the sp^3 fraction [98].

Infrared spectroscopy is especially useful for looking at the C-H vibrational modes and can give very detailed information on the local C-H bonding e.g [29, 41]. The C-H stretching mode peak intensities have been used to obtain sp^3:sp^2 bonding ratios and hydrogen contents [29, 99, 100]. Also, IR can distinguish olefinic and aromatic carbon and can identify sp^1 carbon. However, to obtain reliable concentrations of sp^2 and sp^3 sites, IR requires a uniform distribution of hydrogen over these sites, therefore the information can not really be considered as quantitative, although IR provides useful qualitative information.

Inelastic neutron scattering (INS) is a technique which is less widely available than the three spectroscopic techniques mentioned above, however, it is a good source of complementary information. This relatively new technique investigates the energy range of both rotational and vibrational modes, and therefore provides the opportunity to detect the presence of any H_2 molecules "trapped" within the a-C:H network. Although the C-H vibrational modes are observed [101], INS is probably a richer source of information on the vibrations of the carbon network [102] - information which can not be obtained solely on the examination of IR spectra. Also, the peak intensities from INS are directly proportional to the number of such groups present in the sample, making INS data fully quantitative.

Electron spin resonance (ESR) has been used to investigate dangling bonds in

a-C:H [16, 55], and has given indirect evidence for the presence of a porous structure in a-C:H [40]. Electron energy loss spectroscopy (EELS) can show the presence of sp^2 bonding [79, 103, 104] and has been used to give quantitative information on the relative concentrations of sp^3, sp^2 and sp^1 bonding [105, 18].

Electronic structure studies

Electronic absorption edges for a-C:H have been measured by many different workers, e.g. [106, 28, 16]. Variations in atomic structure and film composition create differences in electronic absorption and the optical gap [105, 107]. From these observations it is then possible to draw conclusions about the structure of a-C:H, in particular, the relative amounts of sp^2 and sp^3 bonding, and the hydrogen content.

Electron energy loss near edge structure (ELNES) is another method of probing the electron energy levels and can be used to detect the presence of π orbitals [108, 109]. The measurements can be made fully quantitative using fully graphitised carbon as a standard.

The complex dielectric function measures the response of a material to an imposed electric field and can be measured by optical or electron loss techniques. From these measurements it is then possible to infer relative numbers of sp^2 and sp^3 hybridised carbon atoms [41], although there are complications with this method for a-C:H which mean that the measurements can only be regarded as approximate.

Other studies

The presence of sp^2 carbon sites can be detected by XANES (X-ray near edge absorption spectroscopy) and EXAFS (extended X-ray absorption fine structure)

[108, 18, 110, 111]. However, neither technique can provide any quantitative statement on the relative amount of sp^2 bonding, so they are of only limited use.

Direct imaging techniques such as tunelling microscopy [112, 93, 113] can be used to reveal the presence of sp^2 bonded layers if stacking of layers occurs to any extent, although high resolution electron microscopy has the potential to provide good information on medium and short range ordering.

Wide band optical spectra and Auger spectra have been used to obtain sp^3 fractions [114].

The experimental techniques that are of most use in studying a-C:H are those which provide quantitative information on the fractions of sp^1, sp^2 and sp^3 carbon present, and on the numbers of CH, CH_2 and CH_3 groups. At present, this kind of detailed information for one sample involves combining the results of several different types of experiment. In addition, computer simulations provide yet another source of information on both the atomic and electronic structure of these materials. It is then a question of piecing all the bits of the puzzle together.

Chapter 3

Theory

3.1 Introduction

In this Chapter the theory of elastic and inelastic neutron scattering is given, together with a basic theory of spectroscopy. The neutron scattering part is described in some detail, starting with particle distribution functions, then moving on to the Schrödinger equation and a quantum mechanical description. Using this approach, it will be shown how the experimentally measured scattering relates to the atomic structure of the material the neutron is being scattered from, and should therefore help to give some physical meaning to the equations commonly quoted in the field. This is important if the experimental results are to be properly understood. The section on inelastic neutron scattering covers with the theory behind inelastic scattering experiments aswell as corrections made to the results of diffraction experiments. These corrections are particularly important for materials containing hydrogen, so special attention is given to this part of the work; a derivation including an extra term shows the inadequacy of analytical methods for a-C:H. Finally, a short revision of spectroscopic

energy levels is given to show how rotations and vibrations are affected by different interatomic potentials.

3.2 Particle distribution functions

Following [115, 116], consider N fixed, identical particles in a volume V with position vectors of the particle centres, $\mathbf{r}_i$. The average number density can then be defined as $\rho_0 = N/V$. All points in space are either occupied or empty, so we can write the single particle density:

$$\rho_1(\mathbf{r}) = \sum_{i=1}^{N} \delta(\mathbf{r} - \mathbf{r}_i) \tag{1}$$

where $\rho_1(\mathbf{r})$ is only non-zero if $\mathbf{r} = \mathbf{r}_i$, and where

$$\int_V \rho_1(\mathbf{r})\mathrm{d}\mathbf{r} = N, \tag{2}$$

the total number of particles. Similarly, we can write the two particle density function,

$$\rho_2(\mathbf{r}_1, \mathbf{r}_2) = \sum_{i=1}^{N} \sum_{j \neq i}^{N-1} \delta(\mathbf{r}_1 - \mathbf{r}_i)\delta(\mathbf{r}_2 - \mathbf{r}_j) \tag{3}$$

which is zero unless particles are present at *both* $\mathbf{r}_i$ and $\mathbf{r}_j$. Integrating over $\mathbf{r}_2$ there will be a non-zero term whenever $\mathbf{r}_2 = \mathbf{r}_j \neq \mathbf{r}_i$, so that

$$\int_V \rho_2(\mathbf{r}_1, \mathbf{r}_2)\mathrm{d}\mathbf{r}_2 = (N-1)\sum_{i=1}^{N} \delta(\mathbf{r} - \mathbf{r}_i) = (N-1)\rho_1(\mathbf{r}_1) \tag{4}$$

Then $\rho_1(\mathbf{r}_1)$ is the average number of particle centres in a volume element $\mathbf{dr}$, and thus $\rho_1(\mathbf{r}_1)\mathbf{dr}$ is the probability of finding a particle in $\mathbf{dr}$. Therefore,

$$\int_V \rho_1(\mathbf{r}_1)\mathrm{d}\mathbf{r} = N \tag{5}$$

Now multiplying equation 4 by $\mathbf{dr}_1$, we obtain

$$\mathbf{dr}_1 \int_V \rho_2(\mathbf{r}_1, \mathbf{r}_2)\mathrm{d}\mathbf{r}_2 = (N-1)\rho_1(\mathbf{r}_1)\mathrm{d}\mathbf{r}_1. \tag{6}$$

Here $\rho_2(\mathbf{r}_1, \mathbf{r}_2)\mathbf{dr}_1\mathbf{dr}_2$ is the probability of particles being present simultaneously in $\mathbf{dr}_1$ *and* $\mathbf{dr}_2$. To account for the fact that occupation of $\mathbf{dr}_2$ may be affected by occupation of $\mathbf{dr}_1$, we introduce the pair distribution function $g_2(\mathbf{r}_1, \mathbf{r}_2)$:

$$\rho_2(\mathbf{r}_1, \mathbf{r}_2) = \rho_1(\mathbf{r}_1)\rho_1(\mathbf{r}_2)g_2(\mathbf{r}_1, \mathbf{r}_2). \tag{7}$$

For large $(\mathbf{r}_1 - \mathbf{r}_2)$, interparticle forces become insignificant and therefore $g_2(\mathbf{r}_1, \mathbf{r}_2) \rightarrow 1$.

Assuming the system is homogeneous, $\rho_1(\mathbf{r}_1) = \rho_1(\mathbf{r}_2) = \rho_0$, the average number density. So that

$$\rho_2(\mathbf{r}_1, \mathbf{r}_2) = \rho_0^2 g_2(\mathbf{r}_1, \mathbf{r}_2). \tag{8}$$

If we make a further assumption that the system is isotropic, then $\mathbf{r}_1 - \mathbf{r}_2 = \mathbf{r} = r$, and using this together with equations 6 and 7, we obtain

$$\rho_0 \int_V g(r)dr = N - 1. \tag{9}$$

$\rho_0 g(r)dr$ gives the probability of finding a particle in the shell $r \rightarrow r + dr$ from an origin particle,where r is the radial distance from the origin particle.

As we shall see, the pair distribution function $g(r)$ is very important as it provides a means of correlating particle positions and may be obtained from experimental data.

At this point it is useful to define the radial distribution function, $J(r)$:-

$$J(r) = 4\pi r^2 \rho(r) \tag{10}$$

where $\rho(r)$ is the number density at a radius r. $J(r)dr$ then gives the average number of particles within a spherical shell of radius r and thickness dr for a particle at the origin. So that, for a gas, the radial distribution function is given by

$$J_0(r) = 4\pi r^2 \rho_0 \tag{11}$$

where, as before, $\rho_0 = N/V$, is the average number density. Thus,

$$g(r) = \frac{J(r)}{J_0(r)} = \frac{\rho(r)}{\rho_0} \tag{12}$$

The Fourier components of the density $\rho(r)$ are

$$\rho_k = \int_V \exp(-i\mathbf{k}.\mathbf{r})\rho(\mathbf{r})\mathbf{dr} = \sum_{i=1}^{N} \exp(-i\mathbf{k}.\mathbf{r}_i) \tag{13}$$

with an autocorrelation function defined as

$$S(\mathbf{k}) = \frac{1}{N}\langle \rho_k \rho_{-k} \rangle \tag{14}$$

For a homogeneous system we can write

$$S(\mathbf{k}) = \frac{1}{N}\left\langle \sum_{i=1}^{N}\sum_{j=1}^{N} \exp(-i\mathbf{k}.\mathbf{r}_i)\exp(-i\mathbf{k}.\mathbf{r}_j) \right\rangle \tag{15}$$

$$= 1 + \frac{1}{N}\left\langle \sum_{i\neq j}^{N}\sum \exp[-i\mathbf{k}.(\mathbf{r}_i - \mathbf{r}_j)] \right\rangle$$

$$= 1 + \frac{1}{N}\left\langle \sum_{i\neq j}^{N}\sum \int\int_V \exp[-i\mathbf{k}.(\mathbf{r}_1 - \mathbf{r}_2)]\delta(\mathbf{r}_1 - \mathbf{r}_i)\delta(\mathbf{r}_2 - \mathbf{r}_j)\mathbf{dr_1}\mathbf{dr_2} \right\rangle \tag{16}$$

But from equation 3,

$$\left\langle \sum_{i\neq j}^{N}\sum \delta(\mathbf{r}_1 - \mathbf{r}_i)\delta(\mathbf{r}_2 - \mathbf{r}_j) \right\rangle = \rho_2(\mathbf{r}_1, \mathbf{r}_2) \tag{17}$$

so that

$$S(\mathbf{k}) = 1 + \frac{1}{N}\int\int_V \exp[-i\mathbf{k}.(\mathbf{r}_1 - \mathbf{r}_2)]\rho_2(\mathbf{r}_1, \mathbf{r}_2)\mathbf{dr_1}\mathbf{dr_2}. \tag{18}$$

Now substituting for $\rho_2(\mathbf{r}_1, \mathbf{r}_2)$ using equation 8:

$$S(\mathbf{k}) = 1 + \frac{1}{N}\int\int_V \exp[-i\mathbf{k}.(\mathbf{r}_1 - \mathbf{r}_2)]\rho_0^2 g_2(\mathbf{r}_1, \mathbf{r}_2)\mathbf{dr_1}\mathbf{dr_2}. \tag{19}$$

For a homogeneous system the origin of the frame of reference may be situated at any of the particle centres, so let us choose it to be at $\mathbf{r}_2$, so that $\mathbf{r}_2 = 0$. Then equation 19 becomes

$$S(\mathbf{k}) = 1 + \frac{1}{N}\int\int_V \exp[-i\mathbf{k}.\mathbf{r}_1]g(\mathbf{r}_1)\mathbf{dr_1}\mathbf{dr_2}$$

$$= 1 + \rho_0 \int_V \exp[-i\mathbf{k}.\mathbf{r}_1]g(\mathbf{r}_1)\mathbf{dr_1}. \tag{20}$$

3.3 Neutron scattering theory and the static structure factor

Following the method of [117], consider a neutron scattered through an angle 2θ (see Figure 5). We can represent the incoming neutron as a plane wave, i.e.

$$\psi_1(\mathrm{r}) = \exp(i\mathrm{k}_1.\mathrm{r}), \tag{21}$$

while at sufficiently large distances from the scattering centre, the scattered neutron has the form of a spherical wave:

$$\psi_2(\mathrm{r}) \sim \frac{\exp(ik_2 r)}{r}. \tag{22}$$

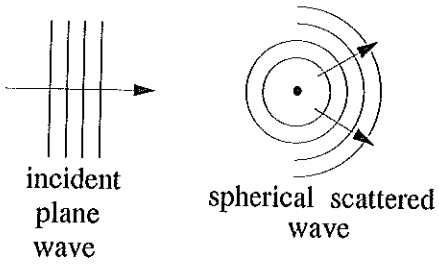

Figure 5: A representation of the incident and scattered waves.

Asymptotically (i.e. as $r \to \infty$), the wavefunction of the neutron behaves as

$$\psi(\mathrm{r})_{\mathrm{r}\to\infty} \sim \exp(i\mathrm{k}_1.\mathrm{r}) + f(2\theta)\frac{\exp(ik_2 r)}{r} \tag{23}$$

where the intensity of the scattered component determines the differential cross-section $d\sigma/d\Omega$ for scattering into a solid angle $d\Omega$ in the direction 2θ, ϕ:

$$\frac{d\sigma}{d\Omega} = |f(2\theta)|^2. \tag{24}$$

Note that from equation 24, $f(2\theta)$ has the dimensions of length, so $d\sigma/d\Omega$ has the dimensions of area.

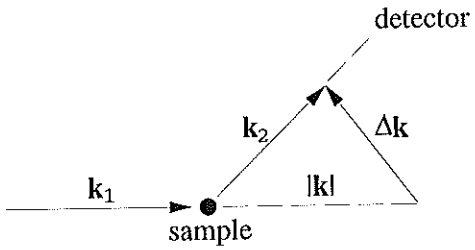

Figure 6: A vector diagram representing a scattering event.

We can represent the scattering event by the vector diagram shown in Figure 6. The momentum transfer from the sample to the neutron is

$$\hbar\mathbf{k} = \hbar\mathbf{k}_2 - \hbar\mathbf{k}_1 \tag{25}$$

Assuming elastic scattering, then

$$|\mathbf{k}_1| = |\mathbf{k}_2| = k \tag{26}$$

and

$$|\Delta\mathbf{k}| = 2k\sin\theta = \frac{4\pi}{\lambda}\sin\theta \tag{27}$$

where λ is the neutron wavelength.

The scattering of the neutron occurs as a result of interactions with atomic nuclei. These interactions are short-ranged, and the total scattering potential $V(\mathbf{r})$ may therefore be approximated by a sum of δ- function (Fermi) pseudopotentials in the form

$$V(\mathbf{r}) = \frac{2\pi\hbar^2}{m}\sum_{i=1}^{N} b_i\delta(\mathbf{r} - \mathbf{r}_i), \tag{28}$$

where b_i is the scattering length of the i_{th} nucleus and N is the total number of nuclei. For most nuclei b_i is positive, but it can also be negative as in the case of hydrogen, and even complex; it varies both with isotopic species and with the spin state of the nucleus. It is possible to obtain an isotopic mixture of hydrogen (negative scattering

length) and deuterium (positive scattering length) such that the average scattering length is zero (see Figure 7).

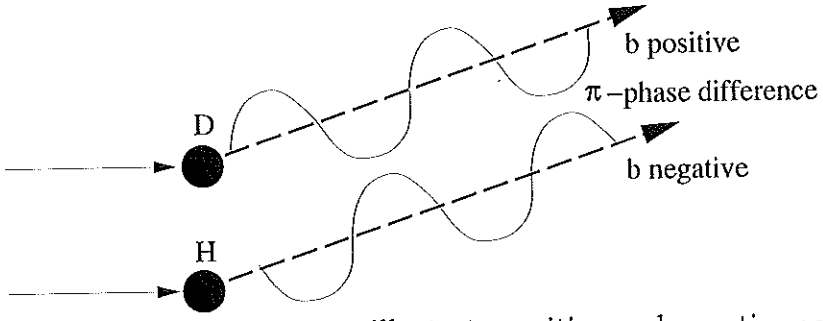

Figure 7: A diagram to illustrate positive and negative scattering lengths.

The wavefunction $\psi(\mathbf{r})$ must also be a solution of the Schrödinger equation:

$$\left(\frac{-\hbar^2\nabla^2}{2m} + V(\mathbf{r})\right)\psi(\mathbf{r}) = E\psi(\mathbf{r}). \tag{29}$$

The general solution that satisfies the boundary condition (equation 23) in the case where the incoming neutron is described by a plane wave is

$$\psi(\mathbf{r}) = \exp(i\mathbf{k}_1.\mathbf{r}) - \frac{m}{2\pi\hbar^2}\int_V \frac{\exp(ik_1\,|\mathbf{r}-\mathbf{r}'|)}{|\mathbf{r}-\mathbf{r}'|}V(\mathbf{r}')\psi(\mathbf{r}')\mathrm{d}\mathbf{r}'. \tag{30}$$

The second term on the r.h.s. of equation 30 represents a superposition of spherical waves that originate from every point in the sample.

Equation 30 is an integral equation for $\psi(\mathbf{r})$. If the interaction is assumed to be weak, a solution can be obtained by making the approximation $\psi(\mathbf{r}) \sim \exp(i\mathbf{k}_1.\mathbf{r})$ (i.e. $\psi(\mathbf{r}') \sim \exp(i\mathbf{k}_1.\mathbf{r}')$) inside the integral. This substitution yields the first Born approximation to $\psi(\mathbf{r})$:

$$\psi(\mathbf{r}) = \exp(i\mathbf{k}_1.\mathbf{r}) - \frac{m}{2\pi\hbar^2}\int_V \frac{\exp(ik_1\,|\mathbf{r}-\mathbf{r}'|)}{|\mathbf{r}-\mathbf{r}'|}V(\mathbf{r}')\exp(i\mathbf{k}_1.\mathbf{r}')\mathrm{d}\mathbf{r}'. \tag{31}$$

If $|\mathbf{r}| \gg |\mathbf{r}'|$, then

$$\begin{aligned} |\mathbf{r}-\mathbf{r}'| &= (r^2 + r'^2 - 2\mathbf{r}.\mathbf{r}')^{1/2} \\ &\simeq r - \hat{\mathbf{r}}.\mathbf{r}' \end{aligned} \tag{32}$$

where $\hat{\mathbf{r}}$ is the unit vector in the direction of $\mathbf{r}$. Since we have already assumed elastic scattering, $k_1\hat{\mathbf{r}} = \mathbf{k}_2$. So taking the limit as $\mathbf{r} \to \infty$ of equation 31 and substituting for $|\mathbf{r} - \mathbf{r}'|$ using the result given in equation 32, we obtain

$$\begin{aligned}
\psi(\mathbf{r})_{\mathbf{r}\to\infty} &\simeq \exp(\mathbf{k}_1.\mathbf{r}) - \frac{m}{2\pi\hbar^2}\int_V \frac{\exp[ik_1(r - \hat{\mathbf{r}}.\mathbf{r}')]}{(r - \hat{\mathbf{r}}.\mathbf{r}')} V(\mathbf{r}')\exp(i\mathbf{k}_1.\mathbf{r}')d\mathbf{r}' \\
&= \exp(\mathbf{k}_1.\mathbf{r}) - \frac{m}{2\pi\hbar^2}\int_V \frac{\exp(ik_1 r)\exp(-ik_1\hat{\mathbf{r}}.\mathbf{r}')}{r} V(\mathbf{r}')\exp(i\mathbf{k}_1.\mathbf{r}')d\mathbf{r}' \\
&= \exp(\mathbf{k}_1.\mathbf{r}) - \frac{\exp(ik_1 r)}{r}\frac{m}{2\pi\hbar^2}\int_V \exp(i\mathbf{k}_2.\mathbf{r}')V(\mathbf{r}')\exp(i\mathbf{k}_1.\mathbf{r}')d\mathbf{r}'. \quad (33)
\end{aligned}$$

Now comparing equations 33 and 23, and remembering that $k_1 = k_2$, we can see that

$$f(2\theta) = -\frac{m}{2\pi\hbar^2}\int_V \exp(-i\mathbf{k}_2.\mathbf{r})V(\mathbf{r})\exp(i\mathbf{k}_1.\mathbf{r})d\mathbf{r}. \quad (34)$$

Note that because the integral is definite, interchange of variables $\mathbf{r}$ for $\mathbf{r}'$ is permitted.

$$\begin{aligned}
f(2\theta) &= -\frac{m}{2\pi\hbar^2}\int_V \exp[i(\mathbf{k}_1 - \mathbf{k}_2).\mathbf{r}]V(\mathbf{r})d\mathbf{r} \\
&= -\frac{m}{2\pi\hbar^2}\int_V \exp(-i(\mathbf{k}.\mathbf{r})V(\mathbf{r})d\mathbf{r}. \quad (35)
\end{aligned}$$

So, the amplitude of the scattered component is given by the Fourier transform of the scattering potential. Also, equation 34 shows that $f(\theta)$ can be expressed as a matrix element of the interaction $V(\mathbf{r})$ between the initial and final wave states of the neutron. Now the "Golden Rule" of quantum mechanical perturbation theory (which will be derived when we consider the dynamic structure factor, see equation 80) states:

$$\text{the cross-section,} \quad \frac{d\sigma}{d\Omega} = \frac{2\pi}{\hbar}|\mathbf{M}|^2 \times (\text{density of final states}), \quad (36)$$

where

$$\frac{d\sigma}{d\Omega} = \frac{\text{the number of neutrons scattered into } d\Omega \text{ per unit time}}{\text{incident flux} \times d\Omega} \quad (37)$$

and M is the amplitude for the process – also called the matrix element (in this case $\equiv f(2\theta)$).

The amplitude contains all the dynamical information and the phase factor contains only kinematic information: it depends on the masses, energies and momenta of the particles. Use of the first Born approximation is therefore equivalent to calculating the cross-section.

An expression for $d\sigma/d\Omega$ can now be derived by substituting for $V(\mathrm{r})$ using equation 28, inserting the result into equation 35:

$$\begin{aligned} f(2\theta) &= -\frac{m}{2\pi\hbar^2}\int_V \exp(-i(\mathrm{k.r})\frac{2\pi\hbar^2}{m}\sum_{i=1}^{N} b_i\delta(\mathrm{r}-\mathrm{r}_i)\mathrm{dr} \\ &= -\sum_{i=1}^{N}\int_V \exp(-i(\mathrm{k.r})b_i\delta(\mathrm{r}-\mathrm{r}_i)\mathrm{dr} \end{aligned}$$

But we know that $\int f(t)\delta(t-t_0)dt = f(t_0)$ so we can write

$$\int_V \exp(-i(\mathrm{k.r})\delta(\mathrm{r}-\mathrm{r}_i)\mathrm{dr} = \exp(-i(\mathrm{k.r}_i) \tag{38}$$

so that,

$$f(2\theta) = -\sum_{i=1}^{N} b_i \exp(-i(\mathrm{k.r}_i) \tag{39}$$

$$|f(2\theta)| = \sum_{i=1}^{N} b_i \exp(-i(\mathrm{k.r}_i). \tag{40}$$

Therefore,

$$\frac{d\sigma}{d\Omega} = |f(2\theta)|^2 = \left|\sum_{i=1}^{N} b_i \exp(-i(\mathrm{k.r}_i)\right|^2. \tag{41}$$

Now taking the thermal average over the co-ordinates,

$$\begin{aligned} \frac{d\sigma}{d\Omega} &= \left\langle\left|\sum_{i=1}^{N} b_i \exp(-i(\mathrm{k.r}_i)\right|^2\right\rangle \\ &= \left\langle\sum_{i=1}^{N}\sum_{j=1}^{N} b_i b_j \exp[-i(\mathrm{k.}(\mathrm{r}_i-\mathrm{r}_j)]\right\rangle. \end{aligned} \tag{42}$$

We can take the statistical average of the scattering lengths over both the isotopic species present in the sample and the spin states of the nuclei; this can be done independently of the thermal averaging. If we introduce the relations;

$$\left.\begin{array}{ll} \left\langle b_j^2 \right\rangle = \langle b^2 \rangle & \langle b_i b_j \rangle = \langle b_i \rangle \langle b_j \rangle = \langle b \rangle^2 \\ \langle b^2 \rangle = b_{coh}^2 & \left(\langle b^2 \rangle - \langle b \rangle^2 \right) = b_{inc}^2 \end{array}\right\} \tag{43}$$

then we can write equation 42 as

$$\frac{d\sigma}{d\Omega} = N \left\langle b^2 \right\rangle + \langle b \rangle^2 \left\langle \sum_{i \neq j}^{N} \sum \exp[-i\mathbf{k}.(\mathbf{r}_i - \mathbf{r}_j)] \right\rangle \tag{44}$$

where the first term corresponds to $i = j$ and the second term to $i \neq j$. Hence,

$$\begin{aligned} \frac{d\sigma}{d\Omega} &= N \left(\left\langle b^2 \right\rangle - \langle b \rangle^2 \right) + \left\langle b^2 \right\rangle \left\langle \left| \sum_{i=1}^{N} \exp(-i\mathbf{k}.\mathbf{r}_i) \right|^2 \right\rangle \\ &= N b_{inc}^2 + N b_{coh}^2 S(\mathbf{k}). \end{aligned} \tag{45}$$

The subscripts "*inc*" and "*coh*" refer respectively to incoherent and coherent scattering. Here $S(\mathbf{k})$ is defined as

$$S(\mathbf{k}) - 1 = \frac{1}{N} \left\langle \left| \sum_{i=1}^{N} \exp(-i\mathbf{k}.\mathbf{r}_i) \right|^2 \right\rangle \tag{46}$$

which is analogous to equation 16.

Now let us examine in detail the meaning of equation 45:

$$\frac{d\sigma}{d\Omega} = N b_{inc}^2 + N b_{coh}^2 S(\mathbf{k}).$$

Coherent scattering corresponds to spherical waves scattered in phase, and analogously, incoherent scattering corresponds to spherical waves scattered out of phase. Structural information is contained entirely within the coherent contribution to the cross-section, with the incoherent scattering providing a featureless background on which the coherent scattering is superposed. There is no incoherent scattering if the

sample consists of a single isotopic species of zero nuclear spin. If, however, the sample consists of a homogeneous mixture of natural isotopes, then it is the coherent contribution which is averaged out over the whole of the sample and such a system is then a purely incoherent scatterer. A common example of an incoherent scatterer is vanadium, and as we shall see (Section 4.4.3) this attribute makes it very useful in neutron diffraction experiments. Finally, note that unlike electron and x-ray scattering, neutrons scatter from a point, i.e. the nucleus, rather than an electron cloud/distribution, so there is no Z-dependent form factor to be taken into account (where Z is the atomic number). So, we have managed to relate that which is measured experimentally, the cross-section $d\sigma/d\Omega$, to $S(\mathrm{k})$, which is defined from pair-wise atomic correlations and therefore the atomic structure of the sample.

If the system is isotropic then $S(\mathrm{k})$ is a function only of the wavenumber $Q = |\Delta\mathrm{k}|$. So we can write equation 20 as

$$S(Q) = 1 + \rho_0 \int_V \exp(-iQr\cos\theta) g(r) dV \tag{47}$$

where $\mathbf{r} \equiv \mathbf{r}_1$ and $r = |\mathbf{r}_1|$.

$$\begin{aligned} S(Q) &= 1 + \rho_0 \int_{r=0}^{\infty}\int_{\theta=0}^{\pi}\int_{\phi=0}^{2\pi} g(r)\exp(-iQr\cos\theta) r^2 \sin\theta dr d\theta d\phi \\ &= 1 + 2\pi\rho_0 \int_0^{\infty} r^2 g(r) \frac{e^{iQr} - e^{-iQr}}{iQr} dr \\ &= 1 + 4\pi\rho_0 \int_0^{\infty} r^2 g(r) \frac{\sin(Qr)}{Qr} dr \end{aligned} \tag{48}$$

which, if we ignore forward scattering, finally gives us:

$$S(Q) = 1 + 4\pi\rho_0 \int_0^{\infty} r[g(r) - 1]\sin(Qr) dr \tag{49}$$

i.e. the structure factor, $S(Q)$, is related to the radial distribution function, $g(r)$, by a Fourier transformation.

So far we have only considered the case of elastic scattering and although this has provided a good insight into the physics of neutron scattering, there are very few systems for which some correction for inelastic scattering does not have to be made. The precise nature of this correction will be examined in Section 3.5, but before that the so-called "dynamic" structure factor will be considered.

3.4 Inelastic neutron scattering: the dynamic structure factor

Consider a time-dependent potential $V(\mathbf{r},t)$ [117]. Energy is no longer conserved by the neutron in the interaction, so we need to use the time- dependent Schrödinger equation:

$$\left(\frac{-\hbar^2}{2m}\right)\nabla^2\psi + V(\mathbf{r},t)\psi = i\hbar\frac{\partial\psi}{\partial t}. \tag{50}$$

Assume that at $t = 0$ the potential is "switched on". The state is initially a plane wave, $\exp(ik_1 z)$, and assume that the potential is weak so that it may be assumed that the change in the wavefunction, $\delta\psi^{sc}$, is small, then

$$\begin{aligned}\psi(\mathbf{r},t) &= \psi_1 + \delta\psi^{sc} \\ &= \exp(ik_1 z)\exp\left(\frac{-iE_1 t}{\hbar}\right) + \sum_{\mathbf{k}_2} a_{\mathbf{k}_2}(t)\exp(i\mathbf{k}_2.\mathbf{r})\exp\left(\frac{-iE_2 t}{\hbar}\right),\end{aligned} \tag{51}$$

where the scattered wave has been expanded in terms of its Fourier components $a_{\mathbf{k}_2}(t)$. E_1 is the initial energy and E_2 is the final energy of the neutron (c.f. in the previous section where we had elastic scattering, $E_1 = E_2$ and $|\mathbf{k}_2| = k_1$). If we now substitute for ψ in the Schrödinger equation 50, we obtain:

$$\left(\frac{-\hbar^2}{2m}\right)\nabla^2\left(\psi_1 + \delta\psi^{sc}\right) + V(\mathbf{r},t)\left(\psi_1 + \delta\psi^{sc}\right) = i\hbar\frac{\partial\left(\psi_1 + \delta\psi^{sc}\right)}{\partial t}. \tag{52}$$

Now the Schrödinger equation for the unperturbed case (i.e. $V(\mathbf{r},t) = 0$, $\delta\psi^{sc} = 0$) gives us,

$$\left(\frac{-\hbar^2}{2m}\right)\nabla^2\psi_1 = i\hbar\frac{\partial\psi_1}{\partial t}. \tag{53}$$

So, returning to equation 52, we have

$$\left(\frac{-\hbar^2}{2m}\right)\nabla^2\psi_1 + \left(\frac{-\hbar^2}{2m}\right)\nabla^2\delta\psi^{sc} + V(\mathbf{r},t)\left(\psi_1 + \delta\psi^{sc}\right) = i\hbar\frac{\partial\psi_1}{\partial t} + i\hbar\frac{\partial(\delta\psi^{sc})}{\partial t} \tag{54}$$

which, using equation 53, reduces to

$$\left(\frac{-\hbar^2}{2m}\right)\nabla^2\delta\psi^{sc} + V(\mathbf{r},t)\left(\psi_1 + \delta\psi^{sc}\right) = i\hbar\frac{\partial(\delta\psi^{sc})}{\partial t}. \tag{55}$$

We can then neglect the $V(\mathbf{r},t)\delta\psi^{sc}$ term since this will be very small - this is known as the Born approximation - and so finally we get

$$\left(\frac{-\hbar^2}{2m}\right)\nabla^2\delta\psi^{sc} + V(\mathbf{r},t)\psi_1 = i\hbar\frac{\partial(\delta\psi^{sc})}{\partial t} \tag{56}$$

which we can write as,

$$\left(\frac{-\hbar^2}{2m}\nabla^2 - i\hbar\frac{\partial}{\partial t}\right)\delta\psi^{sc} = -V(\mathbf{r},t)\psi_1. \tag{57}$$

Now substituting for ψ_1 and ψ^{sc} using equation 51;

$$\left(\frac{-\hbar^2}{2m}\nabla^2 - i\hbar\frac{\partial}{\partial t}\right)\sum_{\mathbf{k}_2} a_{\mathbf{k}_2}(t)\exp(i\mathbf{k}_2.\mathbf{r})\exp\left(\frac{-iE_2t}{\hbar}\right) = -V(\mathbf{r},t)\exp(ik_1z)\exp\left(\frac{-iE_1t}{\hbar}\right) \tag{58}$$

$$\left(\frac{-\hbar^2}{2m}\right)\sum_{\mathbf{k}_2} a_{\mathbf{k}_2}(t)(ik_2)^2\exp(i\mathbf{k}_2.\mathbf{r})\exp\left(\frac{-iE_2t}{\hbar}\right) - i\hbar\left[\sum_{\mathbf{k}_2} a_{\mathbf{k}_2}(t)\exp(i\mathbf{k}_2.\mathbf{r})\left(\frac{-iE_2}{\hbar}\right)\exp\left(\frac{-iE_2t}{\hbar}\right) + \sum_{\mathbf{k}_2}\dot{a}_{\mathbf{k}_2}(t)\exp(i\mathbf{k}_2.\mathbf{r})\exp\left(\frac{-iE_2t}{\hbar}\right)\right] = -V(\mathbf{r},t)\exp(ik_1z)\exp\left(\frac{-iE_1t}{\hbar}\right) \tag{59}$$

where $\dot{a}_{\mathbf{k}_2}(t) = \frac{\partial}{\partial t}(a_{\mathbf{k}_2}(t))$. But $E_2 = \frac{\hbar^2 k_2^2}{2m}$, so we get

$$i\hbar \sum_{\mathbf{k}_2} \dot{a}_{\mathbf{k}_2}(t) exp(i\mathbf{k}_2.\mathbf{r}) \exp\left(\frac{-iE_2 t}{\hbar}\right) = -V(\mathbf{r},t)\exp(ik_1 z)\exp\left(\frac{-iE_1 t}{\hbar}\right)$$

$$i\hbar \sum_{\mathbf{k}_2} \dot{a}_{\mathbf{k}_2}(t) = V(\mathbf{r},t)\exp(i\mathbf{q}.\mathbf{r})\exp\left(\frac{-i(E_1 - E_2)t}{\hbar}\right) \tag{60}$$

where $\mathbf{q} = k_1 z - \mathbf{k}_2$. Now take the Fourier transform using the variables $\mathbf{k}'$ and, correspondingly, E':

$$i\hbar \dot{a}_{\mathbf{k}'}(t) = \int_V \mathbf{dr} \exp(i\mathbf{q}.\mathbf{r}) V(\mathbf{r},t) \left(\frac{-i(E_1 - E')t}{\hbar}\right) \tag{61}$$

then integrate with respect to time to get $a_{\mathbf{k}'}(t)$:

$$\begin{aligned} a_{\mathbf{k}'_2}(t) &\simeq \frac{1}{i\hbar}\int_0^t dt' \int_V \mathbf{dr} \exp(i\mathbf{q}.\mathbf{r}) V(\mathbf{r},t') \left(\frac{-i(E_1 - E'_2)t'}{\hbar}\right) \\ &= \frac{-i}{\hbar}\int_0^t dt' \int_V \mathbf{dr} \exp(i\mathbf{q}.\mathbf{r}) V(\mathbf{r},t') \left(\frac{-i(E_1 - E'_2)t'}{\hbar}\right). \end{aligned} \tag{62}$$

Thus we have an expression for the Fourier components of $\delta\psi^{sc}$, and we could reconstitute $\delta\psi^{sc}$ by summing them all - for the case of elastic scattering from an immobile nucleus this would result in a spherical wave, as might be anticipated.

3.4.1 Quantum Targets

Since the experiments in this work concern scattering from atoms, we will now briefly consider the analogous treatment for quantum targets. In this case the appropriate Fermi pseudopotential is

$$V(\mathbf{r}) = \frac{2\pi\hbar^2}{m} b\delta(\mathbf{r} - \mathbf{R}), \tag{63}$$

where $\mathbf{R}$ is the position of the target particle and b is the scattering length in free space. It is also necessary to use the total wavefunction which contains information

about both the target particle and the neutron. We will assume that the target particle is initially in its ground state, $\phi_0(\mathbf{R})$ with associated energy E_0. The quantities ψ_1 and $\delta\psi^{sc}$ are then given by:

$$\psi_1(\mathrm{r},\mathbf{R},t) = \exp(ik_1 z)\phi_0(\mathbf{R})\exp\left(\frac{-i(E_1+E_0)t}{\hbar}\right) \tag{64}$$

$$\delta\psi^{sc}(\mathrm{r},\mathbf{R},t) = \sum_{n,\mathrm{k}_2} a_{\mathrm{k}_2,n}(t)\exp(i\mathrm{k}_2.\mathrm{r})\phi_n(\mathbf{R})\exp\left(\frac{-i(E_2+E_n)t}{\hbar}\right) \tag{65}$$

where $a_{\mathrm{k}_2,n}(t)$ is the amplitude for the final neutron state to be a plane wave, k_2, and the target final state to be $\phi_n(\mathbf{R})$, the n^{th} excited state. Now by substituting for ψ_1 and $\delta\psi^{sc}$ in equation 56 and performing steps similar to those given in equations 57 to 62 (and noting that we also need to use the fact that the target wavefunctions form a complete set, i.e. any function may be expressed in terms of them), we obtain:

$$\begin{aligned} a_{\mathrm{k}_2',n}(t) \;\simeq\; & \frac{-i}{\hbar}\int_{V'}\mathbf{dR}\int_V \mathbf{dr}\exp(i\mathbf{q}.\mathrm{r})\phi_0(\mathbf{R})V(\mathrm{r}-\mathbf{R})\phi_n(\mathbf{R}) \\ & \times\int_0^t dt'\exp\left(\frac{-i[E_1+E_0]t'}{\hbar}\right)\exp\left(\frac{i[E_n+E_2']t'}{\hbar}\right). \end{aligned} \tag{66}$$

We can now use this to find an expression for $\left|a_{\mathrm{k}_2',n}(t)\right|^2$, the amplitude of the scattered wave. First, substitute into equation 66 the explicit form of $V(\mathrm{r}-\mathbf{R})$ as given by equation 63, then find the modulus squared:

$$\begin{aligned} \left|a_{\mathrm{k}_2',n}(t)\right|^2 &= \left(\frac{2\pi\hbar b}{m}\right)^2\left|\int_{V'}\mathbf{dR}\int_V \mathbf{dr}\exp(i\mathbf{q}.\mathrm{r})\delta(\mathrm{r}-\mathbf{R})\phi_0(\mathbf{R})\phi_n(\mathbf{R})\right|^2 \\ &\quad\times\left[\int_0^t dt'\exp\left(\frac{-i[E_1+E_0]t'}{\hbar}\right)\exp\left(\frac{i[E_n+E_2']t'}{\hbar}\right)\right]^2 \\ &= \left(\frac{2\pi\hbar b}{m}\right)^2\left|\int_{V'}\mathbf{dR}\int_V \mathbf{dr}\exp(i\mathbf{q}.\mathbf{R})\phi_0(\mathbf{R})\phi_n(\mathbf{R})\right|^2 \\ &\quad\times\left[\int_0^t dt'\exp\left(\frac{i[E_n+E_2'-E-E_0)t']}{\hbar}\right)\right]^2. \end{aligned} \tag{67}$$

Consider the final term only, the integral w.r.t. time, putting $\hbar\omega = E_1 - E_2'$, so that

$$\left[\int_0^t dt' \exp\left(\frac{i[E_n + E_2' - E_1 - E_0)t']}{\hbar}\right)\right]^2 = \left[\int_0^t dt' \exp\left(\frac{i(E_n - E_0 - \hbar\omega)t'}{\hbar}\right)\right]^2$$

$$= \left[\frac{\hbar \exp\left(\frac{-i(E_n - E_0 - \hbar\omega)t'}{\hbar}\right)}{-i(E_n - E_0 - \hbar\omega)}\right]_0^t \left[\frac{\hbar \exp\left(\frac{i(E_n - E_0 - \hbar\omega)t'}{\hbar}\right)}{i(E_n - E_0 - \hbar\omega)}\right]_0^t$$

$$= \left(\frac{\hbar}{E_n - E_0 - \hbar\omega)}\right)^2 \times$$

$$\left[1 + 1 - \exp\left(\frac{-i(E_n - E_0 - \hbar\omega)t}{\hbar}\right) - \exp\left(\frac{i(E_n - E_0 - \hbar\omega)t}{\hbar}\right)\right]$$

$$= 2\left(\frac{\hbar}{E_n - E_0 - \hbar\omega}\right)^2 \left[1 - \cos\left(\frac{(E_n - E_0 - \hbar\omega)t}{\hbar}\right)\right]. \quad (68)$$

But,

$$1 - \cos\left(\frac{(E_n - E_0 - \hbar\omega)t}{\hbar}\right) = 2\sin^2\left[\frac{(E_n - E_0 - \hbar\omega)t}{2\hbar}\right]. \quad (69)$$

Hence, we can now introduce,

$$\lim_{t\to\infty} \pi t\delta(w) = \frac{\sin^2(wt/2)}{w^2}. \quad (70)$$

So if we take the limit as $t \to \infty$ of equation 69 and also use $w \equiv (E_n - E_0 - \hbar\omega)/\hbar^2$, then we have,

$$\lim_{t\to\infty} 2\sin^2\left[\frac{(E_n - E_0 - \hbar\omega)t}{2\hbar}\right] = 2\pi t\delta\left(\frac{E_n - E_0 - \hbar\omega}{\hbar}\right)\frac{[E_n - E_0 - \hbar\omega]^2}{\hbar^2}. \quad (71)$$

Substituting this result back into equation 67 gives us:

$$\left[\int_0^t dt' \exp\frac{i(E_n + E_2' - E_1 - E_0)t'}{\hbar}\right]^2 = 2\left(\frac{\hbar}{E_n - E_0 - \hbar\omega}\right)^2 2\pi t \times$$

$$\delta\left(\frac{E_n - E_0 - \hbar\omega}{\hbar}\right)\left(\frac{E_n - E_0 - \hbar\omega}{\hbar}\right)^2$$

$$= 4\pi t\delta\left(\frac{E_n - E_0 - \hbar\omega}{\hbar}\right). \quad (72)$$

And finally, inserting this result into equation 67, we find,

$$\begin{aligned}\left|a_{\mathrm{k}'_2,n}(t)\right|^2 &= 4\pi t\left(\frac{2\pi\hbar b}{m}\right)^2\left|\int_{V'}\mathbf{dR}\exp(i\mathbf{q}.\mathbf{R})\phi_0(\mathbf{R})\phi_n(\mathbf{R})\right|^2\times \\ &\quad \delta\left(\frac{[E_n-E_0]}{\hbar}-\hbar\omega\right) \\ &= 4\pi t\hbar\left(\frac{2\pi\hbar b}{m}\right)^2\left|\int_{V'}\mathbf{dR}\exp(i\mathbf{q}.\mathbf{R})\phi_0(\mathbf{R})\phi_n(\mathbf{R})\right|^2\times \\ &\quad \delta\left([E_n-E_0]-\hbar\omega\right). \end{aligned} \tag{73}$$

We can see from equation 73 that the amplitude of the scattered states grows linearly with time, but only in those states which conserve energy as $t\rightarrow\infty$. For a general potential, V, the corresponding expression is usually written as:

$$\left|a_{\mathrm{k}'_2,n}(t)\right|^2 \simeq \frac{2\pi t}{\hbar}\left|\langle \mathrm{k}'_2,n\left|V\right|\mathrm{k},0\rangle\right|^2\delta\left([E_n-E_0]-\hbar\omega\right), \tag{74}$$

where

$$\langle \mathrm{k}'_2,n\left|V\right|\mathrm{k},0\rangle = \int_{V'}\mathbf{dR}\int_V \mathbf{dr}\exp(i\mathbf{q}.\mathbf{r})\phi_0(\mathbf{R})V(\mathbf{r}-\mathbf{R})\phi_n(\mathbf{R}). \tag{75}$$

In these last two equations we have introduced the Dirac notation for the matrix elements of V. In this scheme, final states are represented in angular brackets to the left-hand side and initial states to the right-hand side.

3.4.2 The partial differential cross-section

To calculate the partial differential cross-section we must sum over all the scattered wavevectors, k'_2, consistent with the neutron

(a) being scattered into a direction within a cone of solid angle $d\Omega$ about θ,ϕ

(b) having an energy in the region E'_2 to dE'_2.

In order to do this, let us suppose that the experiment is contained within a large box of side length, L. By doing this we can say that the allowed wavevectors for the neutron are quantised and the wavefunctions may be normalised.

If we apply periodic boundary conditions to the box, then the allowed values of k_2' are $(l,m,n) \times (2\pi/L)$, where l,m,n are integers. So the allowed states form a lattice in k_2' -space with a unit cell volume $(2\pi/L)^3$ and the normalisation of the wavefunction is $(1/L)^{3/2}$.

To sum over the allowed values of k_2', we need to know two things:

1. the volume in k_2'-space corresponding to $d\Omega$ and dE_2'
2. the density of allowed states in that region,

then the number of allowed states is simply given by the product of these two values.

Consider first the density of allowed states. The volume in k_2'-space in a cone of solid angle $d\Omega$ between k_2' and $k_2' + dk_2'$, is $d\Omega k_2'^2 dk_2'$. However, we know that

$$\begin{aligned} E_2' &= \frac{\hbar^2 k_2'^2}{2m} \\ \Rightarrow dE_2' &= \frac{\hbar^2 k_2'}{2m} dk_2'. \end{aligned} \tag{76}$$

The number of allowed states, $\nu(k_2')$, is given by;

$$\nu(k_2') = \left(\frac{L}{2\pi}\right)^3 d\Omega k_2'^2 dk_2'. \tag{77}$$

The partial differential cross-section is defined analogously to equation 37 by:

$$\frac{d^2\sigma}{d\Omega dE_2'} = \frac{\text{the number of particles scattered per unit time into } d\Omega \text{ and } dE_2'}{\text{the incident flux} \times d\Omega \times dE_2'}. \tag{78}$$

The number of particles scattered into states k_2' and n per unit time is

$$\frac{d}{dt}\left(\left|a_{\mathrm{k}_2',n}(t)\right|^2\right), \tag{79}$$

so we can see that the numerator in equation 78 is

$$\frac{d}{dt}\left(\left|a_{\mathbf{k}_2',n}(t)\right|^2\right)\nu(k_2')N, \tag{80}$$

where N is the number of neutrons in the box. This is often called "Fermi's Golden Rule".

Now the incident flux, I, is defined as:

$$\begin{aligned} I &= \text{the number of neutrons per unit volume} \times \text{the neutron velocity} \\ &= \frac{N}{L^3}\frac{\hbar k}{m}. \end{aligned} \tag{81}$$

Using equation 73 in 80, together with equations 77 and 81, we find that

$$\begin{aligned} \frac{d^2\sigma}{d\Omega dE_2'} &= 2\pi\hbar\left(\frac{2\pi\hbar b}{m}\right)^2\left(\frac{L}{2\pi}\right)^3\frac{mk_2'}{\hbar^2}\frac{L^3 m}{N\hbar k_1}\times \\ &\quad \left|\int_{V'}\mathbf{dR}\exp(i\mathbf{q}.\mathbf{R})\phi_0(\mathbf{R})\phi_n(\mathbf{R})\right|^2\delta([E_n-E_0]-\hbar\omega) \\ &= b^2\frac{k_2'}{k_1}L^6\left|\int_{V'}\mathbf{dR}\exp(i\mathbf{q}.\mathbf{R})\phi_0(\mathbf{R})\phi_n(\mathbf{R})\right|^2\delta([E_n-E_0]-\hbar\omega). \end{aligned} \tag{82}$$

Summing over all the final states of the target and normalising the wavefunctions, we finally obtain:

$$\begin{aligned} \frac{d^2\sigma}{d\Omega dE_2'} &= b^2\frac{k_2'}{k}\sum_n\left|\int_{V'}\mathbf{dR}\exp(i\mathbf{q}.\mathbf{r})\phi_0(\mathbf{R})\phi_n(\mathbf{R})\right|^2\delta([E_n-E_0]-\hbar\omega) \\ &= \frac{k_2'}{k}b^2 S(\mathbf{q},\omega), \end{aligned} \tag{83}$$

where $S(\mathbf{q},\omega)$ is the scattering function, or dynamic structure factor. Looking at equation 83 we can see that transitions occur to the excited states, weighted by the matrix elements of $\exp(i\mathbf{q}.\mathbf{R})$. Also if we compare this case to that for the static structure factor (equation 45, then we notice an apparently extra factor of k_2'/k. This factor does infact appear in the expression for elastic scattering, however, since $k_2' = k$ for this case, the factor is simply equal to one.

3.5 The static approximation and Placzek corrections

In performing a diffraction experiment to measure $S(Q)$ it is assumed that the scattering is elastic, i.e. no energy transfer between the target and neutron takes place: this assumption is known as the static approximation. However, in practice this approximation breaks down for most systems and it is therefore necessary to apply a correction - the so-called Placzek correction - to account for this [118, 119]. Since this inelasticity correction requires a somewhat mathematical treatment, which follows from the derivation of the dynamic structure factor, it will be included in this section, rather than the chapter covering the data analysis techniques (Chapter 4). The method follows that given by Powles [120].

In a generic time-of-flight (*tof*) experiment we observe neutrons arriving at a detector at time t after the neutron burst generated at time t_0 (neglecting for now the time width of the initial neutron pulse and its wavelength dependence). The neutrons counted are labelled solely according to their *tof*. This means that in a real experiment the neutrons counted into any one time channel will have a spread of wavelengths depending on the energy transferred in the scattering process. Thus, unless it is possible to measure the scattered neutron energies as well as knowing the incident energy, we cannot truly measure diffraction, but are constrained to measure the total scattering. In measuring the total scattering, an integral over the scattering function, $S(\mathrm{q},\omega)$, is being performed, and must therefore determine the form of this integral.

Consider neutrons produced at a time t_0 and detected at a time t of wavelength λ_i (variable), which travel a distance L_i at velocity v_i to the scattering centre, then

L_S at v_S to the detector, so that:

$$t - t_0 = \frac{L_i}{v_i} + \frac{L_S}{v_S} = \frac{m}{h}[L_i\lambda_i + L_S\lambda_S]. \tag{84}$$

From simple considerations of scattering geometry, we have,

$$\begin{aligned} k_S &= k_i\left[1 - \frac{2m\omega}{\hbar k_i^2}\right]^{1/2} \\ \text{or} \quad \lambda_S &= \lambda_i\left[1 - \frac{m\omega\lambda_i^2}{\pi h}\right]^{1/2}. \end{aligned} \tag{85}$$

Therefore, substituting for λ_S in equation 84:

$$t - t_0 = \frac{m\lambda_i}{h}\left[L_i + L_S\left(1 - \frac{m\omega\lambda_i}{\pi h}\right)^{1/2}\right]. \tag{86}$$

The number of neutrons detected in a frequency range $\Delta\omega$ at ω is proportional to $S(\mathbf{q},\omega)\Delta\omega$, and therefore the number detected in a time channel of width Δt at t is proportional to $S(\mathbf{q},\omega)\left(\frac{\partial\omega}{\partial t}\right)_{\lambda_i}\Delta t$. The countrate per unit solid angle at time t at fixed detector angle 2θ is:

$$C(2\theta,t) = \int_{-\infty}^{\infty} d\lambda_i f(\lambda_i)F(k_S)\frac{k_S}{k_i}S(\mathbf{q},\omega)\left.\frac{\partial\omega}{\partial t}\right|_{\lambda_i} \tag{87}$$

where we have integrated over the incident spectrum $f(\lambda_i)$, and for a given λ_i, k_S, q and ω correspond to neutrons which arrive at the detector at time t. $F(k_S)$ is a function representing the detector sensitivity and efficiency.

Since we are considering a correction to the case of elastic scattering, it is convenient to look at the countrate as a function of an elastic q, q_e. Now we can define a wavelength λ_e for elastic scattering of neutrons arriving at time t, where

$$t - t_0 = \frac{m}{h}[L_i + L_S]\lambda_e(t). \tag{88}$$

We can also write, for these elastically scattered neutrons, that

$$q_e = \frac{4\pi}{\lambda_e}(t)\sin\theta = 2k_e\sin\theta, \tag{89}$$

where 2θ is the scattering angle. So,

$$\begin{aligned}(t-t_0)q_e &= \frac{m}{h}\lambda_e(t)\frac{4\pi}{\lambda_e(t)}[L_i+L_S]\sin\theta \\ &= \frac{4\pi m}{h}[L_i+L_S]\sin\theta. \end{aligned} \tag{90}$$

The countrate, as a function of q_e, is then given by,

$$C(2\theta,q_e) = \int_{-\infty}^{\infty} d\lambda_i f(\lambda_i)F(k_S)\frac{k_S}{k_i}S(\mathbf{q},\omega)\left.\frac{\partial\omega}{\partial t}\right|_{\lambda_i}\frac{dt}{dq_e}. \tag{91}$$

Since t is fixed we can see that, by the use of equation 86, the integrand may be regarded as a function of λ_i or of ω. Transforming the integration to ω, we get, at constant t,

$$\begin{aligned}C(2\theta,q_e) &= \int_{-\infty}^{\infty} f(\lambda_i)F(k_S)\frac{k_S}{k_i}S(\mathbf{q},\omega)d\omega\left.\frac{\partial\lambda_i}{\partial\omega}\right|_t\left.\frac{\partial\omega}{\partial t}\right|_{\lambda_i}\frac{dt}{dq_e} \\ &= \int_{-\infty}^{\infty} d\omega f(\lambda_i)F(k_S)\frac{k_S}{k_i}S(\mathbf{q},\omega)\left[-\left.\frac{\partial\lambda_i}{\partial t}\right|_\omega\frac{dt}{dq_e}\right]. \end{aligned} \tag{92}$$

From equation 90,

$$t = \frac{4\pi m}{hq_e}[L_i+L_S]\sin\theta + t_0 \tag{93}$$

so,

$$\begin{aligned}\frac{dt}{dq_e} &= -\frac{4\pi m}{hq_e^2}[L_i+L_S]\sin\theta \\ &= -\frac{(t-t_0)}{q_e}. \end{aligned} \tag{94}$$

Now, from equation 86,

$$t = \frac{m\lambda_i L_i}{h} + \frac{m\lambda_i L_S}{h}\left(1-\frac{m\omega\lambda_i^2}{\pi h}\right)^{-1/2} + t_0, \tag{95}$$

which leads to

$$\left.\frac{\partial\lambda_i}{\partial t}\right|_\omega = (t-t_0)^{-1}\lambda_i(1+A)^{-1}, \tag{96}$$

where

$$A = \frac{\frac{m}{h\pi}\lambda_i^2 L_S \omega \left(1 - \frac{m\omega\lambda_i^2}{\pi h}\right)^{-3/2}}{L_i + L_S \left(1 - \frac{m\omega\lambda_i^2}{\pi h}\right)^{-1/2}}. \tag{97}$$

Substituting the results given in equations 94 and 96 into equation 92, we find at constant t

$$\begin{aligned} C(2\theta, q_e) &= \frac{1}{q_e}\int_{-\infty}^{\infty} f(\lambda_i)F(k_S)\frac{k_S}{k_i}S(\mathbf{q},\omega)\lambda_i \frac{(1+A)^{-1}}{(t-t_0)}(t-t_0)\,d\omega \\ &= \frac{1}{q_e}\int_{-\infty}^{\infty} (1+A)^{-1}\lambda_i f(\lambda_i)F(k_S)\frac{k_S}{k_i}S(\mathbf{q},\omega)d\omega. \end{aligned} \tag{98}$$

Suppose now that we calibrate with an "ideal vanadium" (i.e. an isotropic incoherent) scatterer, with a countrate:

$$C_V(2\theta, q_e) = \frac{1}{q_e}\lambda_e f(\lambda_e)F(k_e)N_V b_V^2, \tag{99}$$

and we define the counts ratio

$$R = \frac{C(2\theta, q_e)}{C_V(2\theta, q_e)}. \tag{100}$$

So that, at constant t,

$$N_V b_V^2 R = \int_{-\infty}^{\infty} (1+A)^{-1}\frac{\lambda_i}{\lambda_e}\frac{f(\lambda_i)}{f(\lambda_e)}\frac{F(k_S)}{F(k_e)}\frac{k_S}{k_i}S(\mathbf{q},\omega)d\omega. \tag{101}$$

We have found an expression for what is measured experimentally, and note that it involves $S(\mathbf{q},\omega)$, the dynamic structure factor. To correct for the inelasticity effects we now follow a method first developed by Placzek.

We take $S(\mathbf{q},\omega)$ and expand using a Maclaurin series in powers of ω, i.e. q about q_e:

$$\begin{aligned} S(\mathbf{q},\omega) &= S(\mathbf{q_e},\omega) + (q-q_e)\left.\frac{\partial S}{\partial q}\right|_{q=q_e} + \frac{1}{2!}(q-q_e)^2\left.\frac{\partial^2 S}{\partial q^2}\right|_{q=q_e} + \ldots \\ &= S(\mathbf{q_e},\omega) + \left.\frac{\partial S}{\partial q}\right|_{q=q_e}\delta q_L + \frac{1}{2}\left.\frac{\partial^2 S}{\partial q^2}\right|_{q=q_e}(\delta q_L)^2 + \ldots, \end{aligned} \tag{102}$$

where $\delta q_L = (q - q_e)$.

Before deriving an explicit form for equation 102, consider the effect of including terms in ω^2 rather than the more usual approach which ignores terms higher than ω. To do this we will examine the expression for λ_i/λ_e, the ratio of the incident wavelength (variable) to the wavelength of elastically scattered neutrons.

Using equations 86 and 88 we have:

$$\begin{aligned} \frac{m\lambda_i}{h}\left[L_i + L_S\left(1 - \frac{m\omega\lambda_i^2}{\pi h}\right)^{-1/2}\right] &= \frac{m}{h}\left[L_i + L_S\right]\lambda_e \\ \lambda_i\left[L_i + L_S\left(1 - \frac{m\omega\lambda_i^2}{\pi h}\right)^{-1/2}\right] &= \left[L_i + L_S\right]\lambda_e. \end{aligned} \tag{103}$$

Now, if we apply a binomial series expansion (neglecting terms higher than ω^2), equation 103 becomes,

$$\lambda_i\left[L_i + L_S\left\{1 + \frac{m\omega\lambda_i^2}{2\pi h} + \frac{3}{8}\left(\frac{m\omega\lambda_i^2}{\pi h}\right)^2\right\}\right] = \left[L_i + L_S\right]\lambda_e. \tag{104}$$

Therefore,

$$\begin{aligned} \lambda_e &= \frac{\lambda_i}{L_i + L_S}\left[L_i + L_S + L_S\frac{m\omega\lambda_i^2}{2\pi h} + \frac{3L_S}{8}\left(\frac{m\omega\lambda_i^2}{\pi h}\right)^2\right] \\ &= \lambda_i\left[1 + \frac{L_S}{L_i + L_S}\frac{m\omega\lambda_i^2}{2\pi h} + \frac{3L_S}{8\left(L_i + L_S\right)}\left(\frac{m\omega\lambda_i^2}{\pi h}\right)^2\right] \\ &= \lambda_i\left[1 + \frac{L_S}{L_i + L_S}\frac{m\omega}{\hbar k_i^2} + \frac{3L_S}{2\left(L_i + L_S\right)}\frac{m^2\omega^2}{k_i^4\hbar^2}\right] \\ \frac{\lambda_e}{\lambda_i} &= 1 + \frac{L_S}{L_i + L_S}\frac{m\omega}{\hbar k_i^2} + \frac{3L_S}{2\left(L_i + L_S\right)}\left(\frac{m\omega}{\hbar k_i^2}\right)^2. \end{aligned} \tag{105}$$

Since,

$$\frac{\lambda_i}{\lambda_e} = \left[\frac{\lambda_e}{\lambda_i}\right]^{-1}, \tag{106}$$

we can expand this again as a series:

$$\begin{aligned} \left[\frac{\lambda_e}{\lambda_i}\right]^{-1} = 1 - \frac{L_S}{L_i + L_S}\frac{m\omega}{\hbar k_i^2} &+ \left(\frac{L_S}{L_i + L_S}\right)^2\left(\frac{m\omega}{\hbar k_i^2}\right)^2 - \frac{3}{2}\frac{L_S}{L_i + L_S}\left(\frac{m\omega}{\hbar k_i^2}\right)^2 \\ &+ \ 0 \times \text{higher terms.} \end{aligned} \tag{107}$$

Now,

$$\begin{aligned} \lambda_i k_i &= \lambda_e k_e \\ \Rightarrow \quad \frac{1}{k_i^2} &= \frac{1}{k_e^2}\left(\frac{\lambda_i}{\lambda_e}\right)^2 . \end{aligned} \tag{108}$$

Inserting the results in equations 107 and 108 into 105, we get,

$$\frac{\lambda_i}{\lambda_e} = 1 - \frac{L_S}{L_i + L_S}\frac{m\omega}{\hbar k_e^2}\left(\frac{\lambda_i}{\lambda_e}\right)^2 + \frac{L_S}{L_i + L_S}\left(\frac{m\omega}{\hbar k_e^2}\right)^2\left[\frac{L_S}{L_i + L_S} - \frac{3}{2}\right]\left(\frac{\lambda_i}{\lambda_e}\right)^4 . \tag{109}$$

Equation 109 is a quartic in λ_i/λ_e. For the following typical values:-

$k_e = 9 \times 10^{10} m^{-1}$

$\omega = 7.12 \times 10^{14} s^{-1}$

$L_i = 10m$

$L_S = 1m$

$m_n = 1.675 \times 10^{-27} kg,$

we obtain these roots:

$$\frac{\lambda_i}{\lambda_e} = 0.80956,\ -1.75402,\ 0.47223 \pm 1.61164i.$$

The root corresponding to a physical λ_i/λ_e, then, is $\lambda_i/\lambda_e = 0.80956$. Compare this to the value obtained if we neglect the third term, that containing ω^2. In this case the value of the root we obtain is $\lambda_i/\lambda_e = 0.87216$, a difference of 0.0625. Therefore, including second order term in ω introduces a second order correction of $\sim 7\%$ to the first order correction, so we are therefore justified in ignoring terms in ω^2 and higher powers.

Now, to return to the examination of the exact form of equation 102. First, let us find an expression for δq_L. For neutrons of incident wavenumber k_i scattered at an angle 2θ,

$$q^2 = 2k_i^2 \left[1 - \frac{m\omega}{\hbar k_i^2}\left(1 - \frac{2m\omega}{\hbar k_i^2}\right)^{1/2} \cos 2\theta\right], \tag{110}$$

and from equation 89,

$$\begin{aligned} q_e &= 2k_e \sin\theta \\ \Rightarrow \quad q_e^2 &= 4k_e^2 \sin^2\theta = 2k_e^2\,(1 - \cos 2\theta)\,. \end{aligned} \tag{111}$$

Using a binomial series expansion and neglecting terms higher than ω, we see that equation 110 may be written:

$$q^2 = 2k_i^2 \left[(1 - \cos 2\theta) - \frac{m\omega}{\hbar k_i^2}\,(1 - \cos\theta)\right]. \tag{112}$$

Thus, using equations 110 and 112,

$$\begin{aligned} \frac{q^2}{q_e^2} &= \frac{2k_i^2}{2k_e^2}\frac{1}{(1 - \cos 2\theta)}\left[(1 - \cos 2\theta) - \frac{m\omega}{\hbar k_i^2}\,(1 - \cos 2\theta)\right] \\ &= \frac{k_i^2}{k_e^2}\left[1 - \frac{m\omega}{\hbar k_i^2}\right]. \end{aligned} \tag{113}$$

Recalling the result from equation 108, we have that

$$\begin{aligned} \frac{q^2}{q_e^2} &= \left(\frac{\lambda_e}{\lambda_i}\right)^2 \left[1 - \frac{m\omega}{\hbar k_e^2}\left(\frac{\lambda_i}{\lambda_e}\right)^2\right] \\ \Rightarrow \quad \frac{q}{q_e} &= \frac{\lambda_e}{\lambda_i}\left[1 - \frac{m\omega}{\hbar k_e^2}\left(\frac{\lambda_i}{\lambda_e}\right)^2\right]^{1/2}. \end{aligned} \tag{114}$$

Again this may be expanded as a series to get,

$$\begin{aligned} \frac{q}{q_e} &= \frac{\lambda_e}{\lambda_i}\left[1 - \frac{m\omega}{2\hbar k_e^2}\left(\frac{\lambda_i}{\lambda_e}\right)^2 + 0 \times \text{higher terms}\right] \\ &= \frac{\lambda_e}{\lambda_i} - \frac{m\omega}{2\hbar k_e^2}\frac{\lambda_i}{\lambda_e}. \end{aligned} \tag{115}$$

We can now use equations 105 and 109 to substitute for λ_e/λ_i and λ_i/λ_e, neglecting the terms in ω^2, so that

$$\begin{aligned}\frac{q}{q_e} &= \left[1+\frac{L_S}{L_i+L_S}\frac{m\omega}{\hbar k_e^2}\right]-\frac{m\omega}{2\hbar k_e^2}\left[1-\frac{L_S}{L_i+L_S}\frac{m\omega}{\hbar k_e^2}\left(\frac{\lambda_i}{\lambda_e}\right)^2\right] \\ &= 1+\frac{L_S}{L_i+L_S}\frac{m\omega}{\hbar k_e^2}-\frac{m\omega}{2\hbar k_e^2}+0\ \times \text{higher terms} \\ &= 1-\frac{1}{2}\left(\frac{L_i-L_S}{L_i+L_S}\right)\frac{m\omega}{\hbar k_e^2}. \end{aligned} \tag{116}$$

So,

$$q = q_e-\left(\frac{L_i-L_S}{L_i+L_S}\right)\frac{m\omega q_e}{2\hbar k_e^2}. \tag{117}$$

Therefore,

$$\begin{aligned}\delta q_L &= q-q_e \\ &= -\left(\frac{L_i-L_S}{L_i+L_S}\right)\frac{m\omega q_e}{2\hbar k_e^2} \\ &= -\left(\frac{L_i-L_S}{L_i+L_S}\right)\frac{m\omega}{\hbar k_e}\sin\theta. \end{aligned} \tag{118}$$

Returning to equation 102, we can now write:

$$S(\mathbf{q},\omega) = S(\mathbf{q_e},\omega)+\left(\frac{L_i-L_S}{L_i+L_S}\right)\frac{m\omega}{\hbar k_e}\sin\theta\left.\frac{\partial S}{\partial q}\right|_{q=q_e}+0\ \times \text{higher terms}. \tag{119}$$

This is now ready to be inserted into the integral equation 101. Before doing this, however, we note that other terms in the integrand may be expanded in powers of ω, and here we shall simply quote those results (although they are not difficult to prove).

$$(1+A)^{-1} = 1-\frac{2m\omega}{\hbar k_e^2}\left(\frac{L_S}{L_i+L_S}\right)+0(\omega^2) \tag{120}$$

$$\frac{f(\lambda_i)}{f(\lambda_e)} = 1-\left.\frac{d(\ln f)}{d(\ln\lambda)}\right|_{k=k_e}\frac{m\omega}{\hbar k_e^2}\left(\frac{L_S}{L_i+L_S}\right)+0(\omega^2) \tag{121}$$

$$\frac{F(k_S)}{F(k_e)} = 1-\left.\frac{d(\ln F)}{d(\ln k)}\right|_{k=k_e}\frac{m\omega}{\hbar k_e^2}\left(\frac{L_S}{L_i+L_S}\right)+0(\omega^2) \tag{122}$$

$$\frac{k_S}{k_i} = 1 - \frac{m\omega}{\hbar k_e^2} + 0(\omega^2). \tag{123}$$

Note that for results 122 and 123 we have expanded the function as a series about $\lambda = \lambda_e$ (or $k = k_e$) and then used the fact that

$$\begin{aligned} \frac{df(x)}{dx} &= \frac{df}{d(\ln f)} \frac{d(\ln x)}{dx} \frac{d(\ln f)}{d(\ln x)} \\ &= f \frac{1}{x} \frac{d(\ln f)}{d(\ln x)}. \end{aligned} \tag{124}$$

Finally, if we insert all our results, 119 to 123, into equation 101, we find

$$N_V b_V^2 R(q_e) = S(\mathbf{q_e}) - \frac{m}{\hbar k_e^2} \left[\left(\frac{L_i + 4L_S}{L_i + L_S} \right) + \left(\frac{L_S}{L_i + L_S} \right) \frac{d(\ln f)}{d(\ln \lambda)} \Big|_{\lambda=\lambda_e} \right.$$

$$\left. + \left(\frac{L_i}{L_i + L_S} \right) \frac{d(\ln F)}{d(\ln k)} \Big|_{k=k_e} + \left(\frac{L_i - L_S}{L_i + L_S} \right) \frac{q_e}{2} \frac{\partial}{\partial q} \right] S_1(\mathbf{q})|_{q=q_e} + \ldots, \tag{125}$$

where

$$S_1(\mathbf{q}) \equiv \int_{-\infty}^{\infty} \omega S(\mathbf{q}, \omega) d\omega$$

at constant q,

and we have used,

$$S(\mathbf{q_e}, \omega) = S(\mathbf{q_e}) \delta(\omega)$$

for elastically scattered neutrons.

We can see then, that the second term of equation 125 provides a first order correction to the static approximation. However, it should be noted that analytical methods provide a good approximation to this correction only in cases where the mass of the target atom is large relative to that of the neutron. For samples where this is not the case, a more empirical approach is necessary and this will be discussed in Section 4.4.3.

3.6 Introduction to the theory of spectroscopy

In order to appreciate, to some extent, the kind of information on atomic structure that it is possible to gain from spectroscopic experiments, it is important to understand the processes involved in producing the measured spectra. In this work, both neutrons and infrared radiation have been used to investigate the vibrations and rotations of the bonded units in a-C:H, each providing complementary information. All spectra are produced when transitions are made between different energy states, and although these may be fairly complex for a network structure such as a-C:H, by considering the energy levels associated with simple molecules, it is possible to gain some insight into the origin of the experimentally measured data. Of particular interest in looking at a-C:H, is the question of whether or not molecular hydrogen is present, "trapped" in pores within the network structure. Rotation of any H_2 molecules will be excited by only a small energy transfer and should be obvious from the inelastic neutron scattering spectra. Indeed, this data has the potential to provide the first clear evidence for the presence of H_2 molecules in a-C:H.

In performing any kind of spectroscopic measurement we are looking at the interaction between energy and the atomic/molecular system being studied by measuring the amount of energy either absorbed or emitted. Since the energy levels are quantised, interactions can only occur if the energy source can provide the right quantity of energy for some sort of transition/excitation to occur. Consider two of the energy states of a system, E_1 and E_2, shown in Figure 8.

Transitions can take place between the two levels if the amount of energy, $\Delta E = h\nu = E_2 - E_1$ is supplied. Which means that if this system is exposed to radiation of frequency ν, a transition $E_1 \rightarrow E_2$ may occur. After a time interval the system may well then decay back to state 1. So, either the absorption or emission spectrum

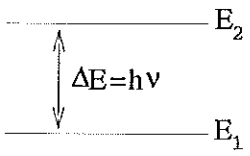

Figure 8: A system of two energy states.

of the system can be measured.

The energy to excite such transitions can have a number of sources depending on the type of energies to be examined and the frequency limitations of the source. Infra-red spectroscopy uses radiation in the region $3 \times 10^{12} - 3 \times 10^{14}$Hz to look at vibrational energy levels, where $\Delta E \sim 10^4$ Joules/mole. In an inelastic neutron scattering experiment the energy is provided by the incident neutrons, and is generally in the region $0 - 2.4 \times 10^{14}$Hz which can excite both rotational and vibrational modes. From these density of states measurements the presence and proportions of such modes can be ascertained. More details about spectroscopic methods can be found in [2].

The forms of the equations defining the "allowed" energy levels for different systems will now be examined. Although a summary of the results will be presented here, full derivations can be found in Section A. This work follows the methods used by [121] which provides a good theoretical introduction to vibrational and rotational spectroscopy.

3.6.1 The vibrating diatomic molecule

The covalent bond existing between two atoms in a stable molecule can be thought of as a spring between two masses. As the atoms vibrate, the atomic positions are continuously changing, and an equilibrium interatomic separation, r_{eq}, is defined

where the energy associated with the system is a minimum. Plotting energy vs. interatomic distance we obtain the familiar graph shown in Figure 9 [2].

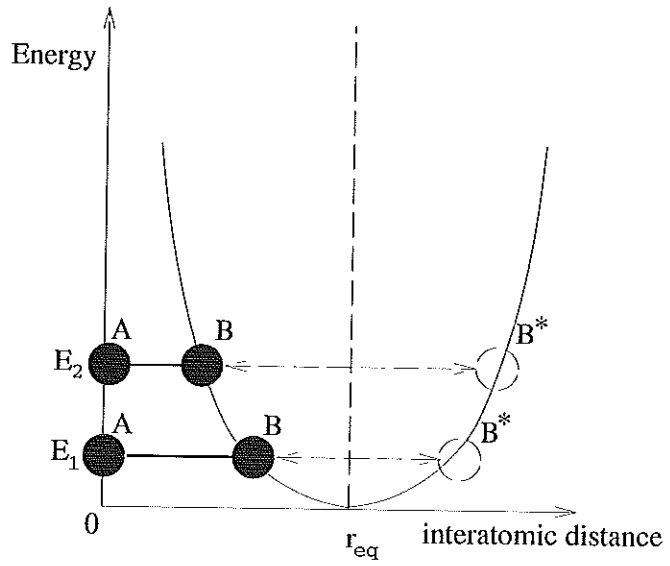

Figure 9: Energy vs. interatomic distance for a covalent bond in a diatomic molecule [2].

If atom A is considered stationary, the other will oscillate between B and B*. Notice that if the energy is increased from E_1 to E_2 the distance BB* is also increased, meaning that the oscillation becomes more vigorous, although the frequency of vibration remains constant. If the bond is considered to be like a spring (i.e. it obeys Hooke's law), the variation of energy with interatomic distance, r, can be written formally,

$$E = \frac{1}{2}k(r - r_{eq})^2 \tag{126}$$

where k is the force constant.

The model in which the energy has a parabolic form is of course the simple harmonic oscillator, and is the simplest model for a vibrating diatomic molecule.

The simple harmonic oscillator

Since vibrational energies are quantised, the allowed energies for any particular system may be determined by solving the Schrödinger equation. For the simple harmonic oscillator it is sufficient to use the one-dimensional Schrödinger equation:

$$-\frac{\hbar^2}{2\mu}\frac{d^2\psi}{dx^2} + V(x)\psi = E\psi, \tag{127}$$

where μ is the reduced mass of the system and the potential, $V(x) = \frac{1}{2}kx^2$ for a force constant k. By use of Lagrange's equation. it can be shown that

$$V(x) = \frac{1}{2}kx^2 = 2\pi^2\mu\omega^2, \tag{128}$$

where ω is the frequency of oscillation. Solution of Schrödinger's equation yields the result that the n^{th} energy level, E_n is given by:

$$E_n = (n + \frac{1}{2})\hbar\omega, \tag{129}$$

so that

$$E_0 = \frac{1}{2}\hbar\omega \tag{130}$$

and

$$\Delta E_n = E_{n+1} - E_n = \hbar\omega. \tag{131}$$

The lowest energy level,$n = 0$, does not give $E_0 = 0$ but $E_0 = \frac{1}{2}\hbar\omega$ - this is called the zero-point energy. Also, notice that for simple harmonic oscillation the energy levels are equally space, i.e. $\Delta E = \hbar\omega$ =constant.

The anharmonic oscillator

For a real molecule the simple harmonic oscillator model provides only an approximation to the actual behaviour. Real bonds do not in fact obey Hooke's law, particularly

for large compressions and extensions. Figure 10 shows a typical energy vs. distance plot for a diatomic molecule.

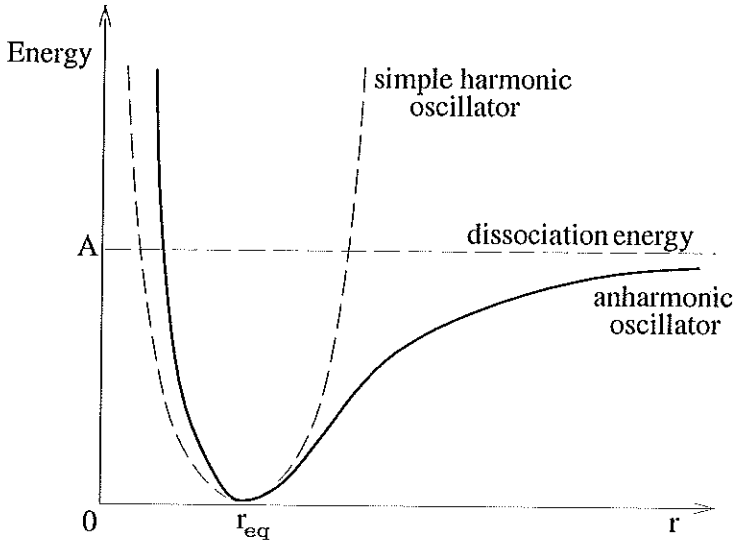

Figure 10: Energy vs. interatomic distance for an anaharmonic oscillator.

The shape of this curve may be described by the Morse function [122],

$$E = A\left[e^{-2\alpha r} - 2e^{-\alpha r}\right] \tag{132}$$

where α is a constant for a particular molecule and A is the dissociation energy. As before, the energy levels can be determined by solution of the Schrödinger equation, although this time V(x) is given by,

$$V(x) = A\left[e^{-2\alpha x} - 2e^{-\alpha x}\right]. \tag{133}$$

The resulting equation for E_n is:

$$|E_n| = A\left[1 - B(n + \frac{1}{2})\right]^2 \tag{134}$$

where

$$B = \frac{\alpha\hbar}{(2\mu A)^{1/2}}.$$

From equation 134 we can see that the energy levels have a quadratic dependence on n, so they will no longer be equally spaced (see Figure 11).

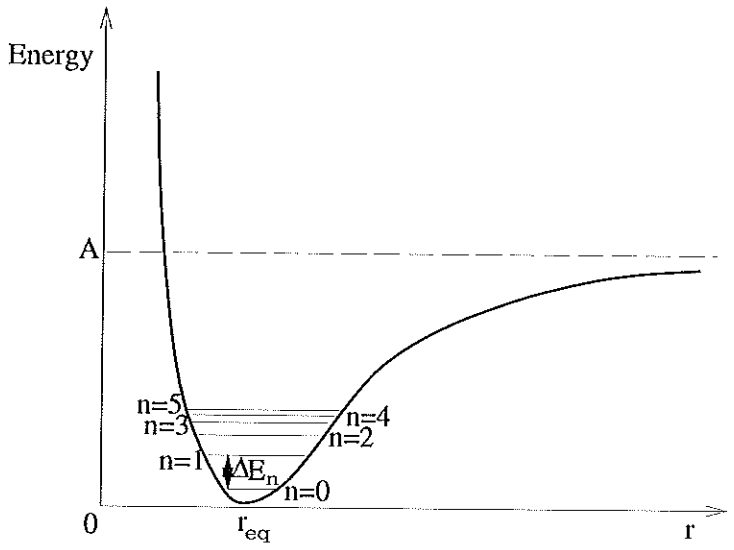

Figure 11: Some of the energy levels for the anharmonic oscillator.

$$\Delta E_n = E_{n+1} - E_n = A\left[B - 2(n+2)B^2\right] \tag{135}$$

So the spacing, ΔE, depends on the value of n. The zero-point energy (n=0) is:

$$E_0 = A\left[1 - B/2\right]^2. \tag{136}$$

3.6.2 The diatomic (harmonic) vibrating-rotator

Consider a rigid rotating diatomic molecule. Schrödinger's equation yields [121] that the rotational energy levels are given by:

$$E_l = \frac{l(l+1)h^2}{8\pi^2 I_e} \tag{137}$$

where l=0,1,2,... and is the rotational quantum number, and I_e is the equilibrium (i.e. $r = r_{eq}$) moment of inertia of the molecule. So that,

$$\Delta E_l = E_{l+1} - E_l = \frac{lh^2}{4\pi^2 I_e}, \tag{138}$$

i.e. the spacing of the energy levels depends on the value of l, as shown in Figure 12.

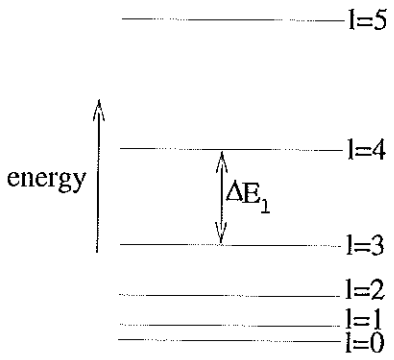

Figure 12: Some of the energy levels for the anharmonic oscillator.

Now we can look at what happens if the molecule is vibrating at the same time i.e. a non-rigid rotator. To do this the vibrational and rotational modes are considered to be independent, to a first approximation, so that the total energy can be written simply as,

$$E_{tot} = E_{rot} + E_{vib}. \tag{139}$$

To determine the energy levels we now use the three-dimensional Schrödinger equation:

$$\left[\frac{-\hbar^2}{2\mu}\nabla^2 + V(r)\right]\Psi(r,\theta,\phi) = E.\Psi(r,\theta,\phi) \tag{140}$$

and then find the radial equation by the method of separation of variables. For the harmonic oscillator the equation for the energy levels becomes (see Section A):

$$E_{n,l} = (n + \frac{1}{2})h\nu_e + \frac{l(l+1)h^2}{8\pi^2 I_e} - \frac{l^2(l+1)h^4}{128\pi^6\nu_e^2 I_e^3} \tag{141}$$

where

$$\nu_e = \frac{1}{2\pi}\sqrt{\frac{k}{\mu}},$$

for a force constant k. The higher order terms are unreliable because of the inaccuracy of the simple harmonic oscillator model.

The first term in equation 141 is that for the vibrational energy of a molecule considered as a harmonic oscillator; the second term is the energy of rotation of a rigid molecule (both these terms we are already familiar with); and the third term is a correction to take into account the stretching of the non-rigid molecule as it rotates. The effect on the rotational energy levels in moving from a rigid to a non-rigid (harmonic) rotator are shown in Figure 13 [2].

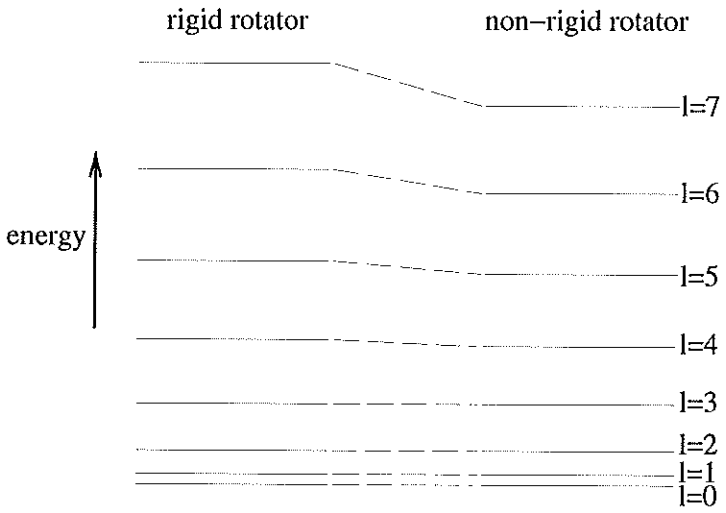

Figure 13: Comparison of the energy levels for a rigid and non-rigid rotator.

The rotational and vibrational energy levels are illustrated in Figure 14.

3.6.3 The diatomic (anharmonic) vibrating-rotator

For anharmonic oscillations vibrational and rotational motions can no longer be considered independent. Solution of the radial part of the Schrödinger equation with the

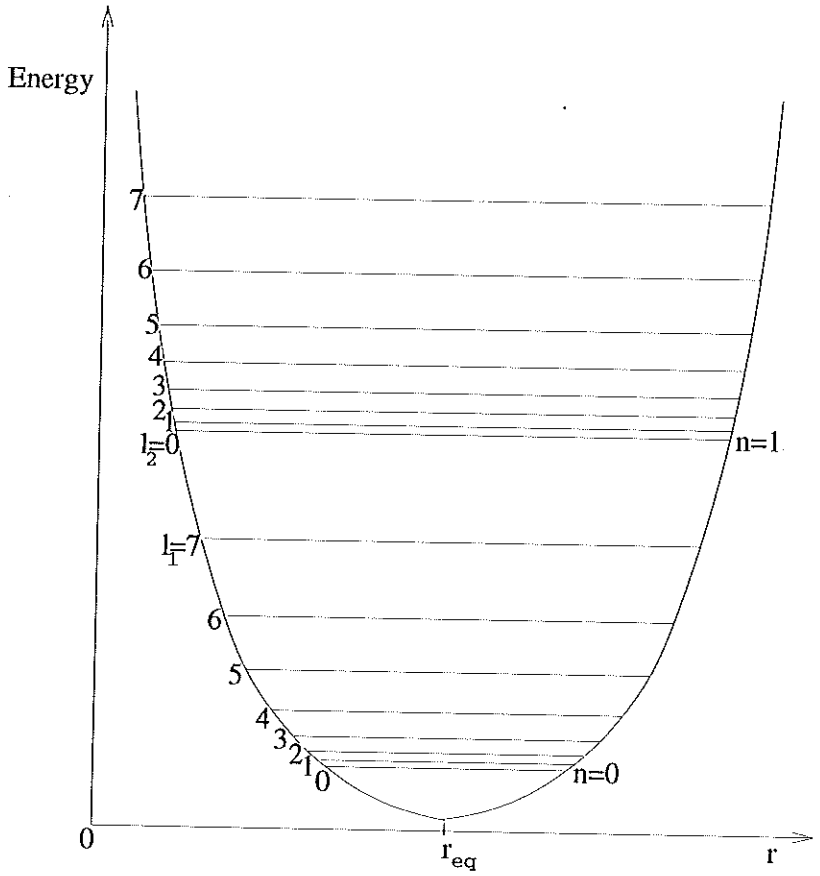

Figure 14: Some of the rotational and vibrational energy levels for a non-rigid (harmonic) vibrating-rotator.

Morse function defined in equation 132 for this complex situation, yields the result (see Section A):

$$\frac{E_{n,l}}{hc} = \omega_e(n+\frac{1}{2}) - x_e\omega_e(n+\frac{1}{2})^2 + l(l+1)B_e + D_e l^2(l+1)^2 - a_e(n+\frac{1}{2})l(l+1) \quad (142)$$

where,

$$\begin{aligned} w_e &= \frac{\alpha}{2\pi c}\sqrt{\frac{2A}{\mu}} \\ x_e &= \frac{h\omega_e c}{4A} \\ B_e &= \frac{h}{8\pi^2 I_e c} \\ D_e &= \frac{-h^3}{128\pi^6\mu^3\omega_e^2 c^3 r_{eq}^6} \\ a_e &= \frac{3h^2\omega_e}{16\pi^2\mu r_{eq}^2 A}\left(\frac{1}{\alpha r_{eq}} - \frac{1}{\alpha^2 r_{eq}^2}\right) \end{aligned}$$

and c is the velocity of light.

Notice that this time the equation for $E_{n,l}$ includes a term involving **both** n and l, indicating an interaction between the rotation and vibration of the molecule. For nearly all molecules this relation gives accurate values for the energy levels.

The results presented in this section have all referred to diatomic molecules. Although the equations will be modified to some extent for polyatomic systems, the trends and effects will be similar to those shown here, and this should provide some insight into the origins of the spectra.

Chapter 4

Experimental

4.1 Introduction

Details concerning the samples used and the experimental techniques employed are given. This includes a description of the production of neutrons at the ISIS pulsed source and the instruments used (LAD and TFXA). Data analysis methods are discussed in detail with some mention as to possible sources of experimental errors. A brief description of the infra-red spectroscopy method is given.

4.2 Samples

A summary of the preparation conditions and properties of the samples studied in this work is given in Table 4. For the samples deposited by CVD, the r.f. glow discharge system was operated at a frequency of 13.56MHz, using a power of 100W. The mean ion energy was measured by an electrostatic 90° energy analyser. For a detailed description of the deposition process see [124, 125]. The remaining samples were produced using a saddle-field fast-atom (i.e. neutral particle) source [126, 127]:

Sample	Precursor gas	Preparation method	Energy (eV)	Pressure (mbar)	C:H (at.%)	Density (gcm^{-3})	Knoop hardness (GPa)
1	C_2H_2	PE CVD‡	~30*	8.2×10^{-3}	56:44	1.4	5
2	C_2H_2	PE CVD	125*	2.1×10^{-3}	66:34	1.7	12
3	C_3H_8	FAS§	500†	1.4×10^{-4}	68:32	1.97	~14 [123]
4	C_2H_2	FAS	500†	1.4×10^{-4}	65:35	1.82	~14 [123]
5	C_2H_2	FAS	800†	$\sim10^{-3}$	78:22	1.25	unknown
6	C_6H_{12}	FAS	1200†	$\sim10^{-3}$	75:25	1.53	unknown
7	C_6D_{12}	FAS	1100†	$\sim10^{-3}$	73:27	1.53	unknown

‡ plasma enhanced chemical vapour deposition § fast atom source
* mean ion energy † effective source energy

Table 4: A summary of the characteristics of the samples studied.

a schematic diagram is shown in Figure 15.

Densities were determined either by a flotation method (PECVD) or a residual volume technique. The hydrogen content of each of the samples was determined by combustion analysis using a commercial CHN combustion analyser.

These samples have been studied using a variety of experimental techniques, although this study has mainly involved neutron diffraction, inelastic neutron scattering and infra-red spectroscopy. The effect of temperature has also been investigated for one of the a-C:H samples. In the following sections a brief overview of each experimental method will be given, together with appropriate remarks concerning data analysis, beginning with neutron diffraction.

4.3 Definitions and useful equations

Before discussing the instrumental set-up and the data analysis, it is useful just to recap on the useful expressions derived fully in Chapter 3.

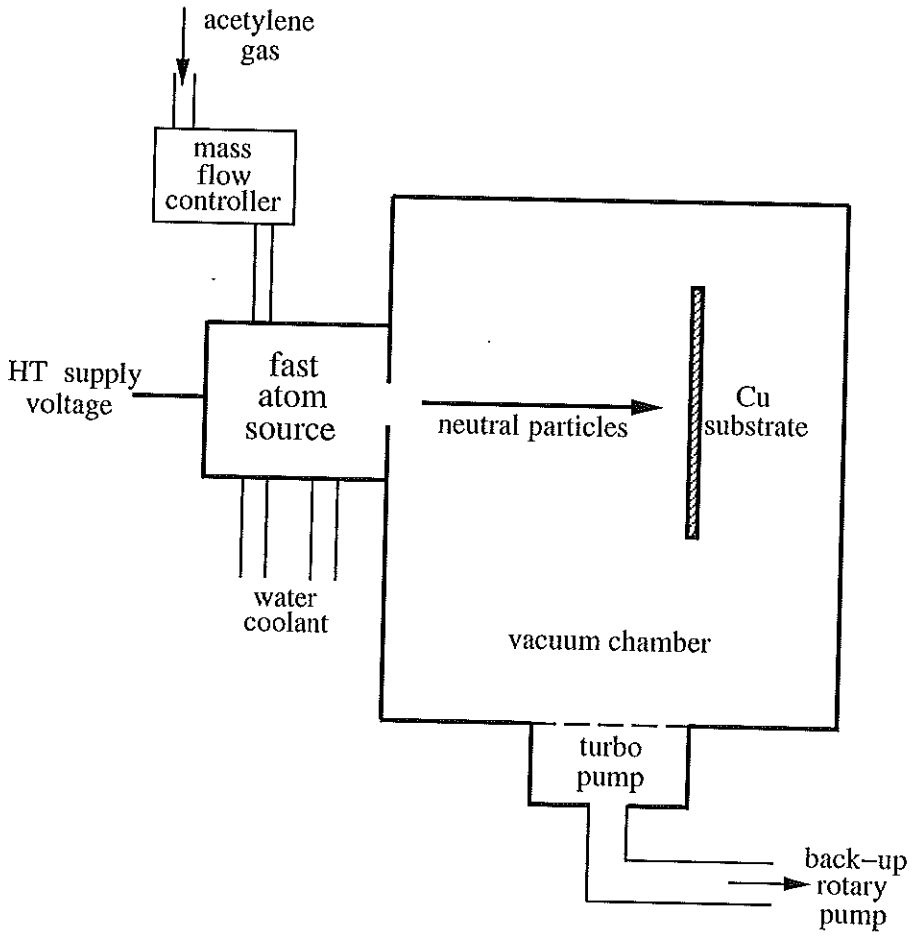

Figure 15: A schematic representation of the fast-atom source.

Neutrons are detected according to their time-of-flight (*tof*), which is defined by:

$$tof = t - t_0 = \frac{L_i}{v_i} + \frac{L_s}{v_s} = \frac{m}{h}\left[L_i\lambda_i + L_s\lambda_s\right], \tag{143}$$

where neutrons are produced at time t_0 and detected at time t. The incident wavelength, λ_i, is variable and the neutrons travel a distance L_i at velocity v_i from the moderator to the scattering centre. They are then scattered with a velocity v_s and wavelength λ_s to a detector at a distance L_s from the scattering centre.

By defining incident and scattered wavevectors, k_i and k_s, we can also define the wavevector transfer,

$$|\mathbf{Q}| = |\mathrm{k}_i - \mathrm{k}_s|, \tag{144}$$

where, for scattering from a liquid or amorphous solid [128],

$$Q = \frac{4\pi}{\lambda}\sin 2\theta \sim \frac{3.177}{tof}\left(L_i - L_s\right)\sin 2\theta, \tag{145}$$

where 2θ is the scattering angle and λ is the neutron wavelength. This allows the conversion of the *tof* measurement into a Q-space measurement. Following all the data corrections, the function we obtain is called the structure factor, S(Q), defined for an amorphous material by:

$$S(Q) = 1 + \frac{4\pi\rho}{Q}\int_0^\infty r dr\left[g(r) - 1\right]\sin(Qr), \tag{146}$$

where ρ is the average number density of atoms in the material and g(r) is the pair correlation function, which can be obtained by Fourier transformation of S(Q), and gives information on atomic correlations in real-space.

In a multi-component system there are contributions to the total structure factor from each atom-type pair. For a binary system such as a-C:H, we therefore have three terms which are weighted to give the total structure factor, S(Q), such that:

$$S(Q) = \sum_\alpha c_\alpha^2 b_\alpha^2 + \sum_{\alpha\beta} c_\alpha b_\alpha c_\beta b_\beta \left[A_{\alpha\beta}(Q) - 1\right], \tag{147}$$

Sample	C-C	C-H	H-H
3	1.85	-0.98	0.13
4	1.27	-0.38	0.11

Table 5: Normalised weighting coefficients for the partial structure factors and pair correlation functions. Units for b are fm, $c_C+c_H=1$.

where c_α and c_β are the atomic fractions, and b_α and b_β are the neutron coherent scattering lengths, respectively, of elements α and β, and $A_{\alpha\beta}(Q)$ are the partial structure factors. The first summation represents the "self-" or "single-atom" scattering, while the second corresponds to "interference" or "distinct" scattering, and contains the basic information on atomic correlations. The derivation of these equations is predicated on the validity of the static approximation [129, 130], which requires that any change in the neutron's energy upon scattering is small compared to it incident energy i.e. the neutrons are elastically scattered, but corrections are made to the data to account for any that are inelastically scattered (see Section 4.4.3).

Fourier transformation leads to the total pair correlation function, G(r), which, according to the Faber-Ziman formalism [128], is given as:

$$G(r) = \sum_{\alpha\beta} \left[c_\alpha c_\beta b_\alpha b_\beta \left(g_{\alpha\beta}(r) - 1 \right) \right], \tag{148}$$

where $g_{\alpha\beta}(r)$ represent the partial terms in G(r). From the weightings of the individual terms in the structure factor and the pair correlation function for two of the samples, as shown in Table 5, it can be seen that the dominant terms will be those arising from the carbon-carbon and carbon-hydrogen correlations. Note the negative carbon-hydrogen term due to the negative scattering length of hydrogen.

It is also useful to define the radial distribution function, J(r):

$$J(r) = 4\pi r^2 \rho G(r), \tag{149}$$

which gives a measure of the number of atoms at a given radial distance, r.

Notice that for the inelastic and infrared spectra each spectrum is plotted as a function of wavenumber (cm^{-1}), rather than energy transfer (meV). These is a convention used by chemists and conversion between the two can be done using the equation:

$$\text{wavenumber}, \quad \frac{1}{\lambda} = h \times \text{velocity of light} \times \text{energy transfer} \tag{150}$$

$$\text{i.e. wavenumber } (cm^{-1}) = 8.0668 \times \text{energy transfer.} \tag{151}$$

4.4 Neutron diffraction

4.4.1 Introduction

All the neutron measurements presented in this work were performed at ISIS at the Rutherford Appleton Laboratory (UK) [131], the most intense pulsed neutron source in the world. Neutrons are produced when synchrotron-accelerated protons at 500-800MeV collide with a target nucleus (usually uranium, tantalum or tungsten). The highly excited nuclear states which result decay either immediately or following a delay, producing nuclear particles such as neutrons, γ rays, neutrinos, etc. For a target of uranium up to 30 neutrons per proton are produced, although for tantalum or tungsten the number falls to around half that value. The "prompt" neutrons, produced immediately on impact, are used for time-of-flight (*tof*) experiments; and the "delayed" neutrons generate a low level time independent diffractometer background. The source at ISIS is pulsed because separate bunches of protons accelerated to 800MeV collide with the target, rather than a continuous stream. This means that neutrons with a wide range of wavelengths are produced in bursts at a rate of 50Hz. The neutron pulse at that stage is less than $1\mu s$ wide.

At the target the neutrons have an energy $\sim 10^9$ times too high to be useful for diffraction so they are slowed down in a moderator, while preserving as far as is practicable the time structure of the pulse. Inside the moderator neutrons scatter many times transferring energy to light moderator nuclei before escaping. Light atoms, as in hydrogen-containing materials, are used for the moderator since the energy transferred in a collision is greatest when the two particles have the same mass. The typical *tof* spectrum as a function of wavelength, λ, from a methane moderator is shown in Figure 16.

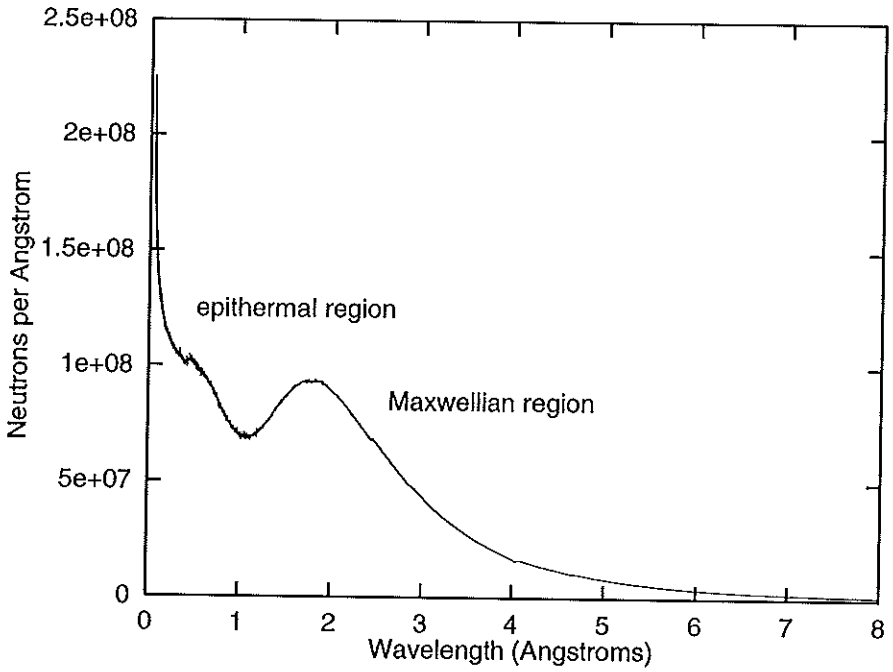

Figure 16: Incident neutron spectrum.

The spectrum has two regions: the epithermal region where intensity $\propto 1/\lambda$, and the Maxwellian region where intensity $\propto (E/T^2)\exp(-E/T)$, where T is the effective moderator temperature and E is the neutron energy. The Maxwellian region arises where neutrons have an effective kinematic temperature which corresponds to the moderator temperature.

From the moderator, where neutrons are travelling in all directions, a beam is collimated towards the sample position. For *tof* diffraction measurements the beam is not monochromated. Neutrons of varying wavelengths are scattered from the sample into fixed angle detectors where the scattering is measured as a function of *tof* (which can be directly related to the momentum transfer assuming "elastic" scattering). So, in a *tof* experiment neutrons with a range of energies from 800MeV downwards are incident on the sample. The complete scattering profile is then obtained by combining spectra from detectors at different angles.

4.4.2 The diffractometer LAD

The diffractometer LAD at the ISIS facility is optimised for the study of liquids and amorphous materials. A schematic diagram of the instrument is shown in Figure 17.

Neutrons arrive at the sample from a methane moderator at 100K with incident wavelengths between 0.25 and 6.5Å. A combination of ^{3}He gas and Li-glass scintillator detectors are used to measure scattering over a wide angular range: 5°-150°, with a Q-resolution varying from $\Delta Q/Q = 11$ at 5° to 0.5 at 150°. This change in resolution with scattering angle is illustrated in the spectra obtained from diamond powder, shown in Figure 18. It is interesting to note here the slight shifts in peak positions for different scattering angles in the diamond powder spectra. This is probably due to a slight miscalibration of the instrument, e.g. the detector positions, and illustrates just one of the sources of experimental error which needs to be considered.

Detectors are in pairs on either side of the incoming beam such that by combining the spectra from each detector, a Q-range of $\sim 0.2 - 50\text{Å}^{-1}$ can be covered. Measurements taken over this wide dynamic range lead to a real-space resolution, $2\pi/Q_{max} \simeq 0.1$Å. The facility to measure the structure factor with high accuracy and

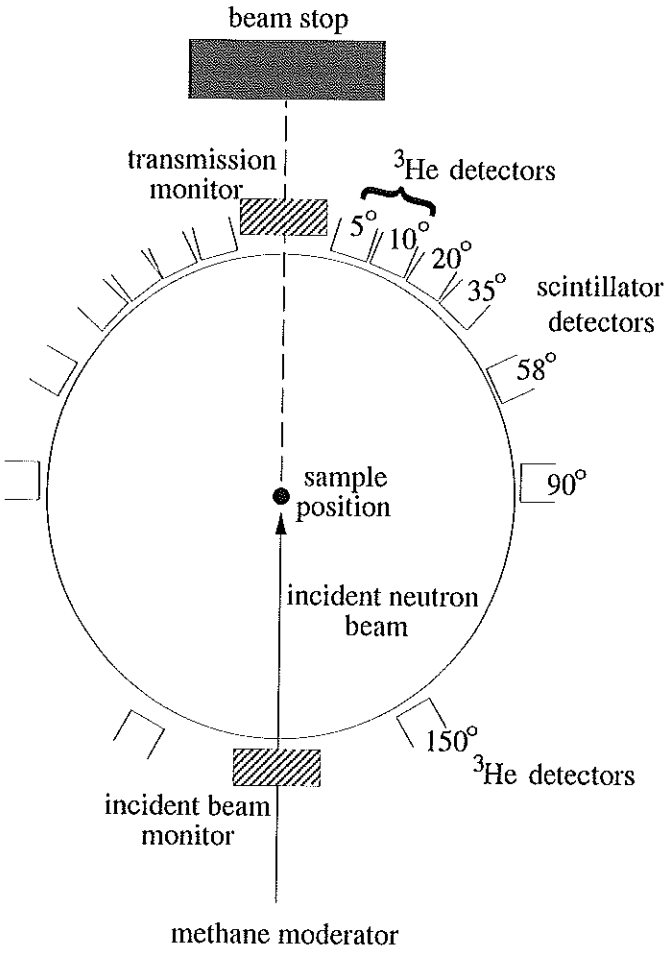

Figure 17: Schematic diagram of the instrument LAD.

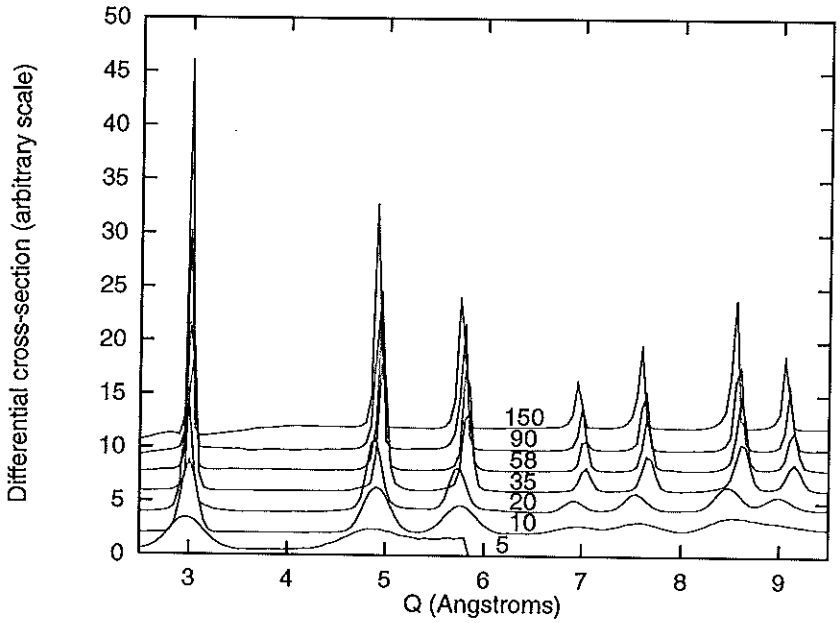

Figure 18: Spectra for diamond powder at different detector angles.

to obtain such a high real-space resolution makes this instrument very well-suited for the study of liquids and amorphous materials, particularly covalently bonded amorphous solids.

The incident beam monitor (before the sample) measures the incident neutron intensity:wavelength profile, and is used to normalise the experimental data. The transmission beam monitor (behind the sample) is used to try and determine the fraction of neutrons scattered by the sample in order to obtain information on the total neutron cross-section, $\sigma_T(\lambda)$, and the density of the sample. Also, the design of LAD and arrangement of its shielding means that the background scattering level is low.

4.4.3 Experimental procedure and data analysis

In order to obtain the normalised scattering from a sample, the following measurements need to be made:-

1. background - with furnace/cryostat, sample and container removed
2. empty furnace/cryostat (if used) - with container and sample removed
3. empty container - in the same environment as the measurement with the sample
4. sample in container
5. vanadium rod - with a geometry comparable to the sample container.

The sample container should ideally be vanadium as it can withstand high temperatures and is predominantly an incoherent scatterer i.e. its scattering profile is essentially flat, which avoids errors in the subtraction of the can scattering. Another material suitable for sample containers is titanium:zirconium, where the alloy composition is such as to give $\sigma_{coh} = 0$. In the experiments carried out on the a-C:H samples in this work vanadium sample cans were used.

The vanadium rod measurement is used to put the scattering on an absolute scale. Vanadium is used because its neutron cross-section is almost entirely incoherent and is well-known. The vanadium calibration is discussed further in Section 4.4.3.

Before obtaining a structure factor, however, several corrections need to be applied to the data, the major ones being for: background, container and multiple scattering, attenuation/absorption and the effects of inelasticity, which is the most problematic correction to make for hydrogenous materials. Details about these corrections can be found in the following sections, but the basic algorithm for data analysis is:

i. normalise to the incident beam monitor

ii. subtract the background

iii. normalise to the vanadium calibration

iv. subtract the multiple scattering

v. apply absorption corrections and subtract the can scattering

vi. apply inelasticity corrections

vii. merge spectra from different detector angles

viii. Fourier transform → pair correlation function, G(r)

ix. generate a radial distribution function, J(r), and fit with Gaussians.

Now consider these steps in more detail [3].

Normalising to the incident beam monitor

Before the normalisation can be done the data is first corrected for detector deadtime and converted from *tof* to Q using equation 145. When a detector detects a neutron, there is a finite time during which, if another neutron arrives, it will not be detected. This is called its deadtime and is typically 1.3μs for ^{3}He detectors and 250ns for scintillators. Following this the spectra are divided by the incident monitor spectrum to normalise to the wavelength dependence of the incident beam - this can be modified by small variations in moderator temperature and proton beam steering.

The transmission monitor

The transmission measurement is used in a more indirect way to provide information about the total neutron cross-section, $\sigma_T(\lambda)$, and the density of the sample. Generally,

the sample's transmission, $T(Q)$, can be written as [3]

$$T(Q) = \int_0^W \exp -\rho\sigma_T(\lambda)L(x)\frac{dx}{W} \tag{152}$$

where x is the perpendicular distance from one edge of the beam, L is the neutron flight path within the sample, W is the beam width (see Figure 19), ρ is the number density of the sample, and $\sigma_T(\lambda)$ is the total neutron cross-section of the sample, and

$$\sigma_T(\lambda) = \text{scattering cross-section, } \sigma_S(\lambda) + \text{capture cross-section, } \sigma_a(\lambda). \tag{153}$$

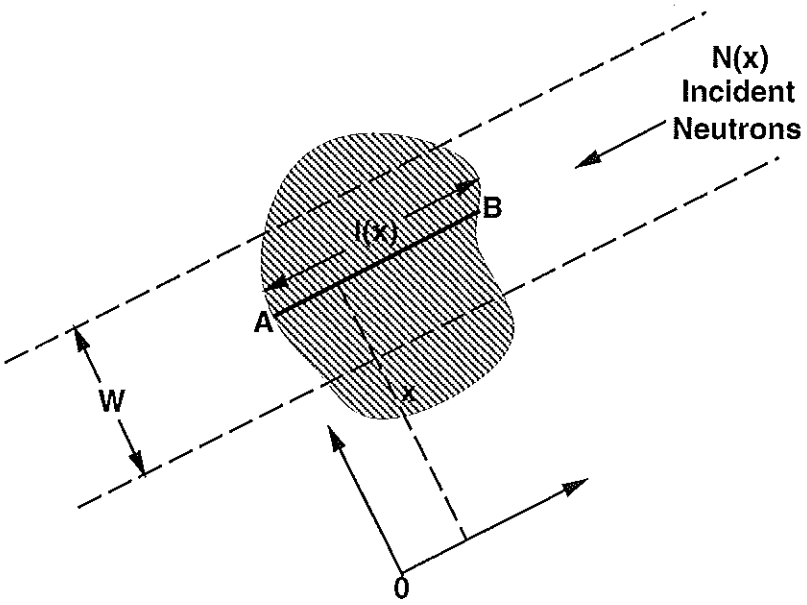

Figure 19: A schematic diagram to illustrate the transmission geometry [3].

Notice that the total neutron cross-section depends on the neutron wavelength, λ (i.e. the neutron energy). This means that $\sigma_S(\lambda)$ varies between its so-called "bound" and "free" values. The bound values correspond to the case of an immoveable nucleus, and would be observed for low energy neutrons. For neutrons of high energy all types of modes (diffusional, rotational, etc.) can be excited in the sample nuclei, so $\sigma_S(\lambda)$

observed is the free value. The bound and free cross-sections are related by,

$$\sigma_S(\lambda)_{free} = \left(\frac{A}{A+1}\right)^2 \sigma_S(\lambda)_{bound} \tag{154}$$

where A is the mass of the nucleus. So, for hydrogen, for example, $\sigma_S(\lambda)_{free} = 0.25\sigma_S(\lambda)_{bound}$, which means that the transmission measurement is very important for samples containing low mass nuclei. An example of a measured cross-section for an a-C:H sample is shown in Figure 20.

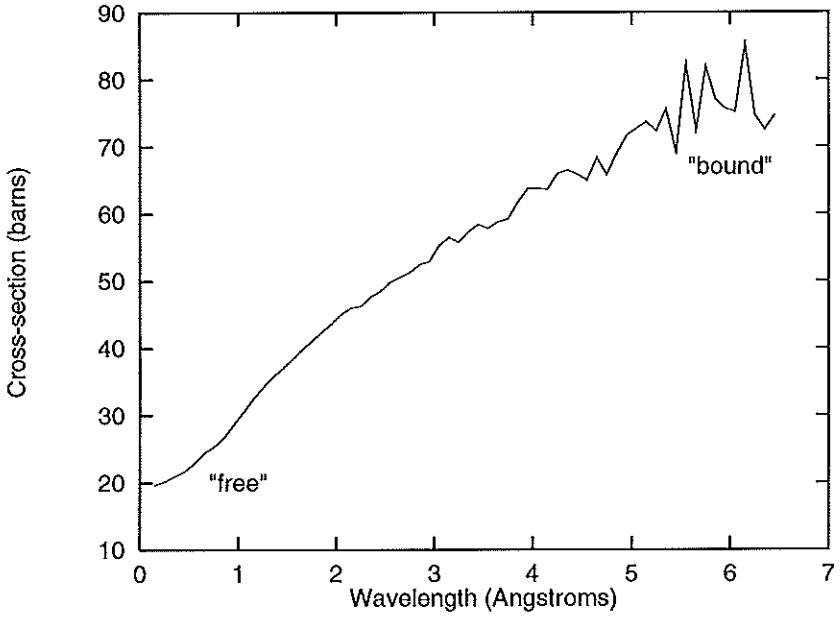

Figure 20: The measured cross-section for an a-C:H sample.

Vanadium calibration

The experimentally measured intensity, $I^E(Q)$, is a convolution of a diffractometer-dependent function, $F(Q)$, which is a function of the detector and the incident flux. So,

$$\text{for the sample,} \qquad I_C^E(Q) = DCS_S(Q).F(Q)$$

$$\text{for the sample + can,} \quad I^E_{CS}(Q) = DCS_{CS}(Q).F(Q)$$
$$\text{for the vanadium rod,} \quad I^E_V(Q) = DCS_V(Q).F(Q)$$

where $DCS_i(Q)$ are the differential scattering cross-sections (which still need to be corrected for absorption, multiple scattering, etc.). Thus,

$$F(Q) = \frac{I^E_V(Q)}{DCS_V(Q)}. \tag{155}$$

As the vanadium has a predominantly incoherent cross-section, $DCS_V(Q)$ can be estimated with reasonable accuracy, so if $I^E_V(Q)$ is measured, $F(Q)$ can be determined. In practice, the measured vanadium intensity is fitted with a smooth curve to minimise statistical errors and remove small Bragg peaks present due to the small amount of coherent scattering. A typical vanadium spectrum normalised to the incident beam monitor and with the background subtracted is shown in Figure 21.

Absorption and multiple scattering corrections

Some neutrons will be absorbed by the sample and some will be scattered more than once within the sample, and the data must be corrected for this. So we have,

$$DCS_{CS}(Q) = I_S(Q)A_{S,CS} + I_C(Q)A_{C,CS} + M_{SC}(Q)$$
$$DCS_C(Q) = I_C(Q)A_{C,C} + M_C(Q)$$

where $A_{S,CS}$, $A_{C,CS}$ and $A_{C,C}$ are the Paalman and Pings [132] attenuation co-efficients, and $M_{SC}(Q)$, $M_C(Q)$ are the total multiple scattering differential cross-sections [133, 134] (see Figure 22).

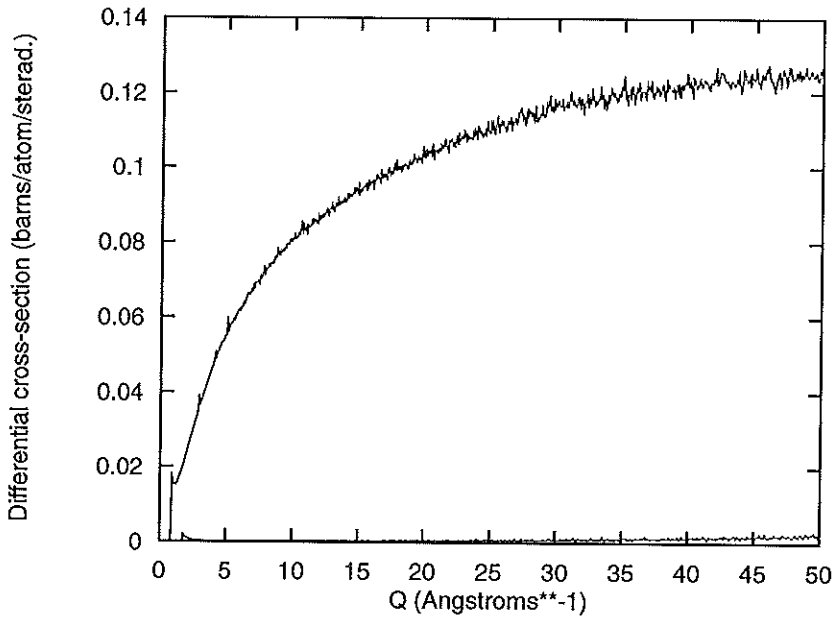

Figure 21: A normalised vanadium spectrum (top) and a background spectrum (bottom).

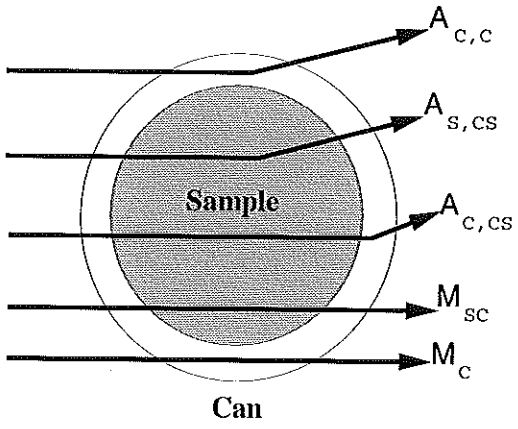

Figure 22: A schematic diagram to illustrate the assignments of attenuation coefficients and multiple scattering differential cross-sections.

Both A_{ij} and M_{ij} depend on the scattering geometry and size of the sample, and the attenuation and multiple scattering terms are functions of the neutron energy due to their dependence on $\sigma_S(\lambda)$ and $\sigma_a(\lambda)$. The attenuation factors can be calculated exactly in the Static Approximation, within the limits of numerical accuracy. The multiple scattering, however, cannot be evaluated very accurately since they require a detailed knowledge of the structure of the sample. Normally the method of calculation of this uses the total measured transmission cross-section and assumes the scattering is isotropic at each neutron energy. To minimise the systematic error introduced in correcting for multiple scattering, the sample should scatter no more than 10-20% of the incident neutrons.

For a-C:H, although the level of multiple scattering is ~20% this is mostly incoherent (due to the high value of σ_{inc} for H) and takes the form of a smoothly varying function of Q and therefore does not lead to problems in the data analysis.

Note that if the sample is also contained within a furnace/cryostat attenuation and multiple scattering corrections must also be carried out for this.

Inelasticity or Placzek corrections

So far the discussion of data corrections has assumed that the scattering is elastic i.e. that the Static Approximation holds. However, and particularly for light nuclei, this is not the case and a method is needed by which the deviation of the total differential scattering cross-section from the Static Approximation can be taken into account. Since it is impractical to measure the complete dynamic structure factor, $S(Q,\omega)$, the static structure factor, $S(Q)$, cannot be obtained by direct integration of $S(Q,\omega)$ and so a method by which the effects of inelastic scattering can be corrected for has to be found.

Placzek [118] found that for nuclei more massive than the neutron the form of the correction is related only to the nuclear mass, sample temperature, incident neutron energy and the geometry and efficiency of the detection process. However, when the nuclear mass is small simplistic approaches such as this break down and an alternative needs to be found.

For a-C:H the high incoherent scattering cross-section of hydrogen gives rise to a large amount of self-scattering which will change the overall level of the measured total scattering without affecting the interference function, to first order. Therefore, isolation of the interference function is possible to a good approximation if the overall shape of the self-scattering can be found. The method adopted is an empirical one which involves fitting a low order polynomial to the underlying curve which is then removed from the spectrum. Since the major impact of the inelasticity corrections is in the self-scattering term, the subtraction of a smooth curve like this provides a reasonable approximation (bearing in mind the fact that current pseudo-analytic approaches to this problem [135, 136, 137] do not cope well with low mass nuclei). This method works well for the data at $Q >\sim 2\text{Å}^{-1}$, however, for the region below $Q \sim 2\text{Å}^{-1}$ it is less robust and as a consequence, the form of the structure factor in this region is not as quantitatively reliable and this may lead to certain problems in the Fourier transformation to the pair correlation function. In other studies of this problem [135] the interatomic distance for nitrogen, for example, is found to be 3% too short, and for deuterium the shift in Q produces a 180° phase shift in the oscillations in $\sin(Qr)$. Therefore it is expected that bond distances and peak areas for correlations involving hydrogen will be less precise in relation to those obtained for carbon.

The effect of these corrections on the experimental data is illustrated for one

detector's spectrum, in Figures 23 and 24.

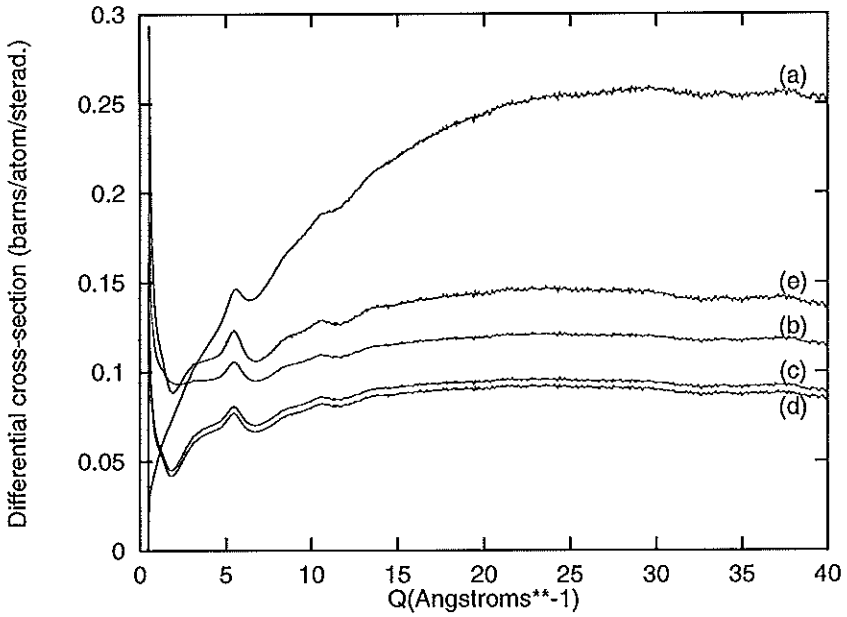

Figure 23: The effect of corrections on the experimental data: (a) corrected for detector deadtime and normalised to the incident beam monitor, with the background subtracted, (b) vanadium calibrated, (c) corrected for multiple scattering, (d) with the can subtracted, and (e) corrected for absorption.

Obtaining the structure factor

Once all the corrections have been made, the 14 spectra of varying Q-range are merged together to produce a structure factor which will typically cover the range $\sim 0.2 - 50\text{Å}^{-1}$. Spectra from each detector angle are merged by weighting each one with the intensity with which it was measured (i.e. inversely with the variance, assuming Poisson statistics for the data - the weighting function is taken from the corrected intensity data of the vanadium calibration).

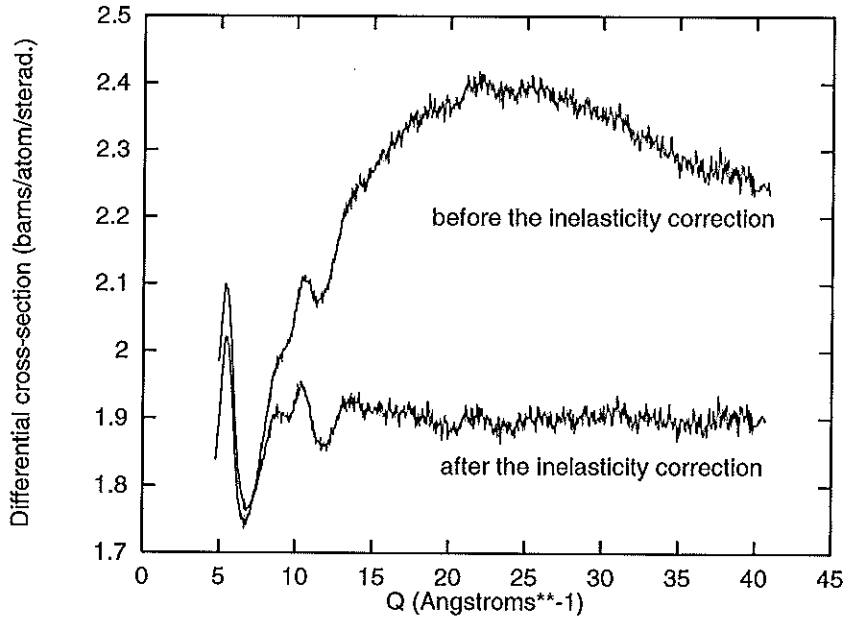

Figure 24: The effect of the inelasticity correction.

Further analysis

There exists a simple Fourier transform relationship between the structure factor, $S(Q)$, and the pair correlation function, $G(r)$:

$$S(Q) = 1 + \frac{4\pi\rho}{Q}\int_0^\infty rdr[G(R) - 1]\sin(Qr) \tag{156}$$

where ρ is the average number density of the sample.

In addition to the second order inaccuracies introduced in performing the inelasticity correction, spurious features in the $G(r)$ can arise from statistical noise in the $S(Q)$ and from its finite range. To minimise the truncation effects in the $S(Q)$, a window function is often introduced in the Fourier transform which downweights the high Q part of the spectrum, thereby damping out the termination ripples. Another source of error is the effect of the resolution function of the instrument. This involves the effects of angular uncertainty in the detectors, timing uncertainties and the width of the neutron pulse, and will be convoluted with the experimental data. This means

that there is little point in taking measurements with a statistical error $<\sim 1\%$, the approximate level of the systematic errors.

Alternative methods for obtaining a pair correlation function from the structure factor are available. These are generally inverse methods, and an example of this is the minimum information method [138].

The radial distribution function, $J(r) = 4\pi r^2 \rho G(r)$ can be generated from the pair correlation function: $J(r)$ is a measure of the number of atoms at a given radial distance from an origin atom. This is then fitted with a series of Gaussians, allowing both position and area to vary. By this method reliable values for the bond lengths and co-ordination numbers can be determined.

4.5 Inelastic neutron scattering

4.5.1 Introduction

Inelastic neutron scattering is a technique used to study the vibrational density of states in molecules or networks. As a complementary technique to infra-red (IR) and Raman scattering it has the advantage that the measured intensity is directly proportional to the vibrational density of states.

4.5.2 The TFXA spectrometer

The inelastic neutron scattering measurements for this work were taken on the TFXA (time-focussed crystal analyser) spectrometer at the ISIS facility at the Rutherford Appleton Laboratory (UK) [131]. Neutron production at ISIS has already been described in Section 4.4.1 and a schematic diagram of the instrument is shown in Figure 25.

that there is little point in taking measurements with a statistical error $<\sim 1\%$, the approximate level of the systematic errors.

Alternative methods for obtaining a pair correlation function from the structure factor are available. These are generally inverse methods, and an example of this is the minimum information method [138].

The radial distribution function, $J(r) = 4\pi r^2 \rho G(r)$ can be generated from the pair correlation function: $J(r)$ is a measure of the number of atoms at a given radial distance from an origin atom. This is then fitted with a series of Gaussians, allowing both position and are to vary. By this method reliable values for the bond lengths and co-ordination numbers can be determined.

4.5 Inelastic neutron scattering

4.5.1 Introduction

Inelastic neutron scattering is a technique used to study the vibrational density of states in molecules or networks. As a complementary technique to infra-red (IR) and Raman scattering it has the advantage that the measured intensity is directly proportional to the vibrational density of states.

4.5.2 The TFXA spectrometer

The inelastic neutron scattering measurements for this work were taken on the TFXA (time-focussed crystal analyser) spectrometer at the ISIS facility at the Rutherford Appleton Laboratory (UK) [131]. Neutron production at ISIS has already been described in Section 4.4.1 and a schematic diagram of the instrument is shown in Figure 25.

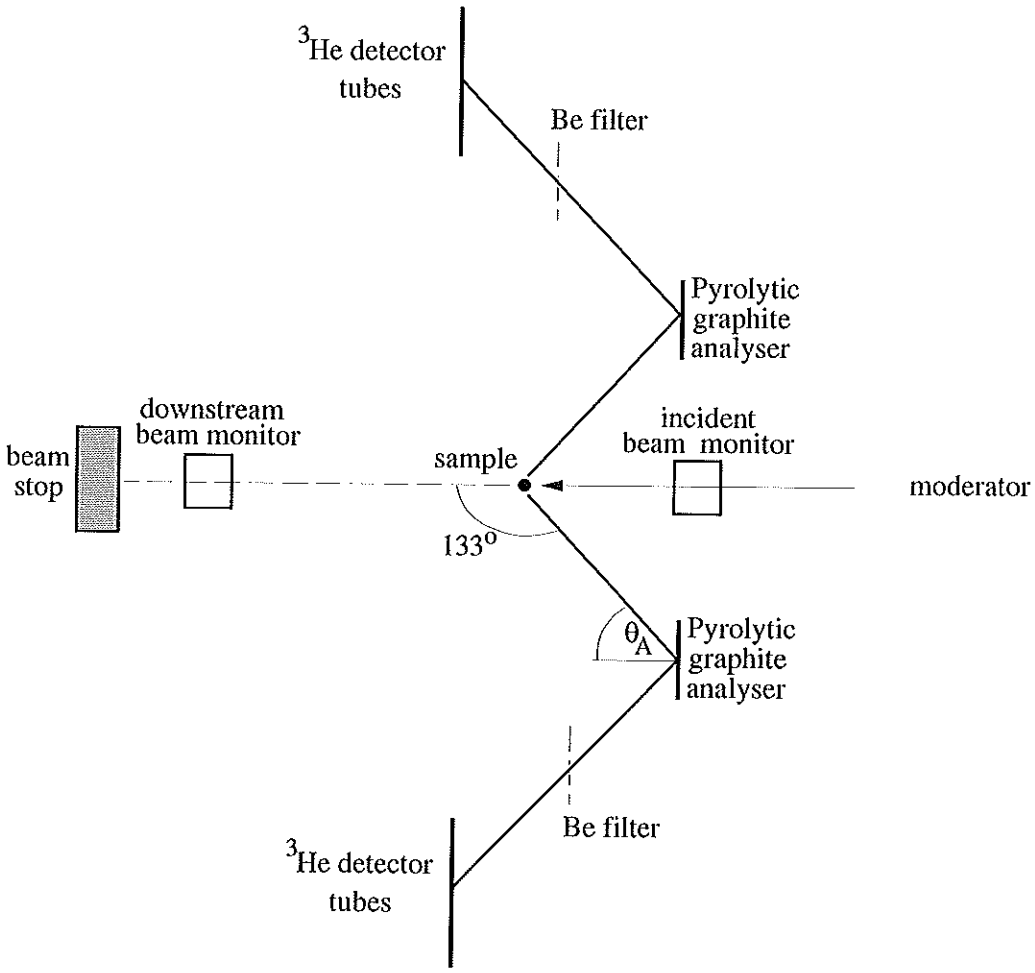

Figure 25: A schematic diagram of the inelastic spectrometer TFXA.

From the diagram it is clear that TFXA is an indirect geometry inelastic scattering spectrometer. Neutrons with incident energies up to ~1eV are backscattered from the sample through 133°. They are then energetically discriminated by a pyrolytic graphite analyser. This type of energy analyser is used because it gives good energy transfer resolution and high count rates over a range of energy transfers. Before the neutrons reach the detectors they pass through a beryllium (Be) filter to remove neutrons from higher order crystal reflections. The neutrons are then detected as a function of *tof* by banks of ^{3}He gas detectors. Energy transfers over the range 2-1000meV can be measured in this way, with a resolution of 1.5-3%.

The sample is usually held in an aluminium foil sachet, so the container does not contribute to the measured intensity. The important thing is not to make the sample thicker than a few millimetres (i.e. so that the total scattering is ~10%), then multiple scattering is avoided.

4.5.3 Data analysis

From the *tof* measurement, the energy transfer, $\hbar\omega$, is determined using the equation,

$$\begin{aligned} \hbar\omega &= E_i - E_S \\ &= \frac{mL_i^2}{2t_i^2} - \frac{mL_S^2}{2t_S^2} \end{aligned}$$

where E_i, E_S are the incident (variable) and scattered (fixed) neutron energies, L_i, L_S are the corresponding flight paths, and t_i, t_S the times of flight, m is the neutron mass.

But,

$$\text{the total } tof, \qquad t = t_i + t_S,$$

$$\text{where,} \qquad t_i = \frac{mL_i}{\hbar k_i} = \frac{mL_i d \sin\theta_A}{\hbar\pi}$$
$$\text{and} \qquad t_S = t - t_i,$$

so that,

$$\hbar\omega = \frac{mL_i^2}{2}\left(t - \frac{mL_i d\sin\theta_A}{\hbar\pi}\right)^2 - \frac{mL_S^2}{2}\left(\frac{mL_S d\sin\theta_A}{\hbar\pi}\right)^2. \qquad (157)$$

Here d is the crystallographic spacing and θ_A the scattering angle of the analyser crystal. All the quantities on the righthand-side of equation 157 are either known or can be measured experimentally, and hence $\hbar\omega$, the energy transfer, can be determined.

Once the intensity as a function of energy transfer has been obtained, the standard corrections for detector deadtime need to be applied. Following this, analysis of the spectra generally involves assigning peaks and regions of the spectrum to vibrational modes in the sample in an analogous way to infra-red spectroscopy.

4.5.4 CLIMAX analysis

In an attempt to extract further information from the inelastic neutron scattering spectra the CLIMAX program [139, 140, 141] was developed. A molecule representative of the bonding environments present in the sample with force constants for its associated vibrations is defined, and an inelastic scattering profile is generated for comparison with the experimental data. Using a process of force constant refinement the fit to the experimentally measured spectrum can be improved so that quantities such as the ratio of CH:CH_2 groups can be determined [142, 143]. However an approach using the model molecule shown in Figure 26 met with little success, indicating the limitations of this kind of analysis when applied to amorphous networks.

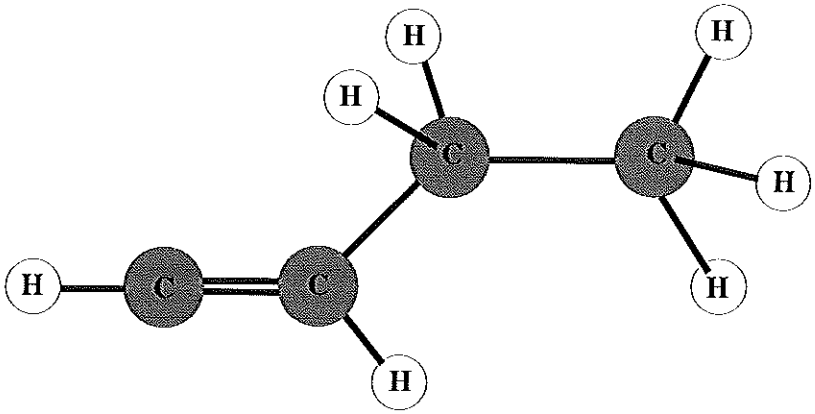

Figure 26: The molecule used for CLIMAX analysis.

4.6 Infrared spectroscopy

4.6.1 Introduction

Infrared (IR) spectroscopy is a popular and commonly used method of investigating the vibrational modes in materials. However, in most cases the spectrum can provide only qualitative information, although this can be very useful, especially where complementary information from other experimental techniques is available.

There are two general types of measurement in IR spectroscopy: those which involve absorption, transmission, or reflection of radiation by the sample and require some kind of standard, or reference, spectra against which to compare the measured intensity, and those which involve measuring the signal emitted by the sample upon irradiation from an IR source. The type of measurement used very much depends on the nature of the sample being studied. For instance, the a-C:H samples studied in this work are highly reflective, so transmission and absorption measurements yield little or no information. Diffuse reflectance measurements, however, can provide good

information, particularly in the low frequency region of the spectrum as the high frequency region can be affected by reflections from the surfaces of the small flakes. For this region, better information can be gained from acoustic emission measurements. The experimental arrangements for each of these techniques are discussed in more detail in the following sections.

Fourier transform infrared (FTIR) spectroscopy is fundamentally different to conventional IR spectroscopy in the way in which the spectra are measured. In the conventional arrangement, radiation from a polychromatic source passes through the sample and is then split-up into its constituent frequencies by either a prism or grating. The spectrum for each frequency in turn is measured by a detector, and these are then combined to produce a total spectrum.

In FTIR spectroscopy, the spectra for all frequencies are measured simultaneously, so that a complete spectrum can be obtained in seconds. Before reaching the sample, the radiation from the IR source passes through an interferometer. The moveable mirror in the interferometer is used to introduce a path difference, δ, between the two arms which results in an interference pattern when the beams are recombined. This interference spectrum is then incident on the sample, and the transmitted/reflected/absorbed intensity is measured in the detector as a function of the path difference, δ (for a mirror moving at a constant velocity, this is effectively a function of time). Using the Fourier transform relations (for an ideal spectrometer) [144]:

$$I(\delta) = \int_0^{+\infty} I(\nu) \cos 2\pi\nu\delta d\nu$$

$$\Rightarrow I(\nu) = 2\int_0^{+\infty} I(\delta) \cos 2\pi\nu\delta d\delta,$$

the measured intensity, $I(\delta)$, can be converted to a frequency spectrum, $I(\nu)$. In this way, it can be seen that the whole of the frequency spectrum can be measured at

once. In practice, the frequency range that can be measured is limited by the finite sampling intervals, and the resolution of the spectrum is limited by the maximum value of δ that can be achieved in the interferometer.

In performing an FTIR measurement, there are several factors that affect the signal, some of which are listed below:

- non-ideality of the beamsplitter in the interferometer
- non-uniform amplifier response
- beam divergence through the interferometer
- mirror misalignment in the interferometer.

The principal noise contribution to the spectrum should result from detector noise, although this is rarely achieved in practice. Careful consideration to any possible sources of noise, from poor sampling to external vibrations.

Only a brief account of FTIR spectroscopy has been given here, and more information can be found in books by Bell [144] and Banwell [2], for example.

4.6.2 Transmission/Absorption spectroscopy

The experimental arrangement for these measurements is shown in Figure 27. As this technique was not useful in the study of a-C:H, no detailed description will be given (see [144]). However, to obtain the information from the recorded spectra it is necessary to perform a standard measurement, i.e. 100% transmission (no sample) or 100% absorption.

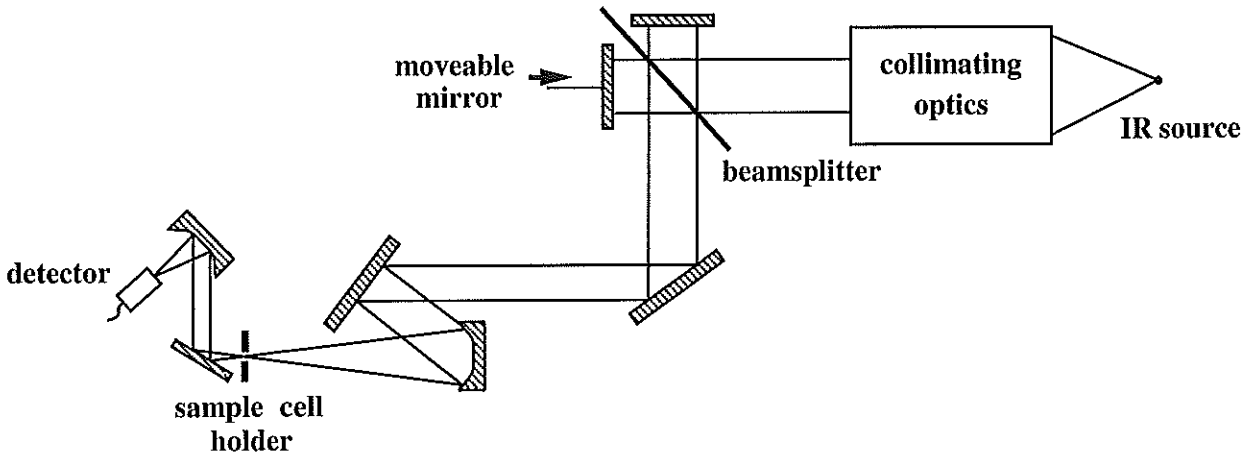

Figure 27: The experimental set up for FTIR transmission/absorption measurements.

4.6.3 Diffuse reflectance spectroscopy

For the samples studied in this work, IR spectra were obtained using a Biorad FTIR FTS60 DRIFT (diffuse reflectance IR Fourier transform) spectrometer, see Figure 28. The IR beam is directed onto the sample and undergoes reflection, refraction and absorption before emerging at the sample surface. This diffuse radiation is then collected by a toroidal mirror and focussed onto the detector. In this way the spectra obtained are measured in terms of a fraction of reflectance, which can easily be inverted to obtain absorption spectra. The energy resolution is $\sim 2 cm^{-1}$. A reference spectrum for carbon black is used (100% absorbance).

4.6.4 Acoustic emission spectroscopy

Here, no reference spectrum is required, as the emission results from vibrational modes excited by the incident IR radiation, and is measured using microphonic detectors. The experimental configuration is shown in Figure 29. The sample compartment is black inside to limit signals other than from the sample reaching the detector. Also,

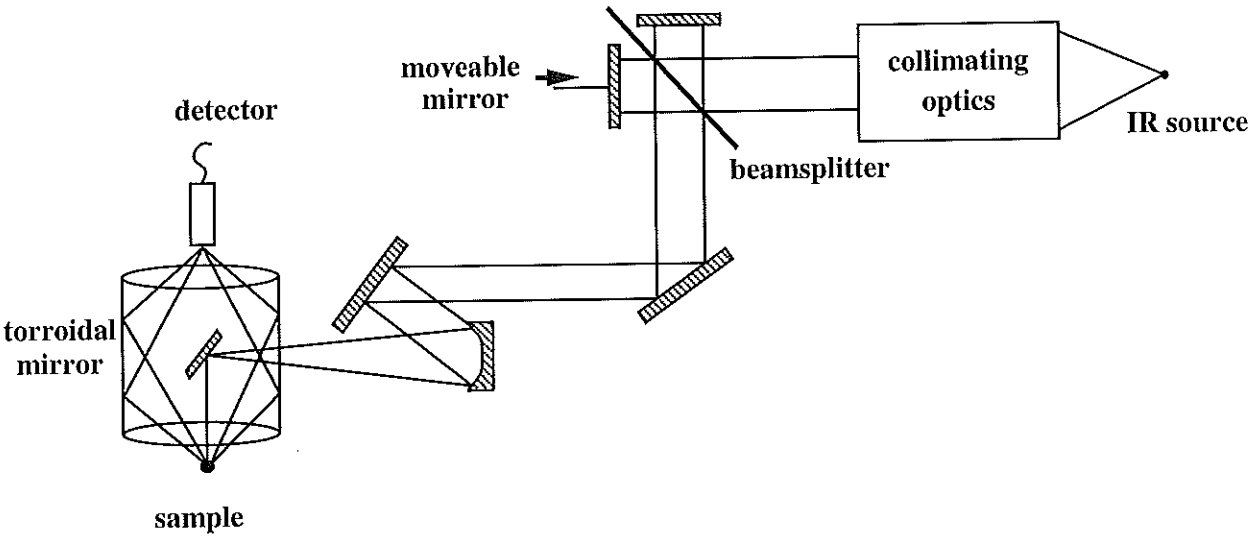

Figure 28: The experimental set up for FTIR diffuse reflectance measurements.

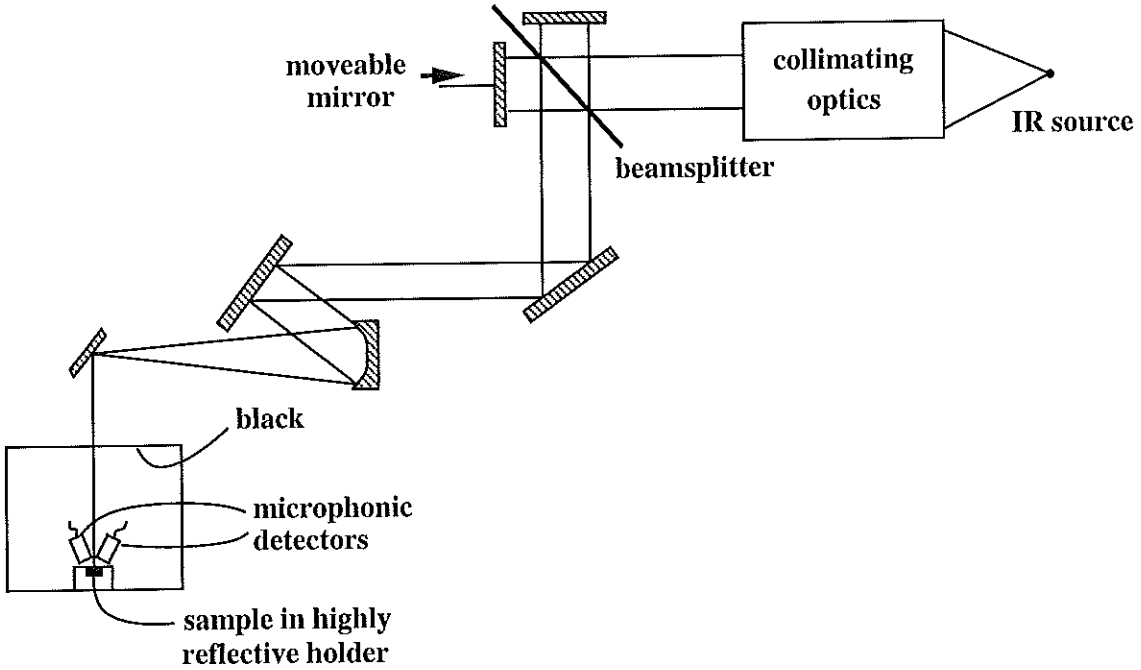

Figure 29: The experimental set up for FTIR acoustic emission measurements.

the sample is held in a highly reflective mount, so that as much of the signal from the sample as possible is detected.

4.6.5 Data analysis

As with other spectroscopic techniques, interpretation of the spectra does not extend much further than assigning peaks to vibrational modes and looking at changes in relative peak sizes. However, in some cases, regions of the spectra can be fitted with a series of Gaussians, with peak positions and areas allowed to vary, to obtain more detailed information. This is particularly useful in the studies of a-C:H presented in Chapters 6 and 7.

Chapter 5

Results I: Neutron diffraction

5.1 Introduction

The total structure factors and pair correlation functions obtained for all the samples are shown in Figures 30 and 31 respectively.

For the real-space data, the pair correlation functions for graphite (8) and diamond (9) are included for comparison, together with some known values for bondlengths (Table 6).

The LAD diffractometer (see Section 4.4.2), is particularly well-suited for the study of covalently bonded amorphous materials, and the exceptional real-space resolution of this data allows us to look in detail at the carbon bonding environments within the amorphous network. Looking at Figure 31 we can make the general peak assignments shown in Table 7.

All the plots show similar features except the deuterated sample (g) where the C-D first neighbour peak is positive. The presence of the peak at ~0.8Å gives direct

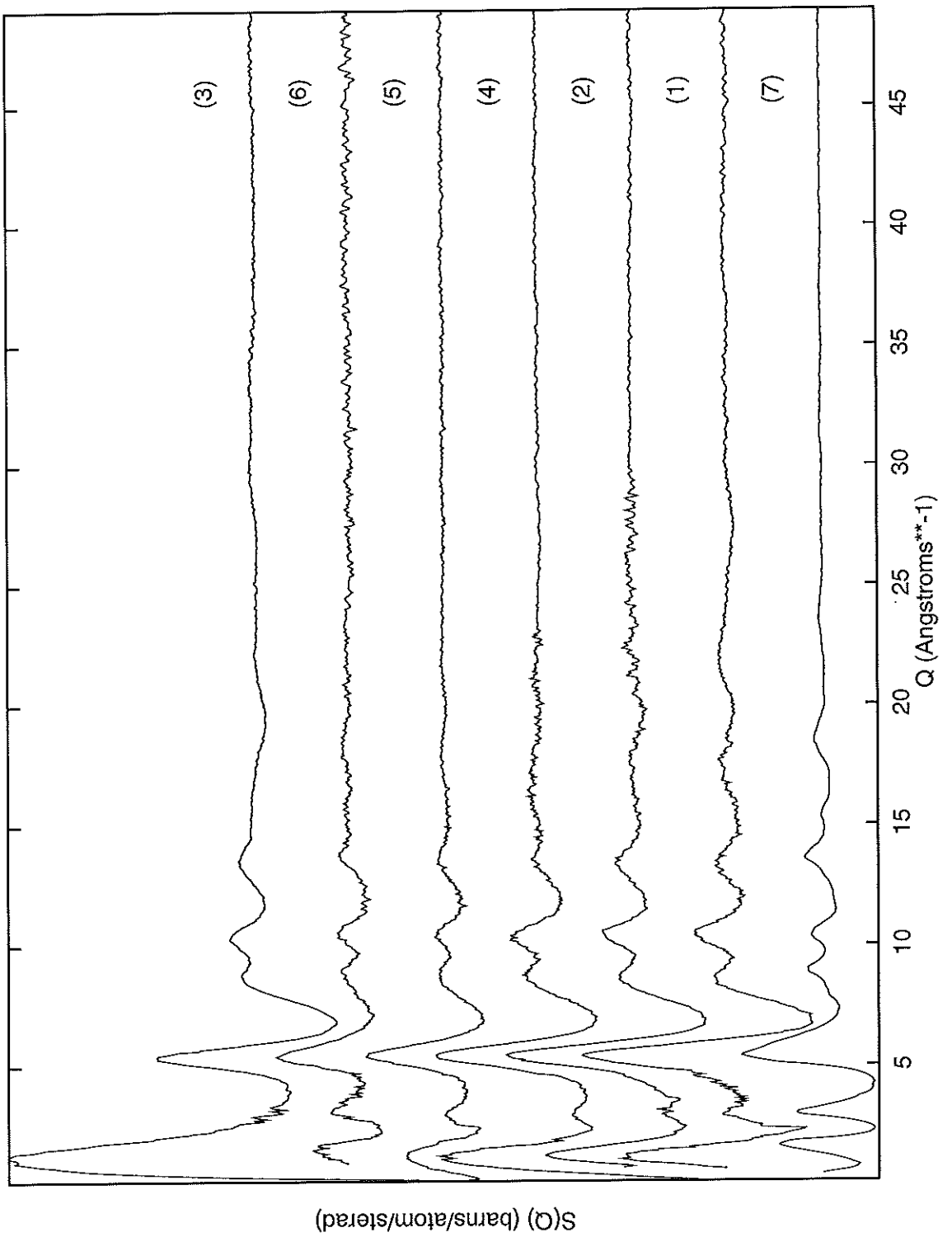

Figure 30: Total structure factors (offset).

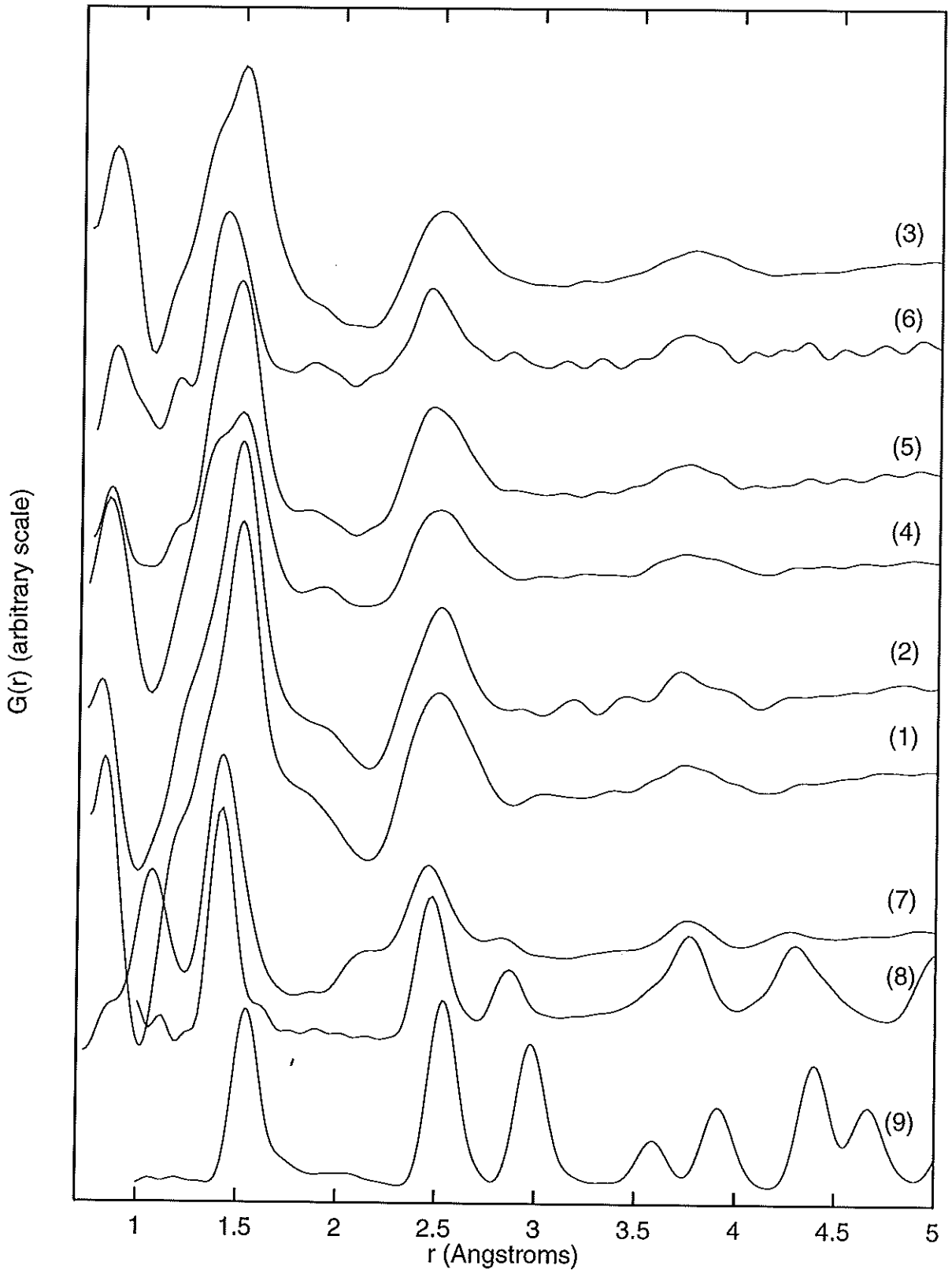

Figure 31: Total pair correlation functions showing also the results for graphite (8) and diamond (9) powders (offset).

sp^3	C-C	diamond	1.54Å
sp^2	C=C	graphite	1.42Å
sp^2	C=C	benzene	1.3954Å
sp^2	C=C	ethene	1.34Å
sp^3	C-H	methane	1.09Å
sp^2	C-H	ethene	1.07Å
	H-H	hydrogen	0.75Å
sp^3	H-C-H		1.80Å
sp^2	H-C-H		1.90Å
sp^2	C-C-H		1.95Å
sp^3	C-C-H		2.16Å

Table 6: Bond lengths and interatomic distances for carbon and hydrogen.

Peak position	Assignment
~0.8Å	H-H
~1.0Å(negative)	C-H
~1.4/5Å	CC 1st neighbour
~1.9Å	H-C-H and C-C-H 2nd neighbours
~2.5Å	C-C-C 2nd neighbours

Table 7: General G(r) peak assignments.

evidence for the presence of molecular hydrogen in all samples, although the magnitude of this peak (and the C-H peak) may be affected by the unreliability of the low Q data, as discussed in Section 4.4.3.

These may be compared with the neutron diffraction data of Gaskell et al. [145] on mass-selected ion-beam (MSIB) produced "amorphous diamond": their small sample having a very low hydrogen content and having graphite inclusions which meant that a "best guess" amount of graphite features had to be subtracted from the data. Also, their diffraction experiment was run on a reactor source diffractometer (Q_{max}=16Å^{-1}). That the correlation functions differ significantly in detail is of little surprise given the very different deposition conditions, hydrogen content, etc. , and there is little point in attempting a detailed comparison.

5.2 The effect of precursor gas

Figure 32 shows the G(r) for samples 3 and 4 prepared from propane and acetylene respectively (see Table 4).

The results of the Gaussian fitting are shown in Figures 33 and 34. with the parameters for each Gaussian given in Table 8.

With such high-resolution data it is possible to go beyond the straightforward assignments given in Table 8. There is a clear indication that molecular hydrogen is present in both samples in relatively small quantities. Also the carbon-carbon bond length in both cases is slightly less than that associated with saturated carbon-carbon in diamond, which is consistent with the proximity of sp^2 carbon atoms to the single bond. Again in both samples, an unsaturated carbon-carbon bond length of 1.34Å is observed which, because of its exact correspondence with the bond length associated with olefinic carbon, would indicate that most of the sp^2 carbon present

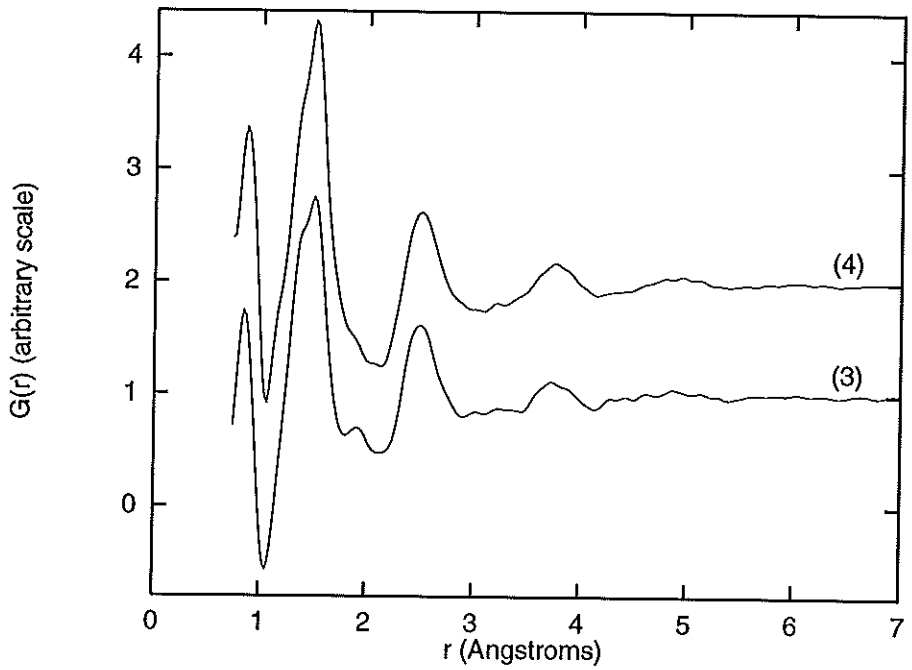

Figure 32: Total pair correlation functions: (4) for the sample prepared from acetylene, and (3) for the sample prepared from propane.

is the olefinic and not the aromatic/graphitic form. The residuals shown in Figure ?? show that the fits obtained using peaks at the bond distance associated with olefinic sp^2 carbon-carbon bonds, ~1.34Å, are better than those obtained when a peak at ~1.42Å, corresponding to graphitic/aromatic sp^2 carbon-carbon bonding is used. The existence of two peaks at ~1.34Åand ~1.52/3Å has recently been confirmed by Bayesian analysis [146].

More information can be gained from the Gaussian fitting process concerning the proportions of sp^3 and sp^2 carbon atom types. Assuming all the carbon atoms are in either sp^3 or sp^2 hybridized states allows us to describe the mix of atom sites in the following form [147]:

$$[sp^3] + [sp^2] + [h] = 1 \tag{158}$$

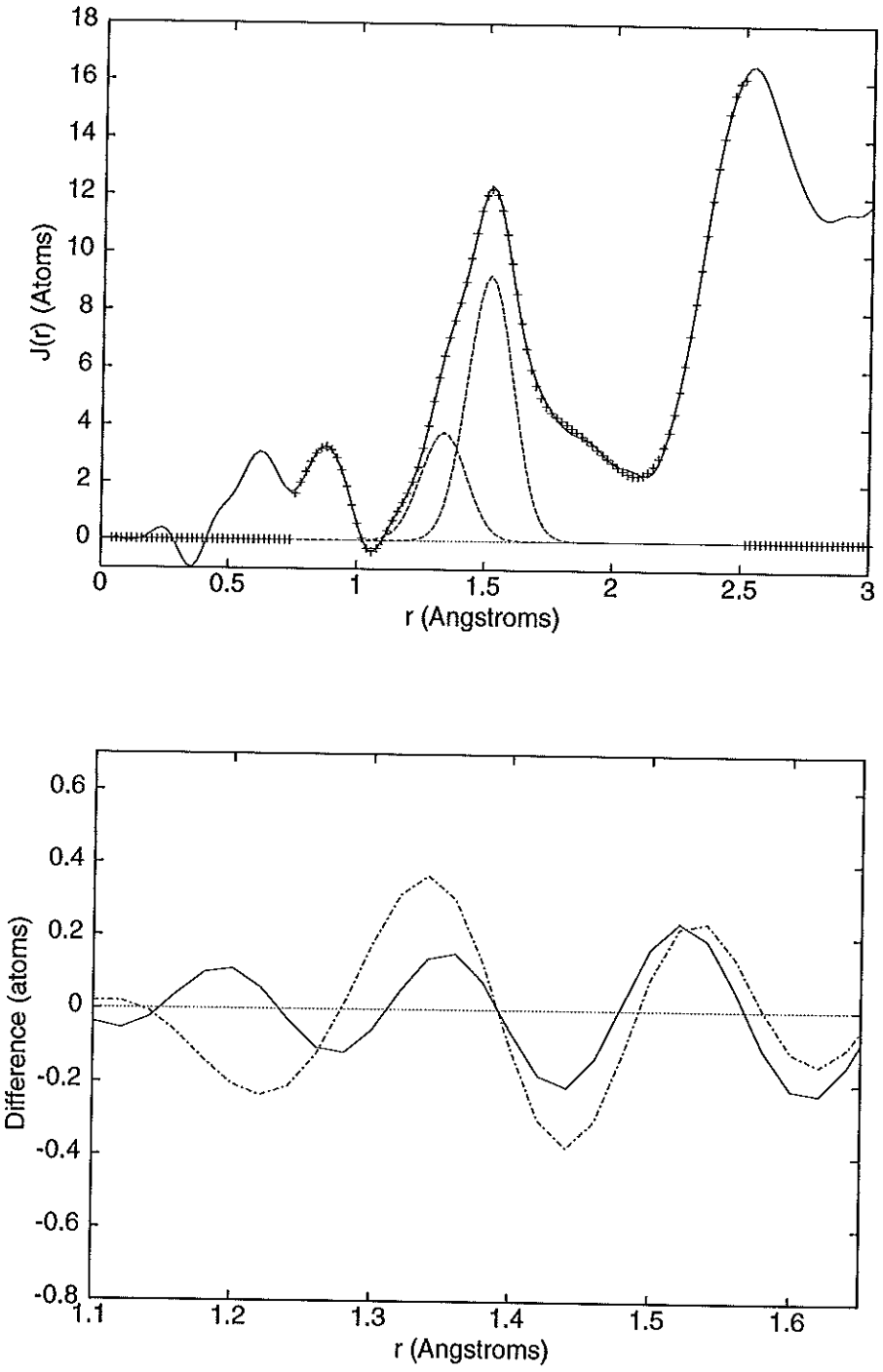

Figure 33: Radial distribution function for the sample prepared from acetylene (4) (top), with the diferences between the observed and fitted J(r) data using peaks at ~1.35 and ~1.53Å (solid line), and using peaks at ~1.42 and ~1.53Å (_. _. _) shown below.

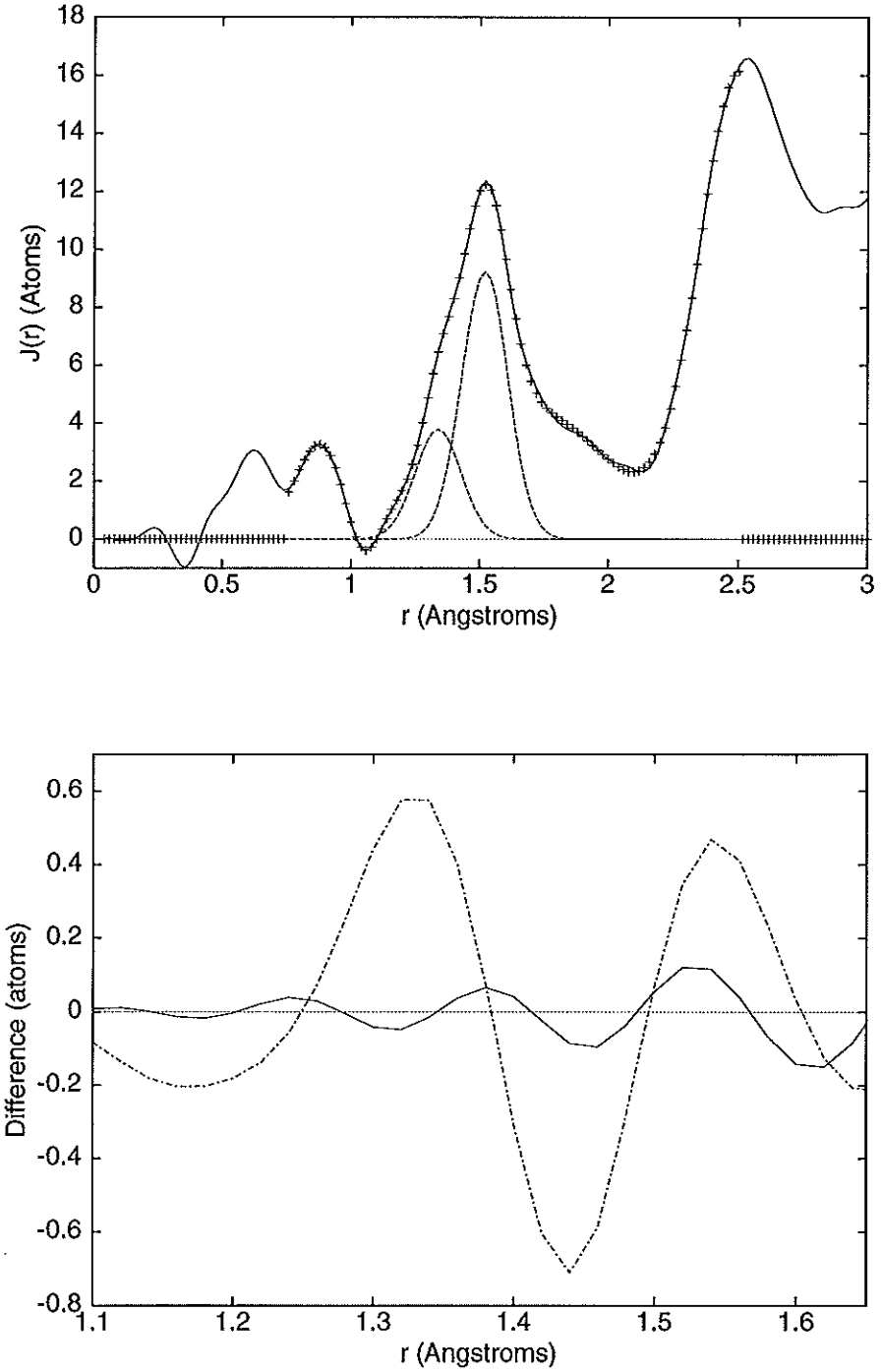

Figure 34: Radial distribution function for the sample prepared from propane (3) (top), with the diferences between the observed and fitted J(r) data using peaks at ~1.35 and ~1.53Å (solid line), and using peaks at ~1.42 and ~1.53Å (_ . _ . _) shown below.

Peak position (±0.01Å)	Peak area (±0.3 atoms)	Assignment
0.88	0.84	H-H
1.03	0.18	C-H and H-C
1.34	0.84	C=C
1.52	2.17	C-C
1.7-2.2		H-C-H and C-C-H
~2.5		C-C-C

Peak position (±0.01Å)	Peak area (±0.3 atoms)	Assignment
0.86	0.41	H-H
1.06	0.16	C-H and H-C
1.34	1.12	C=C
1.53	2.64	C-C
1.7-2.2		H-C-H and C-C-H
~2.5		C-C-C

Table 8: Bond lengths and peak area for the sample prepared from acetylene (4) (top) and propane (3) (bottom), derived from the neutron data.

where $[sp^3], [sp^2]$ and $[h]$ are the atom fractions of sp^3 hybridized carbon, sp^2 hybridized carbon, and hydrogen, respectively. If $r+1$ is the number of unsaturated bonds per sp^2 hybridized carbon atom (i.e. r=0 for olefinic, r=1 for aromatic, and r=2 for graphitic carbon atoms), it is possible to obtain a ratio of saturated to unsaturated carbon bonds, which is the same as the ratio of the ~1.34:~1.52/3Åpeak areas:

$$\frac{\text{area of } \sim 1.34\text{Åpeak}}{\text{area of } \sim 1.52\text{Åpeak}} = \frac{\text{unsaturated bonds}}{\text{saturated bonds}} = \frac{(1+r)[sp^3]}{s[sp^3] + (2-r)[sp^2] - [h]}. \quad (159)$$

However, in this case where we may assume that, to a very good approximation all the sp^2 carbon atom types are in an olefinic environment, we simply put r=0 in equation 159 and together with equation 158 the values of $[sp^3]$ and $[sp^2]$ can be

Sample	Precursor gas	$[sp^3]$ (saturated)	$[sp^2]$ (unsaturated)	C-C:C=C ratio
4	acetylene	0.16	0.49	2.6:1
3	propane	0.13	0.55	2.4:1

Table 9: Carbon bonding environments for a-C:H determined by neutron diffraction.

readily determined. It is therefore possible to calculate the ratio of carbon-carbon single to double bonds. The results of these two calculations for both samples are shown in Table 9.

This computation relies, of course, on the curve fitting to the $J(r)$ and, whilst peak positions may be determined with a high degree of accuracy (± 0.01Å), the associated areas have rather lower reliabilities. Given the level of uncertainty involved (estimated by examining the effect of varying the Gaussian fit parameters, and noting that they are all correlated) it is possible that the carbon-carbon single:double bond ratio could be as high as 3.7:1. Note that although it is not possible to rule out completely contributions from aromatic or (rather less likely) graphitic carbon bonding environments on the basis of this data, it is evident that they can only be present in very low concentrations, which is in agreement with the NMR data [17] and with the molecular dynamics simulation work [14]. Therefore there is no evidence at all for the existence of the relatively large graphitic or aromatic sp^2 clusters which form the basis of the most commonly used of the current structural models: indeed the data presented here implies that such models ought to be radically updated, at least for the family of a-C:H materials exemplified by the samples discussed here.

There are however two aspects of the data which require some comment. There is a general problem faced in the interpretation of any pair distribution function associated with a system as structurally complex as a-C:H which arises from the interplay between features which are close to one-another in r-space. The very high

real-space resolution achieved in this study has alleviated the problem to a significant degree, but the overlap between the (negative) carbon-hydrogen feature at ~1Å and the first carbon-carbon shell correlations at ~1.5Å remains somewhat problematic. The situation is exacerbated by the fact that residual inaccuracies in our empirical approximation to the inelasticity correction 4.4.3 (which are of primary concern to correlations involving hydrogen at $Q<\sim 2Å^{-1}$) mean that as a consequence the amplitudes of features in the G(r) become less reliable at the lowest r values ($<\sim$1Å). Hence, whilst it is evident that the (negative) first shell carbon-hydrogen contribution to the G(r) must be significant, the combined effect of the overlap with the first shell carbon-carbon correlations and the weakly-determined molecular hydrogen feature means that the C-H feature's amplitude may be somewhat suspect. There is also a possibility that there may be a small proportion of sp^1 bonds (~1.2Å) present (see [14]): these have been observed as weak features in infra-red work 7.4. This has, however, no material impact on the conclusions drawn from this work.

Qualitative statements concerning the nature of the correlations beyond the first co-ordination shells can also be made. For both samples, there is a small peak at 1.9Å which requires some explanation. This is possibly the result of a convolution of the large carbon-carbon second shell neighbour peak at ~2.5Å with a "negative feature" at 2.16Å due to an sp^3 carbon-carbon-hydrogen second shell correlation; it is more likely however that it arises from an sp^3 or sp^2 hydrogen-carbon-hydrogen second shell correlation (which would be expected at ~1.8-1.9Å). Indeed, if short chains of sp^3 CH_2 exist as suggested by the NMR data [17], then an associated H-C-H correlation may also appear at higher r values and (wholly or partially) cancel any negative-going C-C-H feature.

Using the carbon-carbon second shell peak centred at 2.5Å , it has been possible to

generate a carbon bond angle distribution which shows a principle peak centred on the tetrahedral angle, but extending towards 120° ; precise statements cannot be made because the broad 2.5Å peak has contributions from several carbon-carbon-carbon correlations.

Returning to a qualitative comparison of these results with those for the MSIB form of amorphous carbon (Gaskell et al. [145]). Their sample, with its high sp^3 carbon content shows a single first shell peak very close to the diamond distance, albeit somewhat broader. Gaskell et al. do, however, note a slight inconsistency in first and second shell co-ordination numbers and propose a "new" form of carbon, intermediate between sp^2 and sp^3 [145]. However, their interpretation assumes that all sp^2 carbon is in a graphitic environment; the results presented here, although on rather different samples, would seem to suggest that this may be a poor approximation for low sp^2 concentrations. Their observed discrepancy between the first and second shell co-ordination numbers is reduced without the need to invoke this "new" form of carbon if the sp^2 carbon is assumed to be all olefinic. A satisfactory method for obtaining accurate second shell co-ordination numbers has not yet been found since the second shell peak has a number of contributory carbon-carbon-carbon correlations.

Although the carbon-carbon peak areas and the single:double bond ratios are the same for the two samples, within the experimental error, there are differences between them which, to some extent, indicate the effects of changing the precursor gas. Fourier transformation of the low Q data, for instance, shows that there is weak medium-range ordering in both samples, although the degree of order is higher for sample 4 (acetylene precursor) than for sample 3 (propane precursor). From Figure 32 it can be seen that the feature associated with the C=C bonds is more pronounced for sample 3 than for sample 4. Also, the higher hydrogen content of the precursor

gas for sample 4 compared to that from which sample 3 was prepared, is reflected in the area of the H-H peaks (see Table 8). NMR work on these samples [17] does pick up quite clear differences between them also, and it is suggested that at least some of the residual differences between experiment and MD simulation [14] arise from the analogous fact that the starting configuration in the MD work comprises separate carbon and hydrogen atoms at low density and high temperature.

Conclusion

The high resolution real-space data presented in this work show that the carbon sites in hard a-C:H are predominantly sp^2 hybridized, even in intermediate hydrogen content samples. The single:double bond ratio is shown to be ~2.5:1. Furthermore, the unsaturated C=C bond distance of 1.34Å is too short to be aromatic or graphitic in character and corresponds very closely to the olefinic bond distance. This implies that current models for the structure of a-C:H (see Section 2.2.3) which rely on large aromatic carbon clusters need revision.

5.3 The effect of deposition energy and method

Details concerning the samples used in the study of these effects are given in Table 4: samples 1 and 2 and samples 4 and 5, although more details can be found in [148, 91] for each pair of samples respectively. The pair correlation functions for these four samples are shown in Figure 35, and the results of the Gaussian fitting are shown in Figures 36 and 37 and in Table 10.

Notice that with this high resolution real-space data from neutron diffraction experiments, it is possible to distinguish the three different carbon-carbon bonding environments: sp^1, sp^2 and sp^3. By taking the ratio of the Gaussian peaks used to fit

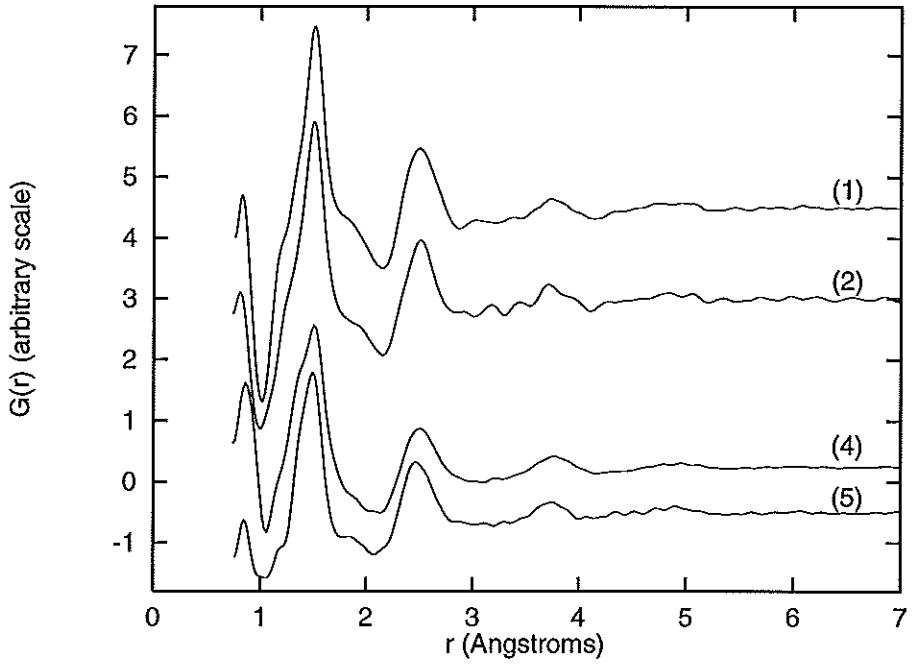

Figure 35: Total pair correlation functions: for samples prepared by PECVD (1) at ~30eV and (2) at 125eV; for samples prepared using a FAS (4) at ~500eV and (5) at ~800eV.

Sample (1)		Sample (2)		Sample (4)		Sample (5)		Assignment
r (±0.01Å)	Area	r (±0.01Å)	Area	r (±0.01Å)	Area	r (±0.01Å)	Area	
0.85	0.18	0.84	0.25	0.88	0.84	0.86	0.09	H-H
1.04	0.78	1.00	0.45	1.03	0.18	1.08	0.04	C-H and H-C
1.18	0.31	1.28	0.42	-	-	1.20	0.07	C≡C
1.34	0.34	-	-	1.34	0.84	1.36	0.40	C=C
1.51	2.40	1.51	2.99	1.52	2.17	1.51	1.33	C-C
~ 1.8		~ 1.9		~ 1.8		~ 1.8		H-C-H and C-C-H
~ 2.5		~ 2.5		~ 2.5		~ 2.5		C-C-C

Table 10: Results of the Gaussian fitting process. Note that the areas quoted here have the units atoms and the error is ~ ±0.3 atoms.

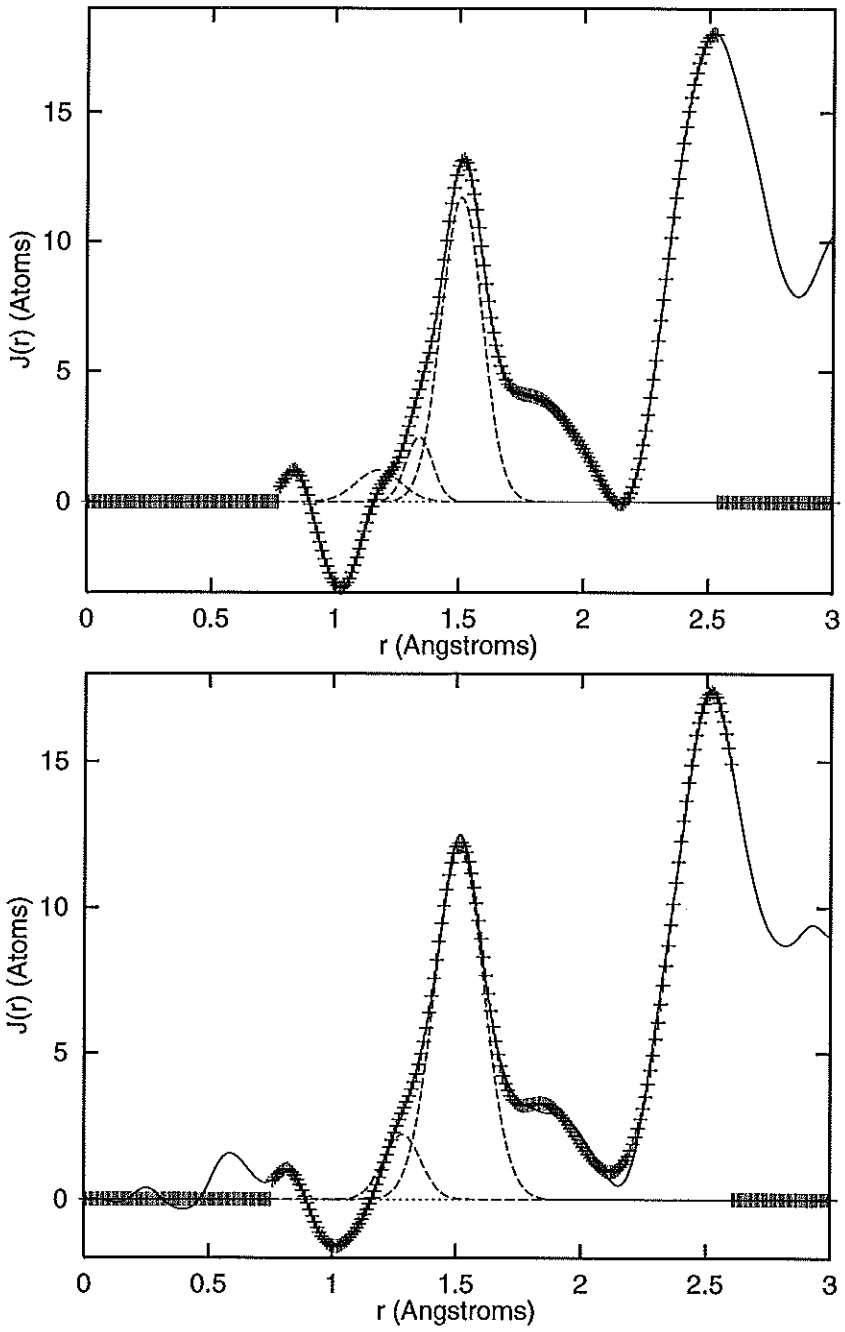

Figure 36: Radial distribution functions showing the Gaussian fits for samples prepared by PECVD at ~30eV (1) (top) and 125eV (2) (bottom).

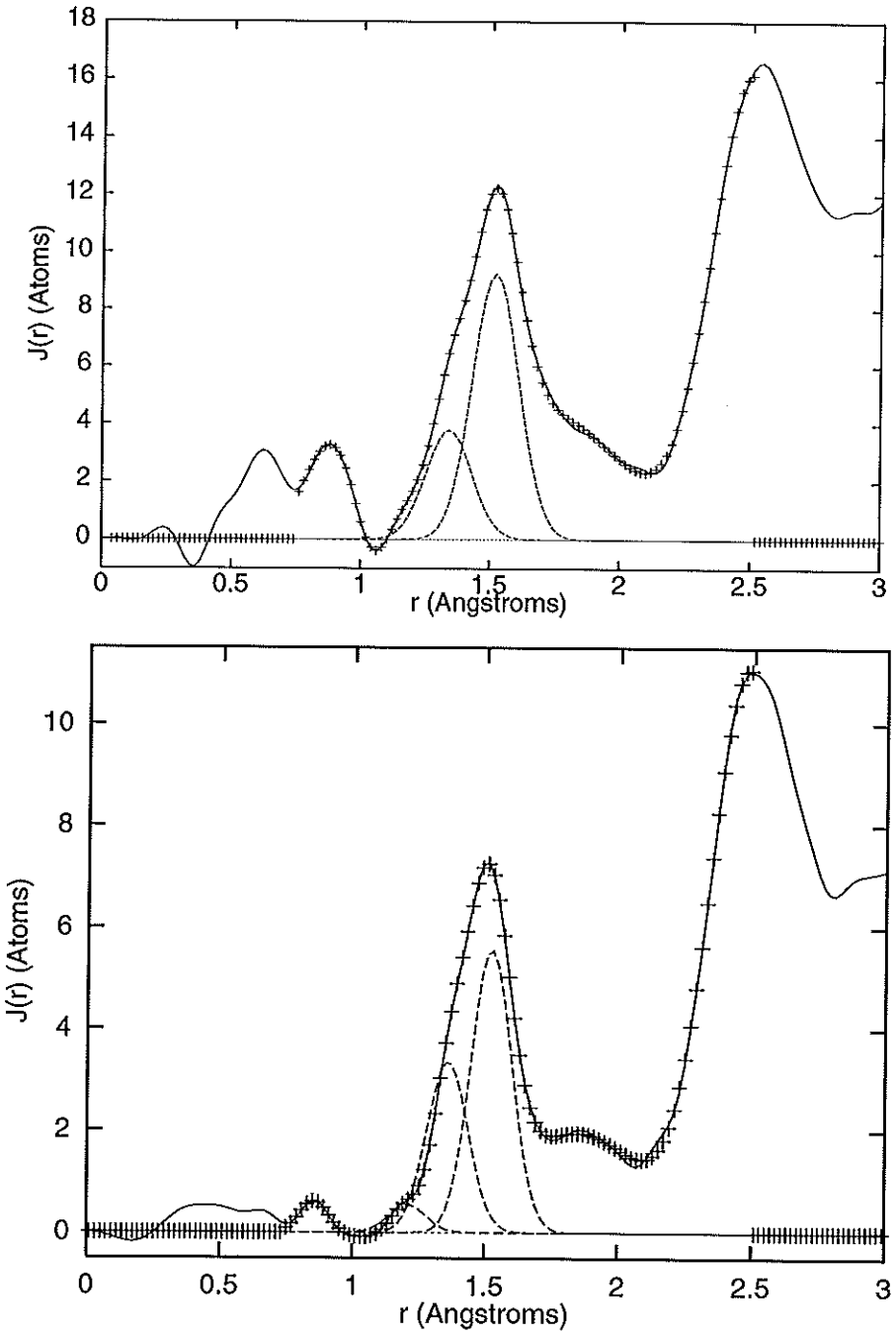

Figure 37: Radial distribution functions showing the Gaussian fits for samples prepared by a FAS at ~500eV (4) (top) and ~800eV (5) (bottom).

Sample	sp^1	:	sp^2	:	sp^3
1	0.14	:	0	:	1
2	0.13	:	0.14	:	1
4	0	:	0.40	:	1
5	0.05	:	0.30	:	1

Table 11: Ratios of bond types for the four samples.

each of these correlations, the relative amounts of each bonding type present in the samples can be determined. These results are given in Table 11.

For both the PECVD and fast-atom deposited samples there is an increased amount of sp^1 bonding in the samples prepared at higher energies, although this is within the experimental errors. However, there is also a simultaneous reduction (and even disappearance in the case of sample 2) in the area of the sp^2 carbon-carbon peak at ~1.34Å. Note that, as has been observed previously (see Section 5.2), this distance corresponds to that of sp^2 olefinic bonding, and there is no evidence in any data set for the significant amounts of graphitic sp^2 carbon-carbon bonding (~1.42Å) predicted by the original Robertson model. For the PECVD deposited samples, the present data lie in contrast to the analogous discussion of data obtained in previous experiments (see for example [10, 149]) which has generally been in the context of the Robertson model, and without the benefit of the kind of detailed structural information made avaiable from neutron diffraction experiments such as these. The hydrogen content of both sets of samples is seen to decrease with increasing deposition energy, see Table 4, and this is consistent with the subplantation description of deposition [89].

Increasing the energy of the impinging species in the ranges given in Table 4, leads to a sharpening of the features corresponding to the carbon first and second neighbour correlations at ~1.5Å and ~2.5Å respectively, for both deposition techniques. This

indicates a tendency towards a single carbon bonding environment, in this case sp^3 bonding with the expected bond angle of $\sim 110°$ (although some sp^1 bonding is also present). However, as can be seen from Figure 35, the structural differences exhibited by each pair of samples are quite subtle, and the dominance of sp^3 carbon bonding is maintained over these energy ranges. There are, however, significant differences in the macroscopic properties of the low and high energy samples prepared by the same method [148, 149], particularly their hardness (see Table 4). From this it is possible to deduce that in the deposition energy region studied, increased hydrogen content and sp^2 bonding lead to a reduction in the amount of cross-linking and therefore to a softer sample.

The areas of the C-H and H-H peaks do not consistently follow the trends mentioned above but, as explained above, these features are less robust in terms of their size; their positions are however correct (within the errors quoted).

Conclusion

The structural changes observed as the deposition energy is increased are found to be consistent with the subplantation model of Lifshitz and are qualitatively independent of deposition method. However, although changes in the macroscopic sample properties with energy are significant, the atomic scale structural differences are subtle. Even with what may be considered to be relatively large differences in effective impact/deposition energy, the a-C:H samples are all found to have broadly similar structures, with the sp^3 carbon-carbon bonding environment remaining dominant. With increasing effective impact energy at the growth site, the olefinic sp^2 carbon bonding is seen practically to disappear, and the fraction of sp^1 carbon bonding increases slightly. Given the preference for hydrogen to bond to sp^3 carbon sites, this

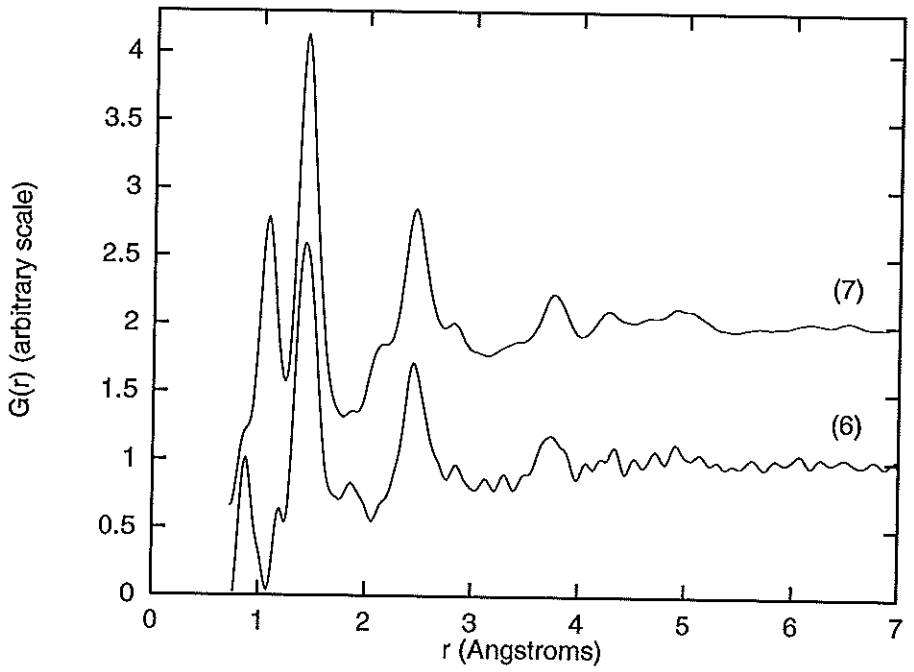

Figure 38: Total pair correlation functions for the deuterated (7) and hydrogenated (6) samples.

observation suggests an overall decrease in network cross-linking with increased particle impact/deposition energy and hence provides a microscopic explanation for the macroscopic changes in hardness.

5.4 The effect of isotopic substitution

The effect of isotopic substitution will be discussed only briefly here since almost all of the work has been carried out by Burke et al. [150] using the SANDALS diffractometer at ISIS. However the data presented here, which was taken on LAD, is new and illustrates well the differences in the G(r) for a-C:H and a-C:D. Figure 38 shows the total pair correlation functions for the hydrogenated and deuterated samples, and the results of the Gaussian fitting are presented in Figure 39 and Table 12.

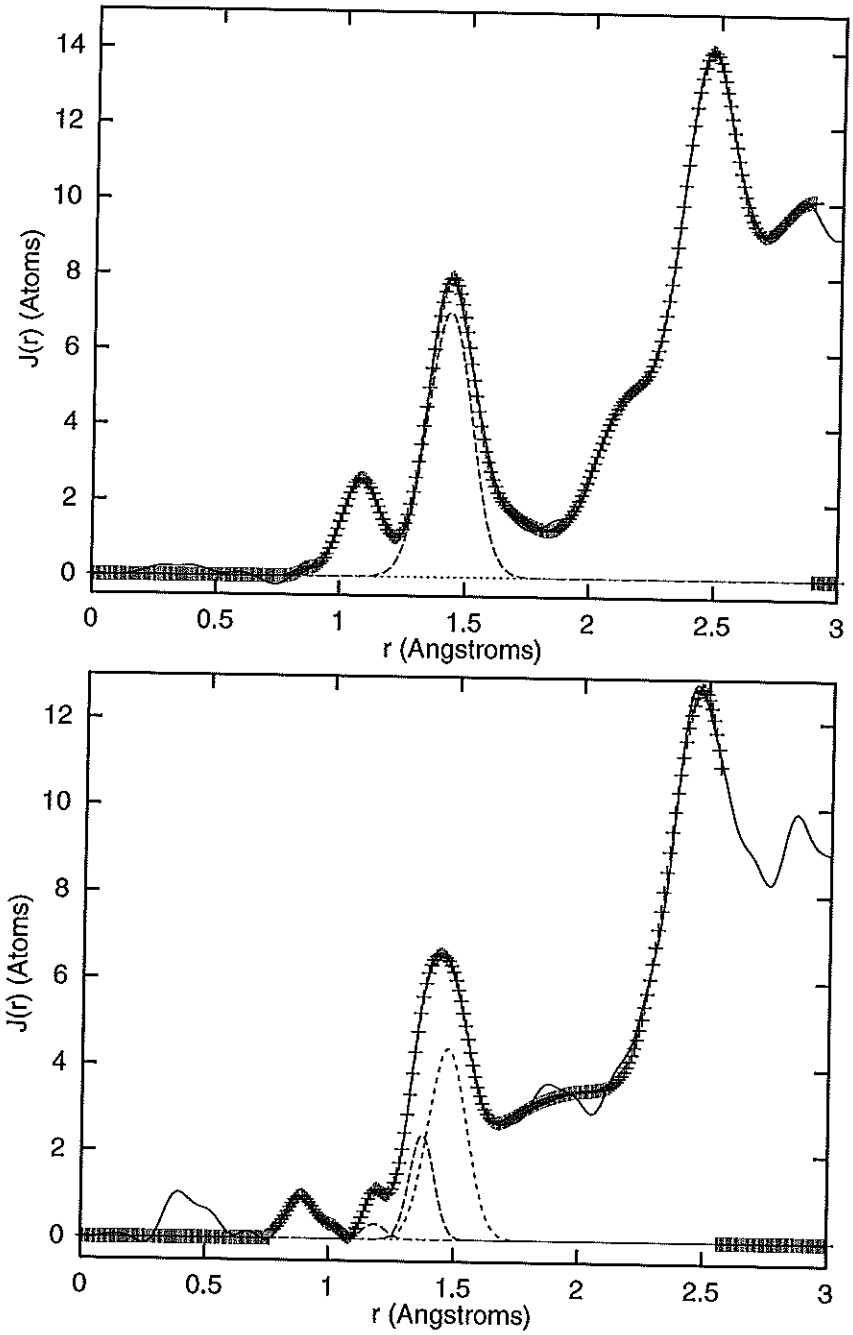

Figure 39: Radial distribution functions showing the Gaussian fits for the deuterated (7) (top) and hydrogenated (6) (bottom) samples.

The first thing to notice is that for the deuterated sample, (7), all the correlations are positive since deuterium, unlike hydrogen, has a positive scattering length: this is especially evident in the first C-H(D) neighbour correlation at 1.08Å. This also enables the clear observation of peaks at ~1.63Å and ~2.14Å corresponding to second neighbour correlations which are more difficult to see in the hydrogenated samples.

For both of these samples the carbon-carbon bondlengths are close to the bond distance found in aromatic/graphitic carbon (see Table 6). This may be due to the samples being prepared at a relatively high energy (~960eV), but may also result from the nature of the precursor gas molecules (hydrogenated/deuterated cyclohexane). Although the samples were prepared at a relatively high energy, the gas molecules are large, so that the average energy per atom will be relatively low. This means that in addition to the average impact energy being decreased, the incident molecular fragments will tend to be bigger, i.e. the molecule remains more intact, and therefore produce a sample with a more aromatic character. The lower incident energy could also mean that the "thermal spike" is lower, and there is less energy to impart to the surrounding region on impact, which results in sp^2, rather than sp^3 carbon-carbon bonding. These effects are further discussed in Section 6.2 of the following chapter. So, from the results of the Gaussian fitting, both samples have an insignificant amount of sp^3 bonding.

Finally, for the hydrogenated sample, a Gaussian peak at 1.18Å has been fitted. This could possibly be evidence for the presence of sp^1 carbon, but is more likely to be a Fourier transform effect due to the high level of statistical noise in the structure factor. This also explains the high-r ripples in the pair correlation function.

Peak position (±0.01Å)	Peak area (±0.3 atoms)	Assignment
0.87	0.01	D-D
1.08	0.50	C-D and D-C
1.43	1.55	C=C (aromatic/graphitic)
1.63-2.2		C-C-D and D-C-D
~2.5		C-C-C

Peak position (±0.01Å)	Peak area (±0.3 atoms)	Assignment
0.88	0.11	H-H
1.08	0.03	C-H and H-C
1.18	0.03	C≡C
1.37	0.37	C=C
1.47	0.80	C=C (aromatic/graphitic)
1.7-2.2		C-C-H and H-C-H
~2.5		C-C-C

Table 12: Bond distances and peak areas for the deuterated (7) (top) and hydrogenated (6) (bottom) samples.

Chapter 6

Results II: Spectroscopy

6.1 Introduction

In this chapter the results of Fourier transform infrared (IR) spectroscopy and inelastic neutron scattering (INS) experiments are presented for the six a-C:H samples listed in Table 4. Both diffuse reflectance (DRIFT) and acoustic emission IR measurements (see Sections 4.6.3 and 4.6.4) were performed on the samples, and the spectra obtained are shown in Figures 41 and 42. The raw INS spectra are also shown in Figure 43. General assignments for regions of the infra-red spectrum for carbon and hydrogen are shown in Figure 40.

In a detailed examination of the spectroscopic results it is more instructive to consider the two different regions of the spectra, 3400-2600cm^{-1} (CH stretch region) and 1800-10cm^{-1} (CC stretch and CH_n deformation region), separately to begin with; I will then attempt to correlate the findings from both in a summary.

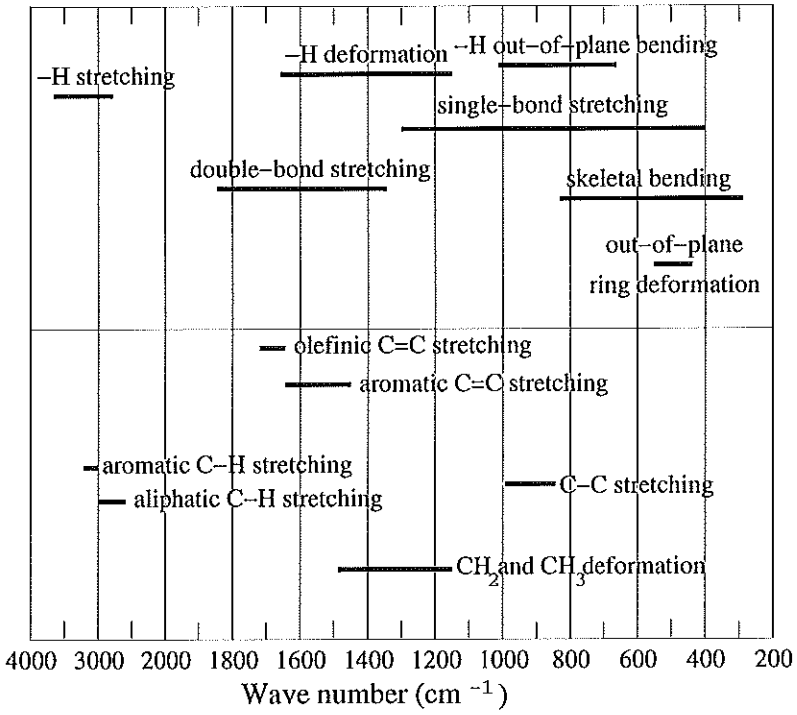

Figure 40: General assignments for regions of the infra-red spectrum.

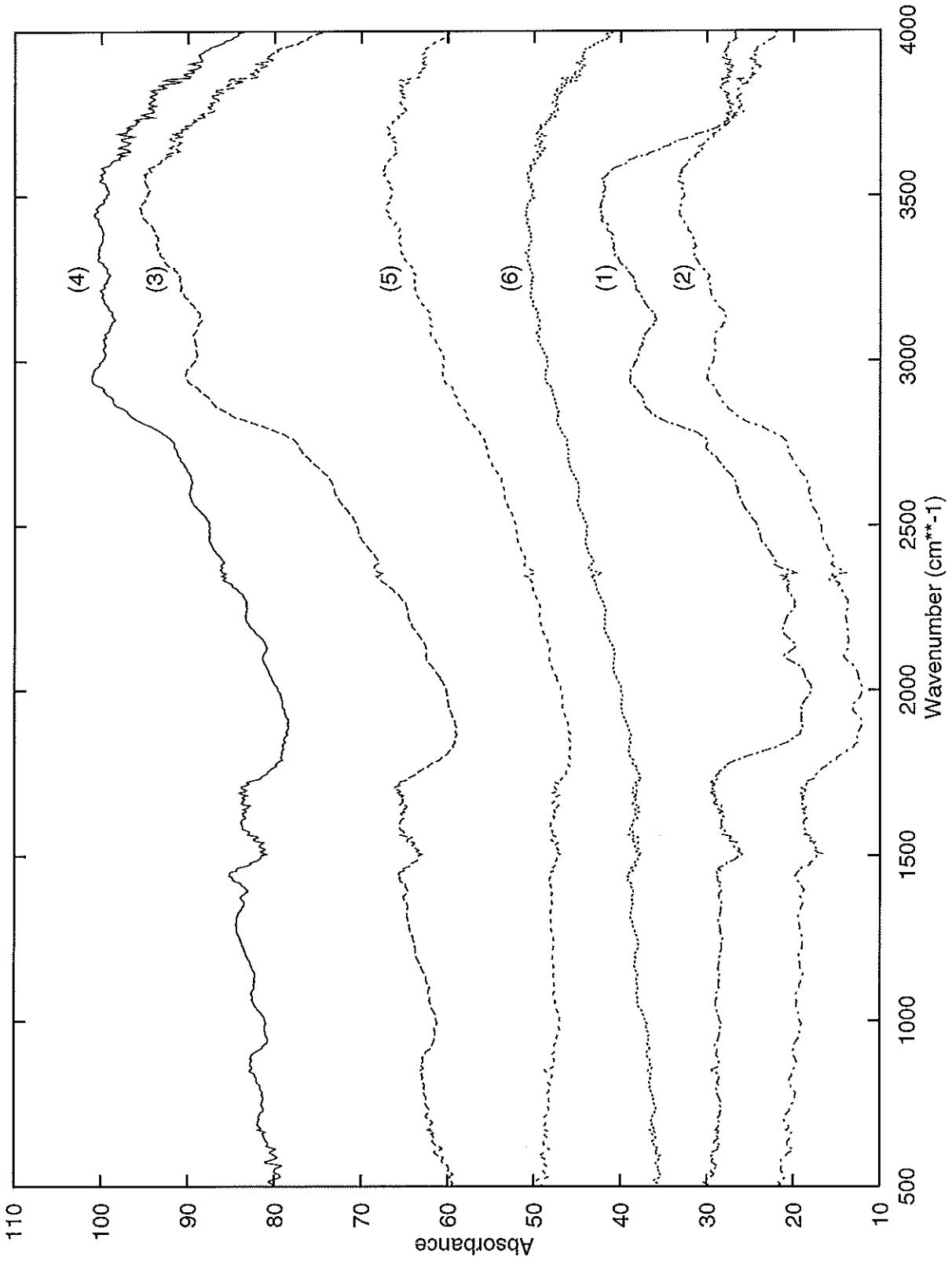

Figure 41: Raw DRIFT infrared spectra.

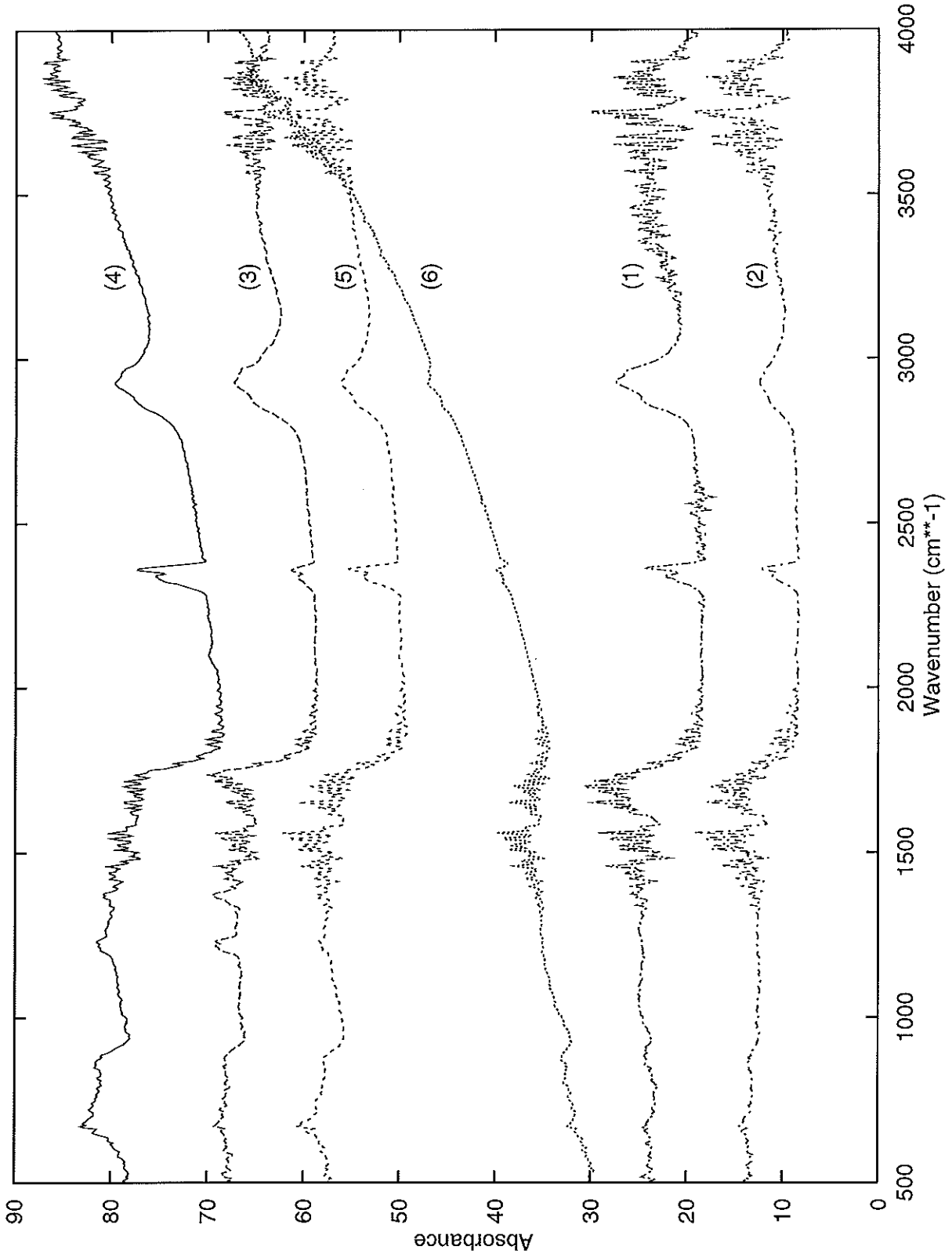

Figure 42: Raw acoustic emission infrared spectra.

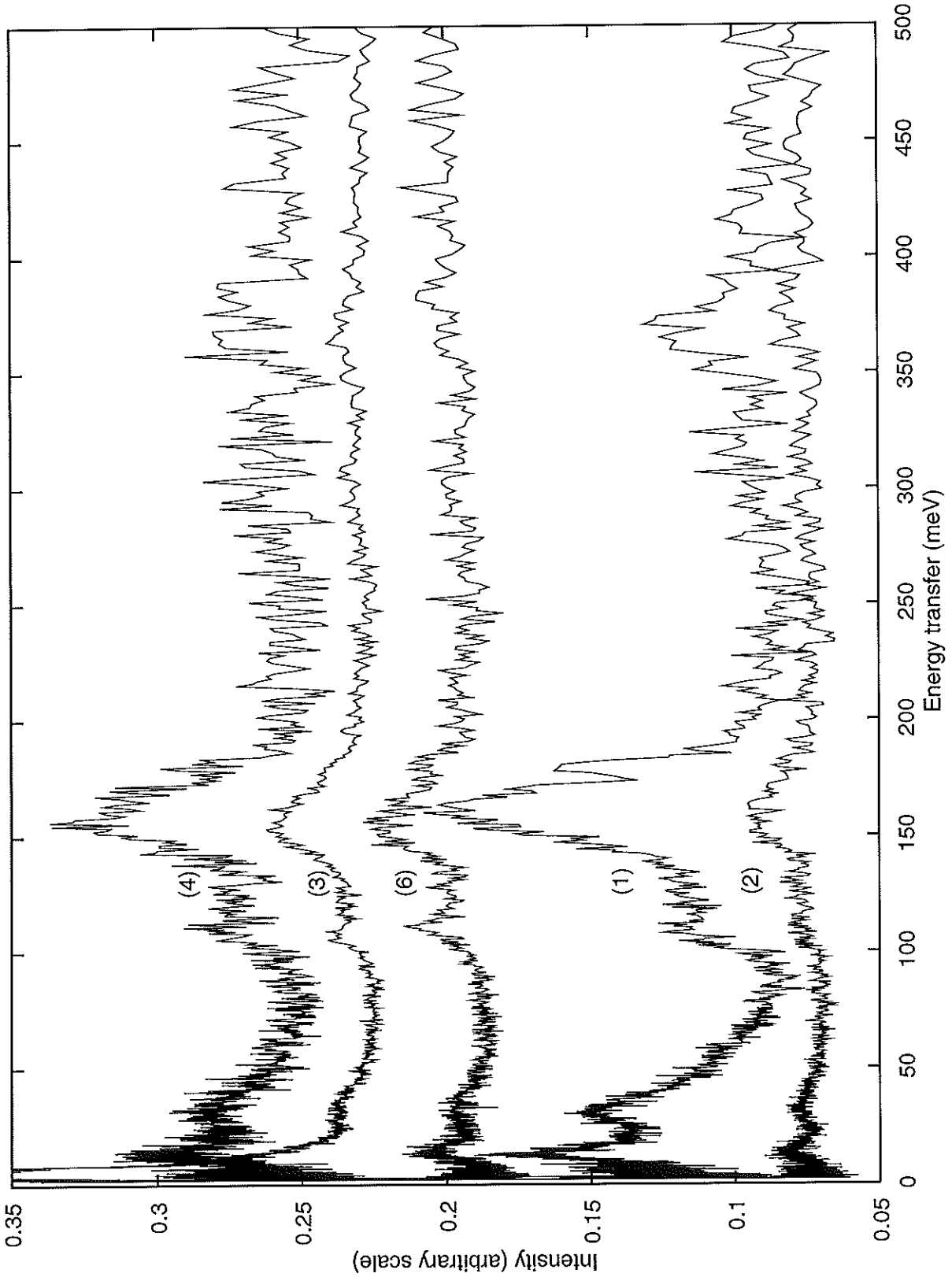

Figure 43: Raw INS spectra.

6.2 The CH stretch region: 3400-2600cm^{-1}

Due to the poor resolution of the INS data in this region (300-500meV), only IR data is discussed for the CH stretching modes. Following a "background subtraction" using a low order polynomial, each spectrum is fitted with a series of Gaussians, allowing position and area to vary using the method of least squares until a best fit is found. Figure 44 shows the fitted Gaussians used to obtain a best fit for each sample. From the positions of the Gaussians, assignment of the observed frequencies to vibrational modes can be made and the peak areas can be normalised to the hydrogen content of the sample and used to look at the relative proportions of each mode present in the samples. Table 13 gives the frequency and associated normalised peak areas derived from this data.

Vibration	sp^2CH (olef./arom.)	sp^3CH_3 (asym.)	sp^3CH_2 (asym.) sp^3CH	sp^3CH_2 and CH_3 (sym.)
Observed frequency	3035-2971	2977-2958	2930-2915	2870-2858
Sample 1	3.52	3.08	26.4	11.0
Sample 2	11.9		13.6	8.5
Sample 3	7.04	4.48	12.16	12.48
Sample 4	1.75	4.55	14.35	14.35
Sample 5	1.32	2.2	12.1	6.16
Sample 6	2.0	1.25	16.0	10.25

Table 13: Frequency assignments and areas obtained from the Gaussian fitting of C-H stretch region of the IR data.

Now if we assume that the peaks associated with the anti-symmetric and symmetric stretching modes for the same group have the same area, it is possible to determine the relative ratios, CH_2:CH_3, sp^3CH:sp^2CH and CH:CH_2, and these are shown in Table 6.2.

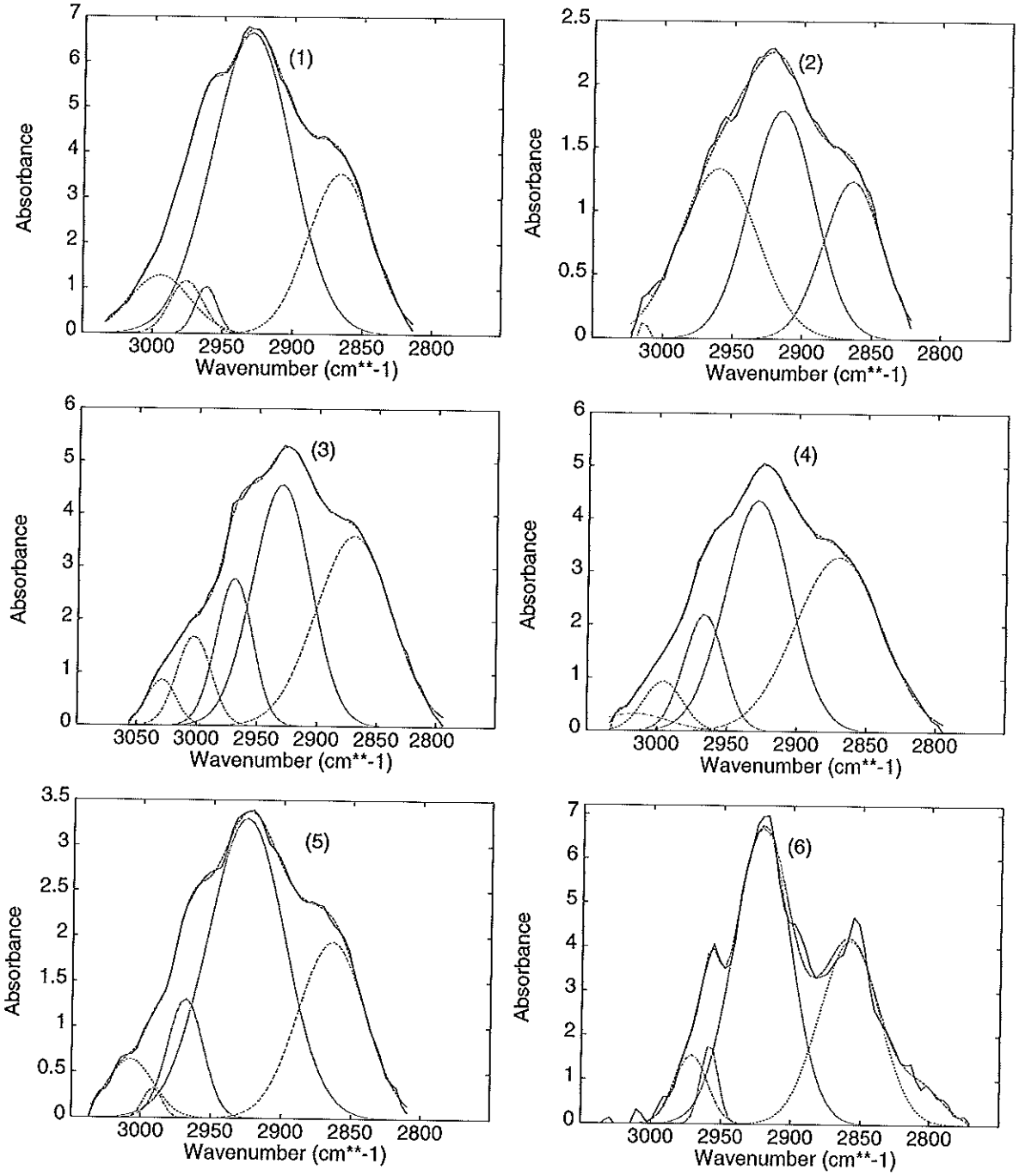

Figure 44: Gaussian fits to the C-H stretch region of the IR data showing the constituent Gaussians, for samples 1-6.

Sample	CH_2:CH_3	sp^3CH:sp^2CH	CH:CH_2
1	~2:1	~6:1	~3:1
2	~2:1	-	-
3	~2:1	~1:1.5	~1.4:1
4	~2:1	~3:1	~1.2:1
5	~2:1	~6:1	~2.4:1
6	~7:1	~3.5:1	~1:1

Table 14: Approximate relative proportions of CH_n groups from the Gaussian fitting.

It is important to remember that these ratios are not absolute; comparisons are only meaningful in a relative way between samples.

Before discussing these results in detail, it is worth pointing out that although frequencies associated with sp^2CH_2 and CH_3 groups are not observed (they are not clearly observed in IR spectra for a-C:H in general [151, 29, 152]), this is due to the weightings of their matrix elements and does not necessarily imply that these groups are absent. From Figure 44, it is clear that the four frequency assignments made are common to all of the samples. For sample 2 the two high frequency bands cannot be resolved, whereas for the other samples there are two peaks in this region (3035-2958cm^{-1}). All samples do show that there is a mixture of sp^3CH and sp^2CH bonds and that both CH_2 and CH_3 groups are present, although the actual number of these cannot be determined. From Figure 42 none of the samples show a peak at ~3300cm^{-1} corresponding to sp^1CH, when it is known from neutron diffraction (see Section 5.3 that two of the samples (5 and 2) contain sp^1 carbon sites. This may simply be explained by the deterioration of the data quality which starts in this region of the spectra, as it has been seen clearly in other IR studies 7.4.

Looking at Table 6.2, the first thing to notice is that all the samples except one (6) have approximately twice the peak area associated with CH_2 groups as with CH_3

groups: for sample 6, CH_2:CH_3 ~7:1. Since this ratio is the same for changes in deposition energy and method, and for preparation from propane and acetylene gases, it is reasonable to assume that this anomalous result is due to the use of cyclohexane (C_6H_{12}) as the precursor gas. This suggests that the relatively high deposition energy used is not sufficient to cause complete dissociation of the cyclohexane molecule, leaving fragments containing CH_2 groups which are incorporated into the a-C:H structure. The existence of such impacting fragments also means that the average energy per atom on impact is lower than if full dissociation had occurred. This could explain why CH_2 groups are not then broken-up on impact. Evidence for some dissociation of the molecule is provided by the presence of CH_3 and CH groups. These impacting atoms and smaller fragments also cause etching of the growing film which is consistent with the observed CH:CH_2 ratio of areas of ~1:1, and with the measured hydrogen content of 25%.

Another feature common to the majority of the samples is that the area associated with sp^3CH is greater than that from sp^2CH bonds. Although we cannot say conclusively from the semi-quantitative evidence of the IR data alone, this is in agreement with the results of NMR data [17], which found that hydrogen is preferentially bonded to sp^3 carbon sites.

Samples 3 and 4, prepared from propane and acetylene, respectively, at the same deposition energy, show only slight differences and these are within the limits of experimental error. The presence of CH_2 groups indicates that these samples do have a polymeric component, and the peak at ~3000cm^{-1} (sp^2CH olefinic/aromatic) shows that olefinic/aromatic carbon-carbon bonds are present. This is all consistent with the results of neutron diffraction experiments on the same samples, presented in Section 5.2.

Now consider the effects of deposition energy for deposition using a fast atom system and acetylene gas, by looking at samples 4 and 5. From the analysis of this CH stretch region, it is clear that the distribution of hydrogen within the network is quite different in each sample. Although a CH_2:CH_3 peak area ratio of ~2:1 is common to both samples, the sp^3CH:sp^2CH peak area ratios differ in that this is equal to ~3:1 for the lower energy sample (4) and ~6:1 for the higher energy sample (5). The CH:CH_2 peak area ratios are also affected: ~1.2:1 for sample 4 and ~2.4:1 for sample 5. From neutron diffraction results in Section 5.3, it was shown that in terms of the carbon network and the distribution of H-H, C-H and C-C bond lengths, these two samples are quite similar, although with this increase in energy it is found that there is a decrease in the number of sp^2 carbon bonds which, to some extent, could account for the relative increase in sp^3CH bonds. Also the increased peak area of CH relative to that of CH_2 groups for the higher energy sample could be explained in terms of a more efficient etching of hydrogen for higher incident particle energies (i.e. within the sub-plantation model), but may also be a result of a more complete breaking-up of the acetylene gas molecule at the higher energy - this could also account for the increased area associated with sp^3 carbon sites, in that there is an increased amount of energy to be dissipated on impact, which causes a larger thermal spike. The decreased relative number of CH_2 groups also means a decreased relative polymeric component in the higher energy sample.

Finally, samples 1 and 2 were both prepared by plasma-enhanced chemical vapour deposition (PECVD) from acetylene gas. Although resolution problems mean that the discussion is necessarily limited, it is clear that the distribution of hydrogen in sample 1 (low energy PECVD) is very similar to that found in sample 5 (high energy FAS), having a relatively low polymeric spectral component and relatively few CH_3

groups. Unfortunately, we are unable to make any further statements about these samples for this particular region of the spectrum.

6.3 The CC stretch and CH_n deformation region: 1800-10cm^{-1}

For this region of the spectrum, INS experiments are the best source of structural information, although intensities at these low energy transfer values are difficult to interpret. The general assignments for this region are: 800-1000cm^{-1} sp^2 C-H out-of-plane and in-plane bending, 1100-1300cm^{-1} sp^3 C-C stretch and -CH_2 wag/twist, 1300-1500cm^{-1} sp^3 CH_2 and CH_3 deformations, and 1500-1700cm^{-1} sp^2 C=C and aromatic C=C stretches; intensity in the region 0-400cm^{-1} is generally due to vibrations of large fragments of the lattice/network. The smoothed INS spectra shown in Figure 45 show that these bands are common to all the a-C:H samples. However, improved insight into the structure of these materials can be gained if the data is compared to spectra for diamond, graphite, polyethylene and polyisoprene (rubber) shown in Figure 46.

In fact, this comparison produces some interesting results. The spectra for a-C:H are really quite dissimilar to those for diamond and graphite, but there is a much greater resemblence to the polymer spectra, with broadening of bands as is expected for an amorphous structure. In the first instance this is in agreement with the model for a-C:H described earlier [153], however the lack of a strong band at ~720cm^{-1} due to CH_2 rock in extended methylene chains (as seen in the polyethylene spectrum) is evidence that the CH_2 chains must be short and/or sparse, which is consistent with the results of neutron diffraction (Chapter 5) and NMR [17] experiments. When making

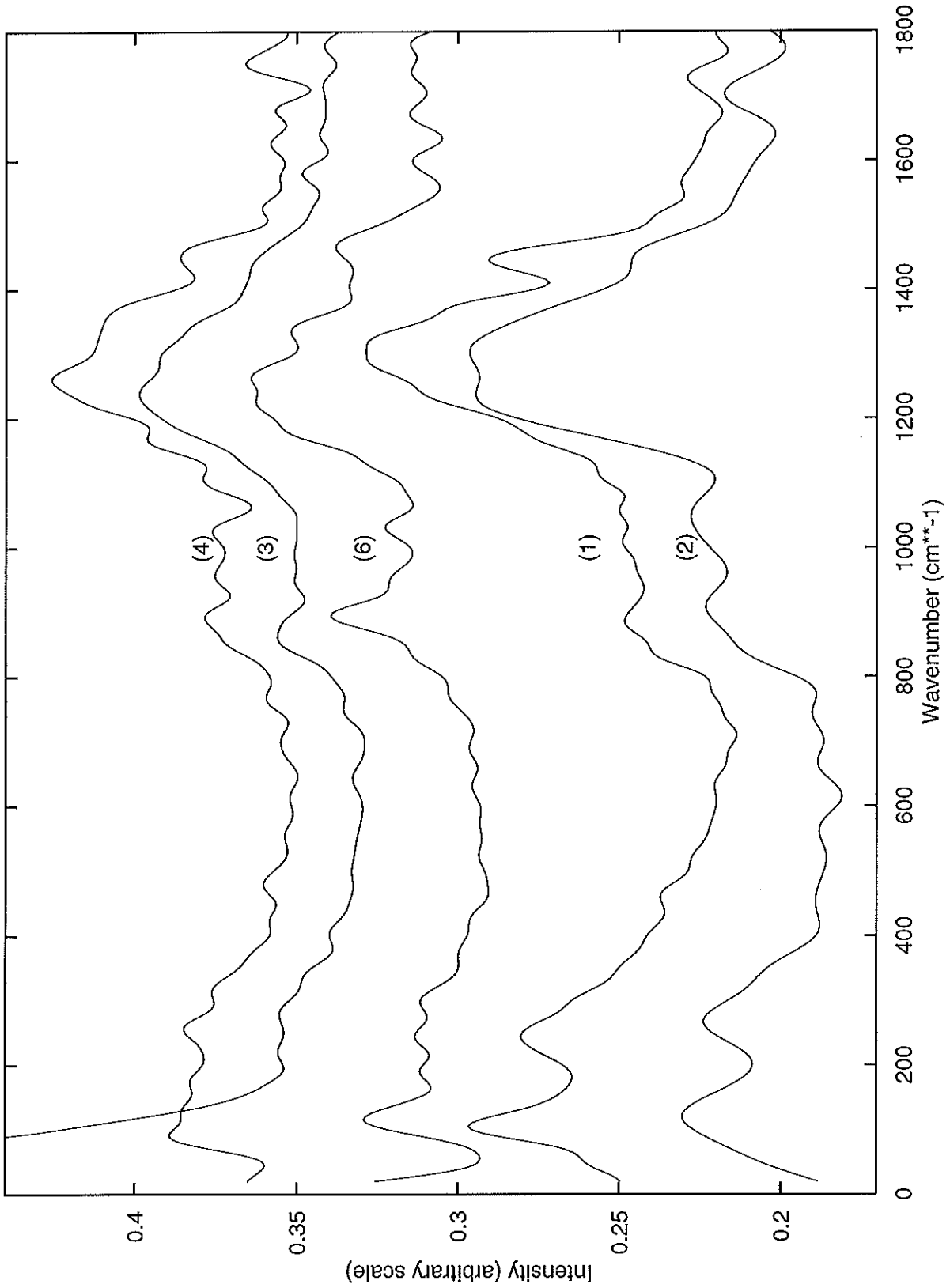

Figure 45: Raw INS spectra.

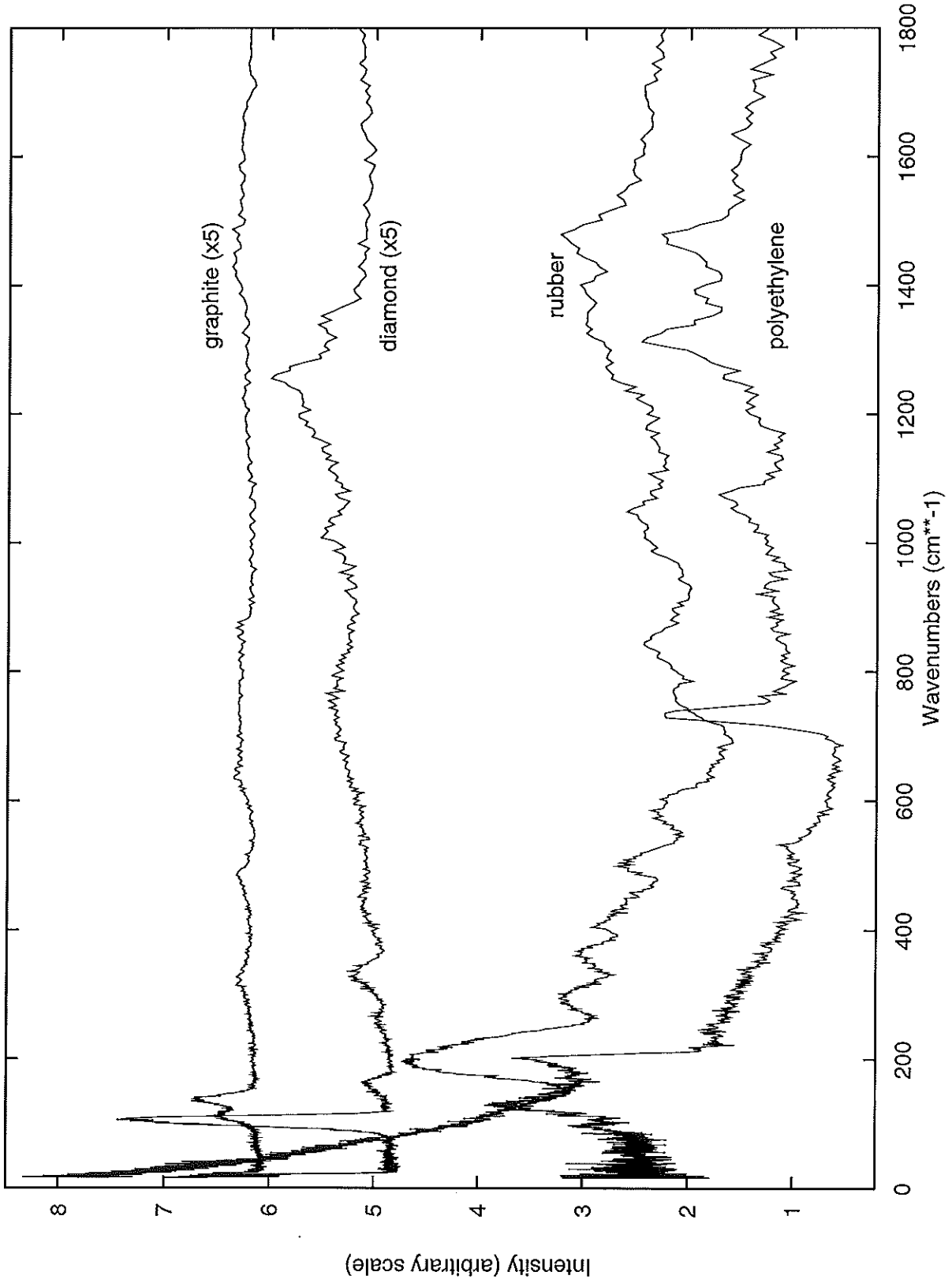

Figure 46: Raw INS spectra in the low energy region for the "standard" samples.

comparisons between the a-C:H samples and these standard materials, it is important to note that the high cross-section of hydrogen will mean that correlations involving hydrogen will tend to dominate the spectra, so it is impossible to say whether or not the carbon-carbon correlations are more similar to diamond or graphite.

Taking a more detailed look at the data, consider first the effect of the precursor gas by comparison of the spectra for samples 3 and 4. The slightly higher sp^3 content of sample 4 is shown by the increased peak height at $\sim$1250cm^{-1}. The increased intensity of the peaks at 1300-1500cm^{-1}, associated with deformations of C-H bonds, are also consistent with the higher hydrogen content of sample 4, although both samples have roughly the same proportion of sp^2 CH bonds ($\sim$850cm^{-1}). Overall the spectra are very similar, as was the case for the C-H stretch region, with both samples showing some evidence for the presence of sp^2 C=C stretch bands above 1500cm^{-1}.

The spectra for sample 6, prepared from cyclohexane at a higher deposition energy, is quite different from those for samples 3 and 4, although it is also more similar to the polymer samples than to the diamond and graphite powders. The strong peak at $\sim$1250cm^{-1} (sp^3 C-C stretch) is much weaker than in the previous two samples, whereas intensity in the region 1500-1800cm^{-1} (sp^2 C=C stretch) has increased. This is also accompanied by an increase in sharpness and intensity of the peak at $\sim$850cm^{-1} (sp^2 C-H wag in- and out-of-plane). Further, the apparent downwards shift in energy of the position of the main peaks is due to a considerable increase in intensity in the region $\sim$950-1200cm^{-1}, which is generally assigned to -CH_2 twisting and wagging vibrations. These changes are all consistent with the increase in the relative number of CH_2 groups observed in the analysis of the C-H stretch region of the IR spectra, and the neutron diffraction data which shows a higher sp^2 carbon content for this sample.

Finally, samples 1 and 2, prepared by PECVD, are similar to samples 3 and 4, prepared by a FAS. The higher hydrogen content in the PECVD samples produces an increased relative intensity of the CH_2 and CH_3 deformation bands either side of the sp^3 stretch band at $\sim$1250cm^{-1}. The differences between the spectra for these two samples are small and on the whole result from the different hydrogen contents. The intensity in the sp^2 C=C stretch region (above 1500cm^{-1}) is about the same for both samples, and similar to that observed in samples 3 and 4. The sp^2 CH in- and out-of-plane bends ($\sim$850cm^{-1}) are also similar in all four samples. The low energy region (0-400cm^{-1}) of the spectra for the PECVD samples show that there are some differences in network vibrations compared to the FAS-prepared samples, however, how these differences relate to changes in the network structure cannot be determined.

The diffuse reflectance IR data shows similar trends between the a-C:H samples.

6.4 Summary

The results of the infrared and inelastic neutron scattering studies for these a-C:H samples are summarised below:-

- in both the IR and INS data the modes are common to all samples, although with varying intensity
- from the INS results, the spectra for all a-C:H samples are *most* similar to those obtained for polymeric materials, rather than diamond and graphite, but with only short chains
- samples 3 and 4 prepared from propane and acetylene respectively, are very similar - this is evident from the neutron diffraction as well as the IR and INS

results

- from neutron diffraction results, samples 3 and 4 (prepared at different deposition energies) have a very similar structure, but IR data shows that the distribution of H within the network changes with deposition energy
- sample 6, prepared from cyclohexane at ~960V, is quite different from the other samples: it has relatively few CH_3 groups compared to the other samples and a much larger sp^2 carbon content - these differences are apparent from all the experimental results
- IR and INS data shows that samples 1 and 2, prepared by PECVD, are similar to samples 3 and 4 (a conclusion which also emerged from the neutron diffraction results), although the increased H content gives increased intensity to CH_n deformation modes in the INS data.

6.5 Conclusions

Perhaps the most important point to emerge from this data is that for all the samples the results are consistent with a structural model for a-C:H derived from our previous work, which includes short, polymeric chains. Certainly the INS spectra for the a-C:H samples bear closest ressemblence to the spectra obtained for the polymer materials, polyethylene and rubber, although the much lower scattering cross-section for carbon means that carbon-hydrogen correlations will dominate the spectra. The effects of varying some of the deposition parameters were also investigated and differences in the relative proportions of bonding environments were detected. It was found that, over the range of deposition conditions explored in this work, all the samples produced

were very similar, except for sample 6, which was produced from cyclohexane gas at high energy. This agrees with the neutron diffraction results in Chapter 5 which show only small differences in the structure between the samples. However, the results for sample 6 can be satisfactorily explained in terms of the subplantation model for deposition.

This work has also illustrated the value of infrared spectroscopy and inelastic neutron scattering as complementary experimental techniques.

Chapter 7

Results III: The effect of temperature

7.1 Introduction

Many of the current and potential applications of these materials require elevated temperature and/or pressure environments, therefore it is important to know how they can withstand such conditions. Here, the structural changes in a-C:H have been investigated as a function of temperature using neutron diffraction and inelastic scattering, combustion analysis and infra-red spectroscopy techniques, up to a maximum temperature of 1000°C. The sample used in this study was prepared from acetylene gas at an effective beam energy of 500eV using a FAS (see Table 4), and therefore corresponds to the hard form of a-C:H.

It is well-known that when a-C:H is heated it suffers irreversible hydrogen loss, and eventually a structural transformation to graphite (see for example [105, 57]); it is this process which has been studied here in more detail. Comparisons have been

Temperature (°C)	C (±2 at.%)	H (±2 at.%)	Density (±0.02gcm^{-3})	Number density (±0.05 atomsÅ^{-3})
25	65.0	35.0	1.81	0.13
100	63.7	36.3	1.73	0.13
200	63.5	36.5	1.72	0.13
300	66.2	33.8	1.77	0.13
380	65.2	34.8	1.76	0.13
460	71.2	28.8	1.76	0.12
550	80.4	19.6	1.80	0.11
630	85.8	14.2	1.75	0.10
800	93.4	6.6	1.75	0.09
1000	98.7	1.3	1.74	0.09

Table 15: Compositional and other information for the sample at different temperatures.

made with previous work on similar systems and a brief summary of these results is given.

7.2 Combustion analysis

Information on the composition and density of the sample at different temperatures is given in Table 15.

From the results of the combustion analysis it is possible to look at the variation of hydrogen content in the sample as a function of temperature (see Figure 47) compared to the data of Lukins [151] and Yusada [154].

It is clear that hydrogen evolution is a continuous process, with irreversible changes occurring even by 300°C, but with a rapid increase in the rate of hydrogen evolution thereafter. This data should be compared with the calorimetry work of Nyaish and

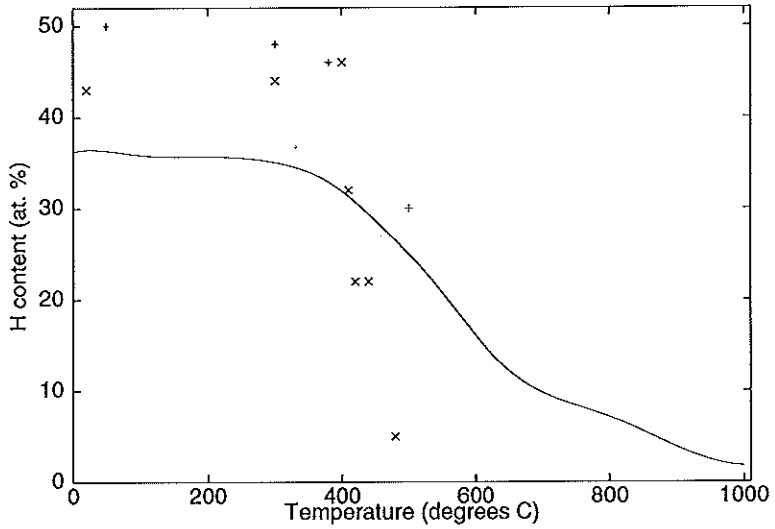

Figure 47: Hydrogen content of the sample as a function of temperature (solid line) compared to the data of Lukins et al. (+) and Yusada (x) (for this data the y-scale is arbitrary).

Mowak [35] on similar materials which suggested the presence of significant exothermic transitions at ~550°C and ~750°C. Differential scanning calorimetry (DSC) measurements carried out on the sample studied here, however, failed to identify any transition temperature, but the combustion analysis would seem to indicate that a "threshold" temperature in the region of 300°C does exist. There is no such supportive evidence for a threshold/transition of any sort at higher temperatures. It is important to note that their sample was prepared in a markedly different way to this one (glow discharge using a methane precursor), and their experiments carried out on a sample prepared in such a way as to maximise its surface area - and hence enhance the effective sensitivity of their DSC instrument [155].

Table 16 compares "threshold" temperatures and maximum hydrogen effusion rates for various samples as compared to the hydrogen content of the as-prepared sample.

Sample	As-prepared H content (at. %)	Temperature at which H evolution begins (°C)	Temperature for maximum rate of H evolution (°C)
Gonzalez-Hernandez [156]	low	~600	-
Gonzalez-Hernandez [156]	medium/high	~400	~500
Nyaiesh at al. [35]	~25	~450	~550
This sample	~35	~300	~500
Dischler [29]	~39	~300	~550
Lukins [151]	~50	~300	~500

Table 16: "Threshold" temperatures and temperatures for maximum rates of hydrogen evolution for various samples.

Note that the general trend is that for samples with an initially high hydrogen content, effusion begins at a lower temperature than for those where the prepared sample has a low hydrogen content, i.e. as the initial hydrogen content increases, the "threshold" temperature for hydrogen effusion decreases. The temperature at which the effusion rate reaches a maximum is generally in the range 450-600°C, irrespective of hydrogen content.

7.3 Neutron diffraction

Figure 48 and Figure 49 show the structure factors and pair correlation functions respectively for each of the temperatures derived from the neutron diffraction spectra.

As before, radial distribution functions were generated from each $G(r)$ and fitted with a series of Gaussians. Therefore the change in carbon-carbon co-ordination number as the temperature is increased can be investigated (see Figure 50).

Also, the positions of the peaks in the $J(r)$ give an indication of the change in average bond length, which for the carbon-carbon first co-ordination shell in particular,

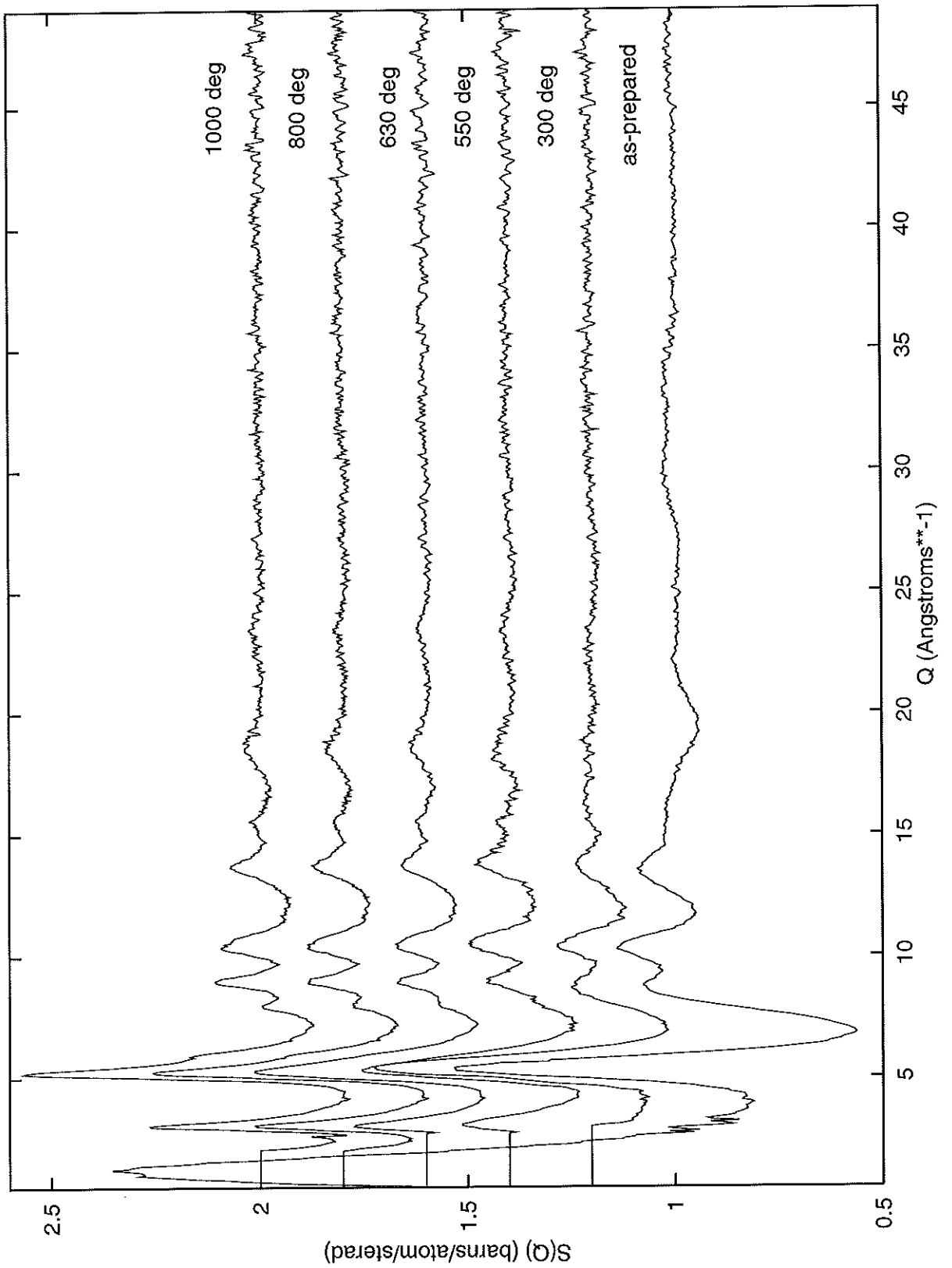

Figure 48: The structure factors derived from the neutron data for various temperatures (offset).

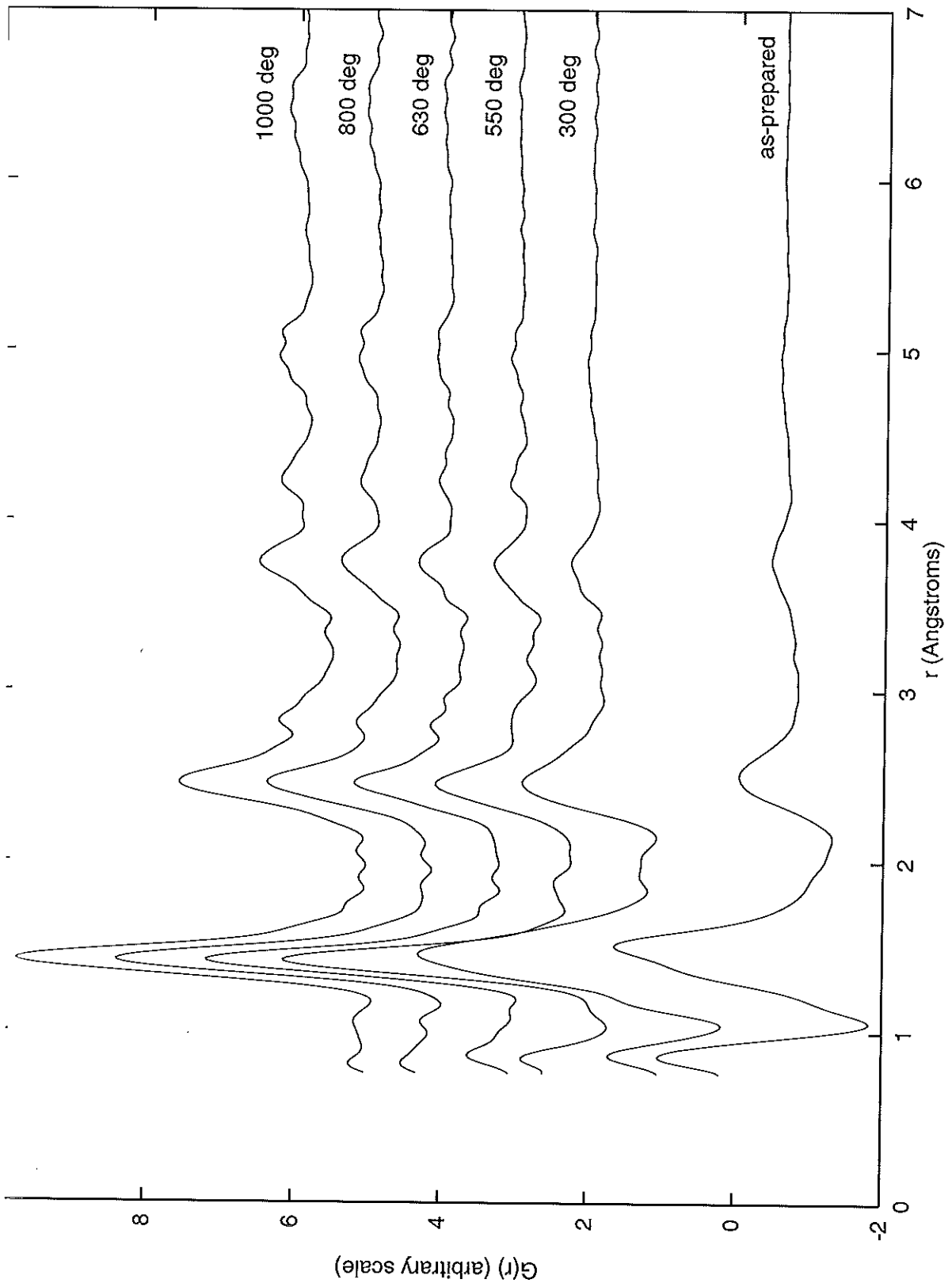

Figure 49: The pair correlation functions derived from the neutron data for various temperatures (offset).

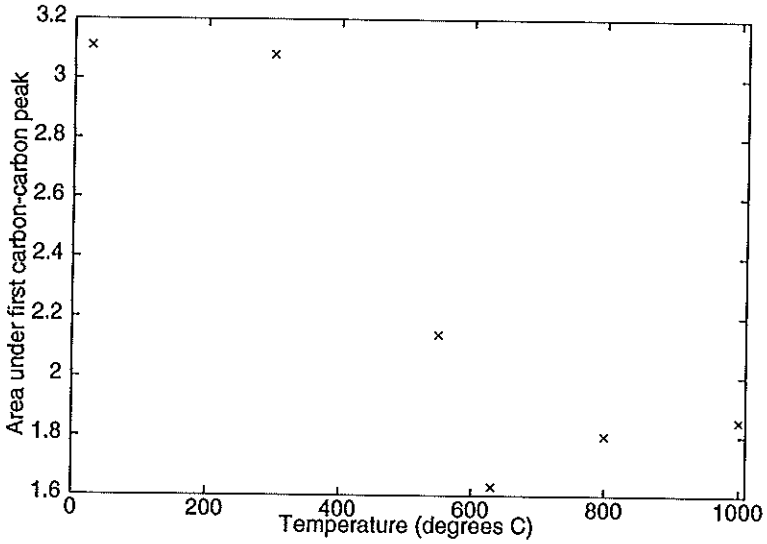

Figure 50: The area under the carbon-carbon first neighbour peak (±0.3) as a function of temperature.

shows clearly the change in the type of bonding (see Table 17).

By taking a look at the general trends across the range of the data, we can see differences in the S(Q) data sets in the region ~17Å^{-1}-~27Å^{-1}, with the gradual appearance of two peaks as the temperature is increased, but a sharper peak at ~7Å^{-1} also emerges with temperature. For the real-space data, in addition to the changes at r<~2.5Åwhich are discussed in detail shortly, there are some interesting differences at higher r-values, although it is impossible to interpret these in terms of changes in bonding environments. Two regions of the data show features at 1000°C which are absent at room temperature: at ~3Å and ~4-6Å. These features indicate a general increase in the amount of ordering in the structure, however, the absence of Bragg peaks in the data shows that the ordering is not too extensive.

From Figure 49, it is clear that as the temperature is increased, the carbon-carbon peak moves from a broad peak at ~1.5Å (- although from the asymmetry of

Temperature (°C)	Position of 1st C-C shell ±0.01 (Å)	Assignment
25	1.34	C=C olefinic
	1.52	C-C
300	1.38	C=C olefinic/ graphitic and/or aromatic
	1.51	C-C
550	1.42	C=C graphitic
630	1.41	C=C graphitic
800	1.42	C=C graphitic
1000	1.42	C=C graphitic

Table 17: Bond distances and their assignments at the different temperatures.

the peak it has already been shown in Section 5.2 that it has two components) to a narrow peak centered at around ~1.4Å; a change already apparent at 550°C. There is therefore a definite trend for the carbon-carbon bonding environment to move from sp^3 to sp^2, and for the olefinic sp^2 to become more aromatic/graphitic in character. Further evidence for this can be found in the decrease in the area under the first-shell carbon-carbon peak shown in Figure 50.

Also, although the quality of the low r data is subject to larger uncertainty due to the empirical nature of the inelasticity correction, there is clearly a gradual weakening of the carbon-hydrogen trough at ~1.0Å and the hydrogen-hydrogen peak at ~0.8Å, as would be expected given that, as the temperature is increased and hydrogen is evolved, the number of carbon-hydrogen bonds and the amount of molecular hydrogen present is reduced. Finally the second-shell carbon-carbon-carbon correlations giving rise to the peak at ~2.5Å should be highlighted. This peak is seen to sharpen as the temperature is increased, which indicates a move from a mixed, towards a single carbon bonding environment. The second shell peak position at 1000°C is consistent with a second neighbour separation of 2.47Å, which implies an average bond angle of 120° (i.e. as would be expected from π-bonded graphite).

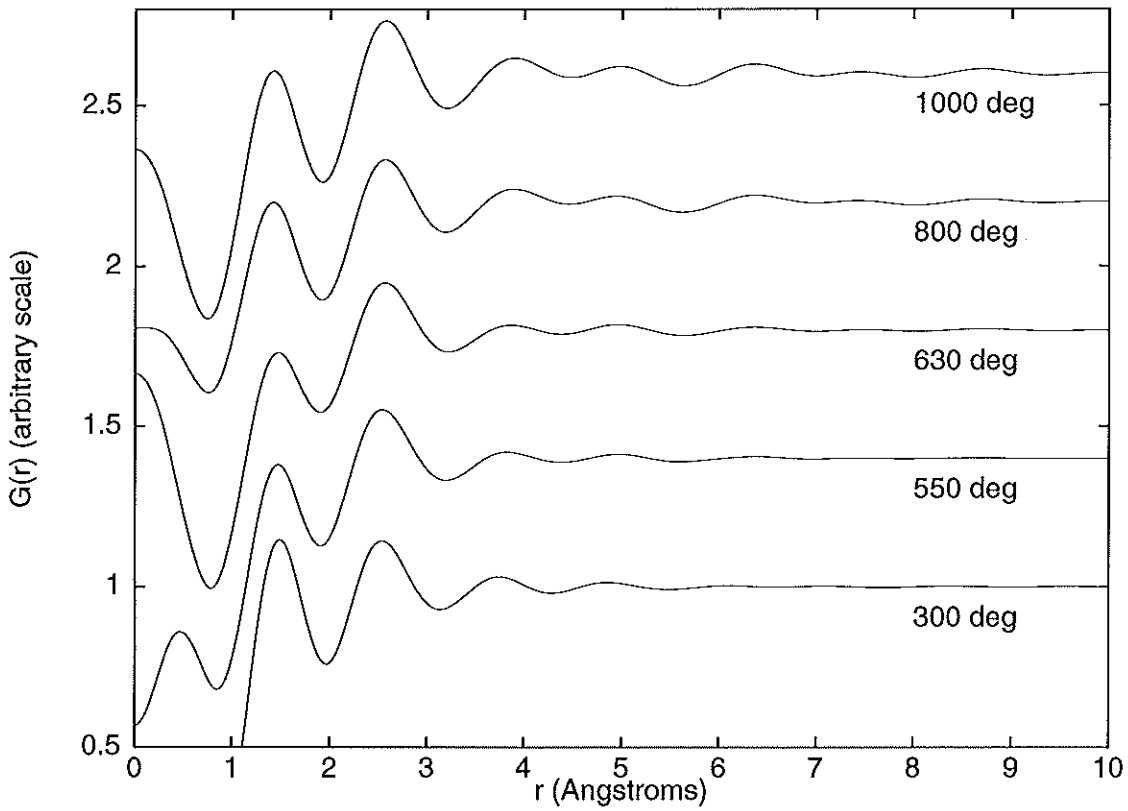

Figure 51: G(r) from the transformation of the low Q region (offset) showing the extent of MRO.

Transformation of the low Q region of the S(Q) data also shows an increase in the MRO with increasing temperature, shown by the extent of the oscillations at high r-values (see Figure 51), which is consistent with a transition to a more ordered structure.

7.4 Infra-red spectroscopy - the C-H stretch region

Assignments for regions of the infra-red spectrum for carbon and hydrogen are shown in Figure 40.

Generally the spectrum is divided into two regions, the C-H stretch region (~2600-3400cm^{-1}) and the C-C stretch region (~500-1800cm^{-1}). In this section of the chapter the first of these regions only will be considered, since the C-C stretch region requires complementary inelastic neutron scattering data for a good interpretation, see Section 7.5. The infra-red spectra for each of the annealing temperatures are shown in Figure 52. For each temperature, the absorbance peaks in the C-H stretch region (3400-2600cm^{-1}) were fitted with a series of Gaussians (see Figures 53 and 54) with the frequency position fixed using published values for the various characteristics modes [29, 41] and the width and height allowed to vary; Table 18 summarises the results for each of the temperatures, together with the vibrational assignments.

By its very nature infra-red data cannot be fully quantitative, but still allows broad conclusions to be drawn on the concentrations of the various structural units observed. Comparison with Dischler's result [29] would indicate that this data is of slightly lower resolution; however, the Gaussian fits obtained are satisfactory as a means of providing qualitative information on the trends occurring. In order to allow comparison between the samples annealed at different temperatures, the peak areas given in Table 18 have all been normalised so that the total area in the range 2600-3400cm^{-1} correlates with the decreasing hydrogen content of the samples. The general decrease in linewidth of the ~3000cm^{-1} peak with increasing temperature is associated with a reduction in the variety of sp^2 CH (olefinic/aromatic) hydrogen

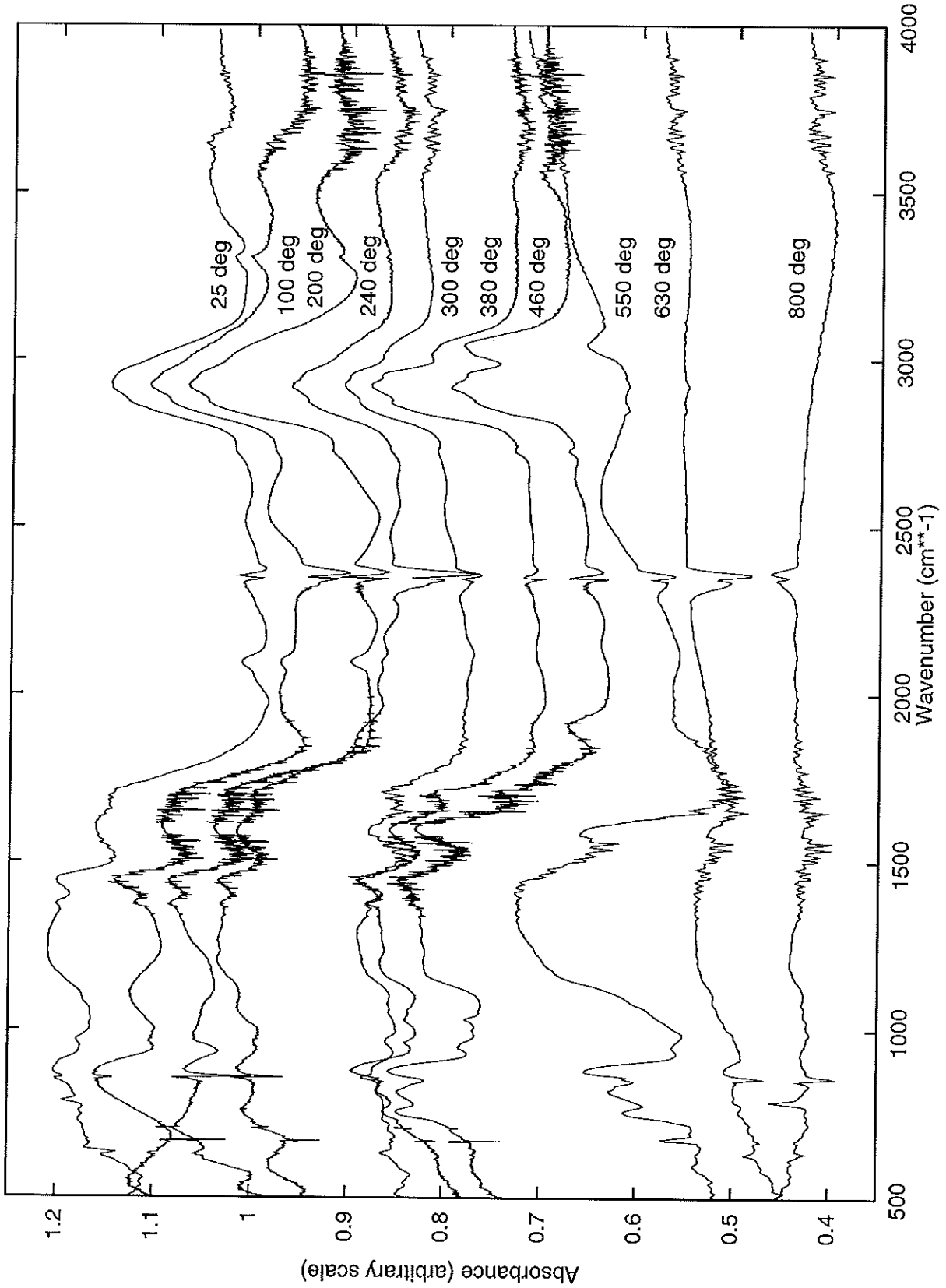

Figure 52: Infra-red spectra for various temperatures.

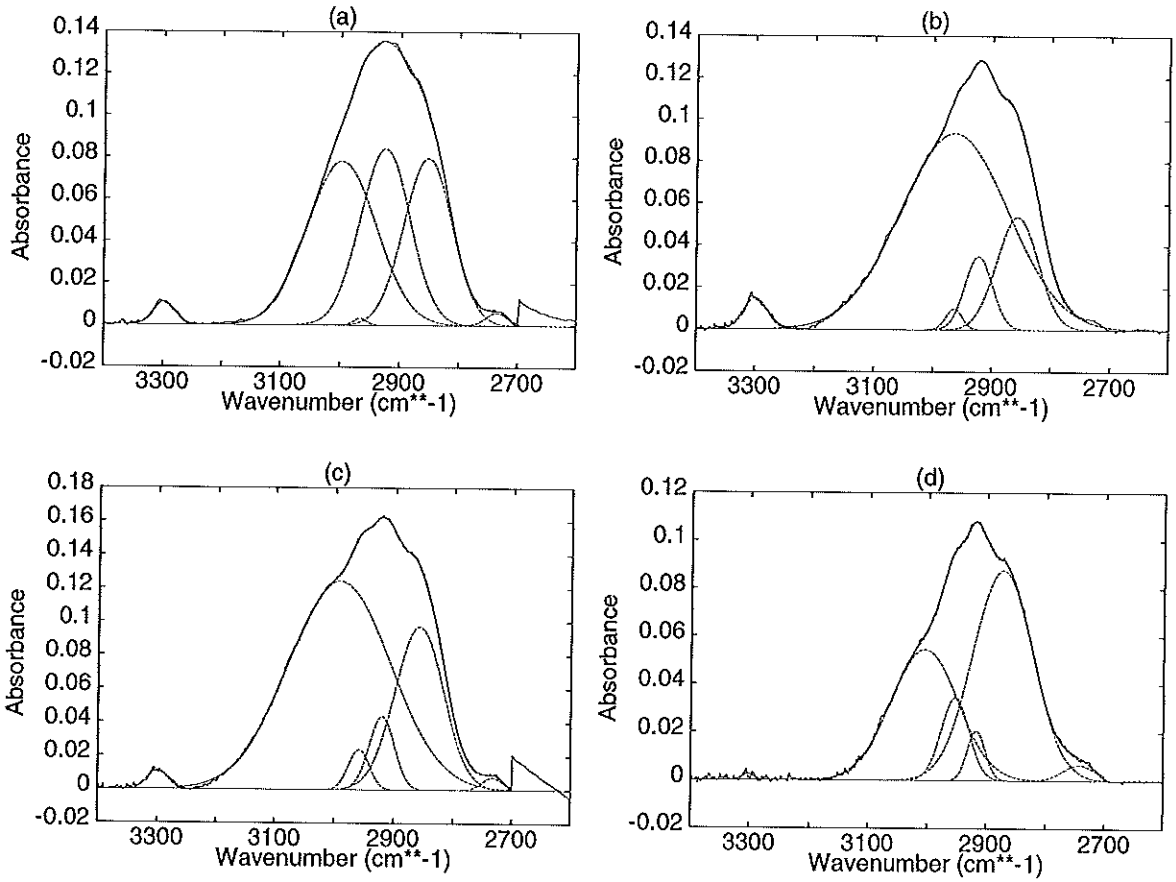

Figure 53: Infra-red spectra with Gaussian fits for: (a) 25°C, (b) 100°C, (c) 200°C and (d) 240°C.

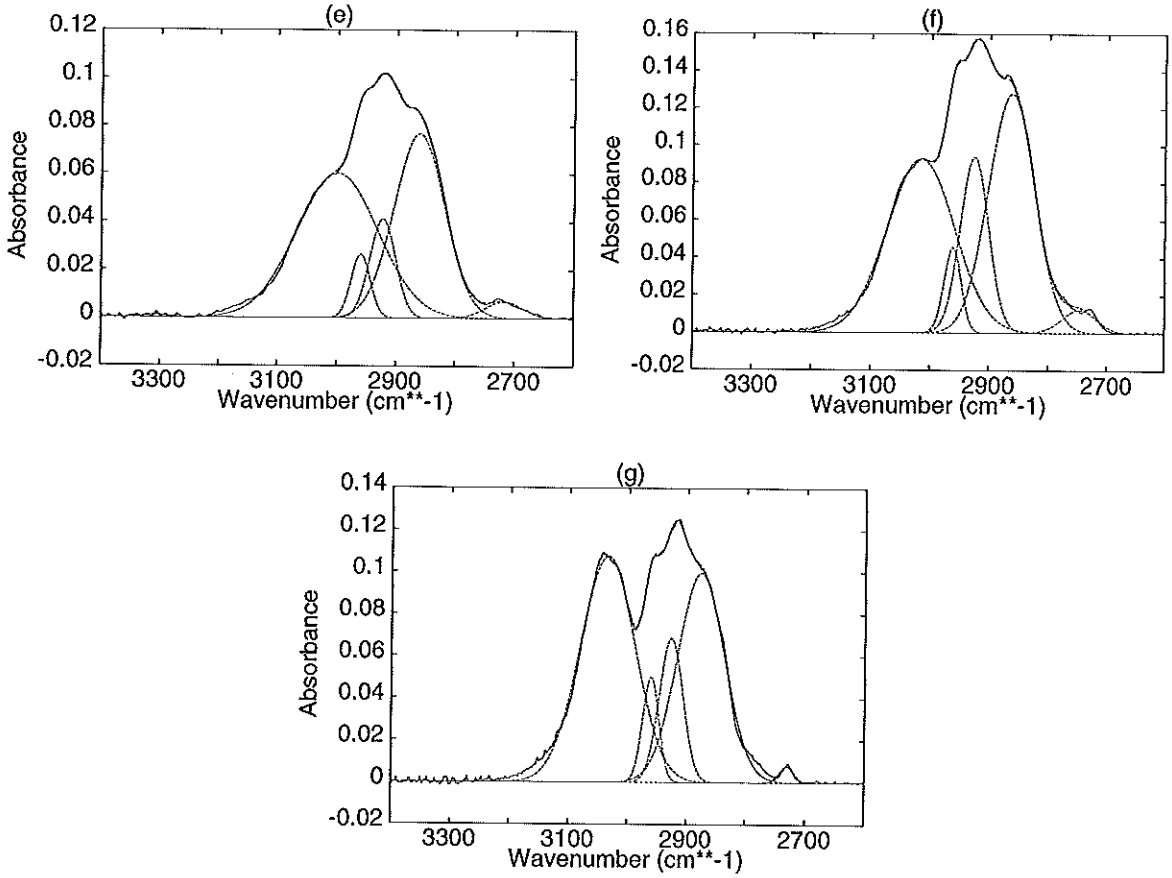

Figure 54: Infra-red spectra with Gaussian fits for: (e) 300°C, (f) 380°C and (g) 460°C.

Assignment	sp^1 CH	sp^2 CH (olefinic/ aromatic	sp^3 CH_3 (asym.)	sp^3 CH_2 (asym.) and sp^3 CH	sp^3 CH_3 and CH_2 (sym.)
Observed frequency (cm^{-1})	3298-3308	2966-3035	2953-2966	2917-2927	2850-2880
Normalised peak area at 25°C	0.69	16	0.12	12	11
Normalised peak area at 100°C	1.1	30	1.1	2.1	7.5
Normalised peak area at 200°C	0.48	28	1.1	2.4	10
Normalised peak area at 240°C	0.11	14	3.9	1.5	20
Normalised peak area at 300°C	0.09	18	1.9	3.9	15
Normalised peak area at 380°C	0.01	16	2.0	6.9	15
Normalised peak area at 460°C	0.00	15	2.1	4.2	12

Table 18: Observed frequencies and normalised areas from the infra-red spectra with their assignments.

bonding environments.

The trends observed are similar to those seen by Dischler [29], Yusada [154] and Lukins [151] where the increasing aromatic character with temperature is seen in the appearance of the sp^2 CH (aromatic) stretch around 3050cm^{-1}, together with a corresponding decrease in magnitude of the sp^2 CH (olefinic) stretch (3000cm^{-1}), and peaks associated with sp^3 CH_2 and CH_3 symmetric and anti-symmetric stretches (2870cm^{-1}, 2920cm^{-1} and 2690cm^{-1}). One other point of note is that the infra-red measurements detect the presence of sp^1 CH, which neutron diffraction cannot without ambiguity (since the strongly negative carbon-hydrogen correlation will obscure a weak sp^1 carbon-carbon correlation).

At room temperature the same features as seen by Dischler and Yasuda are observed in this sample except that, like Lukins, this sample does contain some CH_3 groups (- though we know from the INS and NMR data that these can only be present in small amounts). As the temperature is increased to 240°C, looking at the normalised peak areas in Table 18, we see that, whilst there has been only a small loss of hydrogen, some structural changes have already occurred. The areas for both the sp^3 CH_2 and CH_3 symmetric (~2860cm^{-1}) and the sp^3 CH_3 anti-symmetric (~2960cm^{-1}) stretches have reached their maximum values. However, at the same time, the area of the sp^3 CH_2 anti-symmetric (~2920cm^{-1}) peak is at a minimum. So, there is a definite movement of hydrogen within the network which results in the formation of CH_3 network-terminating groups, at the expense of CH_2 groups. Further evidence for this hydrogen transport comes from the increase in area of the sp^2 CH (olefinic) stretch peak (~3000cm^{-1}) between room temperature and 200°C. As hydrogen is lost from CH_2 groups, it is transported through the network via the formation

of olefinic C-H bonds to CH_3 groups. This would appear to be the first stage in structural re-arrangement that occurs, before significant hydrogen evolution has begun. Following this, there is then a re-organisation of the carbon network. Between 300 and 460°C it is observed that the sp^2 CH (olefinic) stretch peak ($\sim$3000cm^{-1}) moves to a position of $\sim$3050cm^{-1} which may be assigned to sp^2 CH (aromatic) stretching. In Dischler's and Yasuda's data there is a similar transformation, with the gradual loss of the olefinic CH stretch and growth of the aromatic CH stretch peaks. From the data presented here, which are of lower resolution, it is only possible to say that the peak around 3000cm^{-1} is a combination of the olefinic sp^2 CH ($\sim$3000cm^{-1}) and the aromatic sp^2 CH ($\sim$3035cm^{-1}) . With increasing temperature the olefinic peak lessens and the aromatic peak grows, and this manifests itself as a drift in peak position from 3000 to 3035cm^{-1}. So, even before significant loss of hydrogen has occurred, the network has a highly aromatic character. On heating above 460°C all the peaks are seen to decrease (see Figure 54) as hydrogen is rapidly evolved. Also, note that as the sample is heated the area of the peak at 3300cm^{-1} (sp^1 CH stretch) decreases, so that by 460°C no sp^1 CH remains.

These results show quite clearly the general trend from sp^3 to sp^2 bonding. Proposed mechanisms for the structural changes given by [38, 30, 29] in conjunction with these findings would seem to indicate that sp^3 CH is the primary source of hydrogen for effusion, such that, on annealing, molecular hydrogen is formed wherever there are two neighbouring hydrogen atoms. Only on annealing to relatively high temperatures is hydrogen lost from any remaining sp^2 CH, and graphitization is complete.

7.5 Inelastic neutron scattering and infra-red - the C-C stretch region

In examining the results of the INS and IR experiments, the discussion will focus on the changes in the following regions: ~800-1000cm^{-1} (sp^2 C-H out-of-plane and in-plane bending; this is usually associated with aromatic rings but may also involve olefinic groups); ~1100-1300cm^{-1} (sp^3 C-C stretching and -CH_2 wag and twist); ~1300-1500cm^{-1} (CH_2 and CH_3 deformations); and ~1500-1700cm^{-1} (sp^2 C=C and aromatic C=C stretching).

Figures 55 and 56 show the INS and IR data respectively, over the range 0-1800cm^{-1}, at each temperature. Note that the INS data has been smoothed and that it is of much lower energy resolution than the IR data.

The first point to note is that at the highest temperatures, 800-1000°C, the spectra are not featureless, although the results of the combustion analysis measurements show that at these temperatures very little hydrogen remains in the sample. This indicates that these features are due to vibrations involving carbon atoms, specifically, carbon-carbon stretches. These are especially strong in the region ~1100-1300cm^{-1}, and there is also the possibility of one lying "under" the peak at ~1460cm^{-1}, usually assigned to CH_2 and CH_3 (anti-symmetric) deformations. All this information has to be taken into account when interpreting the spectra associated with the lower temperatures. Indeed it is instructive at this point to consider the analogous spectra from graphite and diamond powders (Figure 55). It is evident that the spectra from the annealed a-C:H samples bear the closest similarity to that of diamond powder, particularly the sp^3 C-C stretch region (~1100-1300cm^{-1}). It can be seen that even

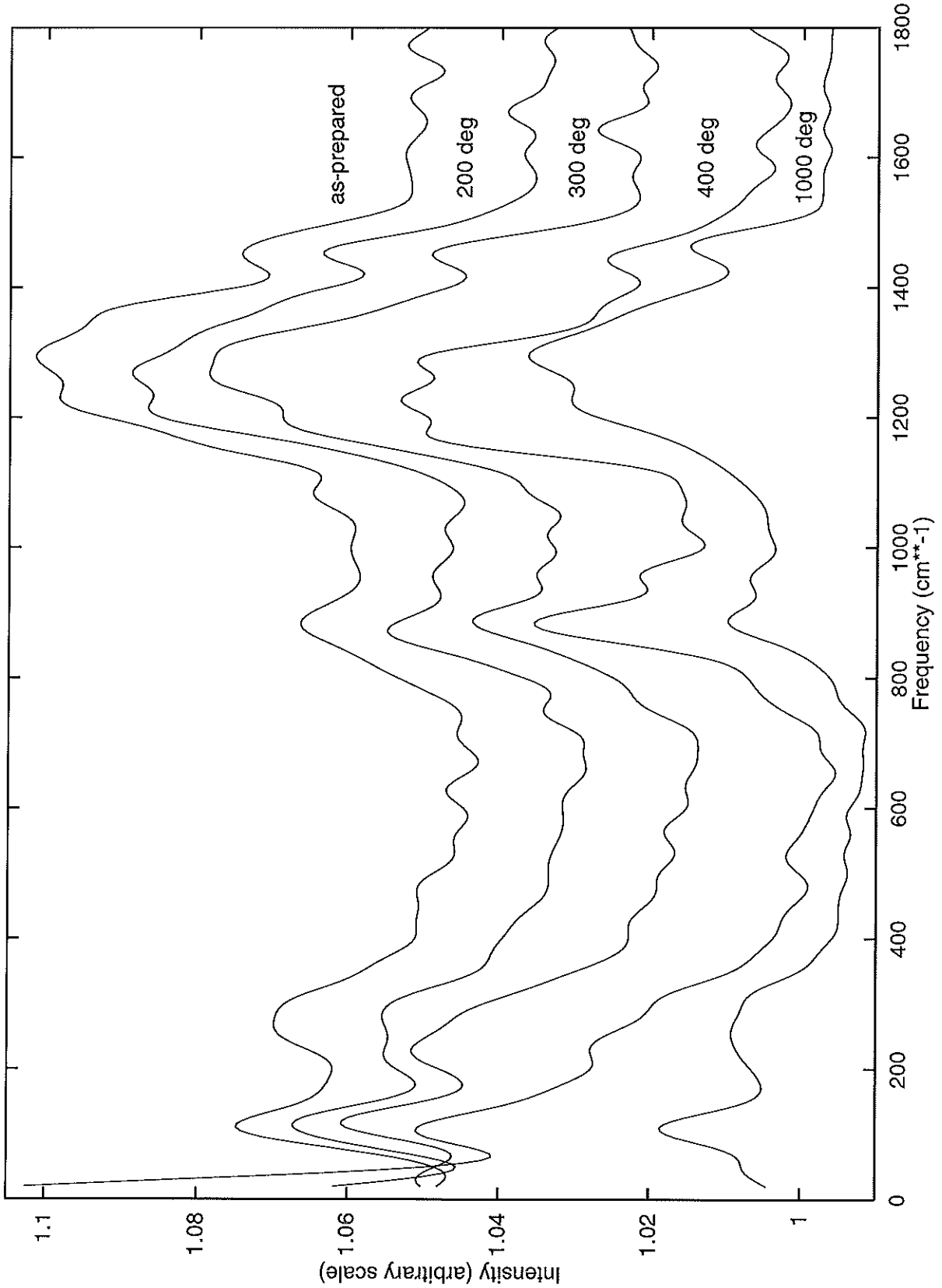

Figure 55: Inelastic neutron scattering spectra for a-C:H at temperatures from 25-1000°C. Statistical errors in intensity are $\pm$ ~0.005 arbitrary units.

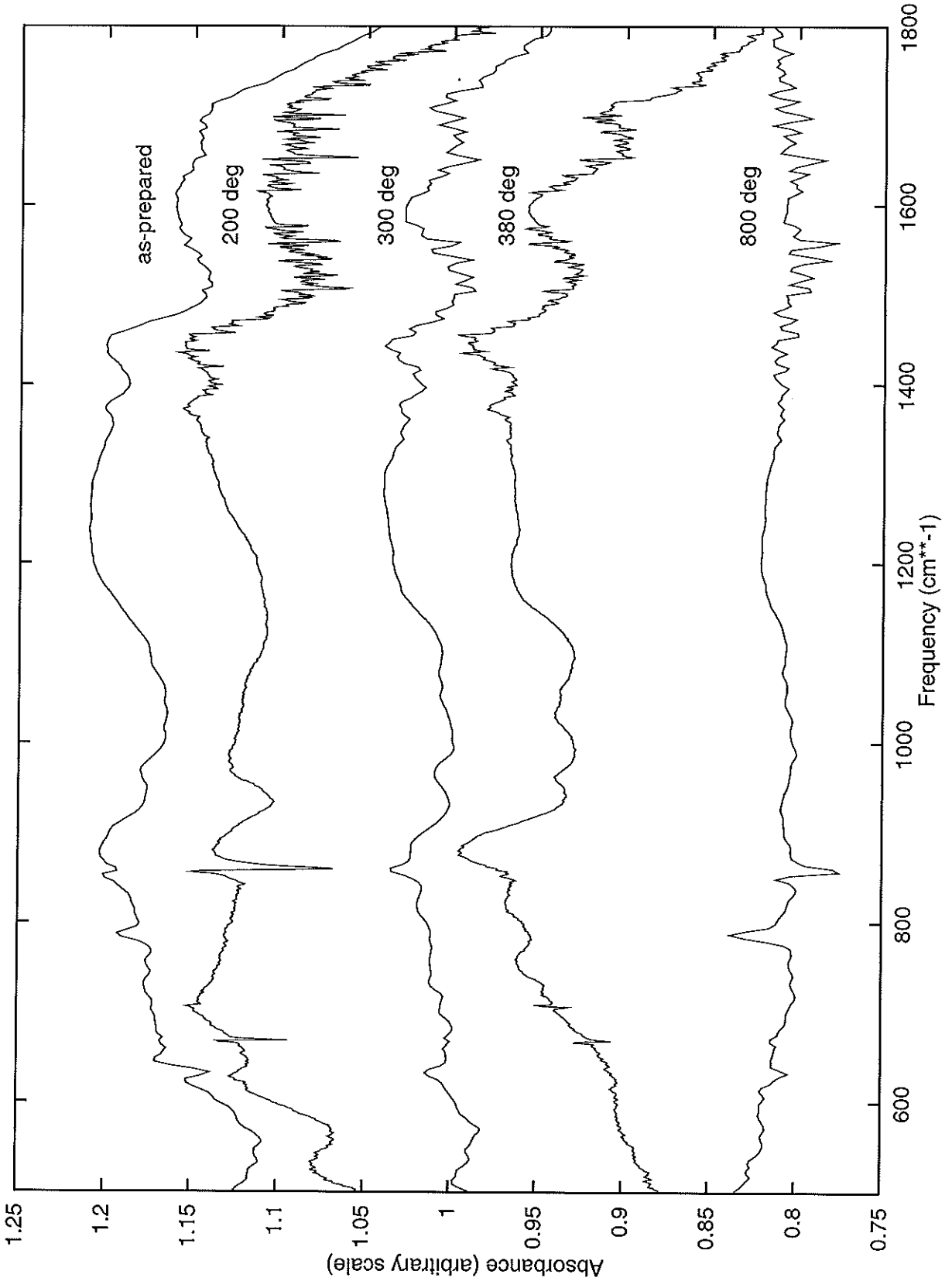

Figure 56: Infra-red spectra for a-C:H at temperatures from 25-800°C.

after heating to 1000°C this similarity is maintained, when we know from the diffraction data (see Section 7.3) that the carbon-carbon bond distance at this temperature approaches that found in graphite (1.42Å). So, although the nature of the bonding becomes graphitic, this clearly does not mean that the structure takes on the ordered layered-ring arrangement which is characteristic of graphite.

On heating to 400°C, the following trends occur: the out-of-plane and in-plane C-H wag peaks (~800-1000cm^{-1}) increase in intensity; the CH_2 and CH_3 deformation peaks (~1370cm^{-1} and ~1460cm^{-1}) decrease in intensity; and the aromatic/sp^2 C=C stretch region (~1500-1700cm^{-1}) shows an increase in intensity. With further heating above 400°C, the whole spectrum shows a decrease in intensity but with some features due to carbon-carbon vibrations remaining, as mentioned above.

Now, consider the INS spectra in more detail. On heating to 200°C, the most noticeable change is that at least one component has been removed from the band at ~1250-1350cm^{-1}. This region of the spectrum has not been well-characterized in previous studies, but from these results it is apparent that a large proportion must be associated with sp^3 C-C stretching since significant intensity remains at the elevated temperatures and by comparison with the spectrum for diamond powder. In an amorphous network there are a variety of environments in which sp^3 carbon can exist, and this would explain the broad nature of this feature. More detailed, definitive comments are not possible but the change does support the contention that some re-arrangement of the carbon network has occurred.

In heating further to 300°C this region of the spectrum is further altered i.e. components attenuated at 200°C, such as those at ~1300cm^{-1}, have returned and others, on the high energy side of the band, have reduced. There is also a significant increase in intensity ~1650cm^{-1}, which is associated with an increase in the number

of sp^2 carbon-carbon bonds and indicates a change to a more aromatic-like structure. However, the presence of this feature at 25°C implies that its interpretation requires some caution since the diffraction data has shown that there is little or no aromatic bonding at room temperature. Although it is generally assigned to aromatic sp^2 carbon-carbon stretching this does not necessarily mean that the structure contains a large proportion of complete aromatic rings; it is entirely possible, indeed probable in an amorphous network, that fragments/sections of "aromatic rings" may give rise to features in this region. In other words, in an amorphous carbon network decorated with hydrogen it is highly likely that a fraction of bonded hydrogen and carbon atoms will find themselves in a potential that has "aromatic" character. This is consistent with MD simulation studies [14]. However, the increase in intensity seen in this region on heating does at least indicate the increasing aromatic nature of the structure. This argument also applies when looking at the increasing intensity in the ~800-1000cm^{-1} (CH wag on aromatic ring) region. This could be interpreted in terms of a change in the carbon network structure, as described above, but also in terms of the migration of hydrogen through the network. Lastly, the relative intensity of the ~1460cm^{-1} peak (CH_2 and CH_3 (anti-symmetric) deformations) to the ~1370cm^{-1} peak (CH_3 (symmetric) deformation) increases in the temperature range to 400°C, which suggests that there is an increase in the number of CH_2 groups in the sample. This is consistent with the results obtained when the C-H stretch part of the spectrum was examined in Section 7.4.

If the sample is heated further to 380°C there is a continuation of these trends. The number of CH_2 groups increases further, as does the intensity of the C-H (aromatic/olefinic) wag band (~800cm^{-1}). Again, the 1150-1300cm^{-1} region changes shape, showing that the structural re-arrangement of the carbon network itself is

continuous. Finally, heating to 800°C causes a dramatic reduction in intensity of all features associated with CH, CH_2 and CH_3 as most of the hydrogen has been lost from the sample. However, there remains a peak at ~1600cm^{-1} (aromatic and olefinic sp^2 carbon-carbon stretch) and some features in the ~1150-1300cm^{-1} region which could be associated with residual sp^3 C-C stretches.

The INS measurements also allow the low energy region (~0-600cm^{-1}) of the spectrum to be examined, see Figure 55. Features in this region arise from vibrations of more extended regions of the network. It is apparent that the principal changes here are that intensity decreases with temperature, which may associated with a more rigid network or a decrease in network connectivity, together with the loss of hydrogen. More subtle changes in peak positions, which are not discussed in detail here, again indicate that structural re-arrangement is continuous. The data taken from IR spectroscopy shows similar trends to those described above: the structure becoming progressively more aromatic in nature up to 400°C and a general reduction in intensity of the features associated with hydrogen thereafter.

7.6 Conclusions

From the evidence it appears that there are two stages to the hydrogen evolution process: up to 300°C very little hydrogen is evolved, but from the neutron diffraction and infra-red results significant structural re-organisation does occur in this temperature region. Above 300°C hydrogen evolution begins to occur at a much higher rate such that, by 800°C, over 75% of the total hydrogen within the sample has been lost. By the same temperature, the process of graphitization is well advanced (evident from the trends seen in both the neutron and infra-red data i.e. the move from sp^3 to sp^2 bonding). It should be emphasized that structural transformations are seen to occur

throughout the heating process i.e. there is no evidence for "transition temperatures" at which dramatic microscopic changes occur. This is in contrast to the differential scanning calorimetry experiments carried out by Nyaiesh and Nowak [35] who found well-defined transitions occurring in their (somewhat different) sample when it was heated.

A summary of the characteristics of samples before and after annealing is given in Table 19.

Whatever the nature of the as-prepared sample there is always an increase in sp^2 C bonding on annealing. The annealed sample is therefore primarily graphitic or aromatic depending on the amount of hydrogen remaining following heat treatment. In some cases, where the initial hydrogen content of the sample was low and the highest temperature reached in the annealing process was relatively high, microcrystalline graphite was observed. Therefore we have a transition from the as-prepared sample to an aromatic ring structure, then to a disordered graphitic ring (or ring-fragment) structure and finally to microcrystalline graphite. It would be interesting to look at these structural changes in more detail using neutron diffraction and inelastic neutron scattering, especially between room temperature and 400°C.

On the mesoscopic scale, it would be of interest to use small angle X-ray scattering (SAXS) to study the effects of temperature on the pore structure. Yin [157] and McKenzie [41] have noted in their samples, on the basis of X-ray reflectometry and electron microscopy studies, an initial increase in pore size followed by a collapse of the porous stucture, and SAXS would provide the analogous information for these samples.

Ref.	Compo -sition	Preparation	Characteristics of as-prepared sample	Characteristics of heat-treated sample
[151]	50% C 50% H	dc magnetron glow discharge C_2H_2-Ar	small significantly substituted aromatic groups; non-aromatic C as highly connective network	70% C 30% H aromaticity ~1.0; aromatic clusters - possible olefinic linking
[38]	50.7% C 42.6% H 7% O	dc magnetron sputtering C_2H_2-Ar	tetrahedral network modified by C=C bonds; crystallites <6Å ; some 5-, 6-, 7-fold rings	66.1% C 32% H 2% O increased amount of sp^2 bonding
[41]	51% C 43% H 7% O	dc magnetron glow discharge C_2H_2-Ar	sp^3 dominates with some aromatic C; much CH_3, some CH_2, some C=C	66% C 32% H 2% O defective graphite planes - possible tetrahedral cross-linking
[157]		dc magnetron glow discharge C_2H_2-Ar	mesoporous; porosity ~0.15	highly microporous throughout; porosity ~0.40
[39]		dc glow discharge C_2H_2	~75% polymeric ~14% diamond-like ~11% graphitic	~82% graphitic
[156]		rf glow discharge CH_4	polymeric; CH_3 dominant; high H content	microcrystalline graphite; condensed ring structure; long range order
[156]		rf glow discharge CH_4	more graphitic, less polymeric; CH_2 dominant; low H content	microcrystalline graphite; condensed ring structure; long range order
[30]		plasma deposition CH_4	sp^2 C-H dominant; high H content; polymeric component	increased sp^2 content more graphitic
[35]	~75% C ~25% H	rf glow discharge CH_4	~19% bonded H; ~6% chemisorbed H; distorted graphite structure	microcrystalline; graphitic
[158]	~100% C	dc PCVD benzene	dominant sp^3 C bonding; diamond-like C	dominant trigonal (sp^2) crystallites; graphitic
[29]	61% C 39% H	rf plasma deposition benzene	sp^3C:sp^2C=2/3:1/3; CH dominant over CH_2	~0% sp^3 C; sp^3C:sp^2C=0.1; completely aromatised

Table 19: A summary from the literature of the effects on annealing on a variety of samples.

Chapter 8

Reverse Monte Carlo (RMC) modelling of a-C:H

Introduction

In this Chapter the results of reverse Monte Carlo (RMC) analysis of the experimental data are presented. However, in order to understand what the results of such a study can tell us, it is also important to explain how the RMC method works. So, before the results are given, an outline of the RMC method and its uses and limitations will be presented. It is also noted that this RMC work has been "developmental" (and, to some extent, still is) so that the work presented here represents the result of many other tried, but failed, attempts and by no means gives the "final" answer.

8.1 The RMC method

RMC is a method for producing three-dimensional models of disordered materials directly from the experimental data, usually diffraction data. Unlike molecular dynamics and most other modelling methods, no interatomic potential describing the

system is required. This is particularly useful for studying a system such as a-C:H where an interatomic potential is very difficult to define, but high quality experimental data is available. Developments of the RMC method now mean the experimental data sets from X-ray and neutron diffraction experiments can be fitted simultaneously, whilst, at the same time, constraints on the atomic coordination numbers can be applied thereby incorporating prior chemical knowledge of the system into the model. In this way, a model consistent with the experimental data and with chemically viable bonding can be produced.

8.1.1 The RMC algorithm

The basic algorithm has been described in detail elsewhere [159, 160]. In essence, "atoms" in a box are moved until the derived pair distribution function, G(r), and/or structure factor, S(Q), matches the experimentally measured data. The principal steps in the method are as follows:

1. Define a box with edge dimensions at least twice the value of r at which statistically significant oscillations in G(r) disappear and then fill the box with "atoms" (either at random, or using a simple lattice) so that the number density matches the measured bulk value. (For a binary system such as a-C:H the numbers of each type of atom must match the percentage composition of the sample.)

2. The atoms are moved at random and at each stage a model S(Q) is calculated. Note that an atom is moved subject to the constraint that it does not overlap with a neighbouring atom (- an "excluded volume" is therefore associated with each atom type).

3. The model $S_{mod}(Q)$ is compared with the experimental $S_{expt}(Q)$ and a new configuration accepted if the associated χ^2 has been reduced:-

$$\chi^2 = \sum_i \left[S_{expt}(Q_i) - S_{mod}(Q_i)\right]^2 / \sigma_i^2.$$

Rejection is subject to a probability function dependent on the experimental error, σ_i.

4. The process is repeated until the model S(Q) reproduces experiment to within the experimental errors. The process is further iterated until an "equilibrium" configuration is obtained. Where more than one data set is used, the χ^2 calculations and acceptance/rejection criteria are applied to each. This is also the case for any constraints on the bonding of the atoms.

This seems a straightforward technique, however, there are some practical problems in trying to apply it. The first concerns the value of the number density chosen when generating the box. The density measured by the residual volume method is the bulk value. This will coincides with the value for the microscopic density only for non-porous materials. So, if the bulk density is used to generate the initial box in the RMC method for a porous material, it may be in error by as much as 40% [13]. The other difficulty is choosing the correct value for the exclusion radii, which define the closest approach distances for different atom types. These are usually taken directly from the G(r) data as the distances at the start of each first neighbour peak. However, for a system containing atoms with a negative scattering length, which results in "negative peaks" in the G(r), the start of each peak is not well defined, which means that the value of the exclusion radius is difficult to determine with much accuracy. Finally, it should be pointed out that the RMC method tends to produce the *most* disordered structure, consistent with the experimental data. This factor is reduced

by the introduction of constraints on the model, but it is still something which has to be borne in mind when discussing the "final" atomic configuration.

8.2 The RMC method applied to a-C:H

On the face of it, a-C:H is a simple binary system of carbon (C) and hydrogen (H) atoms and should present no real difficulty in the RMC method. However, it is complicated by the ability of C to form three different types of bond (sp^1, sp^2 and sp^3 hybridisations), all of which have different bond lengths and different first coordination numbers associated with the C atoms. So, just from simple bonding considerations this system is fairly complex. The situation is complicated still further when the experimental data to be fitted in the RMC process is also considered. As stated in Section 3.3, hydrogen has a negative scattering length for neutrons which means that although correlations for H-H and H-C-H, etc. are positive, those for C-H and C-C-H, etc. are negative. This makes it very difficult, if not impossible, to define the start and end points of each peak and to obtain accurate values for peak areas. As will be seen from the work described in this Chapter, these problems create significant difficulties in trying to produce a physically viable model for a-C:H.

For the RMC modelling undertaken here a box usually containing ~5000 atoms is used, with the box-length chosen to give a number density matching the experimentally measured value. All the models generated in this work started with an initially random distribution of atoms. Details for the models for different experimental data sets are given in Table 20. The very first RMC modelling was carried out on a VAX 3100/38 processor, although the work was quickly moved on to a DEC *alpha* 3000 processor which generates on average $\sim 10^6$ moves in a 24 hour period, depending on the model. The criterion for deciding whether an "equilibrium" configuration has

Sample	Precursor gas	Number of C atoms	Number of H(D) atoms	Box length
3	propane	3400	1600	33Å
6/7	(deuterated) cyclohexane	3750	1250	37Å

Table 20: Parameters for the RMC models.

been reached is based on the ratio of number of moves tried:number of moves accepted, and it is generally decided that equilibrium has been attained when this ratio is $\sim 10^5$:1.

Once a satisfactory model has been obtained, the configuration can be used to generate partial structure factors and pair correlation functions, bond angle distributions, coordination number distributions and ring statistics. However, it should be noted that coordination number and bond angle distributions, and ring statistics, rely on a naive count of all atom centres within a certain radius of some central atom: since no potential is used in RMC modelling, there is no information on whether individual pairs of atoms are actually chemically bonded or not. These analyses also depend critically on the choice of integral limits (i.e. the shell radius chosen around the central atom) which, as discussed above, cannot be defined precisely for a-C:H.

In the remainder of this Chapter, the developments of RMC and its successes and failures with respect to producing a physical model for a-C:H will be presented.

8.2.1 The first models

The very first models of a-C:H were generated using the basic RMC algorithm as given in Section 8.1.1 for sample 3. Both the structure factor, S(Q), and pair correlation function, G(r), obtained by neutron diffraction could be fitted well, independently [161], however, effective coordination number and bond angle distributions associated

with the model showed some atomic arrangements which were unexpected and highly unlikely to occur in the real sample from chemical considerations, and which are termed "unphysical". The main problem was a tendency for the RMC approach to produce 3-membered rings of the same atom type, all equidistant and giving rise to a sharp peak in the C-C-C bond angle distribution at 60° (as well as the broad peak expected at in the region 110-120°). It is possible that due to the high internal stresses in these materials some C-C-C triangles or "triplets" may exist, but only in very small quantities since this is such a highly stressed arrangement of atoms. The presence of triplets can therefore be attributed to an artifact of the RMC modelling process rather than a chemically bonded unit; and indeed might reasonably be expected given the χ^2 convergence criterion since the generation of a triplet provides an efficient mechanism for the rapid reduction of χ^2. Also in these early models a significant number of over-coordinated atoms were found: some C atoms had 5 or 6 near-neighbours and some H atoms had 2 near-neighbour atoms. There was also a large proportion of both C and H atoms with no near-neighbours at all. Clearly this kind of bonding cannot occur and gives further indication that the method needs improving.

8.2.2 The introduction of constraints and developments to RMC

The first obvious constraint to introduce into the RMC method is one that prevents the formation of triplets which were so prolific in the first RMC models. It was thought that fitting to S(Q) initially, rather than G(r), so that the long-range order is introduced into the model preferentially might overcome this problem, but this was unsuccessful, as was the attempt at changing the number density, to try and compensate for the difference between the measured bulk value and the microscopic

value required, as mentioned in Section 8.1.1. So, it was clear that constraints were going to be necessary; and as soon as the RMC code was modified to do this, these unphysical features were removed from the models.

At the same time, the RMC code had also been developed to include constraints on total coordination numbers (to prevent atoms from becoming over-coordinated) and to allow different types of data set to be fitted simultaneously. So that as well as fitting G(r) and S(Q), data from both X-ray and neutron diffraction experiments could be fitted at the same time. Likewise, chemical constraints, which represent prior knowledge of the system, could be incorporated into the model. Principally by fitting two complementary diffraction data sets, and by the introduction of constraints, many of the initial problems with the RMC models were resolved. The need for constraints has also been discussed by others in the field [162], and those introduced for a-C:H were developed originally for work on amorphous germanium [163]. Although the early results of work arising from these changes has been published [164], in order to understand the full impact of these new developments of RMC and the work which has followed since, their implementation will be discussed here in some detail.

The constraint on triplets is straightforward: by looking at the bond angles in the configuration, any such atomic arrangements are removed from the model structure and, as the atoms are displaced, more triplets are prevented from being produced.

The coordination constraint was implemented in terms of a maximum coordination constraint, i.e. C can form a maximum of 4 bonds (3 in the sp^2 hybridisation and 2 in the sp^1 hybridisation) and hydrogen can only form 1 bond. These two constraints cater for basic chemical information about the system.

8.2.3 "Physical" models for a-C:H

Sample 3 (propane)

Constraints as described above were applied, but also X-ray diffraction data was available for this sample, which could be combined with that from neutron diffraction experiments. Given that the X-ray diffraction data approximates to the C-C partial term, it can be used, in principle, to constrain the C atoms in the amorphous network, whilst allowing the hydrogen atoms to exist in any unoccupied volume elements. Then the neutron diffraction data, which contains information on both the C and H correlations, together with the primary constraints mentioned above, may be used to produce a better-defined model.

However, there is a problem in using the data in this way which arises from the difference in resolution between the X-ray and neutron diffraction data. The X-ray S(Q) data is better resolved, but because in this case it only covered the range ~0.4-10Å^{-1} (c.f. the range of the neutron S(Q) is ~0.2-50Å^{-1}) this results in a relatively poorly resolved G(r) when Fourier transformed. Therefore, if the X-ray data is fitted and used to generate positions for the C atoms, the neutron data cannot then be fitted satisfactorily since H atoms are caused to be moved into unphysical positions to compensate for the differences in resolution. To overcome this problem a new approach is required.

One possible solution involved defining atoms to represent the two different types of carbon bonding, sp^2 and sp^3, which are known to be present. This is done simply by giving them different distances of closest approach and different maximum coordination numbers, then treating the model, in effect, as a three component system. However, the constraints are of necessity on the atom type, whereas in the material itself it would be possible (even likely) that a given C atom would be associated with

both single and double bonds. Also, this did not in practice solve the problem of H atoms moving into physically unrealistic positions.

A more successful method was then developed using all the available data sets for sample 3, but with weightings so that one set is fitted preferentially. In order to produce a physically meaningful model the positions of the C atoms are fixed first by fitting a specific region of the neutron G(r), then the H atoms are allowed to move into positions to fit the C-H and H-H correlations. Since the X-ray data cannot be used to define the carbon network directly, the neutron data is used instead: C-C correlations are the sole contributors to the peak in the G(r) centred around ~1.5Å. Therefore, by fitting initially only to this peak in the data, with all the partial weightings set to zero except that for C-C, the first neighbour C-C correlation can be fixed. The X-ray data is then used to provide simultaneously a broad constraint for the medium range C-C order, although the weightings are arranged so that the neutron G(r) data is still fitted preferentially. In this way the C atoms are fixed into positions in the network which fit the experimental data: of course, triplet and maximum coordination constraints were applied throughout. Once this part of the data has been fitted well, the range of the fit can be extended to cover the full range of the neutron G(r) and the neutron S(Q) can be introduced together with the correct weightings for the C-H and H-H contributions. The preferential fitting of the G(r) is maintained so the H atoms are constrained to move into positions which fit the whole data range without altering the initial C-C correlations. Notice that in this method the X-ray diffraction data is used only to constrain the model broadly by introducing a weak post-first shell constraint to the carbon network; it does however improve the overall computational efficiency of the process and the quality of the final fit. This method has been used successfully to model a-C:H.

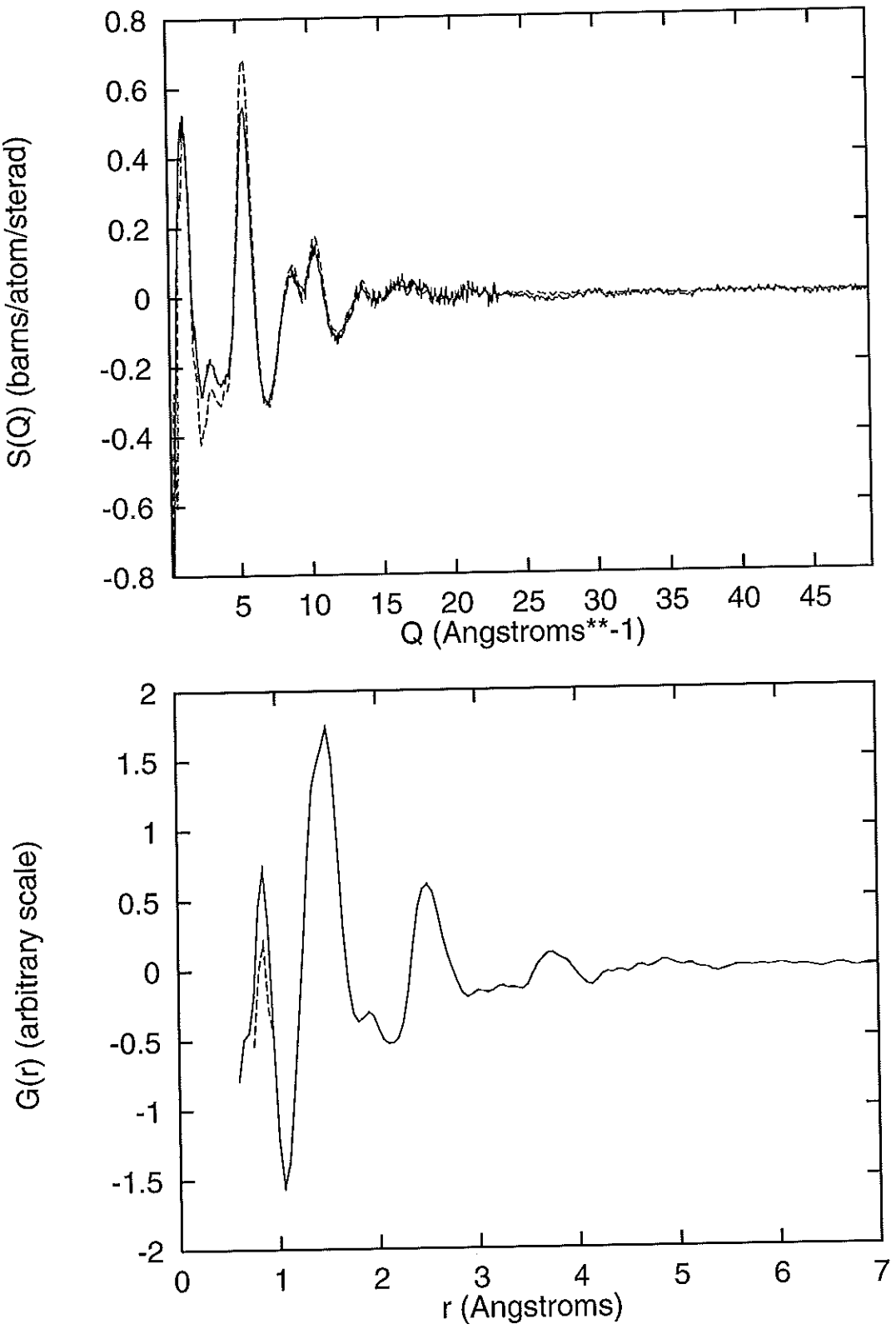

Figure 57: RMC fit (dashed line) to the neutron S(Q) data (solid line).

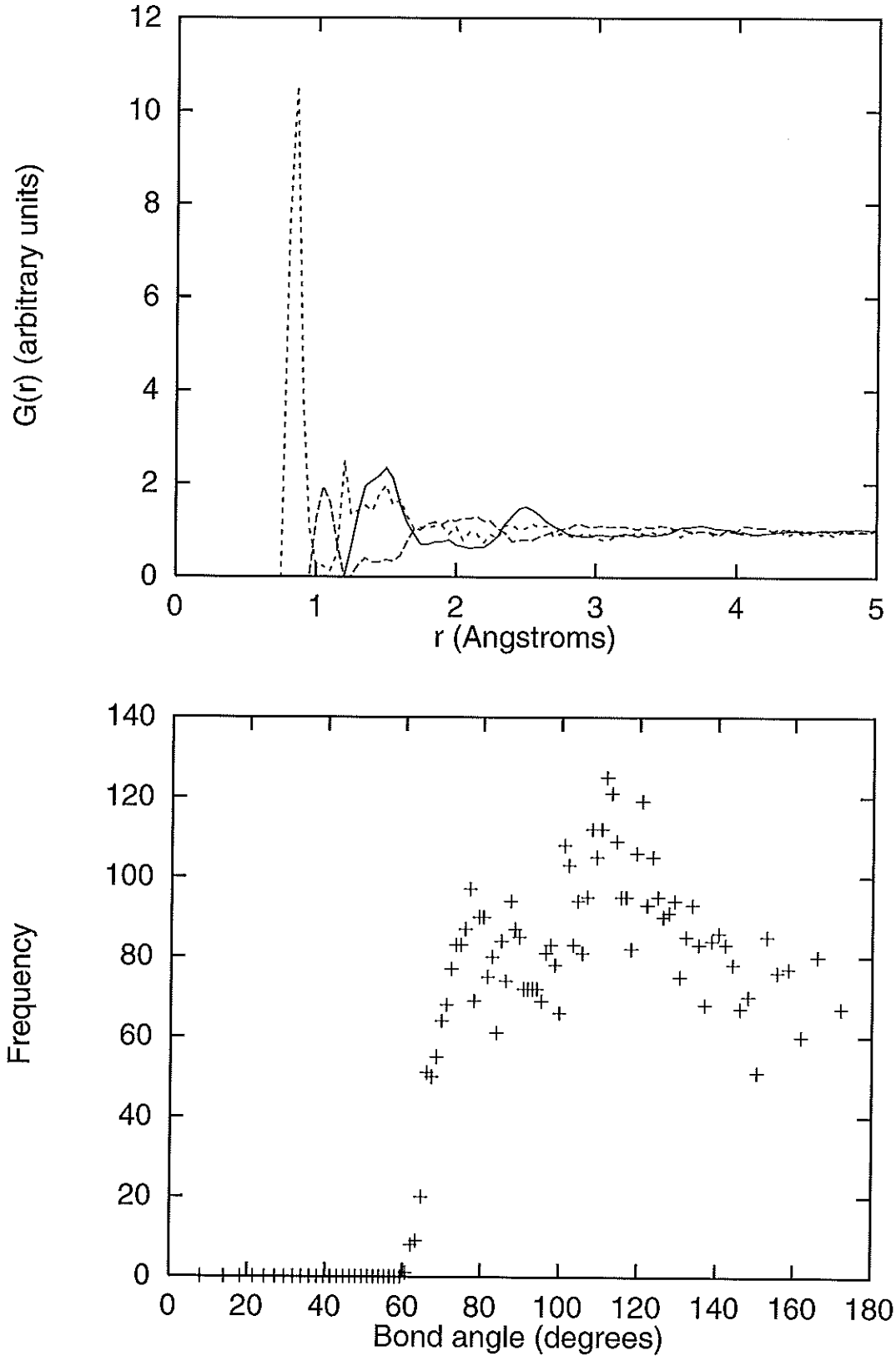

Figure 58: G(r) partials generated from the RMC fit: C-C (solid line), C-H (dashes) and H-H (dots) (bottom), with the associated C-C-C bond angle distribution below.

The fits to the neutron S(Q) and G(r) and the derived (unweighted) partial g(r)'s are shown in Figure 57. Notice that the model has been able to assign the expected C-C and C-H correlations quite clearly, and fits most of the features in the total S(Q) and G(r) data well. The H-H correlation also reveals the presence of molecular hydrogen, however, it is known that the magnitude of the peaks in this region of the data is subject to relatively large uncertainties due to the effects of the inelastic scattering (see Section 4.4.3). This is also likely to affect the C-H correlations to some extent, and should be taken into account when coordination number distributions are considered.

Figure 58 shows the C-C-C bond angle distribution obtained from the model. Notice the distribution of bond angles centred around ~110° but extending to higher angles, as would be expected in a-C:H, and the lack of any sharp feature at ~60°. So, simply by removing triplets, the expected bond angle distribution is obtained. This also indicates that it is unnecessary to constrain the bond angle distribution itself in a more direct way in order to avoid unphysical 3-site correlations. Other workers [162] have employed direct constraints on the angles themselves, which has no better a result, but is computationally more demanding.

Number of neighbours	Total number of atoms	Carbon-carbon	Carbon-hydrogen
0	150	216	2848
1	721	866	513
2	1325	1342	38
3	961	820	1
4	243	156	0

Table 21: Coordination number distribution for carbon from the RMC model.

The coordination number distributions for C and H are given in Tables 21 and 22. For the experimentally measured bulk number density (0.14 atoms$Å^{-3}$) the average

Number of neighbours	Total number of atoms	Hydrogen-carbon	Hydrogen-hydrogen
0	158	1008	750
1	1442	592	850
2	0	0	0
3	0	0	0
4	0	0	0

Table 22: Coordination number distribution for hydrogen from the RMC model.

coordination numbers obtained were: 2.12 for C and 0.90 for H. These were lower than expected, which is probably due to the presence of voids in the sample, making the measured bulk density significantly lower than the microscopic density. Molecular dynamics (MD) simulations [13] for the same material have shown that the measured density is at least 20% too low and that the density could be up to 40% in error, though this is unlikely. However, recently it has been found that the high densities required by the MD simulations may also be inaccurate [165]. Part of this study has centred on an exploration of the effect of density on the RMC model. The number density was increased from 0.14 to 0.17 atoms$Å^{-3}$ in steps of $\sim$0.01 atoms$Å^{-3}$, and the corresponding increases in average coordination number are shown in Table 23. In increasing the density, the G(r) data was not recalculated from the S(Q) each time, although the fits to the data were the same. This shows the expected fact that the number density is a critical parameter in the RMC method. Increasing the density had little effect on the bond angle distribution.

Finally, the model was analysed for ring statistics. Two different ring-finding programs were available for this: the first [163] finds rings by building-up a tree of bonded atoms until the algorithm returns to the origin atom or another atom already in the tree. The second [138] uses a shortest distance analysis, taking pairs of bonds in turn and finding the shortest way of bridging the junction between them

Number density (atoms$Å^{-3}$)	Average coordination number	
	Carbon	Hydrogen
0.14	2.12	0.90
0.15	2.21	0.93
0.16	2.32	0.92
0.17	2.45	0.94

Table 23: Average coordination numbers for C and H with increasing number density.

with bonds of similar type. The distributions of rings obtained by both methods for a number density of 0.17 atoms$Å^{-3}$ are given in Table 24. Interestingly, although

Number of atoms in the ring	Number of rings [163]	Number of rings [138]
1	0	0
2	0	0
3	0	0
4	154	149
5	71	66
6	52	54
7	35	37
8	27	35
9	10	16
10	7	15

Table 24: Ring distributions from the RMC model.

the two methods are quite different the distributions of rings generated by them are similar. The large number of 4-membered rings (and the number of unbonded atoms, see Tables 21 and 22) are indications of residual problems with the model, even though it fits the experimental data. The unexpectedly large number of 4-membered rings results from the exclusion of 3-membered rings and is quite difficult to reduce without fitting the model to a defined ring distribution. This could be implemented, although it would slow down the computation considerably, however,

we have no prior knowledge of the ring distribution in a-C:H, so such a constraint should be introduced with much caution. The problem with the coordination number distributions is intrinsically easier to solve and requires that more of the chemical knowledge of the system and results from the data analysis procedures can be fed into the coordination constraints, with the inclusion of information from different experimental investigations, e.g. NMR and inelastic neutron scattering results. This may also affect the distribution of rings in the RMC model by producing a more coordinated network.

So, by the careful implementation of constraints, it is evident that a substantially more robust and physically reasonable model can be generated, however, it is also clear the the model structure retains significant flaws.

Samples 6/7 (cyclohexane)

So far the developments of RMC have concentrated on obtaining a physical model for a-C:H using data for a sample prepared from a propane precursor (sample 3). However, an equally successful model has been obtained using the data from a series of samples [166] (a-$C_{0.75}$:$H_{0.25}$, a-$C_{0.75}$:$D_{0.25}$, a-$C_{0.75}$:H/$D_{0.25}$) prepared from cyclohexane and deuterated cyclohexane, but by using a slightly different method. Hydrogen has, as has already been stated, a negative neutron scattering length; deuterium, however, has a positive neutron scattering length. It is therefore possible to prepare a sample where the H:D ratio is such that the two scattering contributions cancel each other exactly, leaving only the C correlations to be observed. This is known as the "null mixture" sample. Clearly data from this sample could be used in the same way as previously tried with the X-ray diffraction data, to constrain the positions of the carbon atoms, but this time without the resolution problems previously encountered.

In addition, if the H and D atoms are assumed to occupy the same sites in the a-C:H and a-C:D samples and if the correct weighting co-efficients are used, this essentially provides two independent data sets for the same sample. The constraints on triplets and maximum coordination numbers as described previously, were included throughout.

The resulting RMC fits, when all the above constraints and procedures were applied, to the total S(Q)'s and G(r)'s from neutron diffraction experiments are shown in Figure 59, with the (unweighted) partial g(r)'s presented in Figure 60. The quality of the fit to the experimental data is not as good as that achieved in the previous sample, however this can be attributed, at least in part, to poorer quality experimental data rather than in accuracies in the RMC model. In fact, this illustrates another use for RMC in determining which, if any, of the features of the experimental data arise from poor data analysis, especially for materials such as a-C:H where polynomials have to be fitted to carry out the inelasticity corrections. The partial pair correlation functions show similar features to those for sample 3, but with a little more overlapping of peaks and some features, particularly in the H-H partial which may be unphysical. This model also suffers the same problems of low average coordination numbers for both C and H - $\sim$ 2 and $\sim$0.87, respectively - and a large number of 4-membered rings. The coordination number and ring distributions are given in Tables 25, 26 and 27.

These low values arise from the large number of "unbonded" atoms, and for the case of C, from atoms with a total of only one or two near neighbours. This situation is not acceptable from chemical considerations, so a way of increasing the average coordination numbers is required. The problems with the value of the number density used have already been discussed (see Section 8.1.1), so the density of the atoms in

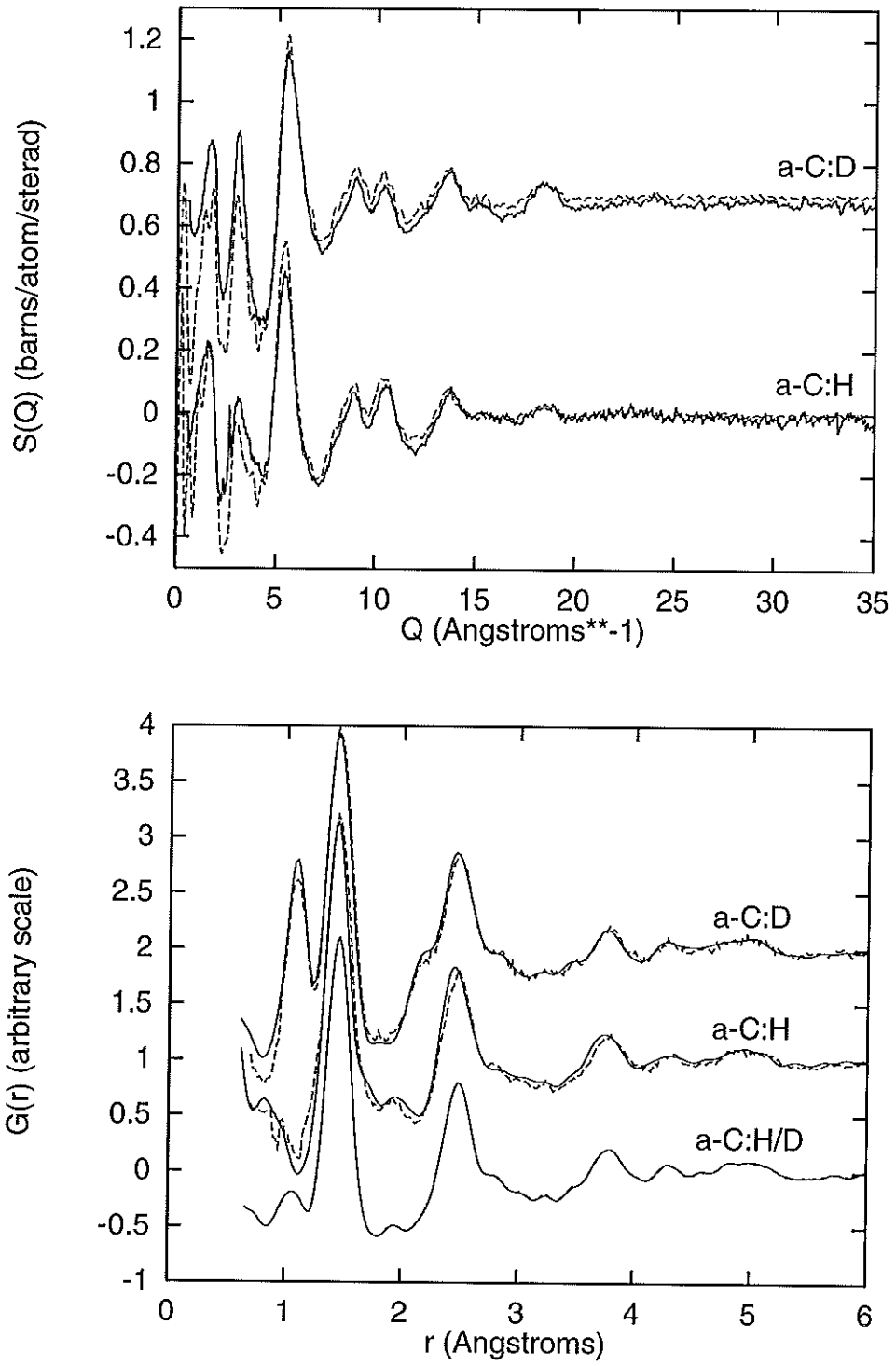

Figure 59: RMC fits (dashed line) to the neutron S(Q) (top) and G(r) (bottom) data (solid line).

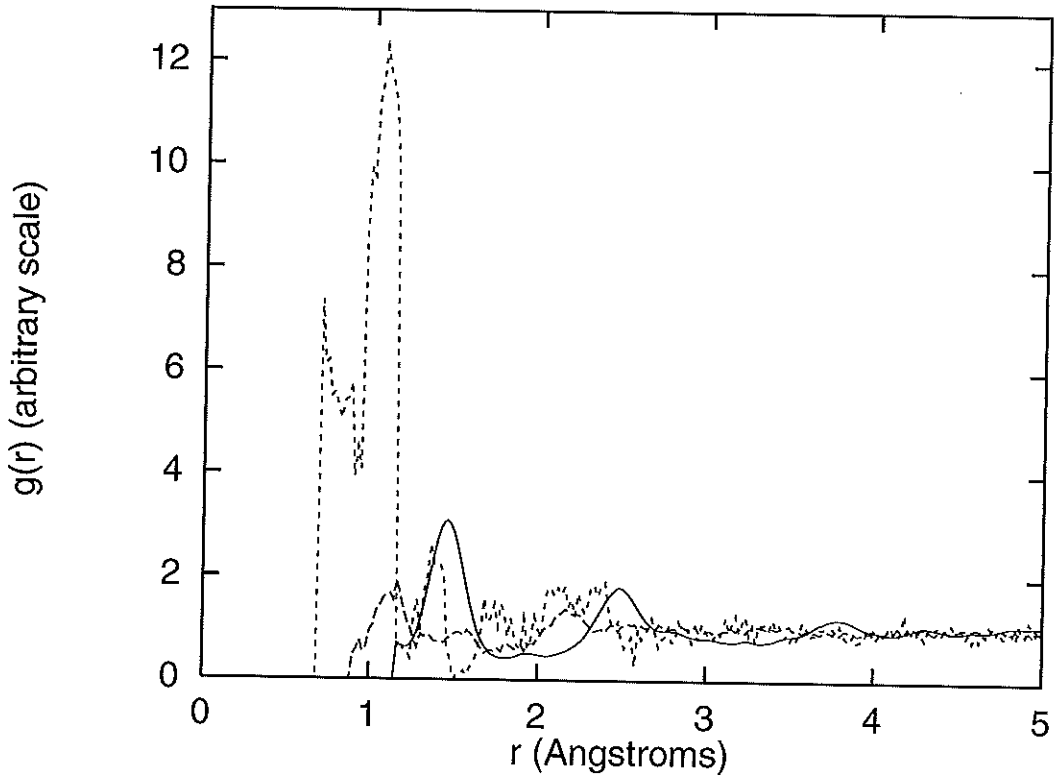

Figure 60: G(r) partials generated from the RMC fit: C-C (solid line), C-H (dashes) and H-H (dots).

Number of neighbours	Total number of atoms	Carbon-carbon	Carbon-hydrogen
0	91	126	3106
1	733	938	523
2	1516	1614	109
3	1070	887	12
4	312	166	0
5	28	19	0

Table 25: Coordination number distribution for carbon from the RMC model.

Number of neighbours	Total number of atoms	Hydrogen-carbon	Hydrogen-hydrogen
0	215	473	992
1	1035	777	258
2	0	0	0
3	0	0	0
4	0	0	0

Table 26: Coordination number distribution for hydrogen from the RMC model.

Number of atoms in the ring	Number of rings [163]	Number of rings [138]
1	0	0
2	0	0
3	0	0
4	107	103
5	39	38
6	35	30
7	17	19
8	14	14
9	7	10
10	7	5

Table 27: Ring distributions from the RMC model.

this box was gradually increased, fully relaxing the box each time, from its initial value of 0.1atomsÅ^{-3} to 0.13sÅ^{-3}. Note that the quality of the fits to the experimental data did not vary throughout this process.

The variation of coordination statistics with increasing density is summarised in Table 28. A 30% increase in number density produced an increase in the average co-

Density (atomsÅ^{-3})	Average coordination number for carbon	Average coordination number for hydrogen
0.100	1.99	0.87
0.112	2.15	0.80
0.120	2.25	0.86
0.123	2.28	0.85
0.127	2.35	0.86
0.130	2.40	0.86

Table 28: Coordination number statistics for carbon and hydrogen from the RMC models, with increasing density.

ordination number for carbon from 2.0 to 2.4, without causing any significant change in the RMC fit to the experimental data. This is a more reasonable value. The value determined by direct Gaussian fitting to the J(r) is higher (at ~1.5 for carbon-carbon), although this method does tend to give an overestimate of the coordination number due to the ambiguous "limits" of the peaks and Fourier transform broadening. The average coordination number for hydrogen was not affected by the increase in microscopic density, which is not surprising given the ease with which the small H atoms can be placed within any given carbon network.

Figure 61 shows the variation of the ring size distribution as the density is increased from 0.12 to 0.13 atomsÅ^{-3}. The relatively high number of four-membered rings results from the exclusion of three-membered rings, and is unlikely to be physical. However, the trends with increasing density are consistent with an increased amount

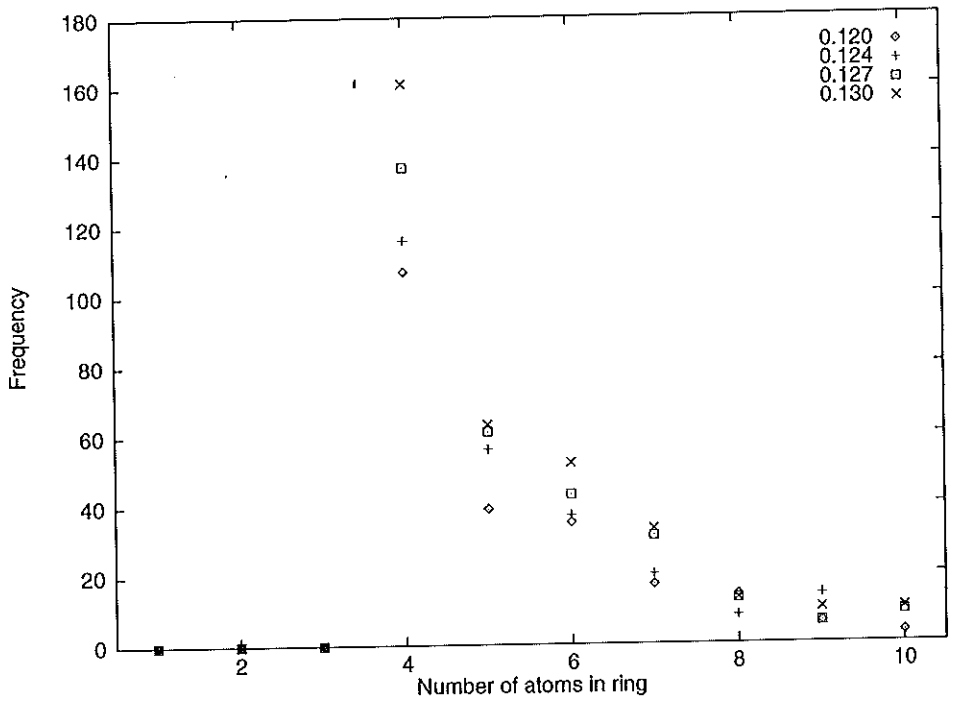

Figure 61: Ring distributions as a function of density from the RMC models.

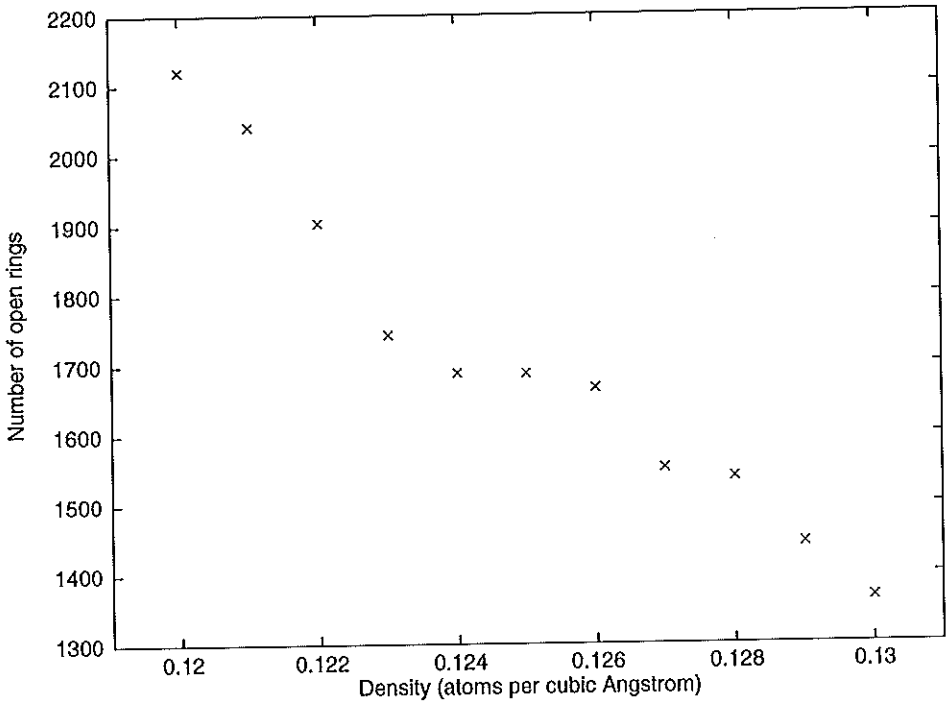

Figure 62: The number of open rings as a function of density from the RMC models.

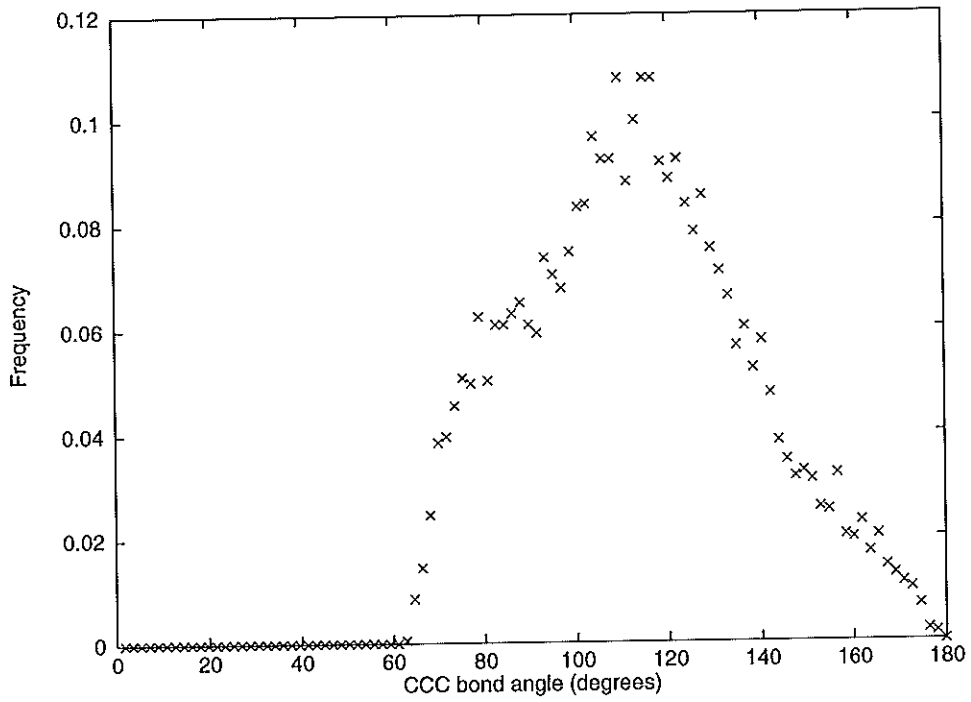

Figure 63: The number of open rings as a function of density from the RMC models.

of bonding within the network, which results in an increase in the number of rings of all sizes. Also, Figure 62 shows the number of open rings as a function of density, i.e. chains requiring more than ten atoms to return to the origin atom. The decrease in the number of open rings with increasing density also illustrates the expected increase in connectivity within the network.

Finally, Figure 63 shows the C-C-C bond angle distribution for the model configuration. This shows a broad distribution with a peak at around 120°. This agrees with the aromatic nature of the bonding, indicated by a carbon-carbon bond distance of ~1.42Å(see Table 12).

8.3 Improvements to the models for a-C:H

Although it has been possible to obtain physically viable models for a-C:H by the methods described above, it is clear that there is still room for improvement. However, refinement at this level requires another new approach to the problem. The basic improvement that needs to be made and is practicable, is to increase the average coordination numbers of C and H, which is known from simple bonding considerations to be too low in the models produced so far. (As was noted before, the problem with the ring distribution is more difficult to tackle as there is no information governing what it should be, and it may improve anyway as a result of increasing the average coordination numbers. Fitting to a bond angle distribution may, in theory, provide some of this information, however this would be extremely difficult, if not impossible, to implement for this system.) Something that has become apparent during this work and from discussions with others also working with RMC [167, 168], is that in order to obtain a "good" physical model of the system, the topology of the starting configuration used in the RMC modelling should resemble quite well that expected from any prior chemical or other knowledge of the system. For a-C:H this means that before trying to fit the experimental data, a configuration of atoms should be obtained in which no atoms are over-coordinated, no atoms are unbonded, there are no triplets, etc.; only after this can small atomic displacements be used finally to fit the experimental data, maintaining certain constraints to avoid undoing the initial model-building work.

Many attempts were made to produce initial models for a-C:H. The most successful method is to start with only C atoms and build up a network, eliminated over-coordinated atoms and forcing 0- and 1-fold coordinated atoms to move to sites with more near-neighbours. The effects of using diamond and graphite crystal starting

configurations were also investigated, but it was found that the number of moves required to satisfy closest approach distances when changing the number density to be equal to that of the sample, was enough to result in an amorphous network similar to those obtained when an initially random distribution of C atoms was used. Once the C network has been generated, the H atoms are added to the structure. Constraints are applied to ensure that all H atoms have 1 near-neighbour atom (either C or H), although the relative proportions of C-H and H-H "bonds" were not controlled. Usually this process involves the addition of more H atoms than are given by the sample composition, followed by the removal of any that can not find a site with a near-neighbour atom. Also, the total coordination number of C is constrained so that it does not exceed 4. Once this process has been completed, the configuration is ready to be used in the RMC algorithm.

Chapter 9

Conclusions

9.1 Summary

Using several experimental techniques (neutron diffraction, inelastic neutron scattering, combustion analysis and infrared spectroscopy) and RMC computer modelling, the structure of a-C:H has been investigated in considerable detail. With the additional information obtained from collaborative NMR [17] and MD [14] simulation studies, a revised model for the structure of a-C:H has been developed. The experimental and molecular dynamics results can be summarized as follows:-

1. The sp^2 C=C bond distance corresponds to olefinic rather than aromatic/graphitic bonding.

2. The single:double bond ratio is evaluated as 2.5:1 from the neutron scattering results (up to a maximum of 3.7:1, given the curve fitting errors), but is estimated as ~4:1 from the NMR results.

3. The numbers of CH and CH_2 groups are approximately equal: the number of CH_3 groups must be very small.

4. The high hardness of this material can be explained in terms of olefinic carbon.

5. The ratio for hydrogen atoms bound to sp^2 and sp^3 is 1:3, respectively.

6. A mean chain length of approximately five CH_2 units is found.

7. sp^2 and sp^3 CH groups are statistically distributed throughout the network.

8. A small gap in the electronic density of states can be produced without the need to introduce graphitic/aromatic clusters into the structure.

9. Models from molecular dynamics simulations are possible which fit the experimental data and show no aromatic/graphitic clusters.

The schematic 2-D model presented in Figure 64 illustrates how these conclusions may be incorporated into the structure of a-C:H.

It has been shown that current models for the structure of a-C:H, which rely on regions of clustered aromatic/graphitic sp^2 carbon, need revision. No definitive experimental evidence for aromatic clustering has been found in any published data, and certainly no results which could not be equally well explained in terms of olefinic sp^2 bonding. A new model is suggested which includes CH_2 chain segments, statistically distributed CH groups and regions of nonhydrogenated sp^3 and sp^2 carbon separating the regions of hydrogenated carbon. This model is consistent with all the experimental results.

The structural changes observed as the deposition energy is increased are found to be consistent with the subplantation model and are qualitatively independent of deposition method. However, although changes in the macroscopic sample properties with energy are significant, the atomic scale structural differences are seen to be small. With increasing impact energy at the growth site, the total sp^2 carbon bonding is seen

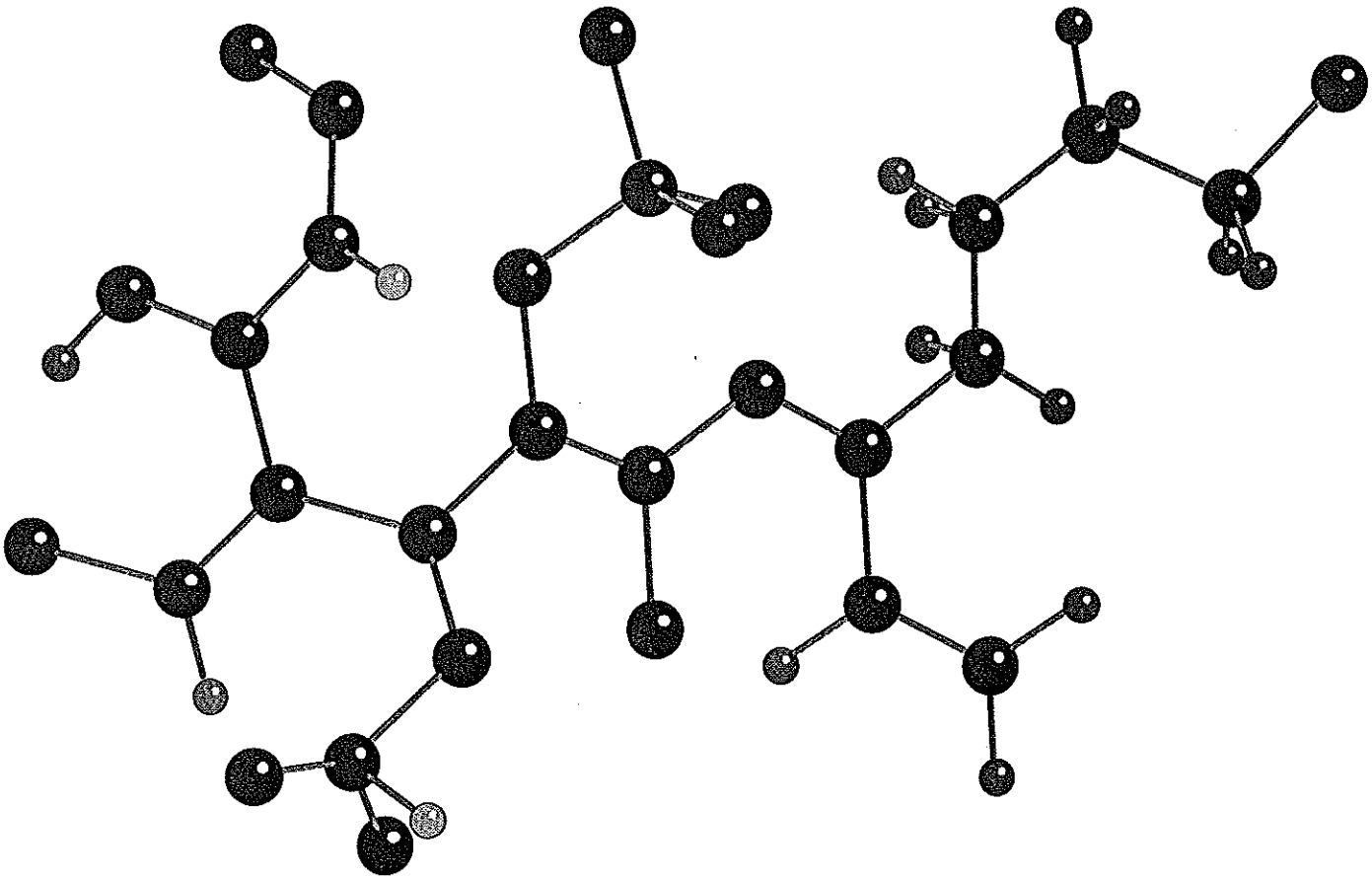

Figure 64: Schematic model of the microstructure of a-C:H based on the experimental data and showing heterogeneity in the structure on a nanometre scale.

to decrease, with some indication of a change in the sp^2 content from purely olefinic to that containing some aromatic/graphitic bonding, although the sp^3 carbon-carbon bonding environment remains dominant.

The effect of temperature on a-C:H also showed some interesting results. From the evidence, there appears to be a two-stage hydrogen evolution process; below 300°C where little hydrogen is lost, but significant structural rearrangement occurs, and above 300°C where hydrogen evolution begins to occur at a much higher rate such that, by 800°C over 75% of the total hydrogen within the sample has been lost. Structural transformations are seen to occur throughout the heating process, i.e. there is little evidence for a "transition temperature" at which dramatic changes occur. By 800°C the process of graphitization is well-advanced.

Finally, the RMC method has been developed for application to a-C:H. Although improvements still need to be made to the method and its application, and indeed, are currently under development, definite progress has been made towards a physically sensible model for a-C:H by the introduction of carefully defined constraints. It is clear from this work that although RMC *appears* to be a straightforward method of modelling experimental data, in practice, particularly for covalently bonded systems, there are potentially severe problems which need to be overcome in order to produce a (physically and chemically) satisfactory structural model. However, it is my opinion that the RMC method alone will not be able model more subtle features of the atomic structure of a-C:H, i.e. differences between sp^2 and sp^3 bonding and a more acceptable distribution of ring sizes. There is also the non-trivial problem in determining the correct density for use in the RMC algorithm. In this work it has been shown that changing the density by as much as 30% produces little effect on the quality of the fit to the experimental data, and this requires further, more detailed investigation.

9.2 Future work

There are several areas for future investigation to emerge from this work. One problem with all the neutron diffraction data is the quality of the low Q data. Although diffractometers are being improved to try and reduce the effects of inelastic scattering, it is likely to remain a problem for some time. However, this region of the data could be improved by doing the same experiments at reactor sources (this is not done as a "first choice" because of the smaller Q-range available) and then the two data sets could be merged.

In this work, the effect of deposition parameters was studied, although with a limited number of samples. It would be interesting, and useful, if a wide range of samples could be produced so that a proper investigation could be carried out.

There is also more work that could be done on the effects of temperature. Small angle X-ray scattering experiments are scheduled for this year, which should give useful information on the changes in pore structure with temperature, and the processes of structural rearrangement on heating could always be studied in more detail by the experimental techniques already used, especially up to 400°C. There are plans to complement this work with NMR experiments where the sample is heated *in situ*, which will give additional detailed information on the changes to the carbon network. Also, once the RMC method is sufficiently developed, it could be applied to the existing data and may provide additional insight into the transformations occurring.

As regards new work, some nitrogen-doped samples, a-C:N:H, have already been deposited using the fast-atom source, together with hydrogen diluted a-C:H. Neutron diffraction experiments for these are scheduled for June this year, and infrared spectroscopy and inelastic neutron scattering experiments are planned. There is also the possibility of small angle X-ray scattering experiments.

Chapter 10

Publications arising from this work

'A high-resolution neutron-diffraction study of the structure of amorphous hydrogenated carbon, a-C:H'
J.K.Walters, P.J.R.Honeybone, D.W.Huxley, R.J.Newport and W.S.Howells
Journal of Physics: Condensed Matter **5** *L387 (1993).*

'The structural properties of amorphous hydrogenated carbon: I. A high resolution neutron diffraction study'
J.K.Walters, P.J.R.Honeybone, D.W.Huxley, R.J.Newport and W.S.Howells
Physical Review B **50** *831 (1994).*

'The structural properties of amorphous hydrogenated carbon: II. An inelastic neutron scattering study'
P.J.R.Honeybone, R.J.Newport, J.K.Walters, W.S.Howells and J.Tomkinson
Physical Review B **50** *839 (1994).*

'The effect of temperature on the structure of amorphous hydrogenated carbon'
J.K.Walters, D.M.Fox, T.M.Burke, O.D.Weedon, R.J.Newport and W.S.Howells
Journal of Chemical Physics **101** *4288 (1994).*

'The atomic-scale structure of amorphous hydrogenated carbon'
J.K.Walters and R.J.Newport
Journal of Physics: Condensed Matter **7** *1755 (1995).*

'The effect of temperature on the structure of amorphous hydrogenated carbon (a spectroscopic study)'
J.K.Walters, J.S.Rigden, R.J.Newport, S.F.Parker and W.S.Howells
Physica Scripta, accepted

'Reverse Monte Carlo modelling of amorphous hydrogenated carbon'
J.K.Walters, J.S.Rigden and R.J.Newport
Physica Scripta, accepted

'A neutron and X-ray diffraction study of deposition conditions on the structure of a-C:H'
J.K.Walters, C.D.Algar, T.M.Burke, J.S.Rigden, R.J.Newport, G.Bushnell-Wye, W.S.Howells S.Sattel, M.Weiler and H.Ehrhardt
Submitted for publication.

'A spectroscopic study of the structure of amorphous hydrogenated carbon'
J.K.Walters, R.J.Newport, W.S.Howells and S.F.Parker
Submitted for publication.

Appendix A

Determination of energy levels

A.1 The vibrating diatomic molecule

A.1.1 The harmonic oscillator

Consider the diatomic molecule as two masses, m and M connected by a bond, with an equilibrium separation r_{eq}. In the simplest case - the simple harmonic oscillator - the extension and compression of the bond may be likened to the behaviour of a spring and it can be assumed that the bond obeys Hooke's law, i.e. the energy is given by

$$E = \frac{1}{2}k(r - r_{eq})^2, \tag{160}$$

where k is the force constant and r is the interatomic distance. The diatomic molecule will have associated with it a certain vibrational frequency dependent on the mass of the system and the value of the force constant. This can be evaluated classically as follows. Consider:

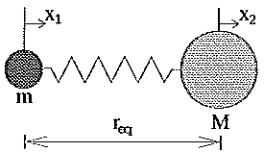

$$\text{the potential energy,} \qquad V = \frac{1}{2}k(\text{extension})^2$$
$$= \frac{1}{2}(x_2 - x_1)^2$$

So, for the whole system,

$$\begin{aligned} L &= \text{kinetic energy - potential energy} \\ &= \frac{1}{2}m\dot{x}_1^2 + \frac{1}{2}m\dot{x}_2^2 - \frac{1}{2}k(x_2 - x_1)^2. \end{aligned}$$

Applying Lagrange's equation:

$$\frac{d}{dt}\left(\frac{\partial L}{\partial \dot{x}}\right) - \frac{\partial L}{\partial x} = 0$$

to x_1 and x_2 to give,

$$m\ddot{x}_1 - k(x_2 - x_1) = 0 \tag{161}$$

$$M\ddot{x}_2 + k(x_2 - x_1) = 0. \tag{162}$$

For normal modes (i.e. for every particle moving at the same frequency):-

$$\begin{aligned} x_1(t) &= x_1(0)e^{i\omega t} \\ x_2(t) &= x_2(0)e^{i\omega t} \end{aligned}$$

Substituting into equations 161 and 162, we obtain the solution,

$$\begin{aligned} \omega^2 &= k\frac{M+m}{m} \\ \text{i.e. } \omega^2 &= \frac{k}{\mu} \text{ where } \mu = \frac{Mm}{M+m} \text{ is the reduced mass} \\ \omega &= \sqrt{\frac{k}{\mu}}, \\ \text{so, } f &= \frac{\omega}{2\pi} = \frac{1}{2\pi}\sqrt{\frac{k}{\mu}}. \end{aligned} \tag{163}$$

The vibrational energies are quantised and may be calculated from Schrödinger's equation. For the case of the simple harmonic oscillator we start from the one-dimensional Schrödinger equation:

$$\frac{-\hbar^2}{2\mu}\frac{d^2\psi}{dx^2} + V(x)\psi = E\psi. \tag{164}$$

For the simple harmonic oscillator, $V(x) = \frac{1}{2}kx^2$, but $f = \frac{1}{2\pi}\sqrt{\frac{k}{\mu}}$, so we can write

$$V(x) = 2\pi^2\mu f^2 x^2. \tag{165}$$

Then equation 164 becomes,

$$\begin{aligned} \frac{-\hbar^2}{2\mu}\frac{d^2\psi}{dx^2} + 2\pi^2\mu f^2 x^2\psi &= E\psi \\ \frac{d^2\psi}{dx^2} + \left[\frac{2\mu E}{\hbar^2} - \left(\frac{2\pi\mu f}{\hbar}\right)^2 x^2\right]\psi &= 0. \end{aligned} \tag{166}$$

Make the substitutions

$$\alpha \equiv \frac{2\pi\mu f}{\hbar}$$

$$\text{and} \qquad \beta \equiv \frac{2\mu E}{\hbar^2};$$

and equation 166 can be written,

$$\frac{d^2\psi}{dx^2} + \left[\beta - \alpha^2 x^2\right]\psi = 0. \tag{167}$$

Introduce a new variable, $\xi \equiv \sqrt{\alpha}x$, so that

$$\frac{d\psi}{dx} = \frac{d\psi}{d\xi}.\frac{d\xi}{d\psi} = \sqrt{\alpha}\frac{d\psi}{d\xi}$$

$$\text{and} \qquad \frac{d^2\psi}{dx^2} = \frac{d}{dx}\left(\frac{d\psi}{d\xi}\sqrt{\alpha}\right) = \alpha\frac{d^2\psi}{d\xi^2}.$$

So equation 167 becomes

$$\alpha\frac{d^2\psi}{d\xi^2} + \left[\beta - \alpha^2\frac{\xi^2}{\alpha}\right]\psi = 0$$

$$\text{i.e.} \quad \frac{d^2\psi}{d\xi^2} + \left[\frac{\beta}{\alpha} - \xi^2\right]\psi = 0. \tag{168}$$

Solutions $\psi(\xi)$ must be found which are continuous and finite for all ξ from $-\infty$ to $+\infty$. These are found to be of the form,

$$\psi(\xi) = e^{-\xi^2/2}H(\xi), \tag{169}$$

where $H(\xi)$ are functions which must be slowly varying compared to $e^{\xi^2/2}$ as $|\xi| \to \infty$. Using equation 169 to evaluate $\frac{d\psi}{d\xi}$ and $\frac{d^2\psi}{d\xi^2}$ and sustituting back into the Schrödinger equation 168, gives

$$\frac{d^2H}{d\xi^2} - 2\xi\frac{dH}{d\xi} + \left(\frac{\beta}{\alpha} - 1\right)H = 0. \tag{170}$$

To solve this equation (the Hermite differential equation) we assume a solution in the form of a power series:

$$H(\xi) = \sum_{n=0}^{\infty} a_n\xi^n = a_0 + a_1\xi + a_2\xi^2 + a_3\xi^3 + \ldots$$

then differentiate and substitute into equation 170 to get

$$1.2a_2 + 2.3a_3\xi + 3.4a_4\xi^2 + 4.5a_5\xi^3 + \ldots$$

$$-2.1a_1\xi - 2.2a_a\xi^2 - 2.3a_3\xi^3 - \ldots$$

$$+\left(\frac{\beta}{\alpha} - 1\right)\left[a_0 + a_1\xi + a_2\xi^2 + a_3\xi^3 + \ldots\right] = 0. \tag{171}$$

Since equation 171 must be true for all values of ξ, the co-efficients of each power of ξ must vanish individually, therefore;

$$\begin{aligned}
&\text{for } \xi^0: && 2a_2 + (\beta/\alpha - 1)\, a_0 = 0 \\
&\text{for } \xi^1: && 6a_3 - 2a_1 + (\beta/\alpha - 1)\, a_1 = 0 \\
&\text{for } \xi^2: && 12a_4 - 4a_2 + (\beta/\alpha - 1)\, a_2 = 0 \\
&\text{for } \xi^3: && 20a_5 - 6a_3 + (\beta/\alpha - 1)\, a_3 = 0
\end{aligned}$$

and in general

$$\begin{aligned}
&\text{for } \xi^n: && (n+1)(n+2)a_{n+2} + (\beta/\alpha - 1 - 2n)\, a_n = 0 \\
&\text{i.e.} && a_{n+2} = -\frac{(\beta/\alpha - 1 - 2n)}{(n+1)(n+2)} a_n \qquad \text{-recursion relation.} \qquad (172)
\end{aligned}$$

This series will terminate if

$$\begin{aligned}
&&& \beta/\alpha - 1 = 2n \\
&\text{i.e.} && \beta/\alpha = 2n + 1 \qquad (173)
\end{aligned}$$

where $n = 0, 1, 2, 3, 4, \ldots$ is an integer. From the substitutions made in equation 167,

$$\begin{aligned}
&&& \frac{\beta}{\alpha} = \frac{2\mu E\hbar}{2\pi\mu f\hbar} = \frac{E}{\pi\hbar f} = 2n + 1 \\
&\text{i.e.} && E = \left(n + \frac{1}{2}\right) h\omega \qquad (174)
\end{aligned}$$

where n is called the vibrational quantum number. Therefore equation 174 defines the energy levels for the simple harmonic oscillator model of a vibrating diatomic molecule.

A.1.2 The anharmonic oscillator

Since real molecules do not exactly obey simple harmonic motion, we introduce an anharmonic form of potential derived by Morse [122]:

$$V(x) = A\left[e^{-2\alpha x} - 2e^{-\alpha x}\right] \tag{175}$$

where α is constant for a particular molecule and A is the dissociation energy. Inserting this into the one-dimensional Schrödinger equation 164, we obtain

$$\frac{d^2\psi}{dx^2} + \left(\frac{2\mu}{\hbar^2}\right)\left[E - ae^{-2\alpha x} - 2Ae^{-\alpha x}\right]\psi = 0. \tag{176}$$

Introduce the new variable ξ, where

$$\xi = \frac{2\sqrt{(2\mu A)}}{\alpha\hbar}e^{-\alpha x}$$

and equation 176 becomes:

$$\alpha^2\xi^2\frac{d^2\psi}{d\xi^2} + \alpha^2\xi\frac{d\psi}{d\xi} + \left(\frac{2\mu}{\hbar^2}\right)\left[E - \frac{A\xi^2\alpha^2\hbar^2}{4(2\mu A)} + \frac{2A\xi\alpha\hbar}{2\sqrt{(2\mu A)}}\right]\psi = 0$$

$$\frac{d^2\psi}{d\xi^2} + \frac{1}{\xi}\frac{d\psi}{d\xi} + \left[\frac{2\mu E}{\hbar^2\alpha^2\xi^2} - \frac{1}{4} + \frac{\sqrt{(2\mu A)}}{\hbar\alpha\xi}\right]\psi = 0. \tag{177}$$

Now make the following substitutions:-

$$s = \frac{\sqrt{(-2\mu E)}}{\alpha\hbar} \text{ and } k = \frac{\sqrt{(2\mu A)}}{\alpha\hbar} - \left(s + \frac{1}{2}\right) \tag{178}$$

to get

$$\frac{d^2\psi}{d\xi^2} + \frac{1}{\xi}\frac{d\psi}{d\xi} + \left[-\frac{1}{4} + \frac{k + s + \frac{1}{2}}{\xi} - \frac{s^2}{\xi^2}\right]\psi = 0. \tag{179}$$

Choose a solution

$$\psi(\xi) = e^{-\xi/2}\xi^s W(\xi) \tag{180}$$

and equation 179 is then given by

$$\xi\frac{d^2W}{d\xi^2} + (2s+1-\xi)\frac{dW}{d\xi} - kW = 0. \tag{181}$$

As before, assume a series solution for $W(\xi)$, so

$$W(\xi) = \sum_{n=0}^{\infty} a_n\xi^n = a_0 + a_1\xi + a_2\xi^2 + a_3\xi^3 + \ldots.$$

Substituting into equation 181;

$$\begin{aligned}
&1.2a_2\xi + 2.3a_3\xi^2 + 3.4a_4\xi^3 + 4.5a_5\xi^4 + \ldots \\
&-1a_1\xi + 2a_2\xi^2 - 3a_3\xi^3 - 4a_4\xi^4 - \ldots \\
&+(2s+1)\left(1a_1 + 2a_2\xi + 3a_3\xi^2 + 4a_4\xi^3 + 5a_5\xi^4 + \ldots\right) \\
&+k\left(a_0 + a_1\xi + a_2\xi^2 + a_3\xi^3 + a_4\xi^4 + \ldots\right) = 0.
\end{aligned} \tag{182}$$

Equating the co-efficients of powers of ξ to zero, gives

$$\begin{aligned}
&\text{for } \xi^0: && (2s+1)a_1 + ka_0 = 0 \\
&\text{for } \xi^1: && [1.2 + 2(2s+1)]a_2 + (k-1)a_1 = 0 \\
&\text{for } \xi^2: && [2.3 + 3(2s+1)]a_3 + (k-2)a_2 = 0
\end{aligned}$$

and in general,

$$\begin{aligned}
&\text{for } \xi^n: && [n(n+1) + (n+1)(2s+1)]a_{n+1} + (k-n)a_n = 0 \\
&\text{i.e.} && a_{n+1} = -\frac{(k-n)}{(n+1)(n+2s+1)}a_n.
\end{aligned} \tag{183}$$

Equation 183 is a recursion relation and can be used to determine all the co-efficients a_n, where n is an integer. For the series to terminate the condition is that $n = k$ i.e.

k must be an integer. Substituting n for k in equations 178, we obtain the following equation:

$$E = A\left[1 - \frac{\alpha\hbar}{\sqrt{(2\mu A)}}\left(n + \frac{1}{2}\right)\right]^2, \tag{184}$$

which defines the energy levels for a vibrating diatomic molecule with an anharmonic potential.

A.2 The diatomic vibrating rotator

A.2.1 The harmonic oscillator

Consider a molecule which is vibrating and rotating at the same time in the Born-Oppenheimer approximation, i.e. the motions are assumed to be executed independently such that the total energy is simply the sum of the vibrational and rotational energies:

$$E_{tot} = E_{rot} + E_{vib}. \tag{185}$$

For a rigid rotator it can be shown that

$$E_{rot} = \frac{h^2 l(l+1)}{8\pi^2 I_e}, \tag{186}$$

where $l = 0, 1, 2, 3, \ldots$ is the rotational quantum number and I_e is the moment of inertia about the centre of the molecule at the equilibrium separation.

However, for the non-rigid rotator, we require the radial Schrödinger equation which can be found using the method of separation of variables. Consider the three-dimensional Schrödinger equation:

$$\begin{aligned}\left[\frac{-\hbar^2}{2\mu}\nabla^2 + V(r)\right]\Psi(r,\theta,\phi) &= E.\Psi(r,\theta,\phi)\\ \left[\nabla^2 + \frac{8\pi^2\mu}{h^2}(E - V(r))\right]\Psi(r,\theta,\phi) &= 0,\end{aligned} \tag{187}$$

which can be expressed in polar co-ordinates as,

$$\frac{1}{r^2}\frac{\partial}{\partial r}\left(r^2\frac{\partial\Psi}{\partial r}\right)+\frac{1}{r^2\sin\theta}\frac{\partial}{\partial\theta}\left(\sin\theta\frac{\partial\Psi}{\partial\theta}\right)+\frac{1}{r^2\sin^2\theta}\frac{\partial^2\Psi}{\partial\phi^2}+\frac{8\pi^2\mu}{h^2}[E-V(r)]\Psi=0. \quad (188)$$

Look for a solution of the form: $\Psi = R(r)\Theta(\theta),\Phi(\phi)$. Substituting for Ψ into equation 188 gives

$$\frac{1}{R}\frac{\partial}{\partial r}\left(r^2\frac{\partial R}{\partial r}\right)+\frac{8\pi^2\mu r^2}{h^2}[E-V(r)]+\frac{1}{\Theta\sin\theta}\frac{\partial}{\partial\theta}\left(\sin\theta\frac{\partial\Theta}{\partial\theta}\right)+\frac{1}{\Phi\sin^2\theta}\frac{\partial^2\Phi}{\partial\phi^2}=0, \quad (189)$$

which is of the form

$$F(r)+G(\theta,\phi)=0.$$

Since (r) and (θ,ϕ) are independent, the only possible solution is

$$F(r)=constant=l(l+1)$$

where l can take any value,

$$\Rightarrow G(\theta,\phi)=-l(l+1).$$

Substituting into equation 189, we obtain

$$\frac{1}{R}\frac{\partial}{\partial r}\left(r^2\frac{\partial R}{\partial r}\right)+\frac{8\pi^2\mu r^2}{h^2}[E-V(r)]-l(l+1)=0 \quad (190)$$

which is the radial Schrödinger equation.

Make a substitution $R(r)=\frac{1}{r}S(r)$, the equation 190 becomes

$$\frac{d^2S}{dr^2}+\left[\frac{8\pi^2\mu}{h^2}[E-V(r)]-\frac{l(l+1)}{r^2}\right]S=0. \quad (191)$$

For a simple harmonic oscillator the potential is described by

$$V(r)=\frac{1}{2}k\left(r-r_{eq}\right)^2, \quad (192)$$

where k is the force constant and r_{eq} is the equilibrium interatomic separation. Substituting for $V(r)$ in equation 191 and introducing a new variable, $\rho = r - r_{eq}$, gives

$$\frac{d^2S}{dr^2} + \frac{8\pi^2\mu}{h^2}\left[E - \frac{1}{2}k\rho^2 - \frac{h^2}{8\pi^2\mu}.\frac{l(l+1)}{(\rho + r_{eq})^2}\right] S = 0. \tag{193}$$

For small values of $(r - r_{eq})$, $V(r)$ is a fair representation of reality, so $(\rho - r_{eq})^{-2}$ can be expanded in terms of a series, neglecting all powers above the second, to give

$$(\rho - r_{eq})^{-2} = \frac{1}{r_{eq}^2}\left(1 + \frac{\rho}{r_{eq}}\right)^2 = \frac{1}{r_{eq}^2}\left(1 - \frac{2\rho}{r_{eq}} + \frac{3\rho^2}{r_{eq}^2} - \ldots\right). \tag{194}$$

Substituting this result into equation 194, gives

$$\frac{d^2S}{dr^2} + \frac{8\pi^2\mu}{h^2}\left(E - \frac{1}{2}k\rho^2 - \frac{h^2}{8\pi^2\mu r_{eq}^2}\left[l(l+1) - \frac{2\rho l(l+1)}{r_{eq}} + \frac{3\rho^2 l(l+1)}{r_{eq}^2}\right]\right) S = 0. \tag{195}$$

If we then make the following substitutions:

$$\sigma = \frac{h^2}{8\pi^2\mu r_{eq}^2} = \frac{h^2}{8\pi^2 I_e^2} \tag{196}$$

$$\text{and} \qquad \xi = \rho - a,$$

$$\text{where} \qquad a = \frac{l(l+1)\sigma r_{eq}}{3l(l+1)\sigma + \frac{1}{2}kr_{eq}^2}$$

so that equation 195 becomes,

$$\frac{d^2S}{d\xi^2} + \frac{8\pi^2\mu}{h^2}\left(E - \frac{1}{2}k(\xi + a)^2 + \frac{l(l+1)}{r_{eq}^2}\left[2\sigma r_{eq}(\xi + a) - \sigma r_{eq}^2 - 3\sigma(\xi + a)^2\right]\right) S = 0$$

$$\frac{d^2S}{d\xi^2} + \frac{8\pi^2\mu}{h^2}\left(\left[E - l(l+1)\sigma + \frac{[l(l+1)\sigma]^2}{3l(l+1) + \frac{1}{2}kr_{eq}^2}\right] - \left[\frac{k}{2} + \frac{3l(l+1)\sigma}{r_{eq}^2}\right]\xi^2\right) S = 0, \tag{197}$$

which can be written in the form,

$$\frac{d^2S}{d\xi^2} + \left[\beta - \alpha^2\xi^2\right] S = 0, \tag{198}$$

where,

$$\beta = \frac{8\pi^2\mu}{h^2}\left(E - l(l+1)\sigma + \frac{[l(l+1)\sigma]^2}{3l(l+1) + \frac{1}{2}kr_{eq}^2}\right) \tag{199}$$

$$\text{and} \qquad \alpha^2 = \frac{8\pi^2\mu}{h^2}\left(\frac{k}{2} + \frac{3l(l+1)\sigma}{r_{eq}^2}\right). \tag{200}$$

Equation 198 is of the same form as equation 167 which led to the condition

$$\frac{\beta}{\alpha} = (2n+1).$$

So, applying this condition, and substituting for α and β using equations 199 and 200, gives:

$$\frac{8\pi^2\mu}{h^2}\left(E - l(l+1)\sigma + \frac{[l(l+1)\sigma]^2}{3l(l+1)+\frac{1}{2}kr_{eq}^2}\right) = (2n+1)\left(\frac{8\pi^2\mu}{h^2}\left[\frac{k}{2} + \frac{3l(l+1)\sigma}{r_{eq}^2}\right]\right)^{\frac{1}{2}},$$

which leads to

$$E = l(l+1)\sigma - \frac{[l(l+1)\sigma]^2}{3l(l+1)+\frac{1}{2}kr_{eq}^2} + \left(n+\frac{1}{2}\right)h\nu'_{eq} \qquad (201)$$

where $$\nu'_{eq} = \frac{1}{2\pi}\left[\frac{kr_{eq}^2 + 6l(l+1)\sigma}{\mu r_{eq}^2}\right]^{\frac{1}{2}}.$$

For real molecules this expression for the enrgy can be simplified considerably without significant loss of accuracy by the use of expansions for $[3l(l+1)+\frac{1}{2}kr_{eq}^2]^{-1}$ and ν'_{eq}, to give

$$E = \left(n+\frac{1}{2}\right)h\nu_{eq} + l(l+1)\sigma - \frac{[l(l+1)\sigma]^2}{\frac{1}{2}kr_{eq}^2} \qquad (202)$$

in which only the first terms of the expansions are included, and where ν_{eq} is given by

$$\nu_{eq} = \frac{1}{2\pi}\sqrt{\frac{k}{\mu}},$$

so that

$$\nu_{eq}^2 = \frac{1}{4\pi^2}\frac{k}{\mu} \Rightarrow k = 4\pi^2\mu\nu_{eq}^2. \qquad (203)$$

Using equations 203 and 196 for k and σ respectively, equation 202 can finally be written

$$E = \left(n+\frac{1}{2}\right)h\nu_{eq} + \frac{l(l+1)h^2}{8\pi^2 I_e} - \frac{l^2(l+1)^2h^4}{128\pi^6\nu_{eq}^2 I_e^3}, \qquad (204)$$

where each term involves either n or l, but not both, i.e. there are no "cross-terms".

A.2.2 The anharmonic oscillator

In the case on an anharmonic potential the situation is more complex. So, consider a vibrating rotator where the potential $V(r)$ is given by the Morse function,

$$V(r) = A\left[1 - e^{-\alpha(r-r_{eq})}\right]^2. \tag{205}$$

Starting again with the radial part of the Schrödinger equation, we have,

$$\frac{d^2S}{dr^2} + \left(\frac{8\pi^2\mu}{h^2}\left[E - A - Ae^{-2\alpha(r-r_{eq})} + 2Ae^{-\alpha(r-r_{eq})}\right] - \frac{l(l+1)}{r^2}\right)S = 0. \tag{206}$$

Now, make the substitution $y = e^{-\alpha(r-r_{eq})}$; equation 206 becomes

$$\frac{d^2S}{dy^2} + \frac{1}{y}\frac{dS}{dy} + \left(\frac{8\pi^2\mu}{h^2\alpha^2}\left[\frac{E-A}{y^2} - A + \frac{2A}{y} - \frac{l(l+1)}{\alpha^2 r^2 y^2}\right]\right)S = 0. \tag{207}$$

Substituting

$$D = \frac{l(l+1)h^2}{8\pi^2\mu r_{eq}^2}$$

into equation 207 to obtain

$$\frac{d^2S}{dy^2} + \frac{1}{y}\frac{dS}{dy} + \left(\frac{8\pi^2\mu}{h^2\alpha^2}\left[\frac{E-A}{y^2} - A + \frac{2A}{y} - \frac{D}{y^2}\cdot\frac{r_{eq}^2}{r^2}\right]\right)S = 0. \tag{208}$$

But,

$$y = e^{-\alpha(r-r_{eq})},$$

so
$$lny = -\alpha(r - r_{eq})$$
$$r - r_{eq} = -\frac{lny}{\alpha}$$
$$\frac{r}{r_{eq}} = 1 - \frac{lny}{\alpha r_{eq}}$$

and
$$\frac{r^2}{r_{eq}^2} = \left[1 - \frac{lny}{\alpha r_{eq}}\right]^{-2}.$$

If lny is expanded using a Taylor series about $(y-1)$ and then a binomial expansion is used, taking the first three terms only and substituting into equation 208, we get

$$\frac{d^2S}{dy^2}+\frac{1}{y}\frac{dS}{dy}+\frac{8\pi^2\mu}{h^2\alpha^2}\times \left(\frac{E-A}{y^2}-A+\frac{2A}{y}-\frac{D}{y^2}\left[1+\frac{2(y-1)}{\alpha r_{eq}}+\left(\frac{3}{\alpha^2 r_{eq}^2}-\frac{1}{\alpha r_{eq}}\right)(y-1)^2\right]\right)S = 0. \tag{209}$$

Equation 209 can be rearranged to give

$$\frac{d^2S}{dy^2}+\frac{1}{y}\frac{dS}{dy}-\left[\frac{b^2}{4y^2}+\frac{8\pi^2\mu}{h^2\alpha^2}.\frac{(2A-c_1)}{y}-d^2\right]S=0, \tag{210}$$

where
$$b^2=-\frac{32\pi^2\mu}{\alpha^2h^2}(E-A-c_0)$$
$$d^2=\frac{8\pi^2\mu}{\alpha^2h^2}(A+c_2)$$
$$c_0=D\left[1-\frac{3}{\alpha r_{eq}}+\frac{3}{\alpha^2r_{eq}^2}\right]$$
$$c_1=D\left[\frac{4}{\alpha r_{eq}}-\frac{6}{\alpha^2r_{eq}^2}\right]$$
and
$$c_2=D\left[-\frac{1}{\alpha r_{eq}}+\frac{3}{\alpha^2r_{eq}^2}\right].$$

The form of the solution is:

$$S(y)=e^{-z/2}z^{b/2}F(\xi)$$

which when substituted into equation 210 gives,

$$\frac{d^2F}{d\xi^2}+\left(\frac{b+1}{\xi}-1\right)\frac{dF}{d\xi}+\frac{\nu}{\xi}F=0, \tag{211}$$

where
$$\nu=\frac{4\pi^2\mu}{h^2\alpha^2d}(2A-c_1)-\frac{1}{2}(b+1). \tag{212}$$

Equation 211 is closely related to the radial equation of the hydrogen atom and may be solved in the same way by assuming a series solution, i.e.

$$F(\xi) = \sum_{n=0}^{\infty} a_n \xi^n = a_0 + a_1\xi + a_2\xi^2 + a_3\xi^3 + \ldots.$$

Substitution into equation 211 yields,

$$\begin{aligned}
&2.1a_2 + 3.2a_3\xi + 4.3a_4\xi^3 + 5.4a_5\xi^4 + \ldots \\
&\left(\frac{b+1}{\xi}\right)(1a_1 + 2a_2\xi + 3a_3\xi^2 + 4a_a\xi^3 + \ldots) \\
&-1a_1 - 2a_2\xi - 3a_3\xi^2 - 3a_4\xi^3 - \ldots \\
&+\frac{\nu}{\xi}(a_0 + a_1\xi + a_2\xi^2 + a_3\xi^3 + \ldots) = 0
\end{aligned}$$

Equating the co-efficients of powers of ξ:

$$\begin{aligned}
\text{for } \xi^0\text{:} \quad & a_2[(2.1) + 2(b+1)] + a_1[\nu - 1] = 0 \\
\text{for } \xi^1\text{:} \quad & a_3[(3.2) + 3(b+1)] + a_2[\nu - 2] = 0 \\
\text{for } \xi^2\text{:} \quad & a_4[(4.3) + 4(b+1)] + a_3[\nu - 3] = 0
\end{aligned}$$

and in general,

$$\begin{aligned}
\text{for } \xi^n\text{:} \qquad & a_{n+1}[n(n+1) + (n+1)(b+1)] + a_n[\nu - n] = 0 \\
& a_{n+1} = \frac{-[\nu - n]}{(n+1)[n + (b+1)]} a_n.
\end{aligned}$$

For the series to terminate the condition is that $\nu = n$, i.e. ν is an integer.

Recall from equation 212,

$$n = \nu = \frac{4\pi^2\mu}{h^2\alpha^2 d}(2A - c_1) - \frac{1}{2}(b+1)$$

but

$$d^2 = \frac{8\pi^2\mu}{\alpha^2 h^2}(A + c_2),$$

therefore,

$$n = \frac{(2A - c_1)d}{2(A + c_2)} - \frac{b}{2} - \frac{1}{2}$$

$$\text{i.e.} \qquad b = \frac{(2A - c_1)d}{(A + c_2)} - (2n + 1),$$

$$\text{and} \qquad b^2 = \frac{(2A - c_1)^2 d^2}{(A + c_2)^2} - \frac{2d(2A - c_1)(2n + 1)}{(A + c_2)} + (2n + 1)^2. \qquad (213)$$

Now, substituting for d in equation 213 gives,

$$b^2 = \frac{32\pi^2\mu}{\alpha^2 h^2} \cdot \frac{(A - \frac{1}{2}c_1)^2}{(A + c_2)} - \frac{2\sqrt{2}\pi\sqrt{\mu}}{\alpha h} \cdot \frac{4(A - \frac{1}{2}c_1)2(n + \frac{1}{2})}{(A + c_2)^{1/2}} + 4(n + \frac{1}{2})^2.$$

But also,

$$b^2 = -\frac{32\pi^2\mu}{\alpha^2 h^2}(E - A - c_0),$$

so finally, we have

$$E = A + c_0 - \frac{(A - \frac{1}{2}c_1)^2}{(A + c_2)} + \frac{\alpha h}{\pi\sqrt{2\mu}} \cdot \frac{(A - \frac{1}{2}c_1)}{(A + c_2)^{1/2}}(n + \frac{1}{2}) - \frac{\alpha^2 h^2}{8\pi^2\mu}(n + \frac{1}{2})^2. \qquad (214)$$

By expanding in terms of powers of c_1/D and c_2/D we can write equation 214 in the form

$$\frac{E}{hc} = \omega_e(n + \frac{1}{2}) - x_e\omega_e(n + \frac{1}{2})^2 + l(l+1)B_e + D_e l^2(l+1)^2 - a_e(n + \frac{1}{2})l(l+1), \quad (215)$$

where c is the velocity of light,

$$\omega_e = \frac{\alpha}{2\pi c}\sqrt{\frac{2D}{\mu}}$$

$$x_e = \frac{h\omega_e c}{4D}$$

$$B_e = \frac{h}{8\pi^2 I_e c}$$

$$D_e = -\frac{h^3}{128\pi^6\mu^3\omega_e^2 c^3 r_{eq}^6}$$

$$\text{and} \qquad a_e = \frac{3h^2\omega_e}{16\pi^2\mu r_{eq}^2 D}\left(\frac{1}{\alpha r_{eq}} - \frac{1}{\alpha^2 r_{eq}^2}\right).$$

Notice that for the anharmonic potential "cross-terms" containing both n and l appear.

Bibliography

[1] J.C. Angus, P. Koidl, and S. Domitz. In J. Mort and F. Jansen, editors, *Plasma deposited thin films*, chapter 4, page 89. CRC Press, Boca Raton, 1986.

[2] C.N.Banwell. *Fundamentals of molecular spectroscopy.* McGraw-Hill Book Company, London, 3rd edition, 1983.

[3] W.S. Howells A.K. Soper and A.C. Hannon. *ATLAS - Analysis of time-of-flight diffraction data from liquid and amorphous samples.* Rutherford Appleton Laboratory, May 1989. Report RAL-89-046.

[4] S.R. Elliott. *Advances In Physics*, **38**:1, 1989.

[5] J. Robertson. *Advances In Physics*, **35**:317, 1986.

[6] A.H. Lettington. In J. C. Angus, R. E. Clausing, L. L. Horton, and P. Koidl, editors, *Diamond and Diamondlike Films and Coatings*, page 481. Plenum, 1991.

[7] S.Aisenberg and F.M.Kimock. *Materials Science Forum*, **52** and **53**:1, 1989.

[8] J. Robertson. *Progress In Solid State Chemistry*, **21**:199, 1991.

[9] M.A. Petrich. *Materials Science Forum*, **52**:377, 1989.

[10] H. Ehrhardt, R. Kleber, A. Krüger, W. Dworschak, K. Jung, T. Mühling, F. Engelke, and M. Metz. *Diamond and Related Materials*, **1**:316, 1992.

[11] J. Robertson. *Diamond and Related Materials*, **1**:397, 1992.

[12] J. Robertson. *Physical Review Letters*, **68**:220, 1992.

[13] T.Frauenheim, P.Blaudeck, U.Stephan, and G.Jungnickel. *Solid State Communications*, **85**:997, 1993.

[14] G.Jungnickel, T.Frauenheim, P.Blaudeck, U.Stephan, and R.J.Newport. *Physical Review B*, **50**:6709, 1994.

[15] M.A. Petrich, K.K. Gleason, and J.A. Reimer. *Physical Review B*, **36**:9722, 1987.

[16] F. Jansen, M. Machonkin, S. Kaplan, and S. Hark. *Journal of Vacuum Science and Technology A*, **3**:605, 1985.

[17] C.Jäger, J.Gottwald, H.W.Spieß, and R.J.Newport. *Physical Review B*, **50**:846, 1994.

[18] J. Fink, T. Müller-Heinzerling, and J. Pflüger. *Solid State Communications*, **47**:687, 1983.

[19] D.R. McKenzie, L.C. Botten, and R.C. McPhedran. *Physical Review Letters*, **51**:280, 1983.

[20] P.W. Atkins. *Physical Chemistry*. OUP, 1978.

[21] F.P.Bundy, H.M.Strong, and R.H.Wentroff. *Chemistry and Physics of Carbon*, volume **10**. Dekker, New York, 1973.

[22] F.P.Bundy and J.S.Kasper. *Journal of Chemical Physics*, **46**:3437, 1967.

[23] A.El-Goresy and G.Donnay. *Science*, **165**:589, 1969.

[24] A.G.Whittaker and P.L.Kintner. *Science*, **161**:589, 1968.

[25] R.B.Aust and H.G.Drickamer. *Science*, **140**:817, 1963.

[26] K.Fujii, N.Shohata, M.Mikami, and M.Yonezawa. *Applied Physics Letters*, **47**:370, 1985.

[27] D.C. Green, D.R. McKenzie, and P.B. Lukins. *Materials Science Forum*, **52&53**:103, 1989.

[28] B. Dischler, R.E. Sah, and P. Koidl. In D.C. Schraum, editor, *Plasma Chemistry - 7^{th} International Symposium*, page 45. Eindhoven, 1983.

[29] B. Dischler, A. Bubenzer, and P. Koidl. *Solid State Communications*, **48**:105, 1983.

[30] P.Couderc and Y.Catherine. *Thin Solid Films*, **146**:93, 1987.

[31] A.Hendry, L.Taub, and H.Gurev. In B.Bendow, editor, *DARPA Workshop on Diamond-like Coatings*, page 100, Albuquerque, 1982. BDM Corp.

[32] J.R.Reimer, R.W.Vaughan, J.C.Knights, and R.A.Lujan. *Journal of Vacuum Science and Technology A*, **19**:53, 1981.

[33] N.R.S. Tait, D.W.L. Tolfree, P. John, I.M. Odeh, M.J. Thomas, M.J. Tricker, J.I.B. Wilson, I.B.A. England, and D. Newton. *Nuclear Instruments and Methods*, **176**:433, 1980.

[34] R.H.Bragg. *Synth. Met.*, **7**:95, 1983.

[35] A.R. Nyaiesh and W.B. Nowak. *Journal of Vacuum Science and Technology A*, **1**:308, 1983.

[36] A.Staudinger and S.Nakahara. *Thin Solid Films*, **45**:125, 1977.

[37] D.E. Polk. *Journal of Non-Crystalline Solids*, **5**:365, 1971.

[38] S.Craig and G.L.Harding. *Thin Solid Films*, **97**:345, 1982.

[39] F.W. Smith. *Journal of Applied Physics*, **55**:764, 1984.

[40] D.J.Miller and D.R.McKenzie. *Thin Solid Films*, **108**:257, 1983.

[41] D.R. McKenzie, R.C.McPhedran, N.Savvides, and L.C. Botton. *Philosophical Magazine B*, **48**:341, 1983.

[42] J.N. Murrell, S.F.A. Kettle, and J.M. Tedder. *The Chemical Bond.* John Wiley & Sons Ltd., Chichester, 1985.

[43] J. Roberston and E.P. O'Reilly. *Physical Review B*, **35**:2946, 1987.

[44] J.L.Bredas and G.B.Street. *Journal of Physics C*, **18**:L651, 1985.

[45] C.Weissmantel. *Thin Films from Free Atoms and Particles.* Academic Press Inc., Orlando, Florida, 1985.

[46] H. Tsai and D.B. Bogy. *Journal of Vacuum Science and Technology A*, **5**:3287, 1987.

[47] P. Koidl, A.Bubenzer, and B.Dishler. *Proc. Soc. Photo-Opt. Instrum. Eng.*, **381**:186, 1983.

[48] P. Koidl, C. Wild, R. Locher, and R.E. Sah. In J. C. Angus, R. E. Clausing, L. L. Horton, and P. Koidl, editors, *Diamond and Diamondlike Films and Coatings*, page 243, New York, 1991. Plenum.

[49] H. Tsai. *Materials Science Forum*, **52** and **53**:71, 1989.

[50] J.E.Field. *Properties of Diamond.* Academic Press, 1979.

[51] B.T.Kelly. *Physics of Graphite.* Applied Science, London, 1981.

[52] P. Koidl, Ch. Wild, B. Dishler, J. Wagner, and M. Ramsteiner. *Materials Science Forum*, **52&53**:41, 1989.

[53] B. Dischler. In P. Koidl and P.Oelhafen, editors, *Amorphous Hydrogenated Carbon Films*, page 189. les Editions de Physique, 1987.

[54] M.F.Ashby and D.R.H.Jones. *Engineering Materials.* Pergamon, 1980.

[55] R.J.Gambino and J.A.Thompson. *Solid State Communications*, **34**:15, 1980.

[56] E.T.Prince and M.M.Romach. *Journal of Vacuum Science and Technology A*, **3**:694, 1985.

[57] D.A. Anderson and W.E. Spear. *Philosophical Magazine B*, **35**:17, 1977.

[58] P.N. Jones, E. Knözinger, W. Langel, R.B. Moyes, and J. Tomkinson. *Surface Science*, **207**:159, 1988.

[59] B.Meyerson and F.W.Smith. *Solid State Communications*, **34**:531, 1980.

[60] D.I.Jones and A.D.Stewart. *Philosophical Magazine B*, **46**:423, 1982.

[61] L.P.Anderson. *Thin Solid Films*, **86**:193, 1981.

[62] B.Bendow. In B.Bendow, editor, *DARPA Workshop on Diamond-like Coatings*, Albuquerque, 1982. BDM Corp.

[63] C.A.Brookes. *Philosophical Magazine A*, **43**:529, 1981.

[64] A.Kelly and N.H.MacMillan. *Strong Solids*. OUP, 1986.

[65] H.J.McSkimin, P.Andreatch, and P.Glynn. *Journal of Applied Physics*, **43**:985, 1972.

[66] X.Jiang, J.W.Zou, K.Reichelt, and P.Grunberg. *Journal of Applied Physics*, **66**:4729, 1989.

[67] X.Jiang, K.Reichelt, and B.Stritzker. *Journal of Applied Physics*, **66**:5805, 1989.

[68] T.Mori and Y.Namba. *Journal of Vacuum Science and Technology A*, **1**:23, 1983.

[69] C.Weissmantel, K.Bewilogua, K.Brater, D.Dietrich, U.Ebersbach, H.J.Erler, B.Rau, and G.Reisse. *Thin Solid Films*, **96**:31, 1982.

[70] K.Enke, H.Dimigen, and H.Hübsch. *Applied Physics Letters*, **36**:291, 1980.

[71] F. Jansen and M. Machonkin. *Thin Solid Films*, **140**:227, 1986.

[72] H.E.Hintermann. *Wear*, **100**:381, 1984.

[73] P.G.Turner, R.P.Howson, and C.A.Bishop. *IOP conference series*, **54**:229, 1980.

[74] A. Bubenzer, B. Dischler, G. Brandt, and P. Koidl. *Journal of Applied Physics*, **54**:4590, 1983.

[75] T.J.Moravec and J.C.Lee. *Journal of Vacuum Science and Technology*, **20**:338, 1982.

[76] L.Holland and S.M.Ojha. *Thin Solid Films*, **58**:107, 1979.

[77] G.Gautherin and C.Weissmantel. *Thin Solid Films*, **50**:L135, 1978.

[78] C.Weissmantel, C.Schürer, R.Frölich, P.Grau, and H.Lechmann. *Thin Solid Films*, **65**:L5, 1979.

[79] C.Weissmantel, K.Bewilogua, and C.Schürer. *Thin Solid Films*, **61**:L1, 1979.

[80] C.Weissmantel. *Thin Solid Films*, **58**:101, 1979.

[81] S.Aisenberg and R.Chabot. *Journal of Vacuum Science and Technology*, **10**:104, 1973.

[82] S.F.Pellicore, C.M.Peterson, and T.P.Henson. *Journal of Vacuum Science and Technology A*, **4**:2350, 1986.

[83] M.L.Stein and S.Aisenberg. US Government Printing Office, Washington, 1981.

[84] S.Aisenberg. *Journal of Vacuum Science and Technology A*, **2**:369, 1984.

[85] J.M.Stevens and M.Stein. In B.Bendow, editor, *Proceedings of the DARPA Workshop on Diamond-like coatings*, page 128, Albuquerque, 1982. BDM Croporation.

[86] *Extended Abstracts of the 13th Biennial Conference on Carbon*, 1977.

[87] *Proceedings of the AAMI 13th Annual Meeting*, 1978.

[88] Y.Lifshitz, S.R.Kasi, and J.W.Rabalais. *Physical Review Letters*, **62**:1290, 1989.

[89] Y.Lifshitz, S.R.Kasi, and J.W.Rabalais. *Materials Science Forum*, **52** and **53**:237, 1989.

[90] J.K. Walters, P.J.R. Honeybone, D.W. Huxley, R.J. Newport, and W.S. Howells. *Journal of Physics - Condensed Matter*, **5**:L387, 1993.

[91] J.K.Walters, P.J.R. Honeybone, D.W. Huxley, R.J. Newport, and W.S. Howells. *Physical Review B*, **50**:831, 1994.

[92] D.Wesner, S.Krummacher, R.Carr, T.K.Sham, M.Strongin, W.Eberhardt, S.L.Weng, G.Williams, M.Howells, F.Kampas, S.Heald, and F.W.Smith. *Physical Review B*, **28**:2152, 1983.

[93] S.Iijima. *J.Cryst.Growth*, **50**:675, 1980.

[94] P.B.Lukins, D.R.McKenzie, and A.M.Vassal lo. Unpublished data.

[95] A.Dilks, S.Kaplan, and A.Van Laeken. *J.Polym.Sci.-Polym.Chem.Ed.*, **19**:2987, 1981.

[96] J.W.Ager, D.K.Viers, and G.M.Rosenblatt. *Physical Review B*, **43**:6491, 1991.

[97] R.E.Shroder, R.J.Nemanich, and J.T.Glass. *Physical Review B*, **41**:3738, 1990.

[98] A.Richter, H.J.Scheibe, W.Pompe, K.W.Brzezinka, and I.Muhling. *Journal of Non-Crystalline Solids*, **88**:131, 1990.

[99] J.W. Zou, K. Reichelt, K. Schmidt, and B. Dischler. *Journal of Applied Physics*, **65**:3914, 1989.

[100] J.W. Zou, K.Schmidt, and K.Reichelt andB.Dischler. *Journal of Applied Physics*, **67**:487, 1990.

[101] P.J.R.Honeybone, R.J.Newport, J.K.Walters, W.S.Howells, and J.Tomkinson. *Physical Review B*, **50**:839, 1994.

[102] J.K.Walters, J.S.Rigden, R.J.Newport, W.S.Howells, and S.F.Parker. *Physica Scripta*, 1994. accepted for publication.

[103] T.J.Moravec and T.W.Orent. *Journal of Vacuum Science and Technology*, **18**:226, 1981.

[104] J.C. Angus, M.J.Mirtich, and E.G.Wintucky. In S.T.Picraux and W.J.Coyke, editors, *Meatstable Material Formation by Ion Beam Implantation*, page 433, Amsterdam, 1982. Elsevier.

[105] J. Fink, T. Müller-Heinzerling, J. Pflüger, B. Scheerer, B. Dischler, P. Koidl, A. Bubenzer, and R.E. Sah. *Physical Review B*, **30**:4713, 1984.

[106] B. Dischler, A. Bubenzer, and P. Koidl. *Applied Physics Letters*, **42**:636, 1983.

[107] S. Kaplan, F.Jansen, and M.Machonkin. *Applied Physics Letters*, **47**:750, 1985.

[108] S.D. Berger, D.R. McKenzie, and P.J. Martin. *Philosophical Magazine Letters*, **57**:285, 1988.

[109] D.R. McKenzie, R.C.McPhedran, N.Savv ides, and D.J.H.Cockayne. *Thin Solid Films*, **51**:247, 1983.

[110] D.Ugolini, M.H.Tuilier, J.Eitle, S.Schelz, J.Q.Wang, and P.Oelhafen. *Applied Physics A*, **51**:526, 1990.

[111] S.Schelz, J.Eitle, R.Steiner, and P.Oelafen. *Applied Surface Science*, **48**:301, 1991.

[112] V.Elings and F.Wudl. *Journal of Vacuum Science and Technology A*, **6**:412, 1988.

[113] S.Prawer and C.J.Rossouw. *Journal of Applied Physics*, **63**:4435, 1988.

[114] Y.Mizokawa, T.Miyasato, S.Nakamura, K.M.Geib, and C.W.Williamson. *Journal of Vacuum Science and Technology A*, **5**:2809, 1987.

[115] J.-P.Hansen and I.R.McDonald. *Theory of Simple Liquids.* Academic Press, 1990.

[116] N.E. Cusack. *The Physics of Structurally Disordered Matter.* IOP Publishing, Bristol, 1987.

[117] J.M.F. Gunn. In B. D. Rainford R. J. Newport and R. Cywin ski, editors, *Neutron Scattering at a Pulsed Source.* Adam Hilger, 1988.

[118] G. Placzek. *Physical Review*, **86**:377, 1952.

[119] J.G. Powles. *Molecular Physics*, **36**:1161, 1978.

[120] J.G. Powles. *Molecular Physics*, **26**:1325, 1973.

[121] L.Pauling and E.B.Wilson. *Introduction to quantum mechanics.* McGraw-Hill Book Company, New York, 1935.

[122] P.M.Morse. *Physical Review*, **34**:57, 1929.

[123] A.Dehbi-Alaoui, A.Matthews, and J.Franks. *Surface and Coatings Technology*, **47**:722, 1991.

[124] W.Dworschak, R.Kleber, A.Fuchs, B.Scheppat, G. Keller, K.Jung, and H.Ehrhardt. *Thin Solid Films*, **189**:257, 1990.

[125] R.Kleber, W.Dworschak, J.Gerber, A.Fuchs, T.Putz, J.Scherer, K.Jung, and H.Ehrhardt. In *Vacuum 1990, Proc. IVC-11 and ICSS-7*, 1989.

[126] J. Franks. *Vacuum*, **34**:259, 1984.

[127] J. Franks. *Journal of Vacuum Science and Technology A*, **7**:2307, 1989.

[128] R.J.Newport. In R. J. Newport, B. D. Rainford, and R. Cywinski, editors, *Neutron Scattering at a Pulsed Source*, chapter 13, page 233. Adam Hilger, 1988.

[129] G.L. Squires. *Introduction to the Theory of Thermal Neutron Scattering.* Cambridge University Press, 1978.

[130] J.M.F. Gunn. In B. D. Rainford R. J. Newport and R. Cywinski, editors, *Neutron Scattering at a Pulsed Source*, chapter 1, page 5. Adam Hilger, 1988.

[131] *User Guide To Experimental Facilities At ISIS*, December 1992. Edited and compiled by B.Boland and S.Whapham.

[132] H.H. Paalman and C.J. Pings. *Journal of Applied Physics*, **33**:2635, 1962.

[133] I.A.Blech and B.L.Averbach. *Physical Review A*, **137**:1113, 1965.

[134] V.F. Sears. *Advances In Physics*, **24**:1, 1975.

[135] J.G. Powles. *Molecular Physics*, **36**:623, 1979.

[136] M.A. Howe, R.L. McGreevy, and W.S. Howells. *Journal of Physics - Condensed Matter*, **1**:3433, 1989.

[137] W.S.Howells. *Nuclear Instruments and Methods*, **223**:141, 1984.

[138] J.D.Wicks. *Studies of disordered materials.* PhD thesis, Oxford University, 1993.

[139] G.J. Kearley. Instructions for climax. January 1988.

[140] G.J. Kearley and J. Tomkinson. *Institute of Physics Conference Series*, **81**:169, 1986.

[141] G.J. Kearley and J. Tomkinson. *Institute of Physics Conference Series*, **107**:245, 1990.

[142] P.J.R. Honeybone, R.J. Newport, W.S. Howells, J. Tomkinson, and P.J. Revell. *Chemical Physics Letters*, **180**:145, 1991.

[143] P.J.R.Honeybone, J.K.Walters, R.J.Newport, W.S. Howells, and J.Tomkinson. *Journal of Non-Crystalline Solids*, **169**:54, 1994.

[144] R.T.Bell. *Introductory Fourier transform spectroscopy.* Academic Press, London, 1st edition, 1972.

[145] P.H. Gaskell, A. Saeed, P. Chieux, and D.R. McKenzie. *Philosophical Magazine B*, **66**:155, 1992.

[146] W.S.Howells. Private communication.

[147] P.J.R.Hoenybone. *Neutron scattering studies of amorphous hydrogenated carbon and silicon carbon.* PhD thesis, University of Kent at Canterbury, 1992.

[148] R.Kleber, K.Jung, H.Ehrhardt, I.Mühling, K.Breuer, H.Metz, and F.Engelke. *Thin Solid Films*, **205**:274, 1991.

[149] R.Kleber, W.Dworschak, J.Gerber, A.Krügler, K.Jung, H.Ehrhardt, S.Schulze, I.Mühling, S.Deutschmann, W.Scharff, F.Engelke, and H.Metz. *Materials Science and Engineering*, **A140**:775, 1991.

[150] T.M.Burke, R.J.Newport, W.S.Howells, K.W.R.Gilkes, and P.H.Gaskell. *Journal of Non-Crystalline Solids*, **164-166**:1139, 1993.

[151] P.B.Lukins, D.R.McKenzie, A.M.Vassallo, and J.V.Hanna. *Carbon*, **31**:569, 1993.

[152] J. González-Hernández, B.S.Chao, and D.A.Pawlik. *Materials Science Forum*, **52** and **53**:543, 1989.

[153] J.K.Walters and R.J.Newport. *Journal of Physics - Condensed Matter*, **7**:1755, 1995.

[154] K.Yusada, H.Masuda, M.Takeda, and A.Yoshida. *Physica Status Solidi (a)*, **95**:249, 1986.

[155] W.B.Nowak. Private communication.

[156] J. González-Hernández, R. Asomoza, A. Reyes-Mena, J. Rickards, S.S. Chao, and D. Pawlik. *Journal of Vacuum Science and Technology A*, **6**:1798, 1988.

[157] Y.Yin, R.E.Collins, and B.A.Pailthorpe. *Journal of Applied Physics*, **71**:3806, 1992.

[158] S.Kumar. *Applied Physics Letters*, **58**:1836, 1991.

[159] R.L. McGreevy and L. Putsztai. *Molecular Simulation*, **1**:359, 1988.

[160] R.L. McGreevy, M.A.Howe, D.A.Keen, and K.Clausen. *IOP conference series*, **107**:165, 1990.

[161] D.W. Huxley, R.J.Newport, A.N.North, and J.K.Walters. In *MRS, Symp. Proc. Volume 170*, page 505, 1992.

[162] L.Pusztai and S.Kugler. *Journal of Non-Crystalline Solids*, **164-166**:147, 1993.

[163] D.W.Huxley. Private communication.

[164] J.K.Walters, J.S.Rigden, and R.J.Newport. *Physica Scripta*, 1994. accepted for publication.

[165] D.A.Drabold, P.A.Fedders, and P.Strumm. *Physical Review B*, **49**:16415, 1994.

[166] T.M.Burke. *An X-ray and neutron scattering study of amorphous hydrogenated carbon.* PhD thesis, University of Kent at Canterbury, 1994.

[167] J.D.Wicks. Private communication.

[168] R.L.McGreevy. Private communication.

[169] M.A. Tamor, W.C. Vassell, and K.R. Carduner. *Applied Physics Letters*, **58**:592, 1991.